AFRL-IF-RS-TR-2001-141
Final Technical Report
July 2001

GENERATION OF REDUCED PARAMETRIC MODELS OF MICRODEVICES FROM HIGH FIDELITY TOOLS FOR SYSTEM LEVEL COMPOSITE COMPUTER-AIDED DESIGN (CAD)

CFD Research Corporation

APPROVED FOR PUBLIC RELEASE; DISTRIBUTION UNLIMITED.

The views and conclusions contained in this document are those of the authors and should not be interpreted as necessarily representing the official policies, either expressed or implied, of the Defense Advanced Research Projects Agency or the U.S. Government.

**AIR FORCE RESEARCH LABORATORY
INFORMATION DIRECTORATE
ROME RESEARCH SITE
ROME, NEW YORK**

20011005 362

This report has been reviewed by the Air Force Research Laboratory, Information Directorate, Public Affairs Office (IFOIPA) and is releasable to the National Technical Information Service (NTIS). At NTIS it will be releasable to the general public, including foreign nations.

AFRL-IF-RS-TR-2001-141 has been reviewed and is approved for publication.

APPROVED: *Claire D. Thiem*

CLAIRE D. THIEM
Project Engineer

FOR THE DIRECTOR: *Michael Talbert*

MICHAEL L. TALBERT, Technical Advisor
Information Technology Division
Information Directorate

GENERATION OF REDUCED PARAMETRIC MODELS OF MICRODEVICES FROM HIGH FIDELITY TOOLS FOR SYSTEM LEVEL COMPOSITE COMPUTER-AIDED DESIGN (CAD)

Marek Turowski, Andrzej Pzekwas, Zhijan Chen,
Zhiqiang Tan, Enchao Yu, Michal Furmanczyk,
Gary Fedder, Tamal Mukherjee, Mark Allen,
Ari Glezer, and Loc Vu-Quoc

REPORT DOCUMENTATION PAGE

1. AGENCY USE ONLY *(Leave blank)*	2. REPORT DATE	3. REPORT TYPE AND DATES COVERED
	JULY 2001	Final Aug 97 - Aug 00

4. TITLE AND SUBTITLE
GENERATION OF REDUCED PARAMETRIC MODELS OF MICRODEVICES FROM HIGH FIDELITY TOOLS FOR SYSTEM LEVEL COMPOSITE COMPUTER-AIDED DESIGN (CAD)

5. FUNDING NUMBERS
C - F30602-97-2-0332
PE - 63739E
PR - E117
TA - 00
WU - 27

6. AUTHOR(S)
Marek Turowski, Andrzej Pzekwas, Zhijan Chen, Zhiqiang Tan, Enchao Yu, Michal Furmanczyk, Gary Fedder, Tamal Mukherjee, Mark Allen, Ari Glezer, and Loc Vu-Quoc

7. PERFORMING ORGANIZATION NAME(S) AND ADDRESS(ES)
CFD Research Corporation
215 Wynn Drive
Hunstville AL 35805

8. PERFORMING ORGANIZATION REPORT NUMBER

4896/15

9. SPONSORING/MONITORING AGENCY NAME(S) AND ADDRESS(ES)
Defense Advanced Research Projects Agency   Air Force Research Laboratory/IFTC
3701 North Fairfax Drive   26 Electronic Pky
Arlington VA 22203-1714   Rome New York 13441-4514

10. SPONSORING/MONITORING AGENCY REPORT NUMBER

AFRL-IF-RS-TR-2001-141

11. SUPPLEMENTARY NOTES
Air Force Research Laboratory Project Engineer: Clare D. Thiem/IFTC/(315) 330-4893

12a. DISTRIBUTION AVAILABILITY STATEMENT
APPROVED FOR PUBLIC RELEASE; DISTRIBUTION UNLIMITED.

12b. DISTRIBUTION CODE

13. ABSTRACT *(Maximum 200 words)*
Microelectromechanical Systems (MEMS), also known as microsystems, consist of interconnected arrays of mechanical, electrostatic, thermal, structural, optical, fluidic, magnetic, and electronic components. Individual components can be simulated using multi-dimensional high fidelity computational tools based on first principles and Partial Differential Equations. For system level design, where large numbers of devices are interconnected, use of detailed 3-D models of each component is unrealistic. A more practical approach is to develop simplified but accurate sub models. A software system for the automated generation of reduced or compact models of microdevices from high fidelity 3-D simulations was developed, demonstrated, and validated. During this effort: fluidic, electromechanical, and thermal phenomena were examined; new concepts for reduced models were pursued; the burden of generating 3-D models from Electronic Design Automation (EDA) layouts and process data was eased; and procedures to exploit interface and import/export CAD/EDA standards were defined. Results of this effort were incorporated into CFD Research Corporation's commercial Computer-Aided Design (CAD) tool suite along with Carnegie Mellon University's NODAS system-level CAD tool. The results of this effort have been applied to a variety of real problems of interest to both the defense industry and commercial Market.

14. SUBJECT TERMS
Computer-Aided Design,CAD, Microelectromechanical Systems, MEMS, Microsystem, Finite Element Method,Fluidic,Electromechanical,Thermal,Matrix Reduction, Reduced Order Model, Compact Model,Partial Differential Equation,Ordinary Differential Equations,Mesh Generation

15. NUMBER OF PAGES
252

16. PRICE CODE

17. SECURITY CLASSIFICATION OF REPORT	18. SECURITY CLASSIFICATION OF THIS PAGE	19. SECURITY CLASSIFICATION OF ABSTRACT	20. LIMITATION OF ABSTRACT
UNCLASSIFIED	UNCLASSIFIED	UNCLASSIFIED	UL

ABSTRACT

This project was a three year team effort (1997 – 2000), led by CFD Research Corporation (CFDRC), with Carnegie Mellon University (CMU), Georgia Institute of Technology (GT), and University of Florida (UF). As a result of this project, we have **developed**, **demonstrated**, and **validated** a **Software System for Automated Generation of Reduced or Compact Models of Microdevices from High Fidelity 3-D Simulations**, including: • new concepts of reduced/compact models of electro-mechanical, fluidic, and thermal phenomena in Micro-Electro-Mechanical Systems (MEMS); • interfaces and import/export procedures for CAD/EDA standards, to enable easy and automatic building of three-dimensional (3-D) models from EDA layouts and process data; • new, updated, and validated features in CFD-ACE+ for reliable high-fidelity simulations of coupled physical phenomena specific for microdevices; • procedures and user-friendly interfaces for extraction of compact-model parameters (characteristics) from 3-D simulations; • output formats compatible with system-level simulators like SPICE, SABER/MAST, VHDL-AMS; • libraries of reduced models for MEMS CAD system-level tools, like NODAS from CMU; • tools in CFD-ACE+ allowing for use of reduced or mixed dimensionality in 1D, 2D, or 3-D simulations of MEMS devices and systems.

The **most important accomplishments** include:

- Compact models (SPICE and SABER) of air-damping in MEMS, validated with CFD-ACE+ 3-D simulations, and inserted into the NODAS MEMS-design-system library from CMU.
- Automatic generation of reduced thermal models (R-networks) for MEMS micro-heaters.
- Developed mixed-dimensional and compact fluidic models of microchannels, microvalves, micropumps, droplet generators, and synthetic jets, and procedures of their generation.
- A new software, CFD-Micromesh, for automatic 3-D solid model generation and meshing from MEMS layouts imported directly from CAD/EDA systems. The popular layout formats (GDSII, CIF, DXF) are imported easily, allowing direct coupling with several commercial IC design tools.
- At CMU: * The compact squeeze film model was compared with experimental data from a CMOS-MEMS bandpass filter. The NODAS simulation results with new model are in excellent agreement with the experimental measurements (error decreased from 20% to 2%). * A first-order model for lateral damping within NODAS. * A new data format GBV (Geometry, Boundary and Volume conditions) for interchange of simulation data between Cadence and CFDRC simulators.
- At GT: * Fabricated synthetic jets with integrated MEMS modulators and measured with PIV. * Measured characteristics of arrays of synthetic jets in active control of microsystem temperature. * The data measured with infra-red camera was successfully compared with numerical simulations at CFDRC, including the use of reduced models in jet arrays.
- At UF: * New matrix reduction techniques for structure dynamics, based on Lanczos method, WYD Ritz algorithm. * Validation of the implementation of Lanczos algorithm through comparison with a MEMS-bridge structure from MIT. * Testing the new methods on the crab-leg flexure MEMS structure. * The tests showed from 600x to 10,000x acceleration in comparison to full 3-D FEM computation time. * Implementation of the WYD algorithm in the CFD-ACE+ code of CFDRC.

The high-fidelity and compact models developed in this effort have already been used in design work by *Kodak* (ink-jets); *Delphi Automotive* (air-damping in accelerometers), *Lucent*

(micromirrors), and contributed to the **DARPA HERETIC** Program in modeling and design of active cooling of VCSEL Arrays (*Georgia Tech, Honeywell),* Microprocessor Chips (*Georgia Tech, Intel*). This effort resulted also in awarding CFDRC with a **new SBIR** contract "High Speed Inertial MEMS Sensors with Field Emitter Array Readout" from U.S. Air Force (**AFRL/VSSE**) to design novel accelerometers and gyroscopes for satellite and vehicle positioning.

TABLE OF CONTENTS

LIST OF FIGURES

LIST OF TABLES

ACKNOWLEDGEMENTS

1   INTRODUCTION

1.1   <u>Background</u>

This project began in August 1997. It was a three year team effort between CFD Research Corporation, Carnegie Mellon University, Georgia Institute of Technology, and University of Florida.

The objective of this project was to develop, demonstrate and validate a software system for automated generation and selection of reduced compact models (CMs) of MEMS devices from high fidelity 3-D models. The developed, extracted, and validated CMs would be used in two types of environments:

- within a system-level behavior simulation (like SPICE or SABER) to support mixed technology CAD tools for microsystems; and
- as subgrid models within CFD-ACE+, a 3-D field simulation environment used for larger scale (system/package) analysis.

Major activities in this program were organized to take advantage of the expertise of each team member:

- **CFDRC:** (Dr. Marek Turowski, Dr. Andrzej Przekwas, Dr. Zhijian Chen) project coordination, new reduced/compact model concepts, software development, validation, demonstration, and applications.

- **Carnegie Mellon University:** (Dr. Gary Fedder, Dr. Tamal Mukherjee) reduced model generation for inertial sensors, interfaces for geometry extraction for 3-D modeling from MEMS standard CAD/EDA systems, interfaces to MEMS synthesis database, library of reduced models, software validation.

- **Georgia Tech:** (Dr. Mark Allen, Dr. Ari Glezer) fabrication of batch of synthetic microjet devices, full field experimental characterization of microjet devices, experimental extraction of compact models and verification against computationally generated models, development of fabrication dependent multi-disciplinary material property database.

- **University of Florida:** (Dr. Loc Vu-Quoc) development of formal mathematical methods for reduced model generation from FEM simulators, development and implementation of model extraction and reduction capability in FEM-STRESS and CFD-ACE+ for stress/deformation simulations in MEMS high-level design.

This report documents the work performed during the three years of the project.

1.2 Project Motivation

Micro-Electro-Mechanical Systems (MEMS) consist of interconnected arrays of mechanical, electrostatic, thermal, structural, optical, fluidic, magnetic, and electronic components. Individual components can be simulated using multi-dimensional high-fidelity computational tools based on first principles and Partial Differential Equations (PDEs). For system level design, where large numbers of devices are interconnected, use of detailed 3-D models of each component is unrealistic. A more practical approach is to develop simplified but accurate enough submodels. Reduced or Compact Models (CMs) expressed in terms of Ordinary Differential Equations (ODEs) or 1D-PDEs would perform this task. For example, a 3-D Navier-Stokes equation system could be reduced to 1D Stokes or Couette type parametric relation CMs, mixing reaction channels/chambers could be reduced to 1D plug flow or 0D stirred reactor equivalents.

Neither Electronic Design Automation (EDA) nor mechanical CAD can adequately support chips that incorporate MEMS devices. The scale is much different and the materials properties are different. At the beginning of the DARPA Composite CAD Program there were many challenges facing those developing design tools for MEMS-on-a-chip. These included a need to integrate EDA and TCAD (Technology CAD) tools with solvers for mechanical, electrostatic, magnetic, thermal, fluidic and optical domains; the slow speed of 3-D mechanical finite-element analysis tools; a lack of software models; and a need to do extensive physical prototyping. The development of design-synthesis and design-validation tools would greatly simplify the process.

Similarly to the VLSI electronic industry, there is a great need of "MEMS synthesis" software tools. A MEMS synthesis tool would generate a physical layout cell for an on-chip MEMS device from user-defined parameters. Synthesis process needs fast simulation tools to optimize the design. This requires reduced or compact models of MEMS devices, based on algebraic models, not partial differential equations. In such a case, the speed of simulation is exchanged for accuracy of modeling. There was a big need to make adequate reduced models to ensure that design constraints have been met. Model generation has been a key problem area in MEMS synthesis and system-level design.

There was also a great need to develop design aids for a "micro-bio-chemical network". In brief, such a system would include "wells" that could contain reaction or observation chambers, and "channels" that might transport microliters of fluids between wells. Researchers are hoping to put hundreds of wells and channels on a single chip, making it possible to analyze a number of different reagents from very small samples. To be able to design an entire system like this, there was a need of software that can use the results from a computational fluid dynamics (CFD) solver, and allow designers to run simulations similar in nature to SPICE. The goal is a tool that can generate and lay out microfluidic circuits according to the user's constraints. Another task was to take the results of a full 3-D simulation, generate a behavioral model and bring it into SPICE for an analysis of interactions with electrical systems.

The existing EDA software needed to be extended in three areas: physical design, analysis and behavioral design. In the physical-design area, there was a great need of a solid model generator using directly layouts from EDA layout editors, which would produce a 3-D representation of what a mixed-technology chip will look like. In the analysis phase, that representation has to be passed to a mixed-domain boundary-element or finite-element analysis tool. This tool should be

able to co-simulate in the electrostatic, thermal, and fluidic domains. For the behavioral level, a behavioral model builder had to be developed so that SPICE type simulations tools should be able to handle mechanical, thermal, and fluidic variables.

1.3   Project Objectives

The objective of this project was to **develop**, **demonstrate**, and **validate**:

- **Software System (in CFD-ACE+) for Automated Generation of Reduced or Compact Models of Microdevices from High Fidelity 3-D Simulations**
  including:

  - new concepts of reduced/compact models of electro-mechanical, fluidic, and thermal phenomena in MEMS;

  - interfaces and import/export procedures for CAD/EDA standards, to enable easy and automatic building of 3-D models from EDA layouts and process data;

  - new, updated, and validated features in CFD-ACE+ for reliable high-fidelity simulations of coupled physical phenomena specific for microdevices;

  - procedures and user-friendly interfaces for extraction of compact-model parameters (characteristics) from 3-D simulations;

  - output formats compatible with system-level models, for simulators like SPICE, SABER/MAST, VHDL-AMS;

  - libraries of reduced models for MEMS CAD system-level tools, like NODAS;

  - tools in CFD-ACE+ allowing for use of reduced or mixed dimensionality in 1D, 2D, or 3-D simulations of MEMS devices and systems.

Classes of Reduced Models to Be Considered:
A.   Phenomenological (behavioral), based on fitted curves, lookup tables, etc.,
-    simulators: SABER (MAST, VHDL-AMS), SPICE, Spectre (from Cadence);

B.   Parametric Models based on Physical Decomposition,
-    physics-based decomposition of the problem into sub-problems that can be described by analytical, parameterized equations,
-    simulators: SABER, HSPICE;

C.   Discrete – reduced-size physical distributed models based on PDEs,
-    "mixed mode" simulators: 2D/3-D PDE solvers coupled with external system/circuit;

D.   Formally Reduced Matrix Systems,
-    FEM models reduced with Wilson-Ritz, Lanczos, or Arnoldi approach;
-    simulators: matrix/vector solvers coupled with external system/circuit (e.g. MATLAB).

Domains and Devices Identified for Investigation in This Project:
1.   Fluidic

- damping: inertial sensors, plates, plates with holes, combs, cantilever beams/plates, moving micromirrors;
  - microjets: single jet, multiple jets, multiple jets for electronic cooling, multiple jets for flow control;
  - microchannels
2. Electro-Mechanical
  - beams, plates, bridges actuated electrostatically
  - electrostatic inertial sensors (comb drives and resonators)
3. Thermal
  - microheaters
  - MEMS packages
  - synthetic-jet based cooling systems

1.4   Summary of Accomplishments

All of the accomplishments aimed for fulfillment of the main objective of this project and its components, as described in the previous section. Following subsections list the most important accomplishments categorized by their role in the contribution to the main objective.

New Reduced/Compact Models of Microdevices

- New nonlinear compact models of squeeze film damping in MEMS, validated with CFD-ACE+ 3-D simulations, and implemented in SPICE and SABER formats (Figure 1), and implemented in NODAS MEMS-CAD system at CMU.
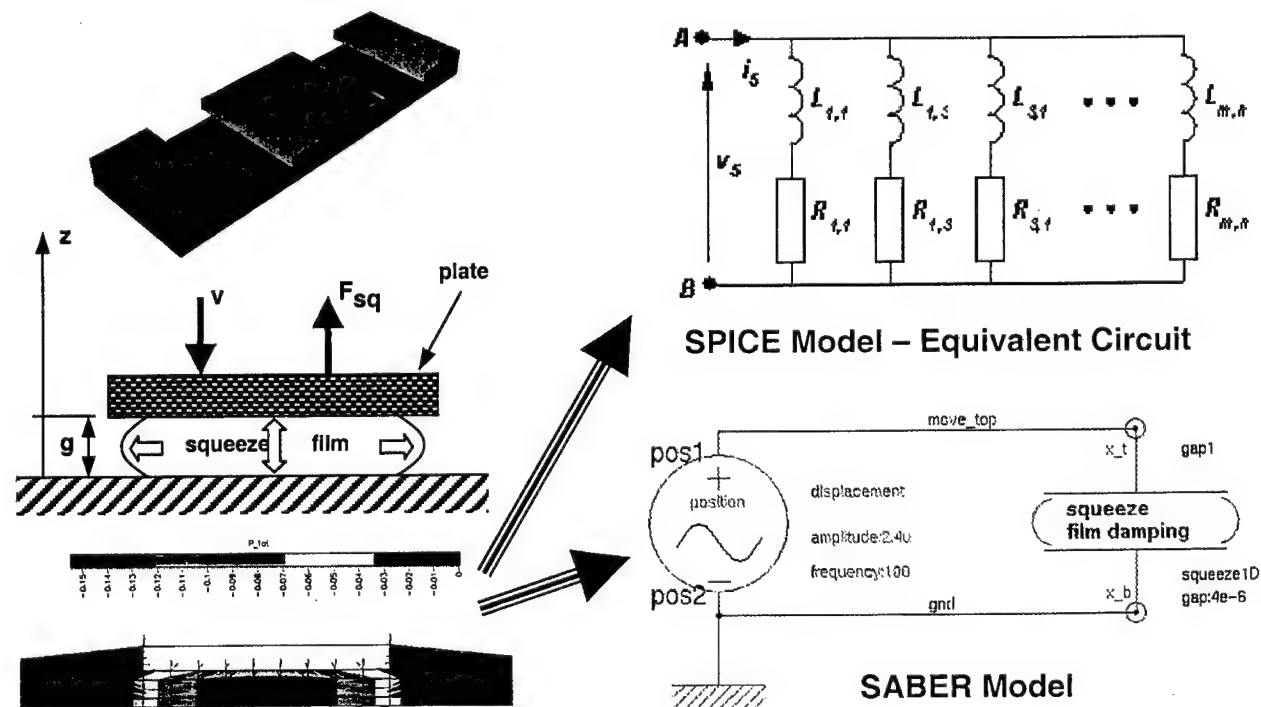
Figure 1. Compact models of squeeze film damping for system-level simulators (SPICE and SABER), derived from high-fidelity simulations.

4

- The new compact squeeze film model was successfully compared with experimental data from a CMOS-MEMS bandpass filter. The NODAS simulation results with the new damping model are in excellent agreement with the measurements.
- New compact model of lateral (shear) damping in MEMS, validated with CFD-ACE+ (Figure 2).
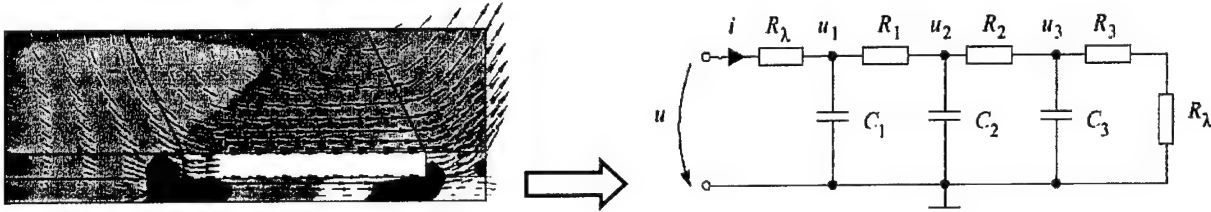
Figure 2. Equivalent circuit representing the lateral shear damping forces, derived and validated with CFD-ACE+ high-fidelity simulations.

- Developed mixed-dimensional and reduced fluidic models of microchannels, microvalves, micropumps, droplet generators, synthetic jets, and piezoelectric micropump.

- Novel concept of compact models for synthetic jets, using a polyhedral control volume capability of CFD-ACE+ software tool, to model complex dynamic 3-D shapes with moving walls with multiple inlets/outlets with a single cell "super element". The model was validated against 3-D high-fidelity simulation data obtained for a range of parameters.

- New equivalent-circuit models, in SPICE and SABER formats, for arbitrary-shaped fluidic microchannels, and procedures of their generation (Figure 3).
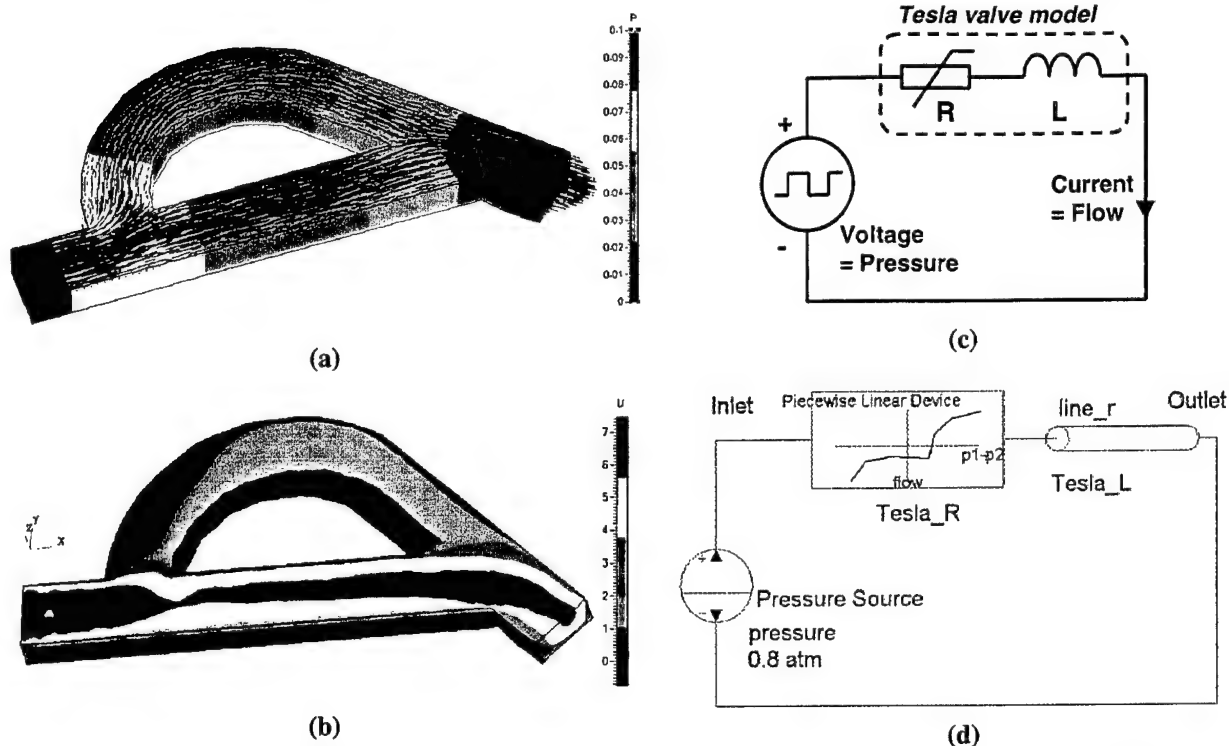
Figure 3. CFD-ACE+ high-fidelity simulations (a and b) are used to generate compact models of an arbitrary nonlinear fluidic microchannel, for SPICE (c) or for SABER (d).

- New Matrix Reduction Techniques for structure dynamics: Lanczos method and WYD Ritz algorithm, developed at UF. Tests showed up to 10,000x acceleration in comparison to full 3-D FEM computation time.

Interfaces And Import/Export Procedures for CAD/EDA Standards, To Enable Easy And Automatic Building of 3-D Models from EDA Layouts And Process Data

- Enhancement of CFDRC software to process CAD data for MEMS design. We are now able to read input files in the formats: **DXF**, IGES, PATRAN, CIF, GDS II, and several others.

- Two new data formats have been implemented in CFD-GEOM, enabling input and conversion from external files coming from Electronic Design Automation (EDA) tools:
  * **CIF** (Caltech Intermediate Form)
  * **GDS II** (Calma stream format)

- Implementation of **VRML** (Virtual Reality Modeling Language) into the computational environment of CFDRC. An interface between CFDRC's FastBEM program and VRML-based GUI have been developed.

- A new software, **CFD-Micromesh**, has been developed during this project at CFDRC, for automatic 3-D solid model generation and meshing from MEMS layouts imported directly from CAD/EDA systems. The popular layout description formats, CIF and GDSII, are imported easily into CFD-Micromesh, allowing coupling the software with

6

several commercial IC design tools. The new tool is fast and equipped with user-friendly graphical user interface (GUI) – see Figure 4.
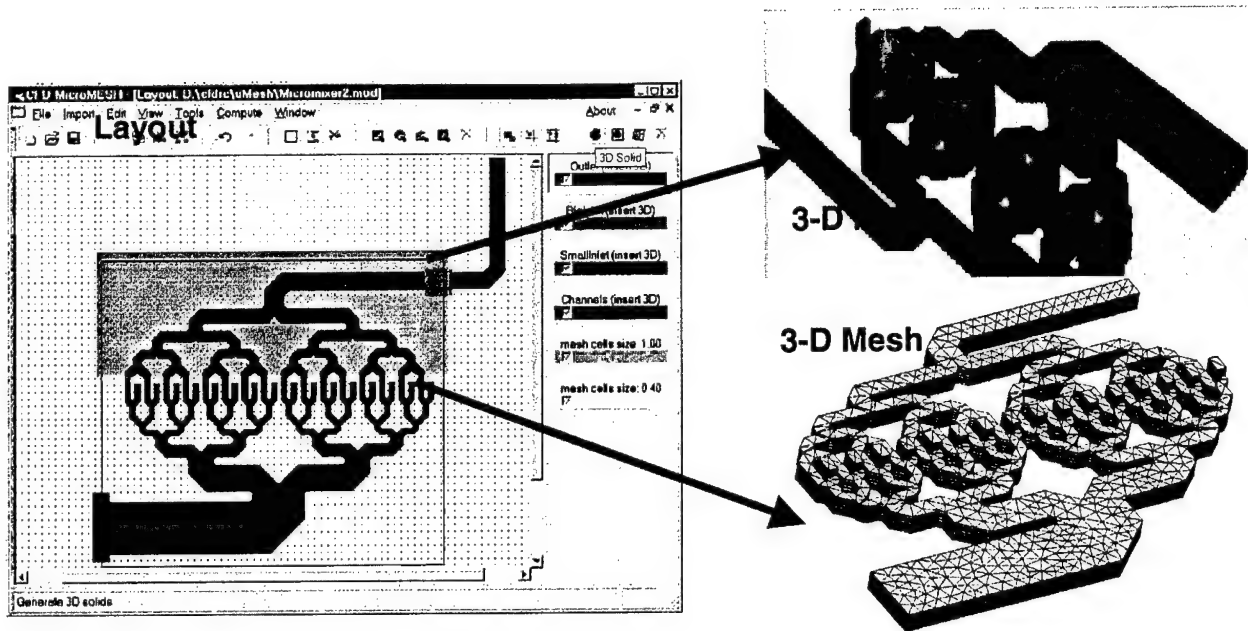
Figure 4. CFD-Micromesh: fast, automatic generation of 3-D device models from layouts (EDA tools) and process data.

By clicking only a single button in CFD-Micromesh, a three-dimensional solid model is generated fully automatically from layout, as shown in Figure 4. Building the 3-D model as well as automatic generation of a full 3-D unstructured computational mesh, again only by clicking a single button in CFD-Micromesh, is performed typically within several minutes on a current PC workstation. The automatically generated three-dimensional device model, with the unstructured 3-D computational mesh in DTF format, is imported directly into CFDRC's simulator CFD-ACE+.

- Developed interfaces between CFDRC software/databases and the following CAD tools:
   * **SABER**
   * **CADENCE**

An agreement with Cadence Design Systems, Inc. has been negotiated to develop interfaces and integration of CFDRC's MEMS simulation software with Cadence CAD tools (see Figure 5). See Section 3.1 for more details.

7
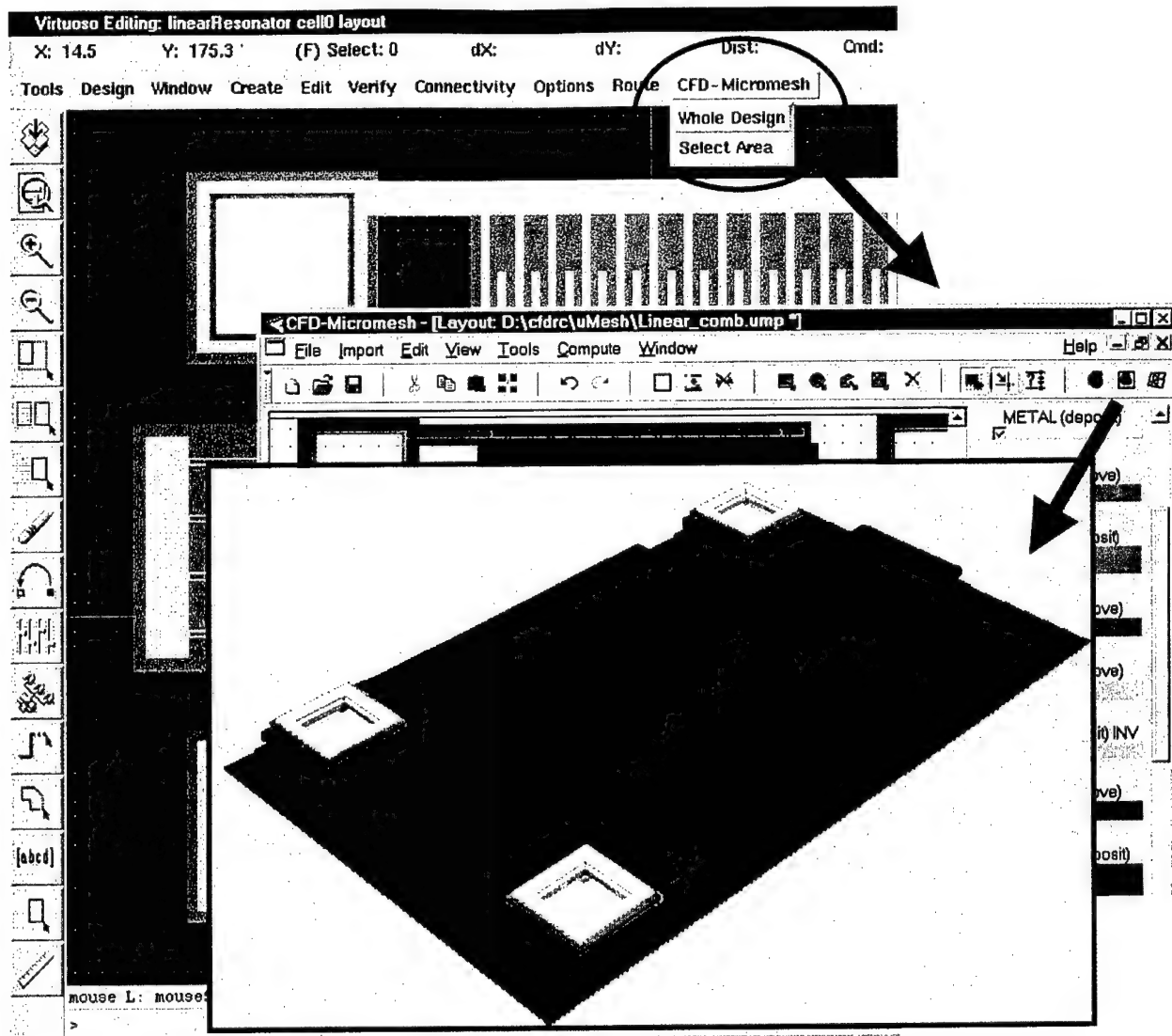
Figure 5. CFD-Micromesh is launched directly from Virtuoso Layout Editor in Cadence Design Framework for 3-D Modeling and Visualization.

- A new data format (called GBV – Geometry, Boundary and Volume conditions) for interchange of simulation data between Cadence Design Framework II schematic view and CFDRC ACE+ simulator has been developed at CMU.

New Features in CFD-ACE+ for High-Fidelity Simulations Specific for MEMS

- Second order boundary conditions for wall treatment.

- Second order time treatment, through modified Crank-Nicolson scheme.

- Automatic grid remeshing for arbitrary moving boundaries/bodies in 6 degrees of freedom (DOFs). A trans-finite interpolation (TFI) technique with mesh smoothing was developed and implemented, which allows for effective simulation of dynamic 3-D motion of mirrors, membranes, gyroscopes, and other MEMS structures.

8

- New capability in CFD-ACE+ for extraction lumped parameters (normal/tangential force, torque, total pressure and/or flow) for compact model generation.

- "Property Manager" - new interactive framework software for MEMS material property database.

Procedures And User-Friendly Interfaces For Extraction Of Compact-Model Parameters (Characteristics) From High-Fidelity Simulations

- Automatic generation of reduced thermal models (R-networks) for MEMS micro-heaters.

- Capability to perform parametric runs in CFD-ACE+ through graphical user interface, for mechanical, electrostatic, and fluidic simulations both steady-state and transient.

- A dedicated computer program Squeeze, written in portable C++ language, for automatic generation of input list in SABER or SPICE format, describing equivalent-circuit model of squeeze-film damping between moving plates.

- Procedures for automatic generation of compact model (extraction of lumped capacitances) of a comb-drive resonator, using results of high-fidelity 3-D electrostatic simulations with FastBEM from CFDRC.

- Procedures for automatic generation of equivalent-circuit models of microfluidic devices from parametric runs of CFD-ACE+; examples of SPICE and SABER compact models of Tesla valve.

- Procedures of FEM model reduction based on Arnoldi method for electro-mechanical microdevices, developed at Prof. Jacob White's group at MIT within the Composite CAD Program, have been implemented and installed at CFDRC and demonstrated and tested in coupling with CFD-ACE+ code.

Libraries Of Reduced Models for MEMS CAD System-Level Tools

- The new compact models of squeeze film damping have been incorporated into the NODAS MEMS-CAD system library from CMU.

- The new compact models of lateral shear damping have also been inserted into the NODAS MEMS-CAD system library.

- The frequency dependent transfer function of lateral damping has been implemented in Verilog-A as a Laplace transform.

Validation/Demonstration of the New CFD-ACE+ Features and the New Reduced Models

- At Georgia Tech (GT):
  - Fabricated micromachined synthetic jets with integrated MEMS modulators.

- Several methods have been used to test the synthetic jets and modulator arrays: visual deflection test, flow modulation test, Schlieren visualization, pitot tube, x-wire anemometer, and particle image velocimetry (PIV).
- Characteristics of performance of arrays of synthetic jets in local active control of microsystem temperature were measured with infra-red (IR) camera.

- The PIV flow data from GT were compared successfully with 2D and 3-D numerical simulations from CFD-ACE+.

- The temperature-system data measured at GT with IR camera were compared successfully with numerical simulations at CFDRC, including the use of reduced models in jet arrays.

- At University of Florida (UF):
  - Validation of the implementation of Lanczos algorithm through comparison with a MEMS structure from MIT.

- At Carnegie Mellon University (CMU):
  - Experimentally verified the squeeze film model using a three resonator CMOS micromachined mechanical filter to show that the improved squeeze film model reduced error in quality factor (Q) computation from 20% to 2%.
  - Experimentally verified the lateral damping model using folded flexure MUMPS resonators. Inclusion of finite size effects reduced errors from 20% to 8%.

- At CFDRC, both the high-fidelity 3-D CFD simulations of Tesla valve and its compact models in SPICE and Saber were successfully compared with characteristics measured at University of Washington.

The mixed-dimensionality, multi-energy domain capability in CFD-ACE+ is the first ever computational software applicable to both micro-scale, system-scale and mixed micro/system-scale simulations. The macro-scale (package) allows the user to verify the performance of the microdevice (sensor, transducer, actuator, power device, optoelectronic array) in an external system or environment.

"Success Stories":

The Project Team has had a strong commitment to demonstrating and validating the usefulness of the newly developed tools to real problems relevant to both the defense industry and the commercial market. Listed below are some examples of such applications contributing to the "Success Stories" of the DARPA Composite CAD Program:

- CFDRC's High-Fidelity and Compact Models of Ink-Jets used by **Kodak**.
- Reduced Models of Synthetic Jets used for Virtual Flight Control Simulation.
- Air-Damping Compact Models used by **Delphi Automotive Systems**.
- Air-Damping Compact Models under development for **Lucent Technologies**, for analysis and design of MEMS-based micromirrors for fast optical switching.

- Reduced Models of Synthetic Jets will be used within the DARPA HERETIC Program (Heat Removal by Thermo-Integrated Circuits), where CFDRC will support modeling and design of Arrays of Synthetic Microjets for active cooling of:
  - VCSEL Arrays (Linear and 2D)   - *Georgia Tech + Honeywell*
  - Microprocessor Chips   - *Georgia Tech + Intel.*

- CFDRC has been awarded a new SBIR contract in 2000, for *U.S. Air Force (AFRL/VSSE),* to develop "High Speed Inertial MEMS Sensors with Field Emitter Array Readout" for application in novel gyroscopes for satellite and vehicle positioning, etc.

2   NEW FEATURES IN CFD-ACE+

2.1   Automatic Grid Remeshing

A new capability has been implemented in CFD-ACE+ at CFDRC to facilitate automatic grid remeshing for arbitrary moving boundaries/bodies in 6 degrees of freedom (DOFs). A transfinite interpolation (TFI) technique with mesh smoothing was developed. This functionality allows effective simulation of dynamic 3-D motion of mirrors, membranes, gyroscopes, and other MEMS structures. Details are described below.

General Dynamic Grid Generation

A new capability of the general dynamic grid generation using TFI (Trans-Finite-Interpolation) methodology has been developed and implemented in CFD-ACE+ code, to enhance the numerical simulation of MEMS flow problems. Due to the deformation of boundary, it is often required to remesh the grids. Without the technique of TFI, a user actually needs to develop grid generation packages for each individual geometry. It is sometimes very difficult for a complicated geometry. Sometimes the transformation without TFI technique cannot guarantee the similarity of geometry.

Without delving into details, TFI transforms any curvilinear grids on ratio of arc lengths in each direction. It is thus inherently "structured". Based on the deformations on boundaries, TFI creates a linear topology mapping to calculate deformation inside the domain, i.e.

$$dr_i = f(dr_{bc}) \tag{2.1}$$

where, dr_i is the deformation vector of internal grids and dr_{bc} is the deformation vector on the boundary. TFI creates the relation function by calculating the ratio of the arc length of each grid point to the boundary points (see Figure 6).

$$f = \sum_{j=W,E,S,N,L.H} dr_j S_j \Big/ (S_j - S_{j+1}) \tag{2.2}$$

where, S_j is the arc length between point i to j, and then remeshing interior grids by

11

$$r_n = r_o + dr_i \tag{2.3}$$

where, r_n and r_o are new and old meshes. TFI preserves the similarity of geometry during the transformation by linear mapping relation function. Figure 7 shows the results of different transformations.
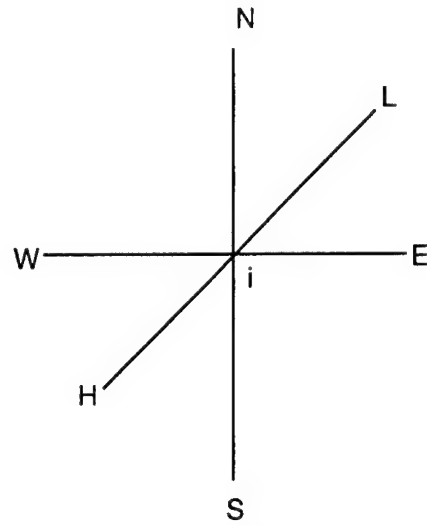
Figure 6. Grid point in a structured mesh and the boundary points.
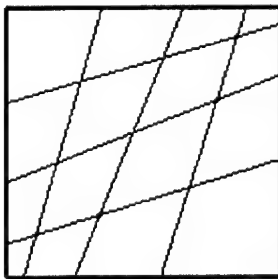
(a) initial grids   (b) original remesh   (c) TFI remesh
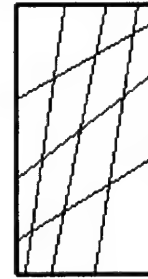
Figure 7. Illustration of Dynamic Grid Remeshing.

2.2   Multiple Parametric Runs

To enable automatic generation of reduced models for MEMS applications, it is often needed that some parameters of several 3-D simulations need to be changed dynamically for subsequent computations. The most typical example is stepping through oscillation frequency of a device simulation, to obtain its characteristics in frequency domain, or stepping through a boundary pressure value for a microfluidic device to obtain its static pressure-flow characteristic.

A new feature of CFD-ACE+, that enables such multiple parametric runs of the program, was developed and implemented in this project. CFD-ACE+ solver reads the definitions of changing analysis parameters from an external text file (file name with the extension *.par*) and

automatically re-runs the jobs, with new input parameters for each run. The new feature helps to calculate multiple cases without stopping the software. The format of a *.par* file looks as follows:

Case n

Surface m : BC_name, motion_type = formula

where,

n = 1, 2, 3 ...,   - number of the case;
m = 1, 2, 3 ...,   - number of the surface;
BC_name   - name of a specific boundary;
motion_type   - definition of a motion.

Below is an example of a *.par* file for two automatic runs of simulations, with oscillation frequencies 100 Hz and 200 Hz.

```
----------------------------------------------------------------
Case 1
Surface 1 : side_wall, Translation_y = 0.01*sin(2*3.14*100*t)

Case 2
Surface 1 : side_wall, Translation_y = 0.01*sin(2*3.14*200*t)
----------------------------------------------------------------
```

Note that a user has a possibility to define multiple formulas for a particular surface, which has to be assigned a specific name before the job is run. The CFD-ACE+ software will read all the formulas from the *.par* file and automatically run all the subsequent jobs, saving required results into another disk file (*.dat*). The required results and the output format specification can be defined in an optional text file with extension *.fmt* (see next section).

A new graphical user interface panel has been also introduced into CFD-GUI to allow easy setup of the parametric runs through graphical windows. The relevant plots of requested characteristics can be ordered through Simulation Manager in CFD-ACE+.

2.3   Output of Integral Surface Results for Static or Transient Characteristics

To be able to use directly the results of CFD-ACE+ simulations to plot device characteristics, or time-dependent waveforms of selected variables, you can order writing the selected integral surface values to a text file in the current simulation directory. The file with results (text tables) will have the extension *.dat*. The data from this file can also be used directly **to create a compact model** of the analyzed device.

To define which values you want to be printed in the output table files, you have to create an external text file, called "format file" with extension *.fmt*. This file should include definitions of surface-output or integral quantities, which you want from ACE+ simulations, and optionally, scaling factors for them (to obtain ready results in desired units).

Below is an example of a *.fmt* file created for a Tesla valve simulation, to obtain static flow-pressure characteristics. In the *Tesla.fmt* file, we order an output text file including the Mass Flow value and the mean pressure value P_mean at the Channel_Outlet surface, and the same for

the Channel_Inlet surface. The Mass Flow value is scaled by (60*2*1e6) to obtain results directly in μL/min (the original value would be kg/s).

```
*********************************************************

          Example of format file:   Tesla.fmt

*********************************************************
Surface  : Channel_Outlet
Variable : Mass Flow, M*60*2*1e6
Variable : P_mean

Surface  : Channel_Inlet
Variable : Mass Flow, M*60*2*1e6
Variable : P_mean
*********************************************************
```

An example of an output file, for the combined parametric runs using *Tesla.par* file, and the integral surface output data ordered with *Tesla.fmt* file, is shown below. Note that the Mass Flow value is scaled, and is printed directly in μL/min, and the P_mean pressure values are in pascals (N/m^2).

```
*********************************************************

          Example of file:   Tesla_CHANNEL_OUTLET.dat

*********************************************************
   Mass Flow
   P_mean
   Case   1 :   Iter. #   100    1.556542E+03   6.869466E+03
   Case   2 :   Iter. #   100    2.385028E+03   1.288921E+04
   Case   3 :   Iter. #   100    3.044021E+03   1.857335E+04
   Case   4 :   Iter. #   100    3.610177E+03   2.405173E+04
   Case   5 :   Iter. #   100    4.114709E+03   2.938847E+04
   Case   6 :   Iter. #   100    4.574686E+03   3.461645E+04
*********************************************************
```

The tabularized results from the output file can be imported directly into many plotting programs, like Excel, Xmgr, etc. An example of the results imported into Excel, and the characteristic plotted directly from the parametric CFD-ACE+ simulations, are shown below. The computed results are plotted together with experimental measurements of the Tesla valve, obtained and published by R. Bardell and F. Forster from University of Washington (ASME 1998, DSC - Vol.66).
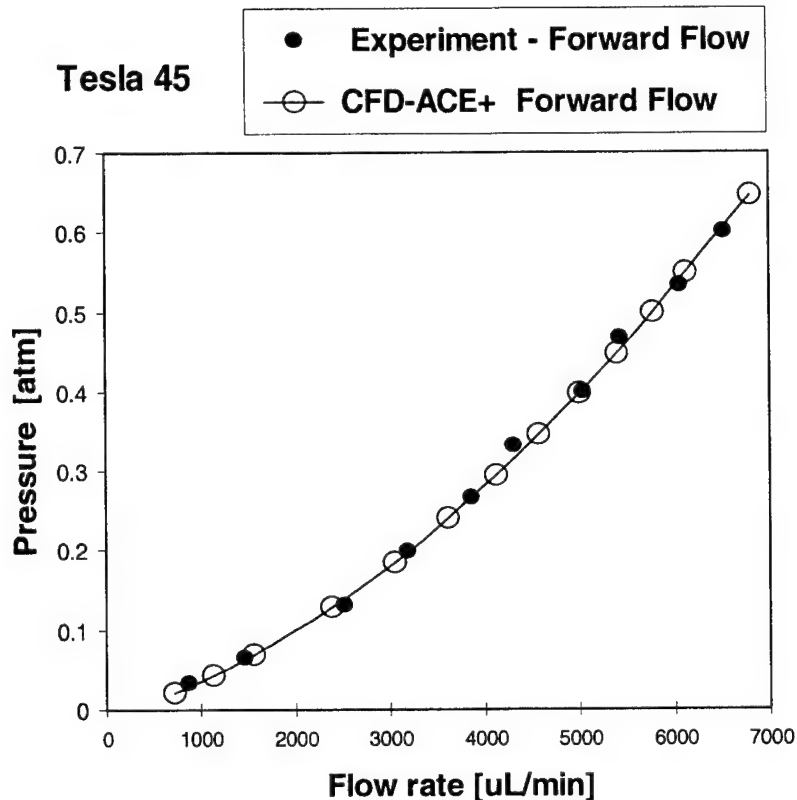
Figure 8. Tesla Valve characteristics plotted directly from the parametric CFD-ACE+ simulations, together with experimental results from the University of Washington.

2.4 Material Properties Database Manager

A reusable, open database for MEMS/microdevices materials data for structural, thermal, and electromagnetic properties has been developed:

- CFDRC has developed "Property Manager" - prototype interactive framework software for MEMS material property database. Property Manager allows for very flexible material property description and storing of data, including searching, sorting, extraction, etc. The new format enables fabrication-dependent material properties (coming from different semiconductor fabs), corresponding to the actual MEMS device being simulated. See detailed description below.

- GT participated in collecting and providing the input of fabrication-dependent data into the database. The material data are being placed in the Material Property Manager developed by CFDRC in this task.

Property Manager (PM) is a database system which will help the user to manage various materials and their associated properties. The basic database functions include Add, Modify, Delete, and Sort. The stand alone version of PM provides the user a simple and fast way to access the material database. Also, it can be integrated to CFD-GUI and other software packages in order to define materials which are part of a problem setup. All data in the Property Manager

15

will be treated as generic data. No physical meaning is programmed into PM so the database can be expanded virtually unlimited.

Data Structure
The data structure of the material database can be represented as the following figure.
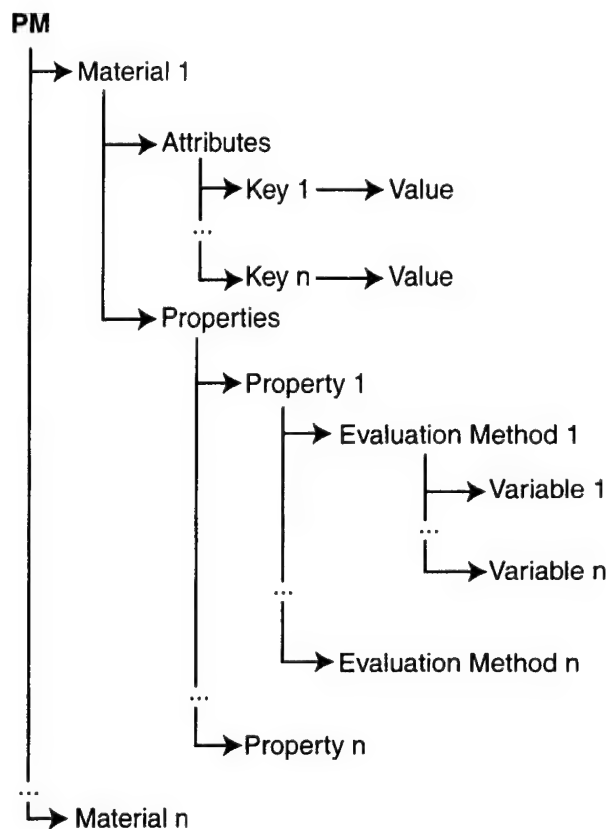
The graphical user interface of PM reflects the above structure.

Usage
Using PM is similar to using a word processor. The user can use the File menu to open, save and import database files. The title of the window shows the current working file name and the status of that file. There is New function to clear all materials and there is a warning for unsaved database.

Under Edit menu, the user can access Add and Delete functions. When the user selects an item, he can edit the name and value in the right side edit panel.

The Preference function provides two sorting methods. The default is Sort by Name. The user can also sort the materials by the Attribute Type. This option is only available when there is at least one Type in the database.

The Material node and Property node only contain its name. The Attribute node was constituted by Key and value. Besides the name, the user can specify if it is the preferred method in the

Evaluation Method node. In the Variable level, the user can enter the variable name, variable type (Integer, Float or String) and its value.

All of the above functions can also be accessed through the toolbar. The user can even access the Edit function by a right mouse click to pop up a menu.

The Refresh function was designed for using after the user has added new items and wants to sort the materials using the current sorting method.

All of the tip and error messages are displayed in the status bar, and the Copy/Paste function is available for user convenience.

2.5   Slip Wall for Rarefied Gases

In the usual macroscopic analysis of transfer processes, fluid media are treated as continua, and macroscopic properties such as density, velocity and temperature are assumed to vary continuously in time and space. However, for very low pressure and/or for very small channel dimensions, the situation may be different.

As an example, let us consider air flowing through a channel of height H. If H is large compared to the mean free path of air molecules (at sea level condition, the mean free path of air, λ, is about $6 \cdot 10^{-8}$ m), the continuum theory postulates existence of boundary layer at the channel wall, i.e., the velocity of air at wall is the same as that of wall. However, if the channel height is of same order as λ, the intermolecular collisions become less frequent and molecules arriving at the wall may not reach equilibrium with the wall. The velocity of air at wall may be discontinuous and the "no slip" wall condition is no longer valid. The so-called "slip" boundary condition must be applied.

The non-dimensional parameter, K_n, Knudsen number, can be used to describe such situation. The definition of the Knudsen number is

$$K_n = \frac{\lambda}{L} \tag{2.4}$$

where, L is the system characteristic length. Based on the Knudsen number, fluid flow can be distinguished into different regimes:

Continuum regime: $K_n < 0.01$
Slip flow regime: $0.01 < K_n < 0.1$
Transitional regime: $0.1 < K_n < 3$
Free, molecular flow: $K_n > 3$

This description focuses on the slip flow regime. Following [Rohsenow and Choi, 1961], we assume that the gas velocity at wall is V_g, and the wall velocity is V_w. The shear stress of flow at the wall is

$$\mu \frac{\partial u}{\partial y} = \beta \left(V_g - V_w \right) \qquad (2.5)$$

where, μ is molecular viscosity of gas, β is proportionality constant. On the other hand, from the theory of molecular dynamics, molecules near the wall have the last collision with wall at an average distance of $\frac{2\lambda}{3}$. The number of molecules striking the wall per unit area and time is $\frac{\overline{V}n}{4}$. Where, n is number density of molecules and $\overline{V}$ is average velocity of a molecule. Thus, the tangential momentum of molecules when they hit wall is

$$m \left(V_0 + \frac{2\lambda}{3} \frac{\partial u}{\partial y} \right) \qquad (2.6)$$

where, m is the mass of gas molecule. If the molecules striking the wall transfer a fraction of F tangential momentum, we can balance the difference of momentum with wall shear stress:

$$F \frac{mn\overline{V}}{4} \left(V_0 + \frac{2\lambda}{3} \frac{\partial u}{\partial y} - V_w \right) = \mu \frac{\partial u}{\partial y} \qquad (2.7)$$

Again, from molecular dynamics theory,

$$\mu = nm\overline{V} \frac{\lambda}{3} \qquad (2.8)$$

Therefore, we have

$$V_0 - V_w = \frac{2}{3} \frac{2-F}{F} \lambda \frac{\partial u}{\partial y} \qquad (2.9)$$

and

$$\frac{\mu}{\beta} = \left(\frac{2-F}{F} \right) \frac{2}{3} \lambda \qquad (2.10)$$

A more refined analysis gives

$$\frac{\mu}{\beta} = \frac{2-F}{F} \lambda \qquad (2.11)$$

The values of F for different gas-surface pairs are listed in the following table.

Table 2.1 Values of F for different gas-surface pairs.

Gas	Surface	F (Accommodation Coefficient)
Air	Oil	0.90
He	Oil	0.87
H_2	Oil	0.93
CO_2	Oil	0.92
Air	Hg	1.00
Air	Machined Brass	1.00
He	Polished Ag_2O	1.00
H_2	Polished Ag_2O	1.00
O_2	Polished Ag_2O	0.99
Air	Polished Ag_2O	0.98

The gas slip velocity at wall is given by

$$V_g - V_w = \frac{2-F}{F} \lambda \left(\frac{\partial u}{\partial y} \right)_{y=0} \tag{2.12}$$

The equation above can be used with standard molecular viscosity value in the slip-flow regime as mentioned above, that is for $K_n < 0.1$. For some particular cases of higher Knudsen numbers and specific geometries, the user may modify the viscosity value in CFD-ACE+, to so-called effective viscosity, using the built-in formula:

$$\mu_{eff} = \frac{\mu}{\left(1 + a \cdot K_n^b \right)} \tag{2.13}$$

where μ is the default viscosity value, a and b are constants given by the user.

For example, in the paper [Veijola, 1995], an effective viscosity model for the Poiseuille flow (squeeze-film damping) has been derived, with the constants $a = 9.638$, $b = 1.159$. The model is valid for Knudsen numbers in the range $0 < K_n < 880$, with less than 5% difference from the solution of Boltzmann transport equation for that case. For a Couette-type flow, that is, a plate moving horizontally over a flat surface, with a very small gap between the plate and the surface, the other set of constants has been proposed in [Veijola, 2000]: $a = 2$, $b = 1$.

This slip wall model has been incorporated into CFD-ACE+ and tested on several cases. As an example, the flow of Helium in a microchannel was analyzed. The channel had a rectangular cross-sections with dimensions 7500 * 52.25 * 1.33 µm. The exit pressure was held constant at 108000 Pa, while the upstream or inlet pressure was varied. The experimental data for mass flow rate for He were published in [Arklic, 1994] for inlet to outlet pressure ratio (P_{inlet}/P_{exit}) of 1.1 to

2.6. For the flow conditions and the microchannel dimensions, the Knudsen number is about 0.08, i.e., in the slip region. A 3-D grid with 60*10*5 cells was built for the channel. Two sets of results were generated. One for "no slip" wall condition and another for "slip" wall condition using the model described above. The computed mass flows with the both wall conditions are plotted in Figure 9, together with experimental data from MIT [Arklic, 1994]. As can be seen, the no-slip wall condition generates higher wall shear with a consequent lower mass flow rate at a given pressure ratio. With the slip wall condition, the shear at wall is lower and the mass flow rate increases. It can be seen in Figure 9 that the numerical results with slip wall condition are very close to the experimental data for this case.
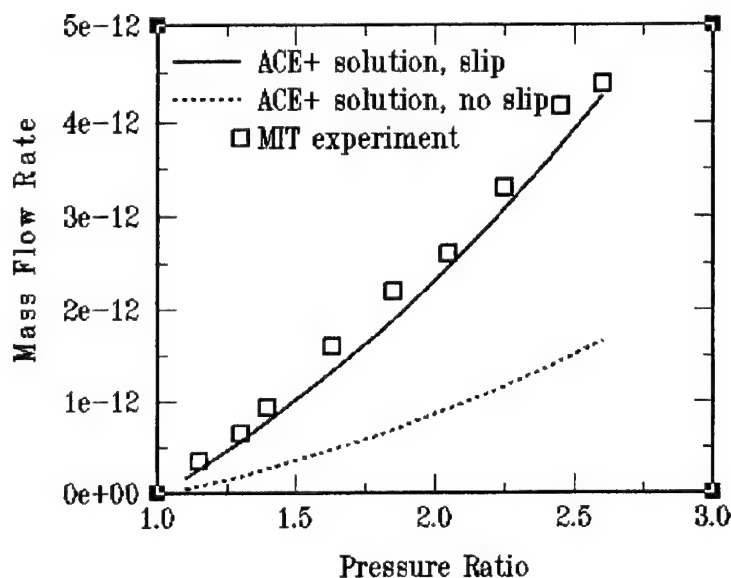
Figure 9. Comparison of mass flow rfate for Kn = 0.08.

2.6 Validation of CFD-ACE+ for High-Fidelity Simulations

The single synthetic jet measurements performed at GT were used to compare with the 2D/3-D simulations of these devices, performed at CFDRC using CFD-ACE+. First, a single synthetic jet was used which was characterized in great detail at GT. The geometry and boundary conditions used for simulations were provided by the GT team. The diameter of the orifice was 6.35 mm and the diameter of the actuator at the bottom 19 mm. The height of the actuator was 95 mm. The oscillation frequency of the bottom wall, diaphragm, was 930 Hz, 700 Hz, and 450 Hz.

The dependence of the actuator stroke length L_o/D on the (rms) cavity pressure for actuation frequency 930 Hz is shown in Figure 10. One can see that the agreement between the measured data and simulation results is very good. The only difference is a kind of discontinuity in the experimental results at the pressure value about 0.1 psig. This effect is probably caused by experimental setup details rather than by basic physical behavior of the synthetic jet.

20
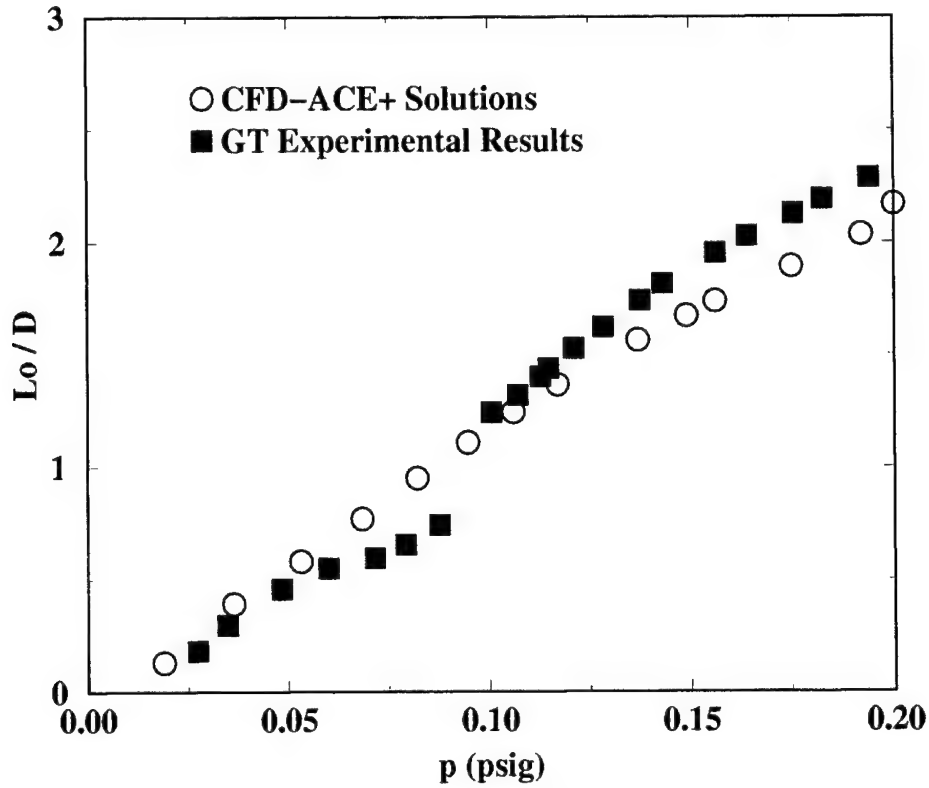
Figure 10. Actuator stroke length L_o/D vs. the (rms) cavity pressure, at frequency 930 Hz, measured with PIV technique at GeorgiaTech, and obtained from CFD-ACE+ 3-D simulations at CFDRC.

Measured and simulated results of vortex formation are shown in the form of contour maps in Figure 11. The measured ensemble-averaged vorticity (w) at $t^* = 0.5$, for L_o/D values between 0.4 and 2.2, at the two formation frequencies are presented, while the simulation results are for the frequency $f_1 = 930$ Hz and four selected L_o/D values. Both vertical and horizontal axes on both sets of results have the same range. This time, with the correct value of the orifice thickness, the agreement between PIV and CFD results is very good.

(a) PIV Measurements　　　　**(b) CFD Simulations**
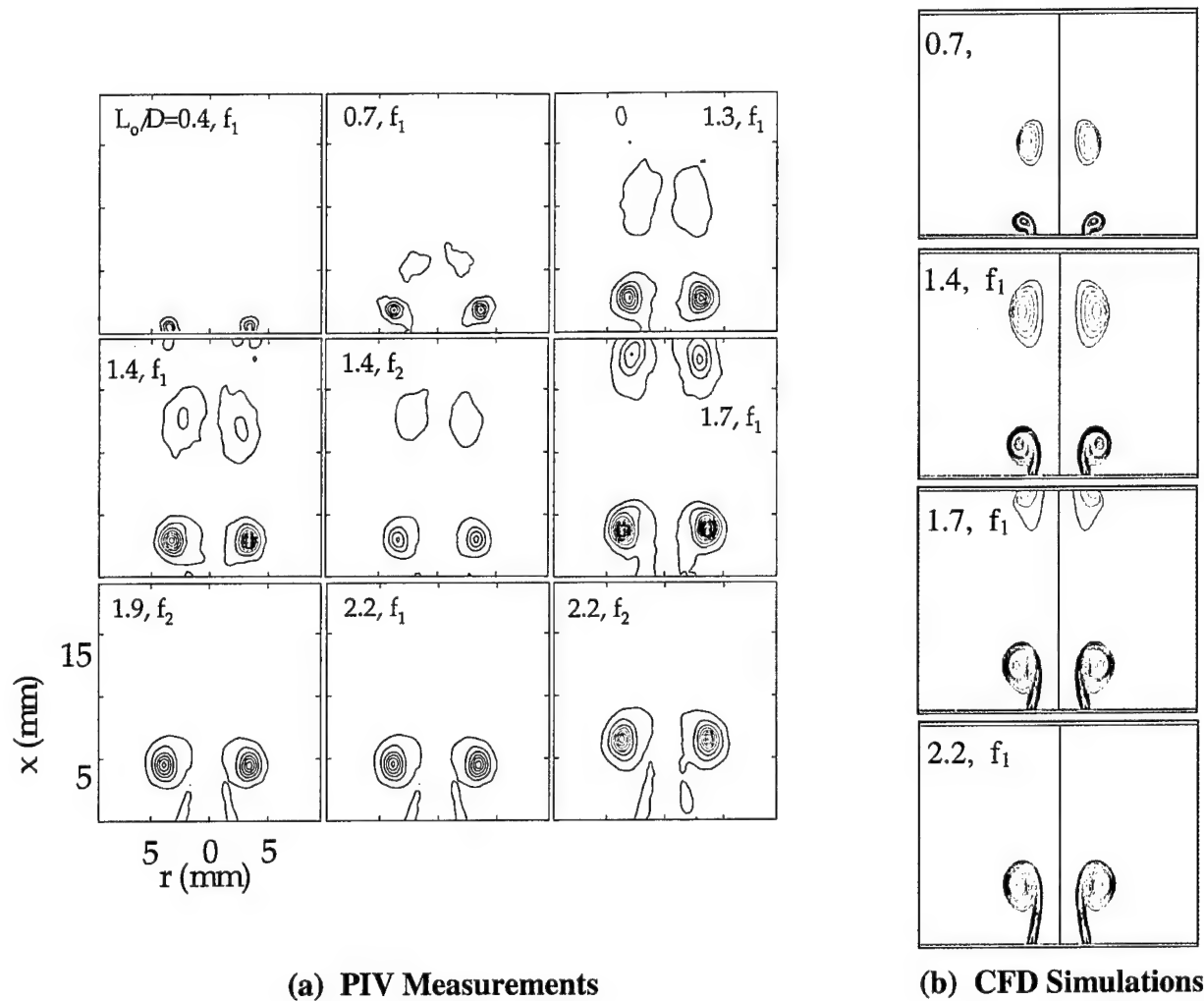
Figure 11. Contour maps of phase averaged dimensional azimuthal vorticity at $t^* = 0.5$.
(a) PIV measurements ($f_1 = 930$ Hz, $f_2 = 450$ Hz), (b) CFD-ACE+ simulations.

3   INTERFACES TO CAD/EDA TOOLS

3.1   CFD-Micromesh: Automatic Generation of 3-D Device Models from Layouts

This project demonstrated the feasibility of automatic generating 3-D MEMS structure models directly from layouts imported from commercial EDA tools. A new software, called CFD-Micromesh, was developed during this project at CFDRC, for automatic 3-D solid model generation and meshing from MEMS layouts imported directly from EDA systems. The popular layout description formats, CIF and GDSII, are imported easily into CFD-Micromesh, allowing coupling the software with several commercial EDA design tools. The new tool is fast and equipped with user-friendly graphical user interface (GUI) - see Figure 12.

22

In Figure 12, we present a layout of a MEMS comb drive resonator, imported from CIF or GDSII file. To assign physical meaning to CIF or GDSII layers, a technology file is used in a special CFD-Micromesh format, for example *MUMPs.umt* file for the MUMPs technology.
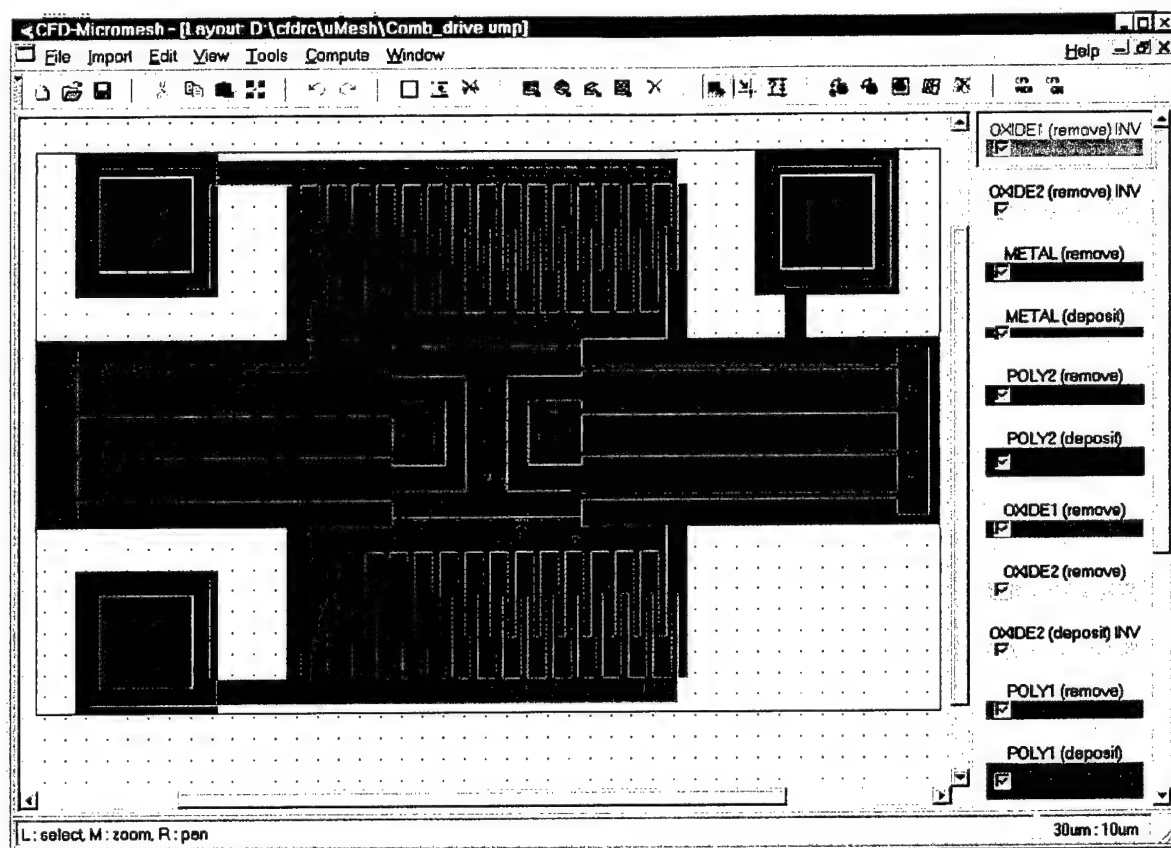
Figure 12. Layout of a comb resonator, imported from CIF file into CFD-Micromesh.

By clicking only a single button in CFD-Micromesh, a three-dimensional solid model is generated fully automatically from layout. Building the 3-D model of the comb-drive resonator, presented in Figure 13, took only 40 seconds on a 700 MHz Pentium PC. A "3-D Quick View" option in CFD-Micromesh builds 3-D models of planar structures in 1-2 seconds.

23
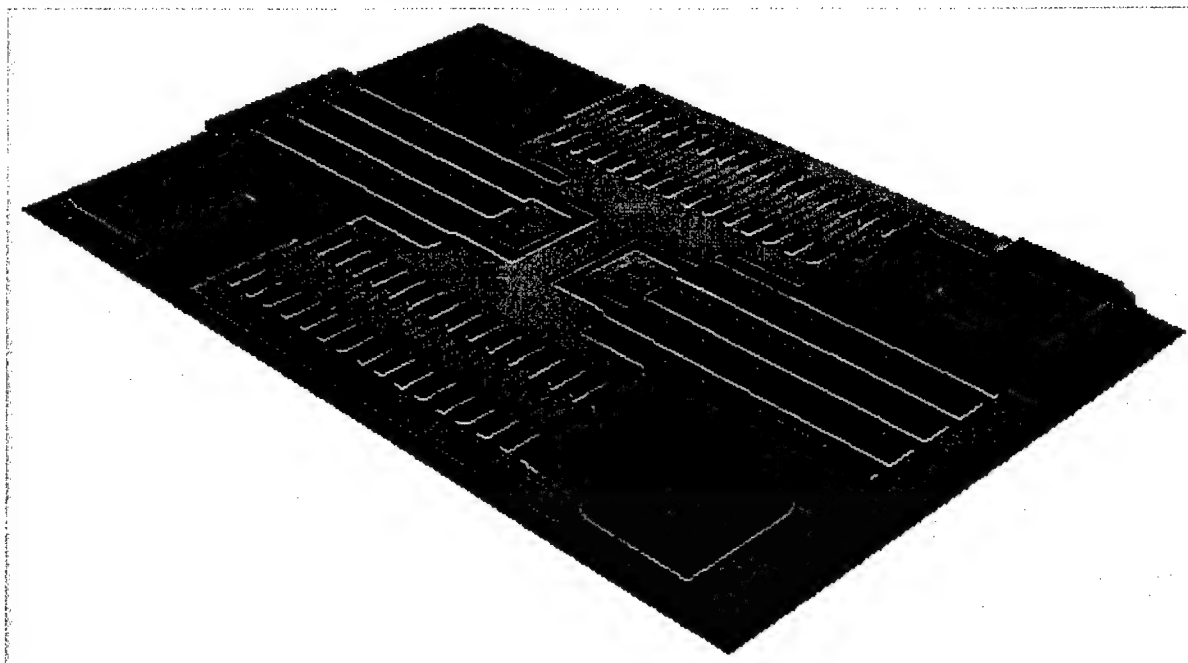
Figure 13. A 3-D solid model generated automatically from layout in Figure 12.

Sixty more seconds were needed to generate automatically a full 3-D unstructured computational mesh in DTF format, again only by clicking a single button in CFD-Micromesh. Such a mesh for the analyzed comb-drive resonator is shown in Figure 14.
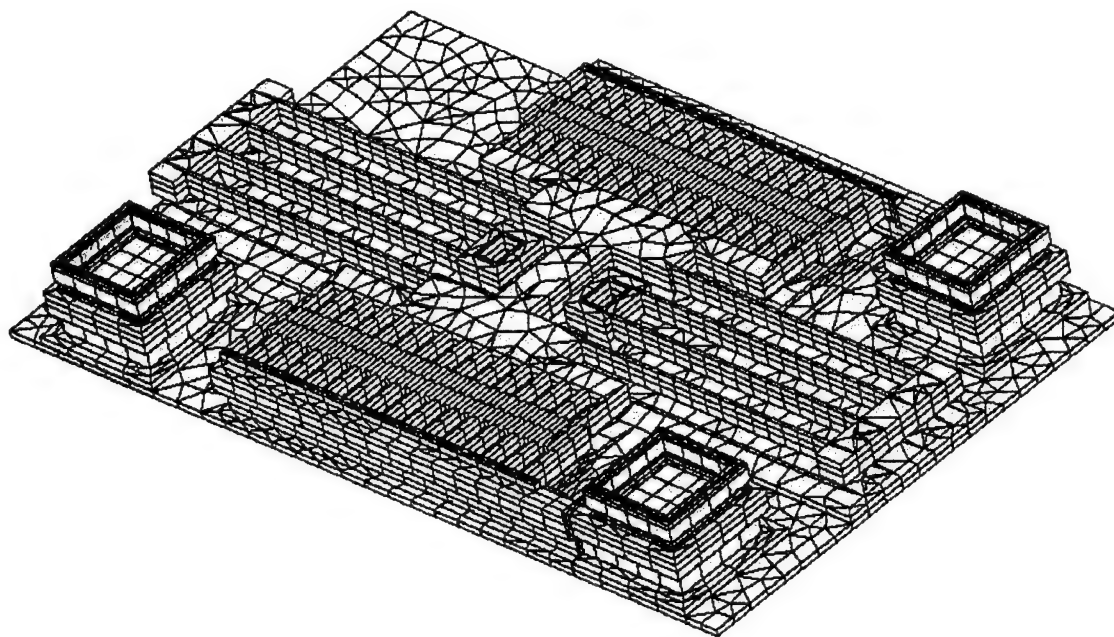
Figure 14. A 3-D computational mesh, generated automatically from layout in Figure 12.

The automatically generated three-dimensional device model with the unstructured 3-D computational mesh in DTF format can be imported directly into CFDRC's simulator CFD-ACE+ for subsequent high-fidelity 3-D simulations, both steady-state or transient.

CFD-Micromesh was recently extended with a capability to read a fabrication process (layer structures) description in a standard format called **SIPPs** (Standard Interconnect Performance Parameters). The format is being developed by several big semiconductor companies, like Si2, AMD, Motorola, IBM, Cadence, Avanti, Mentor Graphics, and others, with participation of CFDRC (more info: http://www.si2.org/sipps/). SIPPs layer data are typically imported in connection with a layout in GDSII format, which makes together a complete 3-D description of a design. This capability makes CFD-Micromesh a very attractive modeling tool also for VLSI electronics industry, in particular for analysis of interconnects and PCBs.

The new version of CFD-Micromesh imports CIF and GDSII layouts, reads the SIPPs process description format, and includes direct interface to Virtuoso$^{(TM)}$ layout editor from Cadence. The evaluation version (available from http://www.cfdrc.com/~micromesh) builds automatically 3-D solid models from layout and process data, and allows the user to view them interactively.

Finally, CFDRC has negotiated an agreement with **Cadence Design Systems**, Inc. to develop interfaces and integration of CFDRC's MEMS simulation software with Cadence CAD tools. CFD-Micromesh will be a part of Cadence CAD Environment, used as a "3-D Project Viewer" from Virtuoso layout editor from Cadence (see Figure 5).

The "3-D Project Viewer" interface to Cadence has been included into the commercially available CFD-Micromesh package. The appropriate linking procedures (in Cadence's SKILL Script) and basic documentation of the interface are available in the CFD-Micromesh package.

The interface and all of the involved procedures of coupling CFD-ACE+ with SABER system-level simulator have been described in detail in the following publications:

- M. Furmanczyk, M. Turowski, E. Yu, and A. Przekwas, "Coupled System-Level and Physical-Level Simulation", ASSURE 2000 (Avant! Saber Simulator Users Resource Meeting), Portland, Oregon, May 10-12, 2000.

- M. Furmanczyk, M. Turowski, E. Yu, and A. Przekwas, "Coupled System-Level and Physical-Level Simulation", Int. Conf. MSM 2001, Hilton Head Island, South Carolina, USA, 19-21 March 2001.

3.2 Schematic Driven Design Entry for MEMS

The goal of this task, performed mainly by the CMU team in collaboration with CFDRC, was to develop an integrated CAD environment composed of schematic driven design entry and automated generation of 3-D mesh and solids description for rapid design of MEMS structures.

Design process of MEMS structures is typically very time-consuming, especially in terms of design verification and redesign issues. To make it faster and more effective, we have proposed to introduce a schematic entry into the existing design flow sequence, similarly to the established

EDA procedures for VLSI integrated circuits. The modified MEMS design flow would consist of the following steps:
1)   introducing the idea in a form of MEMS schematic,
2)   verification by means of complex 3-D and multidomain simulations, (optionally go to step 1)
3)   layout generation and verification, (optionally go to step 1).

In the frame of this project, we have developed a CAD environment allowing to generate 3-D mesh and solids description in PLOT3-D and DTF formats (viewed in CFD-VIEW package) from MEMS schematics (created in Cadence Schematic Editor).

New CAD tools allow to create 3-D mesh description of any MEMS device build from NODAS library elements e.g. folded flexure resonator (in MUMPS technology) directly from Cadence Schematic Editor within several seconds and in the way that any changes in the mesh description are being done by only changing values of symbol parameters.
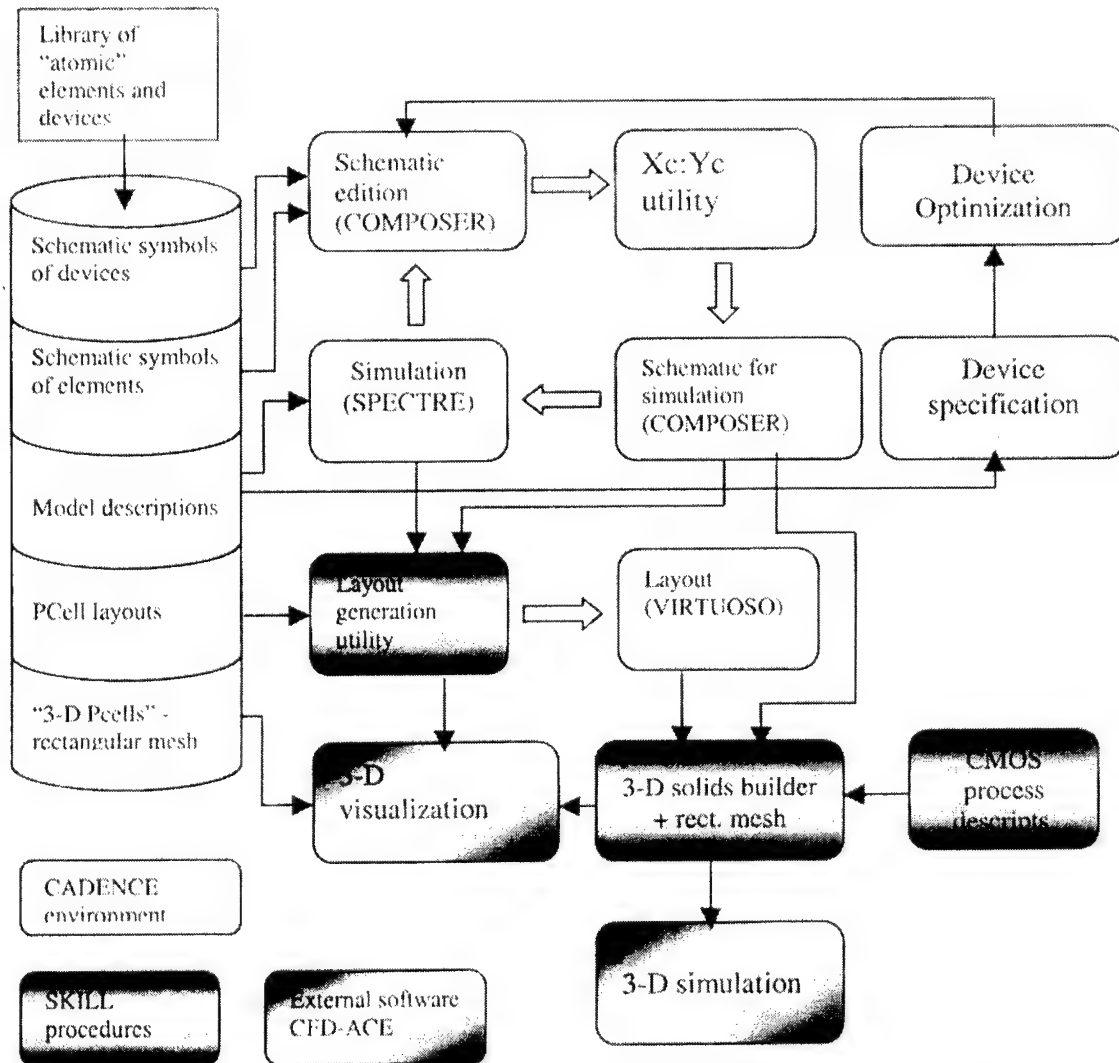
Figure 15. The full design flow for MEMS structures. The shaded areas indicate the field of interest in this project.

26

CMU NODAS CAD tools allow fast design and verification of MEMS devices built from a set of "atomic" elements like beams, plates, combs and anchors. Figure 15 describes in general view the design flow with the shaded areas indicating the field of interest in the frame of this part of the project. The design of MEMS structures, where the influence of the surrounding environment on device functioning has to be taken into account, requires 3-D and multidomain simulations. In the case of e.g. CMOS ultrasonic structures, air damping effect strongly determines the device performance.

The developed in Cadence SKILL language CAD procedures use the description of NODAS symbols parameters taken from the schematic database separately for each type of symbols. Then, a 3-D rectangular mesh description is created separately for each set of symbols as well. The output format can be PLOT3-D (structured grid with blanking) or DTF format developed at CFDRC. Any changes of 3-D description are made by editing parameter values in Edit Properties window invoked from Cadence Schematic Editor window. Redesign of such a structure in terms of changes in geometric dimensions takes up to several seconds only. The developed CAD procedures are accessed by the user through the GUI in Cadence environment. An exemplary design views of folded flexure resonator in MUMPS technology, as well as the GUI elements are shown in Figure 16.
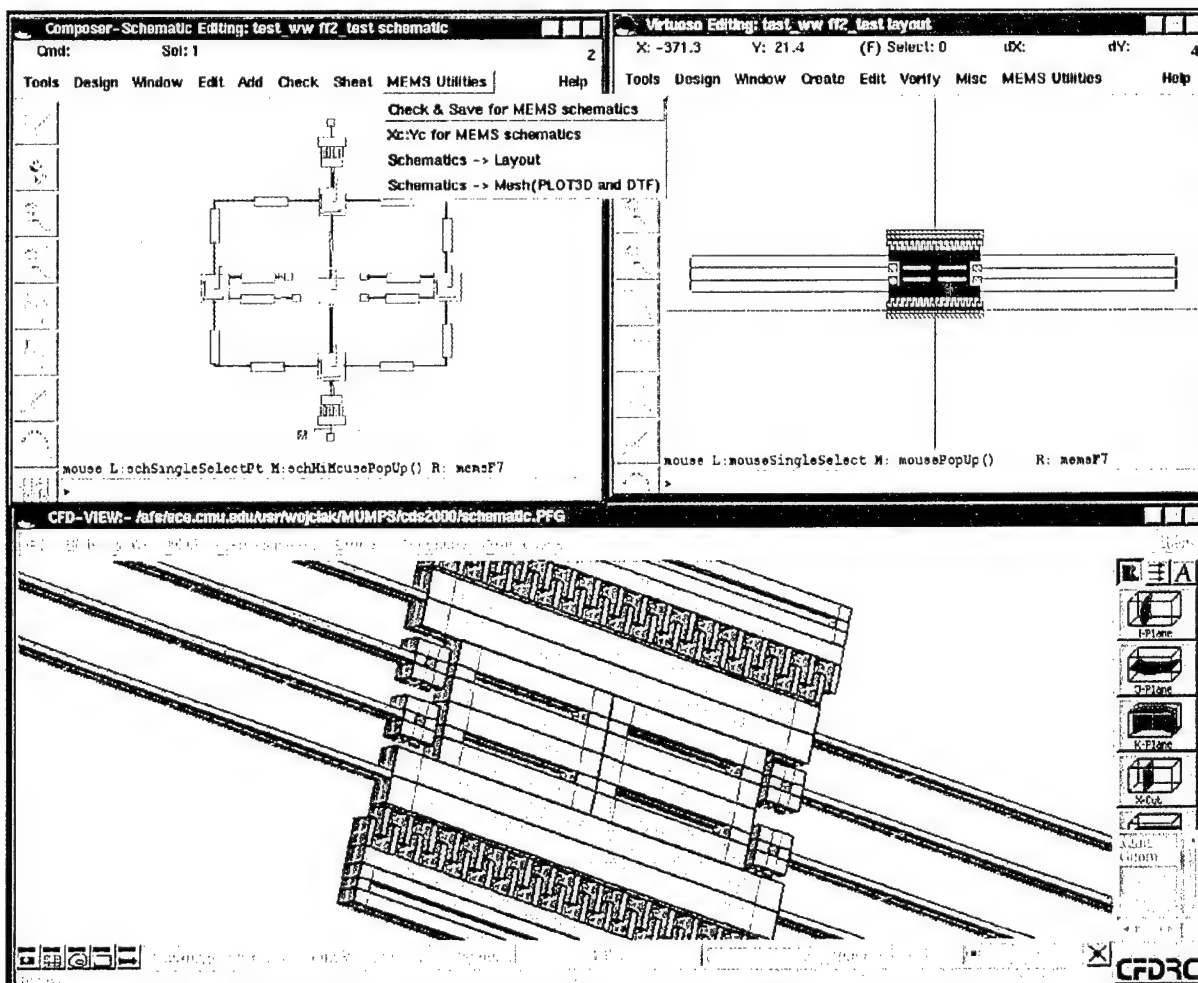
Figure 16. Schematic, layout and 3-D visualization views of MUMPS folded flexure resonator.

As a demonstration, the new technology has been applied to:
- 3-D simulations of CMOS MEMS ultrasonic sensor.
- A folded beam MEMS structure

3.3   CAD Tools Integration for MEMS Design

This sub-task aimed at developing an integrated CAD environment that combines the ease of schematic driven design entry and automated generation of 3-D mesh and solids for accurate continuum simulation of MEMS devices. This effort links the NODAS schematic simulation environment with the 3-D visualization and device verification capabilities in CFD-ACE+.

There are two focus points for this sub-task:

- 3-D visualization in which the schematic needs to be translated into a meshed geometry for visualization in CFD-VIEW.
- Device verification in which both the schematic geometry as well as the source excitations on the schematic need to be translated. The source excitations in the schematic become boundary conditions for the CFD-ACE+ solver.

We have developed a new data format (called GBV – Geometry, Boundary and Volume conditions) for interchange of simulation data between CADENCE Design Framework II and CFDRC ACE simulator. Based on this format, Cadence design data extraction procedures (SKILL) and program (C) translating data from GBV format to CFDRC-DTF format have been created. The design flow is based on generation of text GBV file directly from CADENCE Schematic Editor by reading out schematic database, running layout generation and meshing procedures. The layout meshing is accomplished using the algorithms detailed in [Hasnain Lakdawala, Bikram Baidya, Tamal Mukherjee and Gary K. Fedder, "Intelligent Automatic Meshing Of Multilayer CMOS Micromachined Structures For Finite Element Analysis," in *Proc. MSM 1999,* pp. 297-300]. The geometry data obtained after layout meshing is combined with boundary and volume conditions data taken from schematic view in order to create a file with a data description in GBV format. Next, the text file (GBV) is translated into binary DTF file, which is required by the CFD-ACE solver. Generation of the new DTF file can be performed by changing values of symbol parameters in the Cadence Schematic Editor. GUI procedures, integrating CADENCE tools with the CFDRC ACE simulator for the mentioned design flow, have been also developed.

The examples in the figures below demonstrate the capability of the resulting link between NODAS and CFD-ACE+. Figures 17 and 18 demonstrate the visualization capabilities. Figures 19-21 demonstrate the capability of passing schematic sources as boundary conditions to CFD-ACE+.
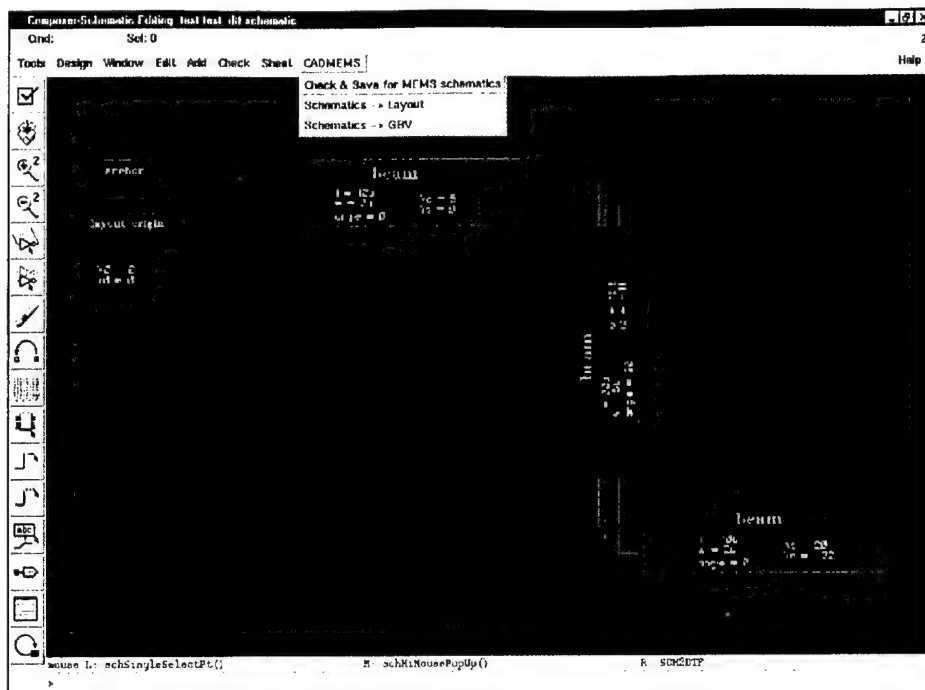
Figure 17. Example MEMS Schematic in Cadence.
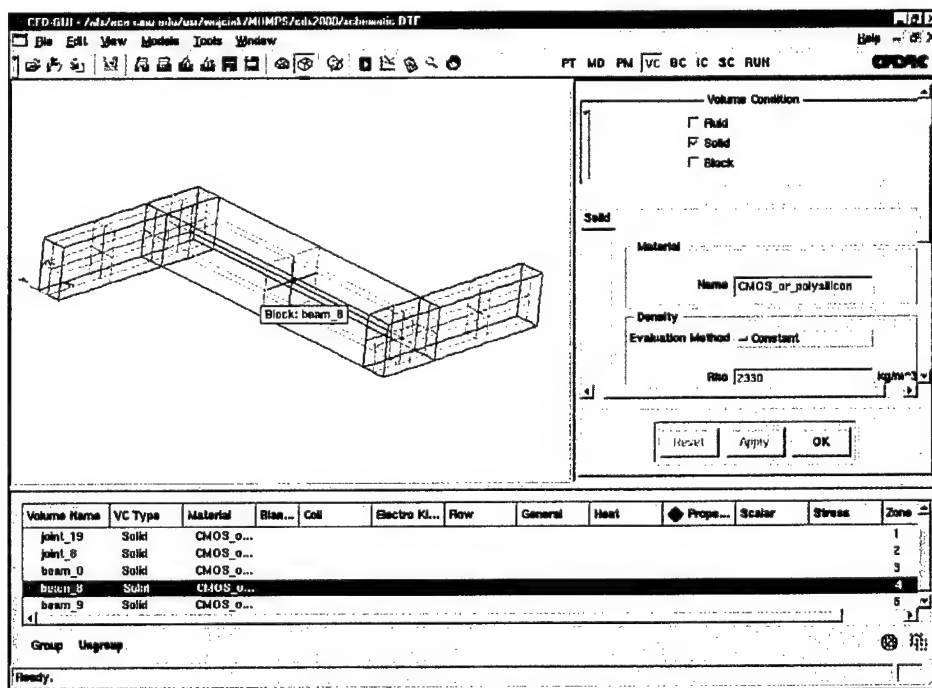
Figure 18. CFD-GUI view of the beams and beam corners.
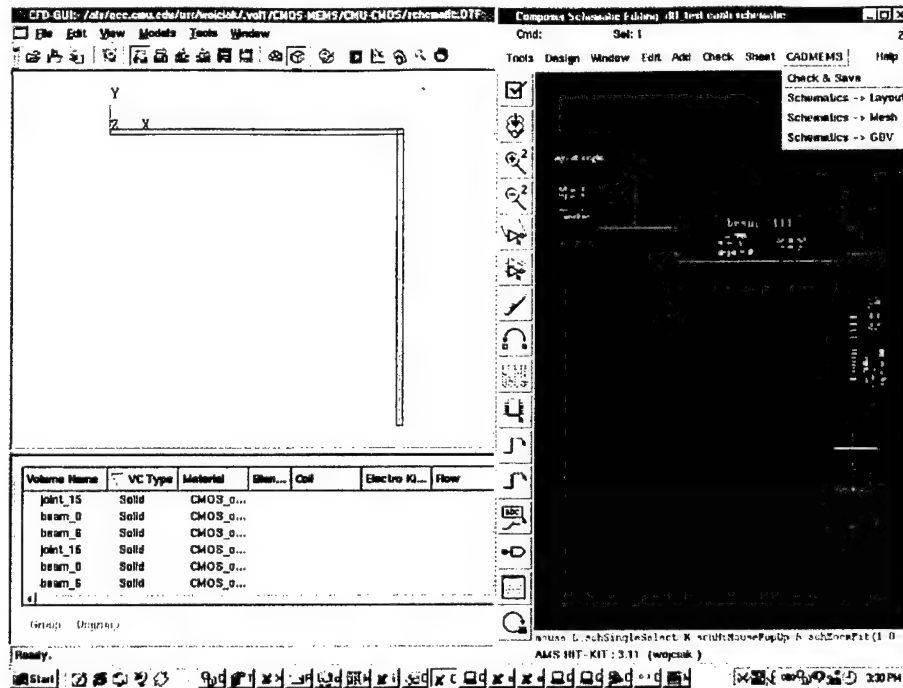
Figure 19. Snapshots of Cadence Schematic Editor with anchor-beam-beam-dc_force_source test design and its view in CFDRC-GUI after translation to DTF format.
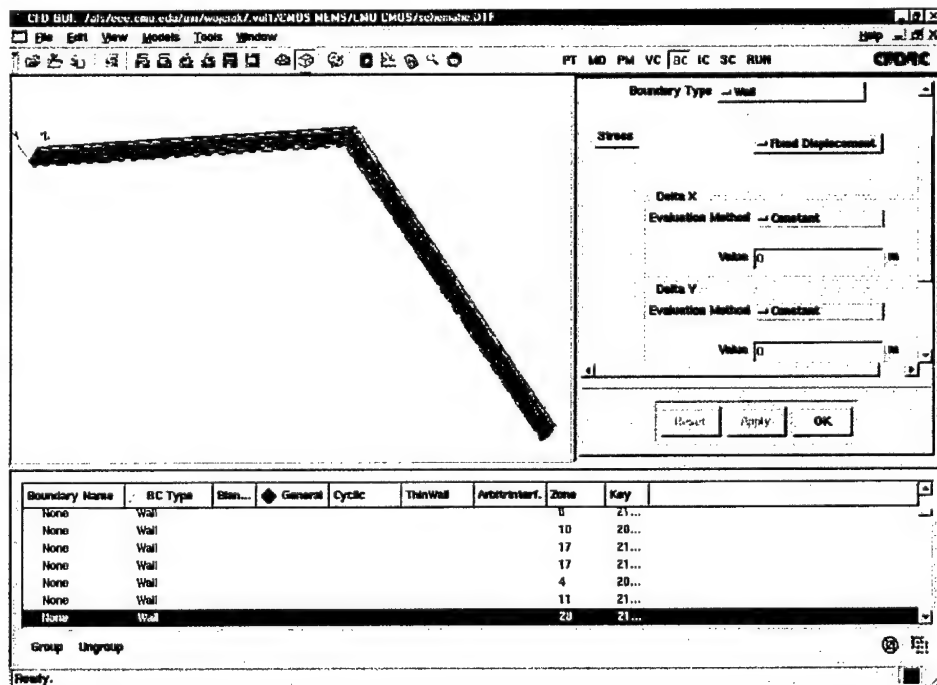
Figure 20. Snapshot of CFDRC-GUI with test design showing its layers (eight CMOS layers) and Boundary Condition description for the wall connected to the anchor on schematic view (Fixed Displacement dx=0, dy=0, dz=0).
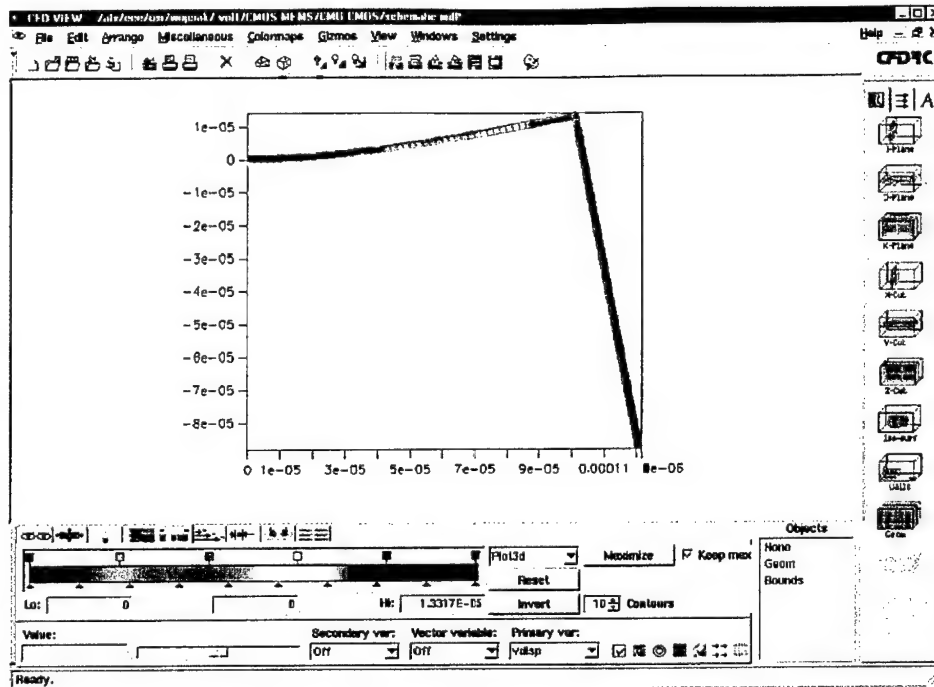
Figure 21. Simulation results for the test design: analysis type: steady, dc_force value: 100uN new, reduced and compact models

4 NEW REDUCED AND COMPACT MODELS

4.1 Air Damping Models

4.1.1 Nonlinear Compact Model of Squeeze Film Damping

MEMS devices are characterized by very small gaps between the moving elements and the fixed parts. A gas (air) film between two closely spaced plates is squeezed and produces forces that oppose the motion of the plate. The viscous and compressibility effects dissipate the energy of the moving plate, which is known as squeeze-film damping (Figure 22a). Several authors have already analyzed the squeeze-film behavior, but all the solutions have been shown only for small amplitudes of the motion. An analytical solution of the linearized compressible isothermal Reynolds equation was proposed by Blech in [Blech, 1983], under the assumption that the motion of the plates and the pressure variations are small. The analytical solution for the squeeze-film force consists of two components: one is in phase with the plate velocity (the viscous damping force), the other is in phase with the plate displacement (the spring force due to the compressibility of air).
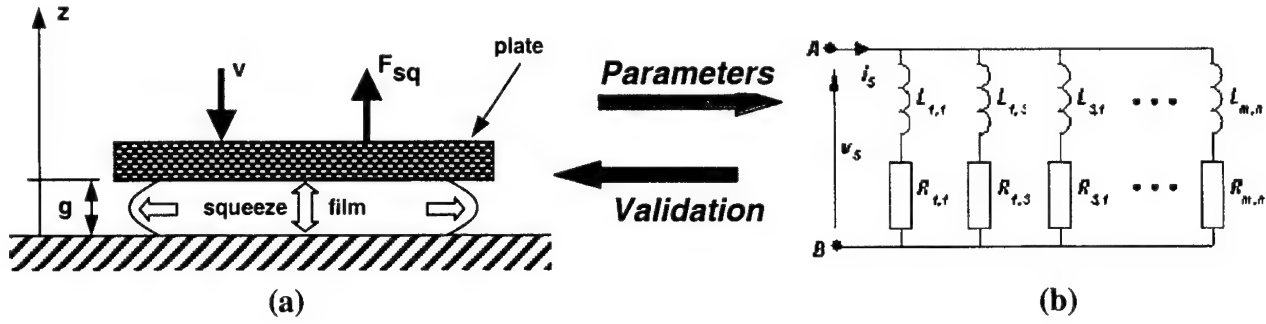
Figure 22. Squeeze film between plates (a), and its equivalent-circuit model (b) The arrows show the role of CFD-ACE+ high-fidelity simulations.

On the basis of the Blech's solution, an equivalent-circuit model of squeeze-film damping was proposed in [Veijola 1995], realized with a ladder of RL (resistor and inductor) branches (Figure 22b) satisfying the frequency dependence of both analytical components: damping force and spring force. This model was also derived with the assumption of small amplitudes of motion and small pressure changes, and for such conditions a good agreement of the circuit model with measurements was demonstrated in [Veijola 1995]. A modification of the R and L values in the equivalent circuit, as nonlinear functions of displacement, was also proposed in [Veijola 1995], but neither was it verified nor any large-amplitude results were shown.

The same problem was investigated by Yang and Senturia in [Yang 1996], where squeeze-film effects were modeled numerically under small-amplitude sinusoidal conditions by a finite element package, as well as under large amplitude motion by a finite difference codes. For the large displacement, the maximum oscillation amplitude in that work was equal to 30% of the nominal gap thickness, for which only numerical finite-difference solution was shown. Also the most recent papers reporting compact analytical models of squeeze film damping, like [Yang 1997], [Darling 1997] , [Burgeois 1997]or [Pan 1998], are limited to small amplitude motion as one of their main assumptions, which may be not necessarily true in real MEMS behavior.

In this project, we performed, demonstrated, and published simulations of isothermal compressible squeeze-film damping effects between plates of MEMS devices for arbitrary large amplitudes, using a behavioral model based on equivalent nonlinear RL circuit. The results of the compact model were verified using a 3-D high-fidelity transient solution of full Navier-Stokes equations, obtained with CFD-ACE+ from CFDRC. The compact model, based on the format proposed in [Veijola 1995], is shown in Figure 22b. The component values in the RL ladder are:

$$L_{m,n} = (mn)^2 \frac{\pi^4 (g - z)}{64 \cdot lwP_a} \tag{4.1}$$

$$R_{m,n} = (mn)^2 \left(\frac{m^2}{w^2} + \frac{n^2}{l^2} \right) \frac{\pi^6 (g - z)^3}{768 \cdot lw\eta_{eff}} \tag{4.2}$$

where: l and w are the length and width of the plate, respectively, g is the nominal gap height (Figure22a), z is plate displacement, and P_a is the static pressure. The effective viscosity η_{eff} in Equation (4.2) depends on the gap height g and the mean free path λ of the gas, through the Knudsen number $K_n = \lambda/g$. An expression for the effective viscosity is given in [Veijola 1995]. The coefficients m, n are odd indices 1,3,5,..., reflecting the series expansion form of the squeeze film solution. In practice, only a few sections are needed for sufficient accuracy. In our simulations we have used the first six RL sections, for $(m,n) = (1,1), (1,3), (1,5), (3,1), (3,3), (5,1)$.

The above mentioned electrical equivalences for mechanical and fluidic domains are used here: the voltage/current pair represents velocity/force. Hence, the plate velocity V and the squeeze force F_{sq} in Figure 22a are represented by the voltage v_s and the current i_s in Figure 22b, respectively. The plate displacement z can be calculated from the flux ψ of the resonator inductance L_{spr}, if we add to the equivalent circuit an additional inductor $L_{spr} = 1/k$, representing the device elastic spring constant k. If the inductor L_{spr} was connected between pins A and B in Figure 22b, the displacement would be: $z = \psi = L_{spr}i_L$, where i_L denotes the current through the inductor L_{spr}. If there is no spring constant representation in the circuit, the displacement z can be calculated by integrating the velocity which is directly represented by the voltage v_s in the electric equivalent circuit.

SPICE implementation and comparison with 3-D numerical simulations

The equivalent RL model was implemented in our case first in PSpice running on PC. The SPICE versions known to us do not have nonlinear models of resistors R and inductors L that would allow for direct implementation of Equations (4.1) and (4.2). As explained above, the z value in the equations for L and R comes either from current in another branch, or from integrating the voltage v_s in the circuit. Therefore, in the SPICE model, the nonlinear elements $L_{m,n}$ and $R_{m,n}$ have to be represented by nonlinear controlled sources. In our implementation for PSpice, we have used voltage-controlled voltage sources (VCVS) for inductors $L_{m,n}$, and voltage-controlled current sources (VCCS) for resistors $R_{m,n}$.

To verify the results of the equivalent circuit model for large amplitudes, comparisons between the 3-D high-fidelity simulations and compact model results were done, in frequency and time domains, for periodic plate displacements. The 3-D numerical calculations were done using CFD-ACE+. They involved solution of full Navier-Stokes equations, as described in the previous section. Our effort in **this project demonstrated for the first time the squeeze film behavior in MEMS for very large amplitudes**, up to 90% of the nominal gap thickness, and our results have been published in several papers (see "Publications Resulting from This Project").

Example results obtained with full 3-D Navier-Stokes solution and equivalent-circuit RL model (solved by SPICE), for periodic oscillations of frequency 100 Hz, are presented in Figure 23 and Figure 24. The nonlinear compact-model results agree very well with 3-D results even for the very large amplitudes of plate motion, accompanied by significant changes of pressure. In the

figures, the displacement amplitude equals 90% of the nominal gap height (4 micrometers in this case), and the resulting relative pressure change with respect to static ambient pressure, due to the squeeze force, reaches the maximum of about 3, which is not even close to the small amplitude and small pressure change assumptions made previously.

CFD-ACE: 3-D model

SPICE: RL model
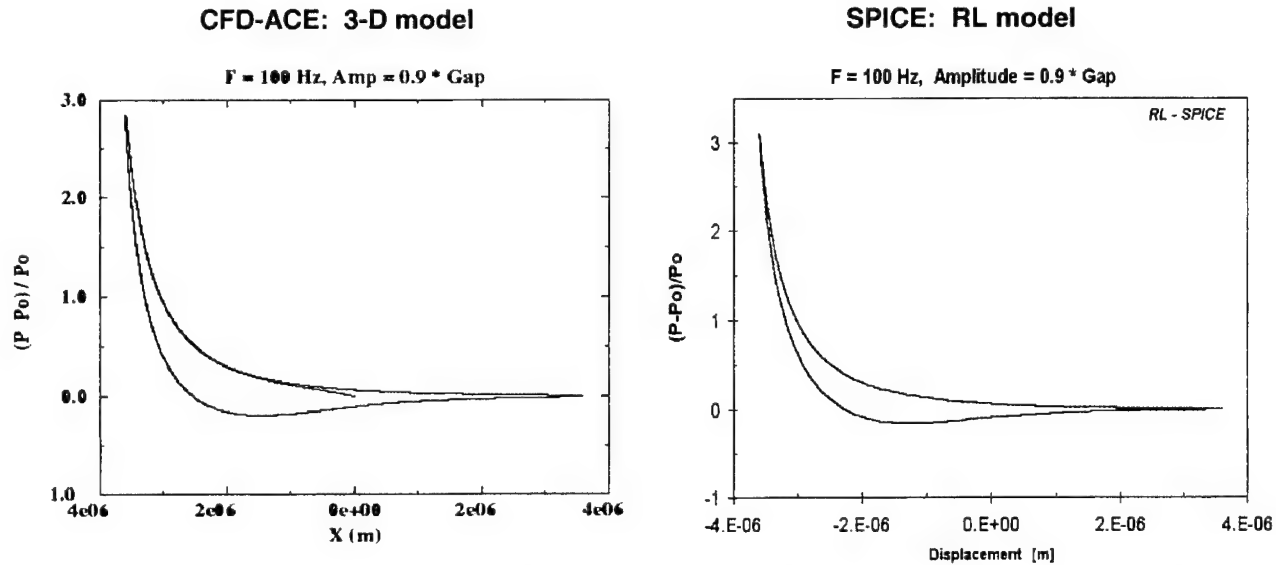
Figure 23. Relative pressure change with respect to static ambient pressure as a function of plate displacement, obtained with 3-D Navier-Stokes solution (using CFD-ACE) and equivalent-circuit model (solved by SPICE), for the displacement amplitude equal to 90% of the nominal gap height.

CFD-ACE: 3-D model

SPICE: RL model
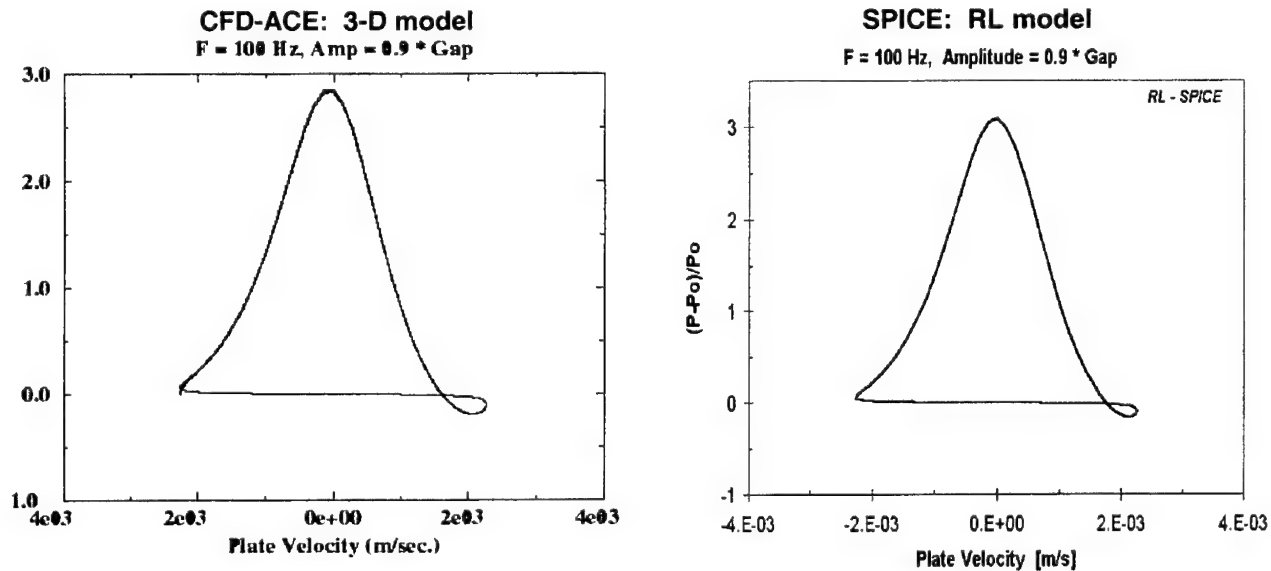
Figure 24. Relative pressure change with respect to static ambient pressure as a function of plate velocity, obtained with 3-D numerical solution and equivalent-circuit model, for the displacement amplitude equal to 90% of the nominal gap height.

In Figure 25, the calculated relative pressure change due to squeeze effect is presented for very high operating frequency, equal 100 kHz. The displacement amplitude is again 90% of the

34

nominal gap height (4 micrometers in this case as well). The resulting relative pressure change is 10 to 15 times bigger than the static ambient pressure, which means even bigger changes of pressure than for low frequencies. The agreement between RL-circuit and 3-D model for the high frequency is not as good as for low frequencies, but the shape of characteristics is preserved and we believe the equivalent-circuit RL model still can be used even for high frequencies, after some parameter fitting.
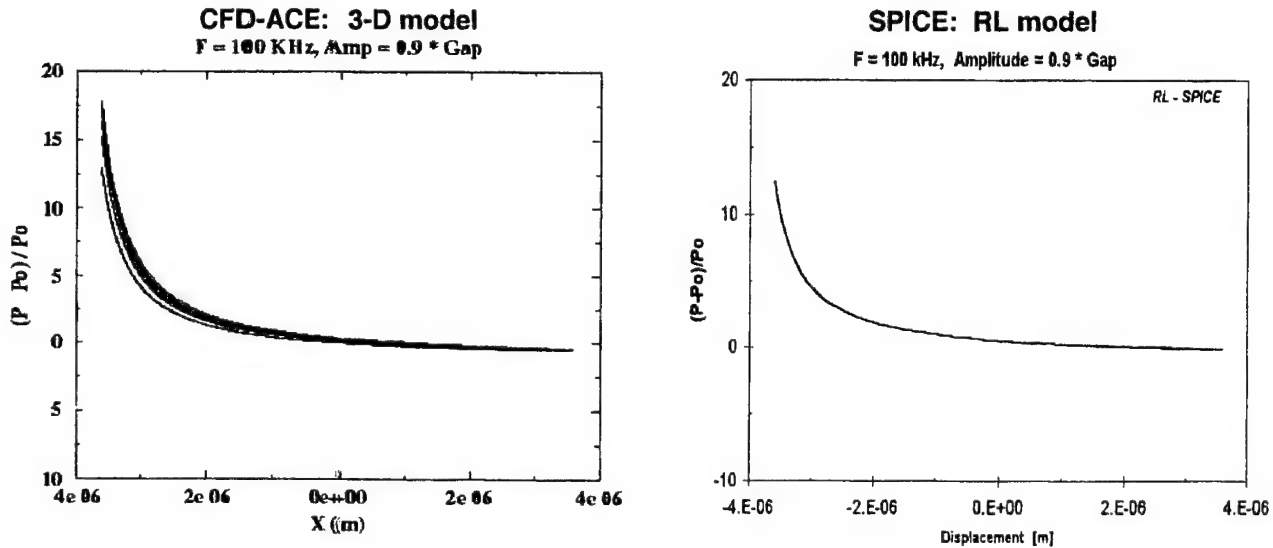
Figure 25. Relative pressure change with respect to static pressure as a function of plate displacement for frequency 100 kHz and displacement amplitude 90% of the nominal gap.

Saber-MAST implementation

The equivalent-circuit model of the squeeze film behavior has been also implemented for the Saber simulator with models written in MAST, an analog hardware description language [MAST, 1997]. The Saber-MAST version of the behavioral squeeze film model uses directly mechanical quantities: position as input (across variable) and damping force as output (through variable), which is compatible with hierarchical representation for system-level design of MEMS, like the NODAS methodology developed at Carnegie Mellon University [Vandemeer, 1998], partly also in the frame of the DARPA Composite CAD Program . The developed model, together with the simple test circuit containing also a mechanical translation source available in Saber, is shown in Figure 26. The description of the model is included in a MAST template called *squeeze1D*. This version of model is only one-dimensional (1D), or for one degree-of-freedom (DOF). The squeeze damping model in one direction has only two mechanical nodes (say, "top" and "bottom"), with their displacements (x_t, x_b) as across variables, and resulting squeeze force as through variable.

35
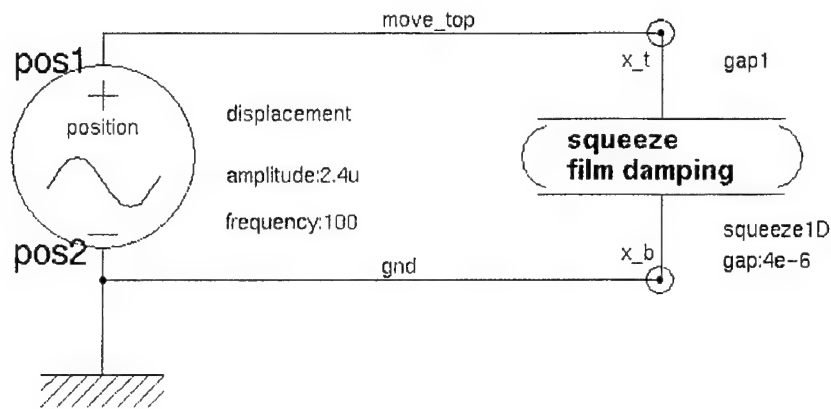
Figure 26. Squeeze film behavioral model in Saber simulator, together with mechanical displacement source for testing.

Similarly as in SPICE, the models of resistors R and inductors L available in Saber libraries do not allow for direct implementation of Equations (4.1) and (4.2). Therefore, special MAST templates had to be written for the nonlinear elements $L_{m,n}$ and $R_{m,n}$ in the equivalent circuit.

The z value denoting plate displacement has been directly inserted into the MAST templates, called *Lsq* and *Rsq*, thanks to the possibility of mixing mechanical and electrical signals in one model. The MAST code of the *squeeze1D* template, modeling the squeeze film behavior with mechanical inputs (position) and output (force), is shown in Figure 27. The template is generated automatically by a special routine written in C, taking as input all the basic parameters of the plate, gap, gas pressure, etc. The same C program, after switching one parameter, generates automatically input files for Spice simulations as well.

Behavioral characteristics obtained with Saber using the MAST implementation of the RL-circuit are of course almost identical as the ones obtained with Spice, presented on the right-hand side of Figures 23-25. As another example, in Figure 28, we show transient waveforms of the squeeze-film force in response to oscillatory movement of the top plate with amplitude equal 60% of the gap height (amplitude = 2.4 μm), calculated both with 3-D CFD-ACE model and the Saber behavioral model.

36

```
###    MAST code for RL Squeeze-Film Model:   squeeze1D.sin
#
#      Marek Turowski, (C) 1998, CFD Research Corporation, Huntsville, AL
#
# MOVING PLATE:
# gap = 4.00e-006 m,   length = 2.96e-003 m,   width = 1.78e-003 m
# Pgas = 430.0 Pa,     Area = 5.27e-006 m2,    Static_Force (Pgas*A) = 2.27e-003 N

element template  squeeze1D   x_t, x_b = gap

translational_pos   x_t, x_b          # displacement of 'top' and 'bottom' plate
number              gap = 4u          # gap between plates [m] (with default value)

{         # start template body
branch   Fsqz_x = frc_N(x_t->x_b)     # through variable: 1D squeeze force [N]
val      nu      F_rel                # Relative Squeeze-Force, F/Fa = Fsq/(Area*Pamb)
                 F_rel = i(dxdt.v)/2.265584e-003

#  dxdt - template converting mechanical movement to voltage
dxdt.v  x_t  x_b    vel   0       # vel = velocity of plates = voltage for RL model

Lsq.L1_1        vel     4        x_t  x_b =    Llin = 6.717990e+002
Rsq.R1_1        4       0        x_t  x_b =    Rlin = 2.286073e+017
Lsq.L1_3        vel     5        x_t  x_b =    Llin = 6.046191e+003
Rsq.R1_3        5       0        x_t  x_b =    Rlin = 6.428883e+018
Lsq.L1_5        vel     6        x_t  x_b =    Llin = 1.679497e+004
Rsq.R1_5        6       0        x_t  x_b =    Rlin = 4.214366e+019
Lsq.L3_1        vel     7        x_t  x_b =    Llin = 6.046191e+003
Rsq.R3_1        7       0        x_t  x_b =    Rlin = 1.414578e+019
Lsq.L3_3        vel     8        x_t  x_b =    Llin = 5.441572e+004
Rsq.R3_3        8       0        x_t  x_b =    Rlin = 1.666548e+020
Lsq.L5_1        vel     9        x_t  x_b =    Llin = 1.679497e+004
Rsq.R5_1        9       0        x_t  x_b =    Rlin = 1.064511e+020

  Fsqz_x = i(dxdt.v)                    # template equation for through variable
}         # end template body
```

Figure 27. The MAST code of the *squeeze1D* template.
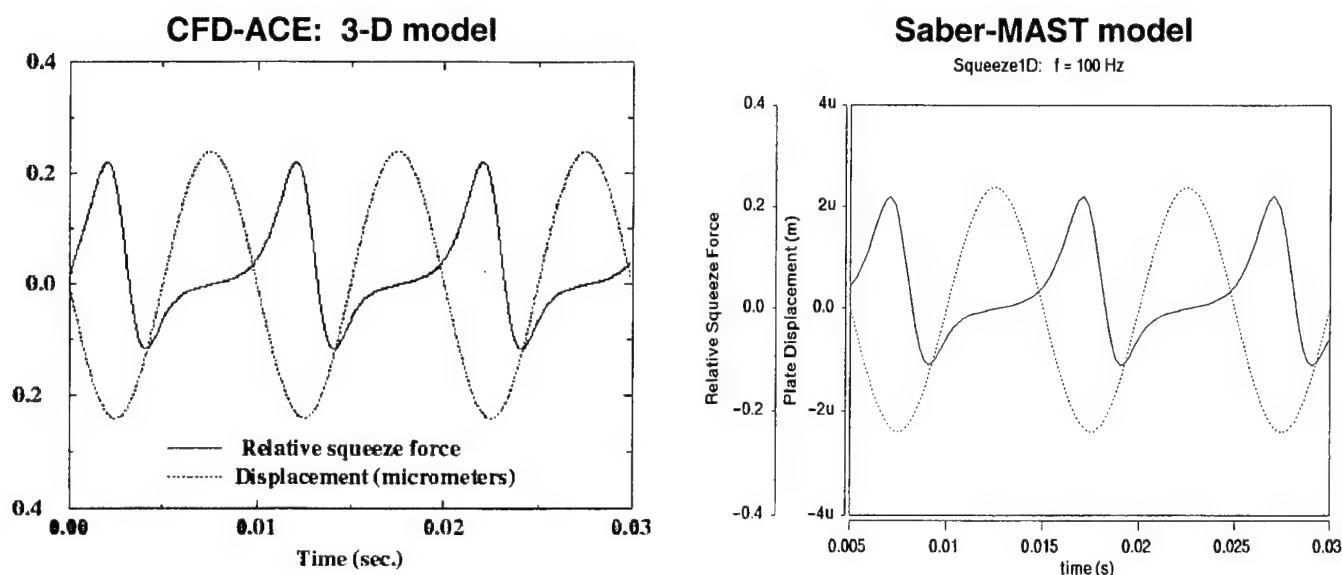
Figure 28. Calculated transient waveforms of the squeeze-film force in response to oscillatory movement of the top plate with amplitude equal 60% of the gap height (amplitude = 2.4 μm).

The equivalent-circuit format of a compact (or behavioral) model has obvious advantages: it can be readily implemented in various system-level simulators, among which SPICE and Saber seem to be the most popular examples. With such circuit simulators, linear and nonlinear device analyses, both in frequency and time domains, can be easily performed. In addition to the standard analyses, advanced circuit simulators offer noise analysis, sensitivity analysis, stability analysis, Monte Carlo simulation, electro-thermal simulation, optimization, parameter sweeps, and ready graphical processing of the simulated data. When the MEMS device itself has an electrical interface, an analysis with the surrounding interface electronics, including feedback, is easily achieved. Moreover, the analysis is not restricted to a single component, but complex systems including MEMS can be build by means of a large network.

A successful circuit-level modeling of entire micromechanical accelerometer, including the circuit submodels for squeezed gas film, was presented in [Veijola 1998(a)]. The compact squeeze-film model presented here, in the form of nonlinear RL circuit, is very promising not only for parallel motion of a rectangular plate, but also for comb drives and micromirrors. On the basis of the solution given in [Darling 1997], the RL equivalent-circuit model can be adapted to reflect more complex boundary (venting) conditions as well as the tilting motion of a plate (e.g. for torsional micromirrors), including two modes of the motion: normal to the surface and a rotating motion. The RL compact model allowed also for successful modeling of a plate with holes, by fitting parameters for all the R and L elements through optimization. Such a procedure was shown in [Veijola 1998(b)] using the APLAC circuit simulator.

The use of **high-fidelity 3-D numerical simulations**, together with the procedures described above**, allow to obtain very useful compact/behavioral models** of squeeze-film effects for wide range of MEMS devices and driving conditions.

4.1.2 Equivalent Circuit Model of Lateral Viscous Damping

For our compact model of the parallel viscous damping, an analytic expression derived in [Veijola 2000] was used, which models the damping force of an oscillating plate as a function of frequency. This general dynamic model, valid in both the frequency and the time domain, is implemented approximately as an electrical equivalent circuit.

Two derive the model, we assumed two surfaces bounding a flat gas film. The first surface, at $z = d$ moves with velocity v_r in the direction of the x axis, while the second at $z = 0$ does not move, see Figure 29. The surfaces are assumed large compared with other dimensions, and thus the border effects are ignored here.
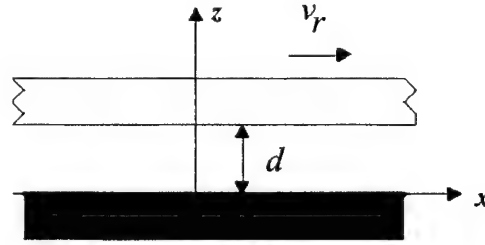
Figure 29. Structure of the air-gap for the lateral damping model.

At low surface velocities (Re<<1), the gas velocity profile can be assumed to be linear, and due to the gas rarefaction, the gap width effectively increases by 2λ, where λ is the mean free path of the gas. According to [Burgdorfer, 1959], the shear stress at one of the surfaces is

$$\tau_{xz} = \frac{\eta A}{d + 2\lambda} v_r \tag{4.3}$$

where A is the surface area and η is the viscosity coefficient. The contribution of the mean free path can be included into the effective viscosity:

$$\eta_{eff,s} = \frac{\eta}{1 + 2K_n} \tag{4.4}$$

where K_n, the Knudsen number, is the measure of the rarefaction effect. It is the ratio between the mean free path λ and gap height d: $K_n = \lambda/d$. The resulting damping coefficient ξ is then simply

$$\xi = \frac{\tau_{xz}}{v_r} = \frac{\eta_{eff,s} A}{d} \tag{4.5}$$

This model assumes a full established Couette flow ignoring the inertia effect of the gas. To extend the damping model to be valid at higher frequencies, the time-dependent velocity profile of the gas must be considered. The dynamics of the gas is modeled with the one-dimensional diffusion equation [Veijola, 2000].

The resulting relation between the shear stress τ_{xz} and the velocity v_r in the frequency domain is derived as:

39

$$\overline{\xi} = \frac{\overline{\tau_{xz}}}{v_r} = \eta A q \frac{\cosh(qd) + q\lambda \sinh(qd)}{(1 + q^2 \lambda^2)\sinh(qd) + 2q\lambda\cosh(qd)} \tag{4.6}$$

where η is the viscosity coefficient, A is the surface area, λ is the mean free path, $q = \sqrt{j\omega/v}$, ω is the angular frequency, v is the kinematic viscosity $v = \eta/\rho$, and ρ is the gas density. The damping coefficient is $\text{Re}(\overline{\xi})$.

As proposed in [Veijola 2000], the general dynamic model of the lateral shear damping, valid in both the frequency and the time domain, can be implemented approximately as an electrical equivalent circuit, presented in Figure 30. In this circuit, electrical voltage represents mechanical velocity v_r, and current represents the shear stress at the moving surface, τ_{xz}.
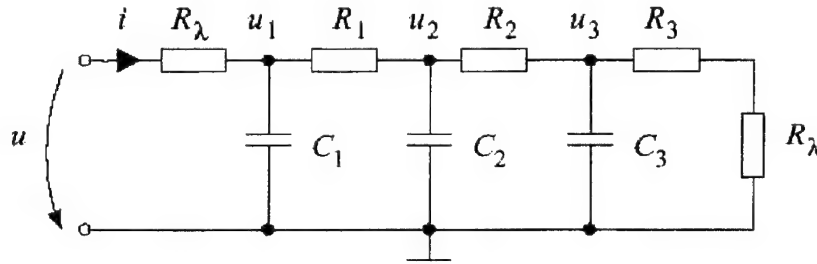
Figure 30. Electrical equivalent circuit which represents the lateral shear damping forces.

The behavior of the damping coefficient $\text{Re}(\overline{\xi})$ was studied in [Veijola 2000] using the equivalent circuit model shown above, as a function of frequency when various parameters change; such as the mean free path (Figure 31), gap height, or pressure. The equivalent-circuit characteristics of the shear damping coefficient were compared with 3-D high-fidelity simulations performed at CFDRC using CFD-ACE+. A series of 3-D and 2D simulations were run to extract the damping coefficient from high-fidelity CFD results (Figure 33). To simulate the gas rarefaction effect and mean free path influence ($\lambda = \lambda_{air}$ in Figure 31), the slip-wall boundary conditions (BC) were used in CFD-ACE+ simulations. Figure 32 shows the corresponding results obtained with CFD-ACE+ without slip-wall BC ($\lambda = 0$), and with slip-wall BC activated (corresponding to $\lambda = \lambda_{air}$).
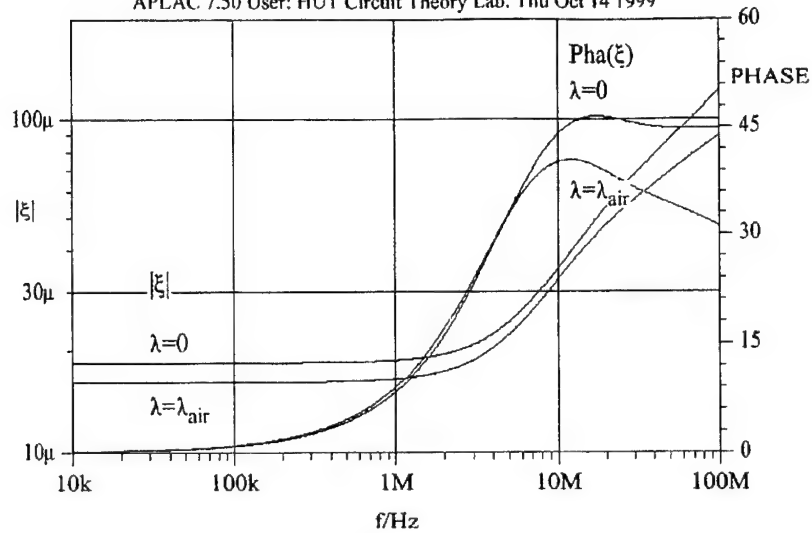
Figure 31. The contribution of the finite mean free path λ to the damping coefficient at atmospheric pressure. Gap separation is 1 µm and the surface area is 1 mm×1 mm.
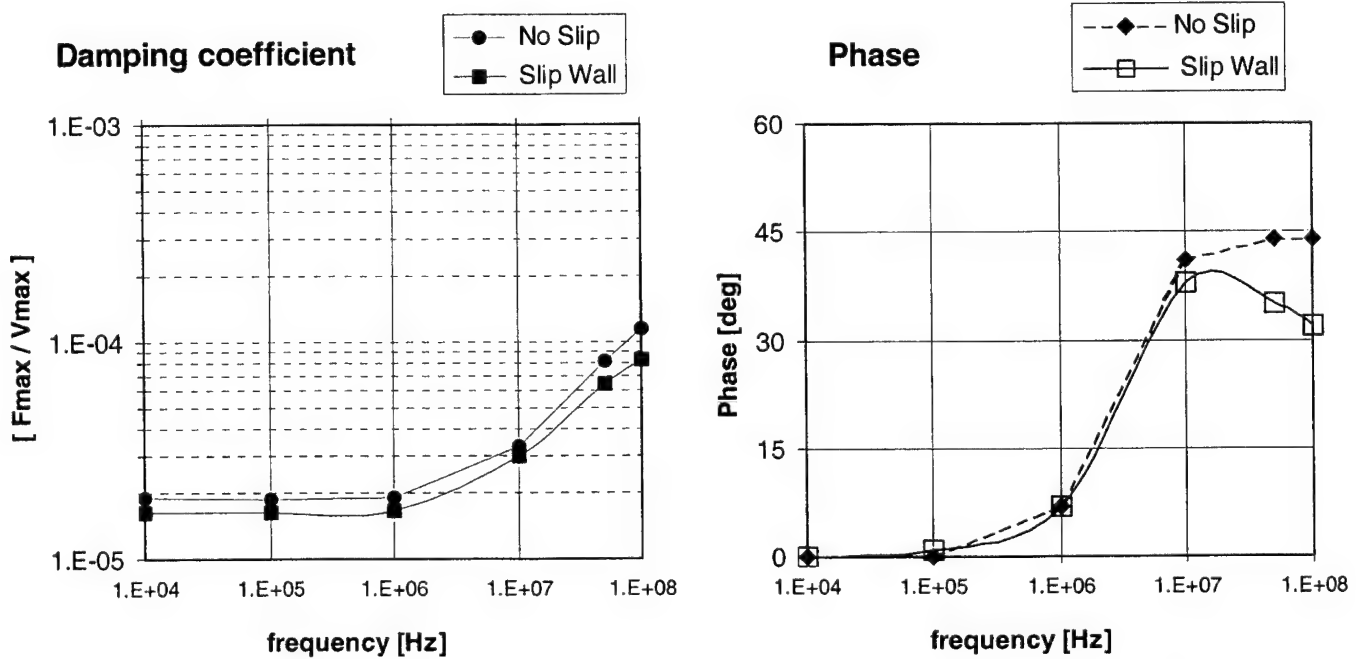
Figure 32. Damping coefficient (Shear-Force/Velocity) characteristics calculated with CFD-ACE+, using Slip Wall boundary condition to account for mean free path contribution.

f = 10 kHz, sin. amplitude 1 μm

f = 100 MHz, sin. amplitude 0.01 μm
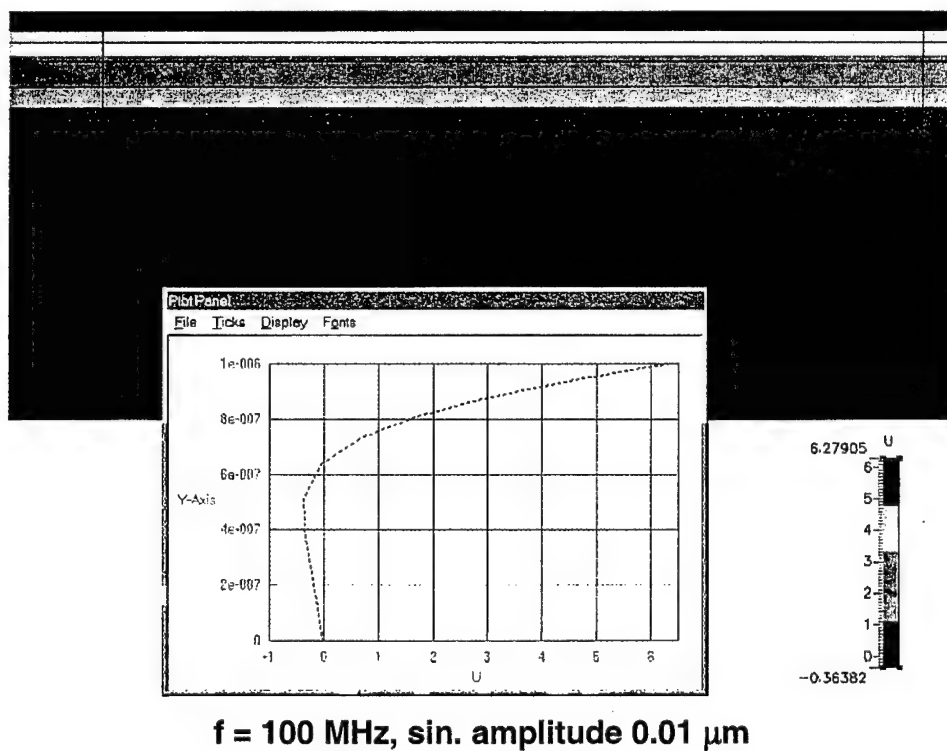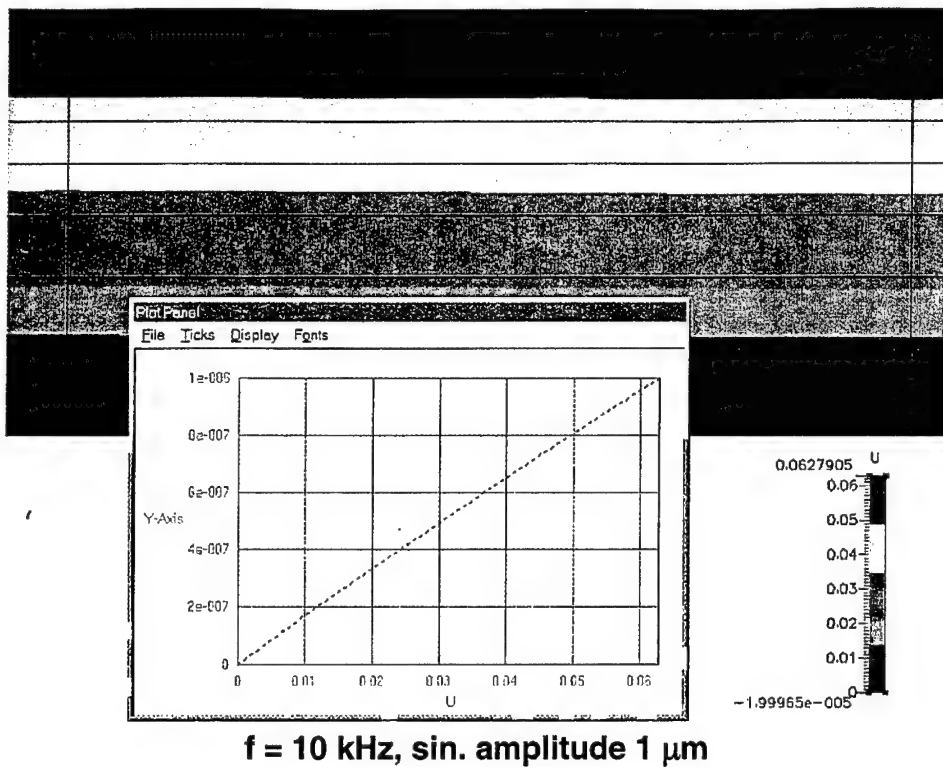
Figure 33. Velocity profiles (shown at peak velocity) obtained by 2D simulations with CFD-ACE+ to extract the damping coefficient. Gap separation is 1 μm, the moving plate edge is 1mm.

The frequency characteristics of the shear damping coefficient obtained with 2D high-fidelity simulations using CFD-ACE+ (Figure 32) agree very well with the characteristics obtained with the equivalent-circuit (Figure 31).

CFD-ACE+ simulations were also used to extend the model validity for small plates and wide range of pressures. The gas rarefaction effects were studied and implemented in the form of slip-wall boundary conditions in modeling. The equivalent-circuit characteristics of the shear damping coefficient were compared with 3-D high-fidelity simulations performed at CFDRC using CFD-ACE+ for a wide range of frequencies and various ambient pressures. Figure 34 shows the corresponding results. A paper on this work was submitted in June 2000 to *IEEE Journal on MEMS* (by T. Veijola and M. Turowski).
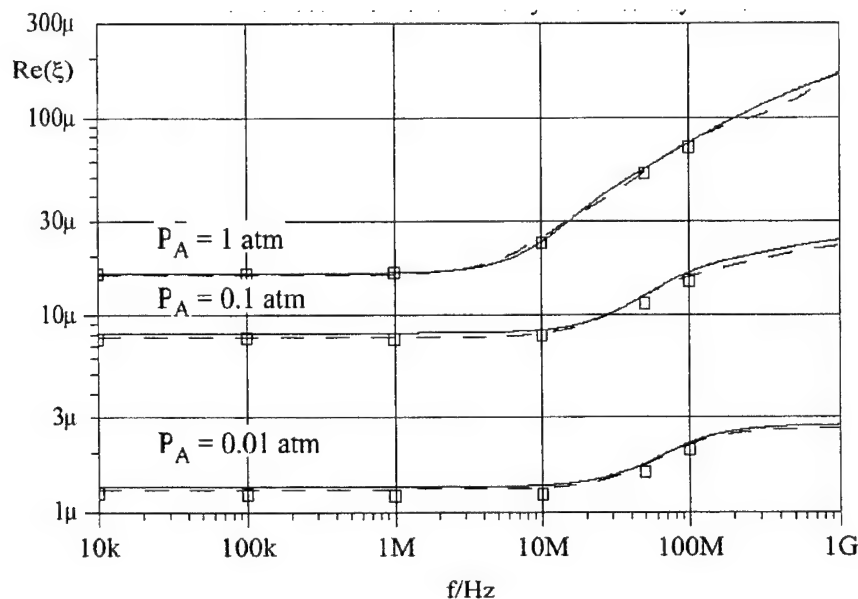
Figure 34. Frequency response of the analytic damping coefficient (lines), the real part of the equivalent circuit admittance (dashed lines), and results extracted from CFD-ACE+ simulations (square symbols) at three pressures. Gap separation is 1 μm and the surface area is 1 mm×1 mm.

The further work on enhancement and validation of the compact/behavioral model of lateral viscous damping in MEMS was continued by the partner group in this project at Carnegie Mellon University (G. Fedder, T. Mukherjee, S. Vemuri) – see below.

4.1.3 Improvement and Validation of Viscous Damping Compact Models

Experience with experimental verification of the synthesis methodologies developed by the CMU team under the DARPA Composite CAD BAA 96-16 project on "Foundations for MEMS Synthesis" (MEMSYN) demonstrated that the off-the-shelf lateral damping models had a 20% error in predicting the Q-factor for folded-flexure resonators. As the MEMSYN project was evolving to synthesis of accelerometers, the damping models governing the dynamics of

43

accelerometers, namely squeeze film damping was considered most important. We therefore first present the work on squeeze-film modeling, and then on modeling of lateral damping.

4.1.3.1 Parametrized Models of Squeeze Film Damping in MEMS

There were four stages to the development of parametrized models for squeeze-film damping. First, we developed a squeeze-film damping model for use in NODAS as none had existed at that time. Next, we compared existing models with continuum simulation using CFD-ACE+ to screen for model limitations. Next we developed an extended model to overcome the limitations, and finally, we verified the extended model first using CFD-ACE+, and then with experimental measurements.

The starting point squeeze-film damping model was [J.J.Blech, "On Isothermal Squeeze Films," Journal of Lubrication Technology, v. 105, 1983 ,pp. 615-620], with extensions into an equivalent circuit model [T. Veijola, H. Kuisma, J. Lahdenpera, and T. Ryhene, "Equivalent-Circuit Model of Squeezed Gas Film in a Silicon Accelerometer," Sensors and Actuators A, vol. 48, 1995, pp.239-248] and to a non-linear behavioral model [M. Turowski, Z. Chen and A. Przekwas, "Squeeze Film Behavior in MEMS for Large Amplitude Motion – 3-D Simulations and Nonlinear Circuit/Behavioral Models,Proc. IEEE/VIUF Intl. Workshop on Behavioral Modeling and Simulation (BMAS '98), Orlando FL, Oct 27-28 1998].

As these models were derived using electrical equivalent R-L circuits, we first derived a mechanical analog for spring and damping effects from [J.J.Blech, "On Isothermal Squeeze Films," Journal of Lubrication Technology, v. 105, 1983, pp. 615-620]. The use of mechanical equivalent circuit models had previously been demonstrated to be less confusing in a behavioral modeling system like NODAS that has both electrical and mechanical models.

$$k_{mn} = \frac{6lw\,P_a}{\left(mn^2\right)\pi^4(g+z)^3} \tag{4.7}$$

$$B_{mn} = \frac{768(lw)^3\eta_{eff}}{\left(mn^2\right)\left(m^2l^2+n^2w^2\right)\pi^6(g+z)^3} \tag{4.8}$$

The model contains parallel branches of series-connected damper and spring elements (Figure 35). The expressions for the damper and spring elements are where m, n are odd integers, w is the width and l the length of the squeeze film, g is the nominal gap which is equal to the thickness of the squeeze film, P_a is the ambient pressure, η_{eff} is the effective viscosity of the air, and z is the displacement of the oscillating top plate, which squeezes the air film.
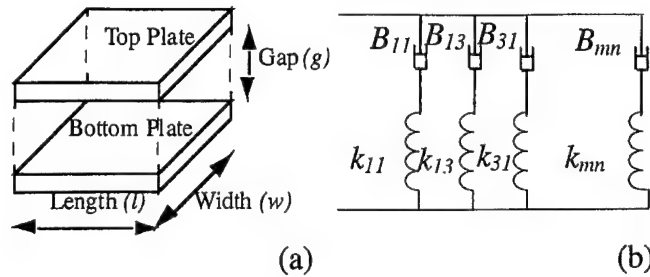
Figure 35. (a) Squeeze film between two parallel plates, (b) Spring-damper behavioral model.

The B-k values are related to the component values of the R-L equivalent circuit model presented in [T. Veijola, H. Kuisma, J. Lahdenpera, and T. Ryhene, "Equivalent-Circuit Model of Squeezed Gas Film in a Silicon Accelerometer," Sensors and Actuators A, vol. 48, 1995, pp.239-248] as $B_{mn} = 1/R_{mn}$ and $k_{mn} = 1/L_{mn}$. The velocity (across variable) of the top plate was mapped to the voltage across the R-L branches and the damping force (through variable) was mapped to the current.

Once the existing state of the art model had been incorporated into NODAS, we began a series of simulations comparing the model with CFD-ACE+. These simulations indicated that at the scale of the squeeze-film found in the differential comb finger configurations of lateral accelerometers (where comb fingers are 2-5 μm thick), the behavioral squeeze film model was off by as much as 50%. This error occurs because the behavioral model inherits Blech's original assumption of trivial boundary conditions that set the gauge pressure to zero at the plate edges. This assumption is not true in practice. As shown from the pressure distribution obtained by CFD-ACE+, the gauge pressure is zero *only at some distance* from the plate edges (Figure 36).
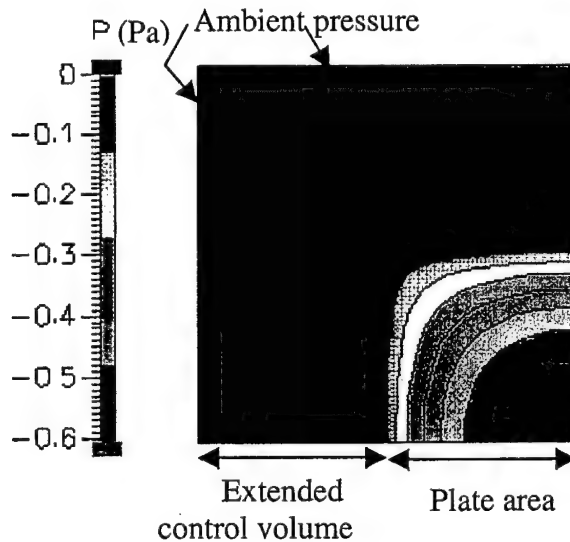
Figure 36. Pressure distribution on the surface of an oscillating plate (Quarter plate shown).

45

One approach to handling the edge effects is to increase the plate size in the behavioral model by δL to match the numerical simulation results with non-trivial boundary conditions. With the extension of the plate dimensions, the effective width and the length become $w_{eff} = w + \delta L(w)$ and $l_{eff} = l + \delta L(l)$. These effective dimensions are used in equations (4.1) and (4.2). δL depends on the geometry of the squeeze film and the oscillation frequency. To screen the importance of these factors, 3-D numerical simulations with frequencies in the ranges of 100 Hz to 10 kHz, gap sizes from 1.5 µm to 4 µm and plate sizes in the range of 10 µm to 1 mm were performed and the values of plate extensions (δL) needed to match the behavioral and numerical results determined. These variable-screening experiments indicated a strong dependence of δL on the gap and the plate size. Simulations were performed to determine the dependence of δL on these variables. The values of $\delta L/g$ that gave the closest match between the behavioral and the numerical simulations are determined for plate sizes in the range of 10 µm to 100 µm (Figure 37). Through a linear fit minimizing the sum of squared errors, a second-order model for equivalent plate extension is $\delta L(d) = g(0.8792 + 0.01d)$ where d is a variable representing l or w in microns. The relation indicates that δL is increasing with the plate size. This is as expected because larger plates squeeze more air and cause greater pressure perturbation at the plate edges. The pressure settles to ambient pressure further away from the plate edges.

Simulation results from behavioral models with and without inclusion of plate extension for plate sizes varying from 10 µm to 100 µm are compared to the FEA results. Figure 38 plots the error in the two behavioral models. The model with plate extensions is *always* more accurate. The error of the original model increases drastically for plate sizes less than 60 µm on a side, and is still about 10% for large plate sizes due to the trivial boundary conditions assumed in its derivation. The enhanced plate-extended model matches the FEA results to within 3% for all the plate sizes in the range of 10 µm to 100 µm.

These results were summarized in [S. Vemuri, G. K. Fedder, T. Mukherjee, "Low order squeeze film model for simulation of MEMS devices", Proc. MSM, 2000.] and form the current NODAS squeeze film model.
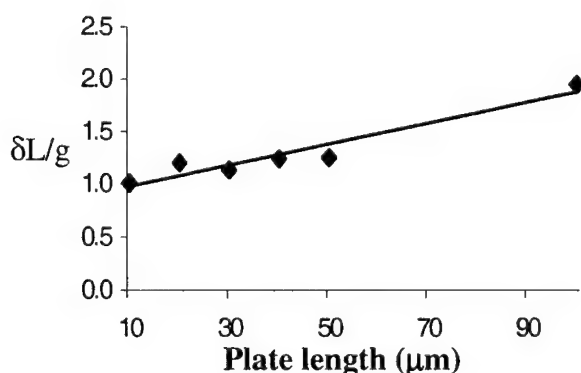
Figure 37. δL/gap values that best match the behavioral and numerical results for different plate sizes.

Accuracy comparison of the models
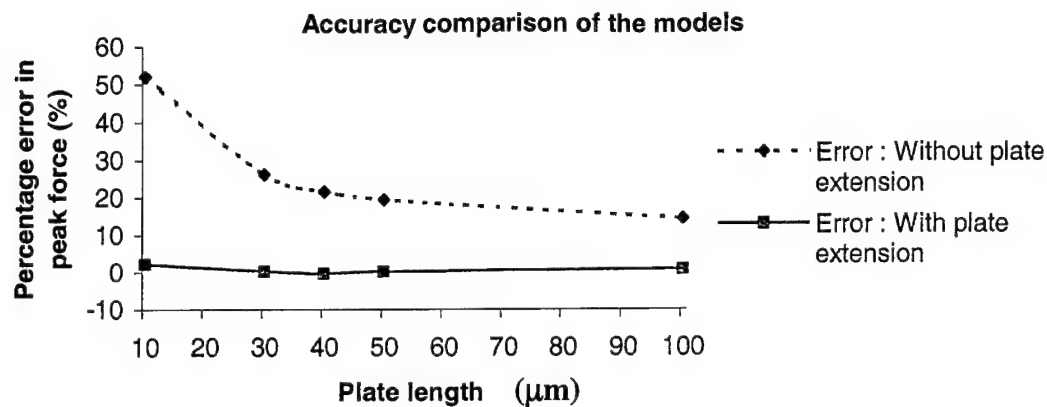
Figure 38. Accuracy of the modified model as compared to the original one for different plate sizes.

The final verification step involved experimental verification using a micromechanical bandpass filter fabricated in the CMOS-MEMS process [Q. Jing, H. Luo, T. Mukherjee, L. R. Carley, and G. K. Fedder, "CMOS Micromechanical Bandpass Filter Design Using a Hierarchical MEMS Circuit Library," Proc. of 12th IEEE Intl. Conf. on Micro Electro Mechanical Systems (MEMS '00), Miyazaki, Japan, pp. 187-192, January 23-27, 2000].

Figure 39 shows the NODAS schematic of the bandpass filter. The filter consists of 3 crab-leg resonators, with differential comb transduction of the input signal from the electrical domain to the mechanical domain (on the left resonator), as well as back from the mechanical domain to the electrical domain (on the right resonator).
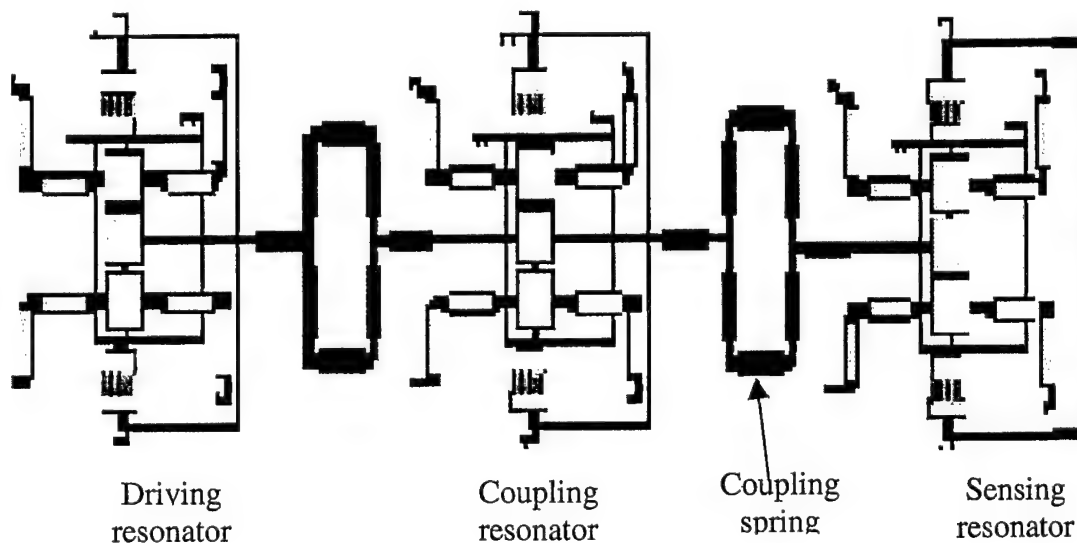
Figure 39. NODAS schematic of a bandpass filter

47

The frequency response of the filter using the original and extended NODAS models and the experimental results are shown in Figure 40. The simulation results are in excellent agreement with the experimental measurements. The results show that the error in computing Q due to the damping model was reduced from 20% to 2%.

			Experimental
			NODAS simulation with edge effects
			NODAS simulation without edge effects
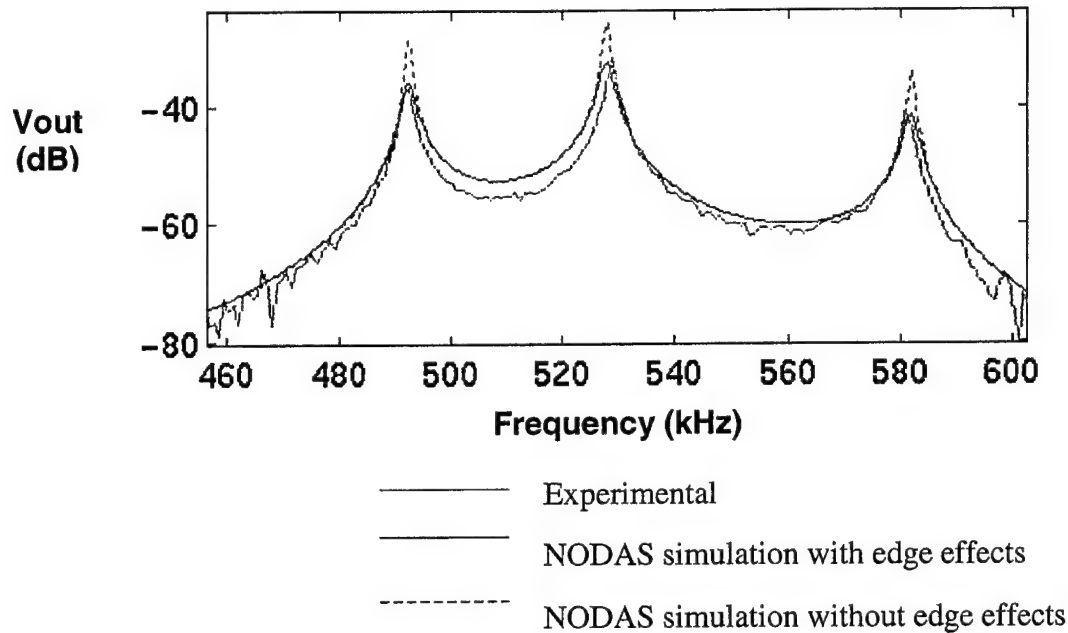
Figure 40. Output voltage of a micromechanical CMOS bandpass filter.

4.1.3.2 Parameterized Models of Lateral Damping in MEMS

As with the squeeze-film damping, this sub-task also involved four stages: we first implemented an existing lateral-damping model; then we compared the model with CFD-ACE+; and studied the comparisons to determine how best to extend the model; finally we verified the extended model against both CFD-ACE+ and experimental measurements.

When a planar structure oscillates laterally over an immobile substrate plane, the resulting gas flow exerts a damping force. The damping force has a spring component that is in phase with the displacement and a damping component in phase with the velocity. The complex damping coefficient representing the force is given by the equation (4.9). The real part represents the damping force and the imaginary part represents the spring or the inertial force [T. Veijola, "Compact Damping Models for Lateral Structures Including Gas Rarefaction Effects", *Proc. MSM*, 20]

$$\bar{\xi} = \frac{\eta_{eff} A}{v_0} \frac{\partial v(z)}{\partial z}\bigg|_{z=0} = \eta_{eff} A q \frac{cosh(qg) + q\lambda sinh(qg)}{(1 + q^2\lambda^2)sinh(qg) + 2q\lambda cosh(qg)} \tag{4.9}$$

where η_{eff} is the effective viscosity coefficient of the gas, A is the plate area, g is the gap between the plate and the substrate, λ is the molecular mean free path of gas at the operating pressure and

temperature, and q is the complex frequency given by $\sqrt{j\omega\rho \big/ \eta_{eff}}$, with ρ is air density and ω is the plate oscillation frequency.

The frequency dependent transfer function is implemented in Verilog-A as a Laplace transform [S. Vemuri, "Behavioral Modeling of Viscous Damping in MEMS," *Master's Thesis, Carnegie Mellon University*, August 2000]. The one dimensional slide film model has two pins indicating the displacement of the oscillating plate and the substrate. This is converted into relative velocity using time derivative operator. This relative velocity is used to compute the damping force in frequency domain and inverse Laplace transformed back to damping force in time domain. The input parameters include the length and the width of the plate, the gap and the ambient pressure.
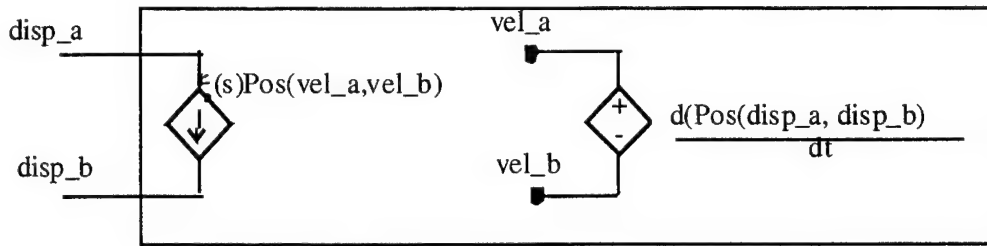
Figure 41. Lateral Damping Behavioral Model.

To include the edge effects in the behavioral model, the length and the width of the plate are each increased by 4 μm. To study the accuracy of the model, we compare the behavioral simulation results with the finite element simulation results. As the frequency domain model is intended for use in non-linear transient analysis, a comparison of square wave displacement patterns is reported below. The first three dominant harmonics of a square wave as the input displacement for a 100 μm square plate and a 2 μm gap. The damping force resulting from the oscillating square wave displacement is shown to be in good agreement with CFD simulations in Figure 42. The bottom of the slide film is considered to be the immobile substrate.
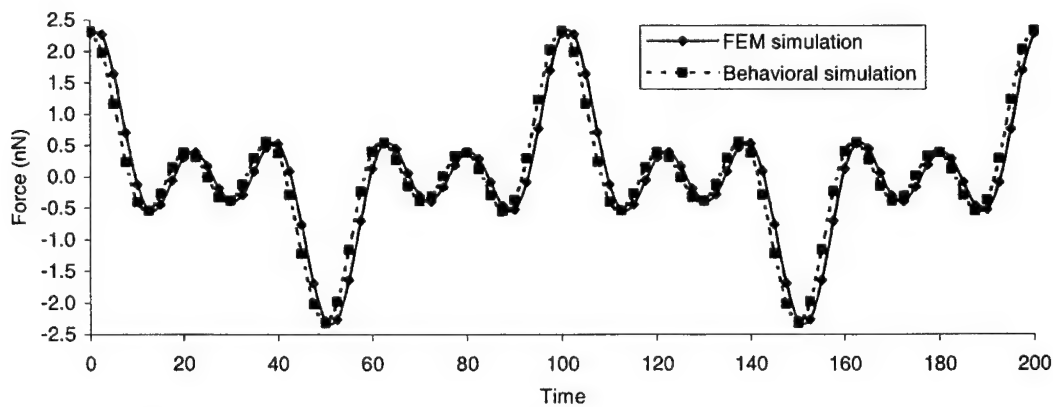
Figure 42. Slide-film model comparison for an oscillating square wave displacement on the top-plate.

To study the behavioral model performance with varying frequency, the magnitude and the phase of the damping force with respect to the plate velocity was obtained for an 100 μm square plate and a 2 μm gap. Figure 43 shows the magnitude of the damping force Figure 44 shows the phase of the damping force, both indicating that the lumped extended plate model matches well with continuum simulation.
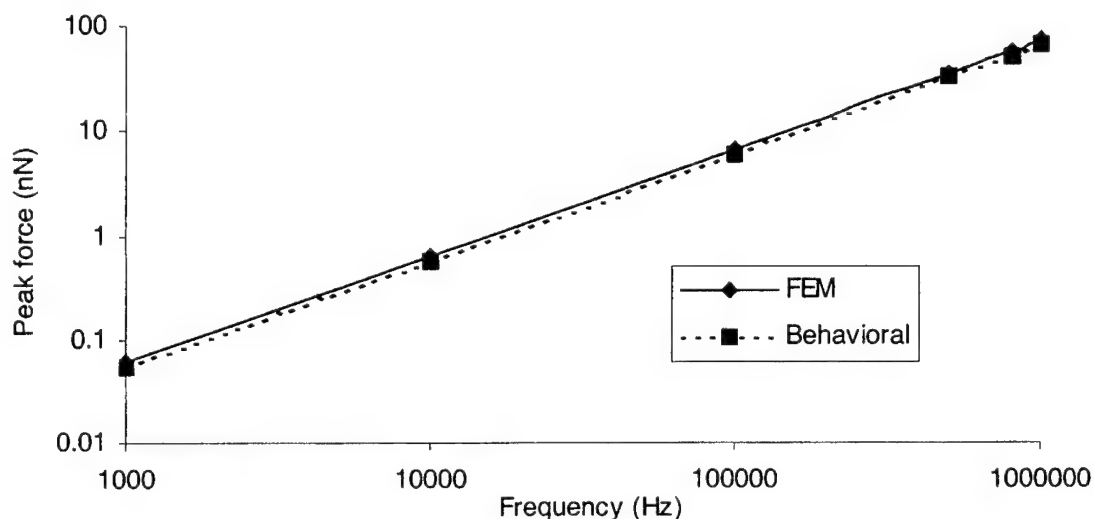
Figure 43. Magnitude of peak force with respect to oscillating frequency of the top plate.
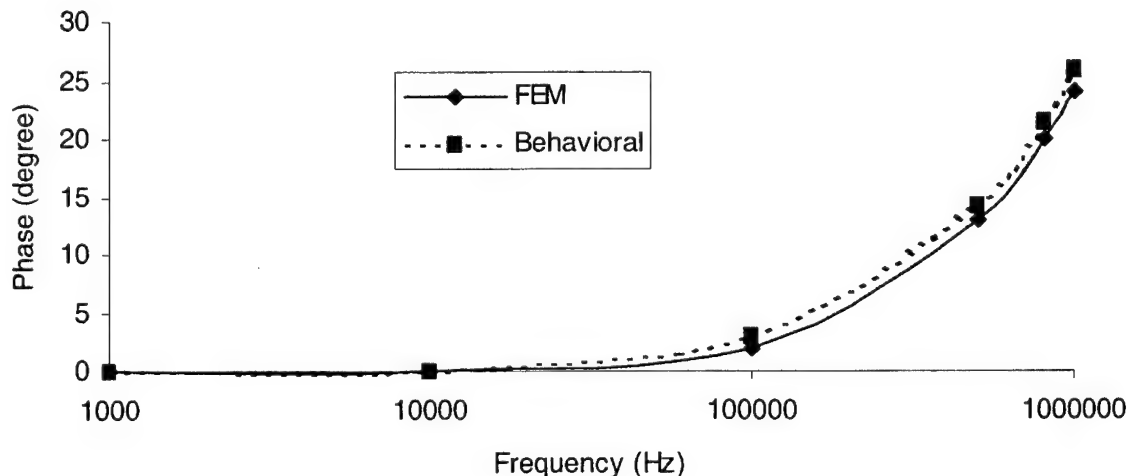
Figure 44. Phase of damping force with respect to oscillation frequency of top plate.

For experimental comparison, we verified the model against the lateral folded-flexure resonators synthesized using the resonator synthesis module [T. Mukherjee, S. Iyer, and G. K. Fedder, "Optimization-based synthesis of microresonators," Sensors and Actuators A, 70 (1998), pp 118-127] developed as part of the DARPA Composite CAD BAA 96-16 "Foundations for MEMS Synthesis" project. The measured quality factors indicated an error of 20% with the

original model with the error reducing to 8% with the extended model. Unlike the squeeze film model where extensive CFD-ACE+ simulations were used to first screen for the best variables, in the lateral damping case we extrapolated the results from the squeeze-film model to determine fixed plate extension length and width parameters. The CFD-ACE+ suite of runs needed for parameter fitting could not be completed by the end of the project, so a fixed plate extension of 4 μm was used. This is the primary reason behind the lower accuracy of the lateral damping model.

4.2   High-Fidelity and Reduced Models of the Synthetic Jets

The synthetic jets were fabricated and measured at GT, and CFDRC in this project was developing models of the devices, providing high-fidelity simulation results, design tools, and reduced model generation techniques. The research included development of reduced-order models of the synthetic jets: single-cell domain model, implemented in 3-cell and 4-cell models of the entire device, and their application in large-scale simulations of synthetic jet arrays, for active electronic cooling and air flow over an aircraft wing. All the details of the synthetic jets fabrication and measurements are described below.

4.2.1   Synthetic Jets Fabrication and Measurements

4.2.1.1 Research Highlights

- Microfabricated two types of synthetic jet modulator arrays
  - Electrostatic Microvalve-type Modulators
  - Electrostatic Membrane-type Modulators
- Utilized New Microfabrication Technologies for Synthetic Jet Modulator Arrays
  - Dry Etching of Silicon Using Bosch Deep-Trench Silicon Etch Process and Plasma Therm ICP
  - Lamination of Dielectric and Metal Layers onto Silicon Substrates
  - Polymer Sacrificial Layer Removal by Two-Sided Barrel Etch Step
- Explored New Characterization Techniques for Synthetic Jet Modulator Arrays
  - Particle Image Velocimetry
  - Infrared Imaging of Heated Surface Cooled by Synthetic Jet Device
- Compiled MEMS Materials Database for Device Modeling/Simulation

4.2.1.2 Introduction to Synthetic Jets

Conventional jets are formed by fluid flowing from an area of high pressure to an area of lower pressure. In the example in Figure 45, a pressure drop exists across an orifice plate resulting in a jet flow from left to right, as drawn, so long as pressure $P_1 > P_2$.
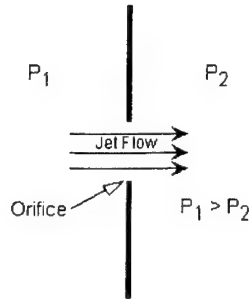
Figure 45. Conventional jet flowing through orifice plate due to pressure drop $\delta P = P_1\text{-}P_2$.

Unlike a conventional jet, a synthetic jet is formed by an oscillatory flow that is acoustically induced near the edge of an orifice. A synthetic jet actuator consists of a fixed actuator cavity bound on one side by a flexible membrane and on the other by an orifice (Figure 46). When the membrane is vibrated rapidly, air is repeatedly drawn into the cavity through the orifice (Figure 46a) and then ejected out of the cavity through the same orifice (Figure 46b). As the outgoing flow passes the sharp edges of the orifice, the flow separates forming a series of vortex rings, which propagate normally away from the orifice plate. The vortices are formed at the excitation frequency, and the nominally round, turbulent jet is synthesized by the interaction of the vortices downstream from the orifice. Since the vortices are generated by an oscillatory flow near the edge of the orifice, the actuator transfers momentum to the air without net mass injection into the overall system.
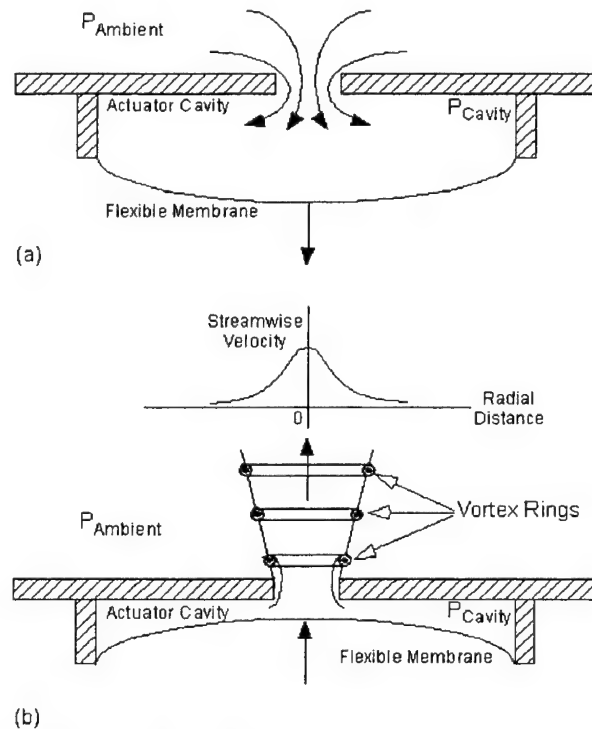
Figure 46. Cross section of typical synthetic jet actuator showing entrainment of ambient fluid 2a ($P_{\text{Cavity}} < P_{\text{Ambient}}$) and vortex generation 2b ($P_{\text{Cavity}} > P_{\text{Ambient}}$). Figure 2b also shows a typical streamwise velocity profile as measured downstream of the orifice plate.

52

4.2.2 Modulation of Synthetic Jets Using Micromachined Modulator Arrays

Three synthetic jet modulation schemes have been the focus of our investigations. In the direct approach, an array of micromachined membrane actuators is used to generate the synthetic jet flow (Figure 47).
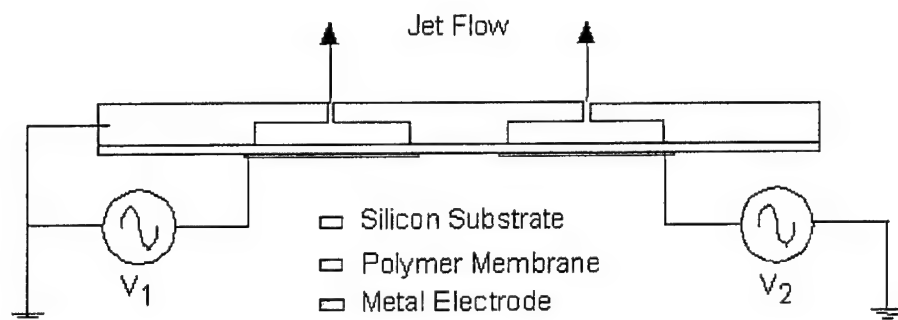
Figure 47. Direct generation/modulation of synthetic jets using micromachined membrane actuators.

Modulation of the jet flow is achieved by varying the electrostatic drive signal sent to the membrane actuators. So, across an array of such devices, drive signal amplitudes, frequencies, and phasing can be varied giving the most flexibility in terms of tuning synthetic jet array output. A disadvantage of this approach is that to obtain that flexibility, a high voltage amplifier and an oscillator circuit are required for each element of the microjet array.

Since high jet velocities can be difficult to achieve with a micromachined electrostatic membrane actuator, a variation of this method uses the micromachined membrane actuators as modulators of jet flow generated by another source, typically a piezoelectrically-driven membrane as in Figure 48.
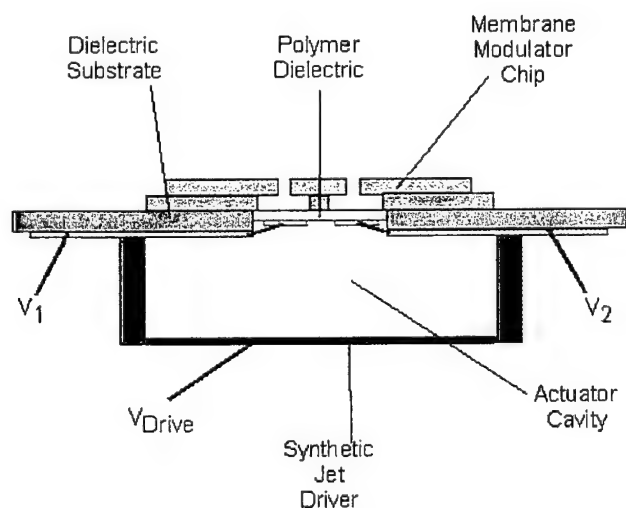
Figure 48. Schematic of membrane modulation scheme (not drawn to scale).

In this configuration, the piezoelectric membrane pneumatically drives the membranes of all microjet array elements in parallel, so only one high voltage amplifier is required. To modulate an individual array element, a DC voltage can be applied to the membrane electrode of that microjet to electrostatically increase the apparent stiffness of that membrane, reducing the overall membrane movement for a given pneumatic pressure. Clamping of the membrane across the orifice hole is not required to completely shut off jet flow; instead, reducing the membrane deflection below the range of motion required for synthetic jet generation is sufficient. The polyimide membrane also reduces the chance of arcing by more completely isolating the actuator electrode from the substrate.

The third modulation method investigated utilizes an array of micromachined valves to modulate the output of a synthetic jet generated by a piezoelectrically driven membrane (Figure 49).
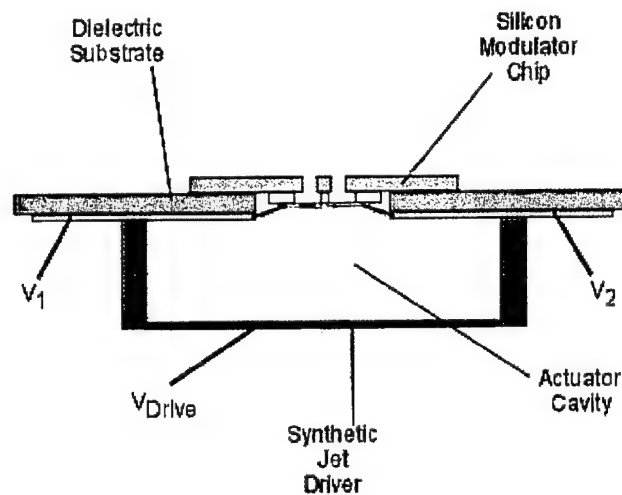
Figure 49 Schematic of electrostatic micromachined valve modulator structure (not drawn to scale).

The microvalve modulators function as normally-open valves which close upon application of a sufficiently high potential difference between the actuator and the substrate. For actuation to occur the gap between the actuator and the substrate must be relatively small, otherwise the electrostatic force will be too small to close the valve. The small gap distance produces significant flow degradation when comparing similar size orifice holes with and without modulator valves positioned over them. In addition to overcoming the inherent stiffness of the microvalve suspension, the applied voltage must also be able to overcome the force of the air flowing in and out of the orifice. If the applied voltage becomes too large, arcing can occur which will permanently damage the valve. Again, a high voltage amplifier supplies the drive signal for synthetic jet generation. A DC voltage applied between the metal valve structure and the substrate ground plane deflects the valve plate towards the substrate, closing the valve.

4.2.3 Fabrication of Synthetic Jet Modulators

Since the majority of the experimental work has focused on the development and testing of microvalve modulators, we begin by discussing the fabrication of the silicon microvalve

modulators. Three methods have been investigated for fabricating the silicon microvalve modulator arrays (Figure 50). The traditional method utilizes standard spin coating and sputter deposition techniques to deposit the polyimide and metal layers, respectively. The advantages of the traditional method include good control over layer thickness as well as the use of standard cleanroom processing equipment. The lamination method offers quick assembly and the ability to obtain thicker layers than typically achieved using conventional approaches. All three methods utilized the Bosch deep silicon trench etching process to etch orifice holes through the silicon substrate leaving near vertical sidewalls. Using oxygen based plasma, the samples are barrel etched to remove polyimide located under the actuator and its moving supports. Figures 52-55 show several examples of actuators fabricated using the lamination method.

Not pictured in Figure 50 (due to its similarity to the traditional method) is the electroplating technique in which the sputter deposition step is used for seed layer deposition. A negative image of the actuator photolithography mask is used to create a mold of thick photoresist, and electroplating is used to fill that mold with an appropriate metal, typically a Ni/Fe alloy. Prior to the release etch, the mold and exposed seed layer are removed. The main disadvantage of this method was the occasional delamination of the electroplated plated metal due to the heat generated during the barrel etching process.
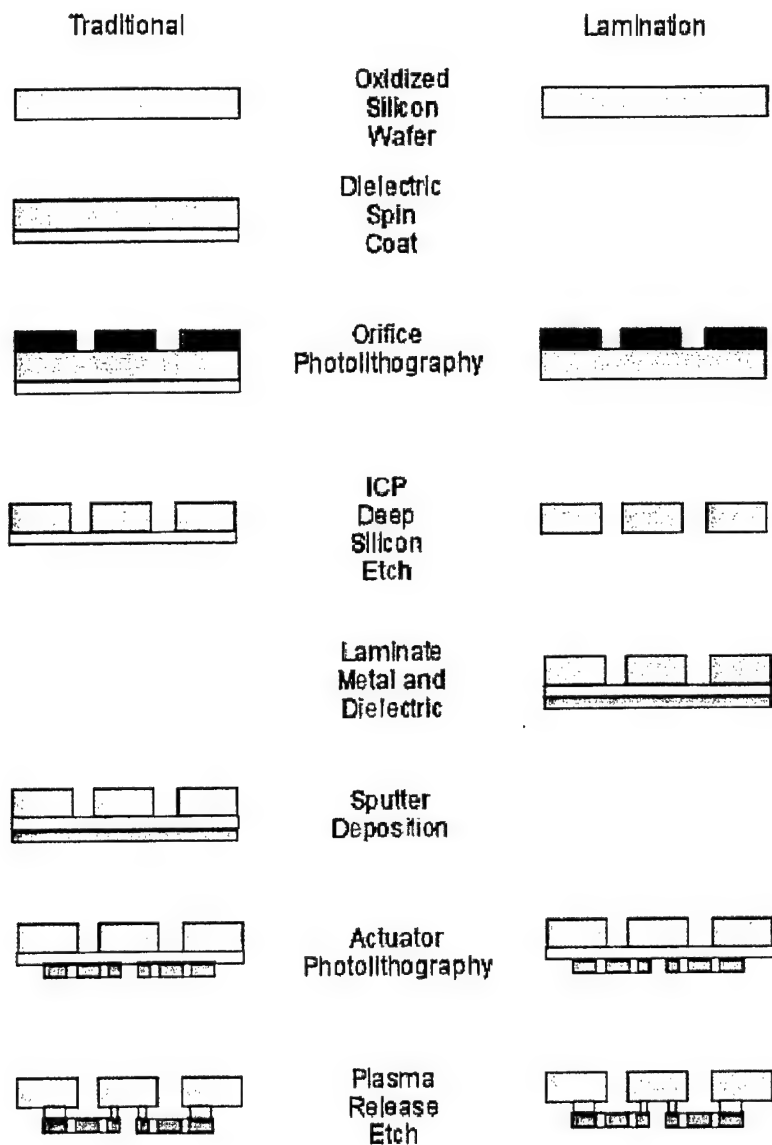
Figure 50. Microvalve modulator fabrication using both traditional and lamination methods.

Figure 51. Photograph of one microvalve of a modulator array fabricated using traditional fabrication techniques.

56
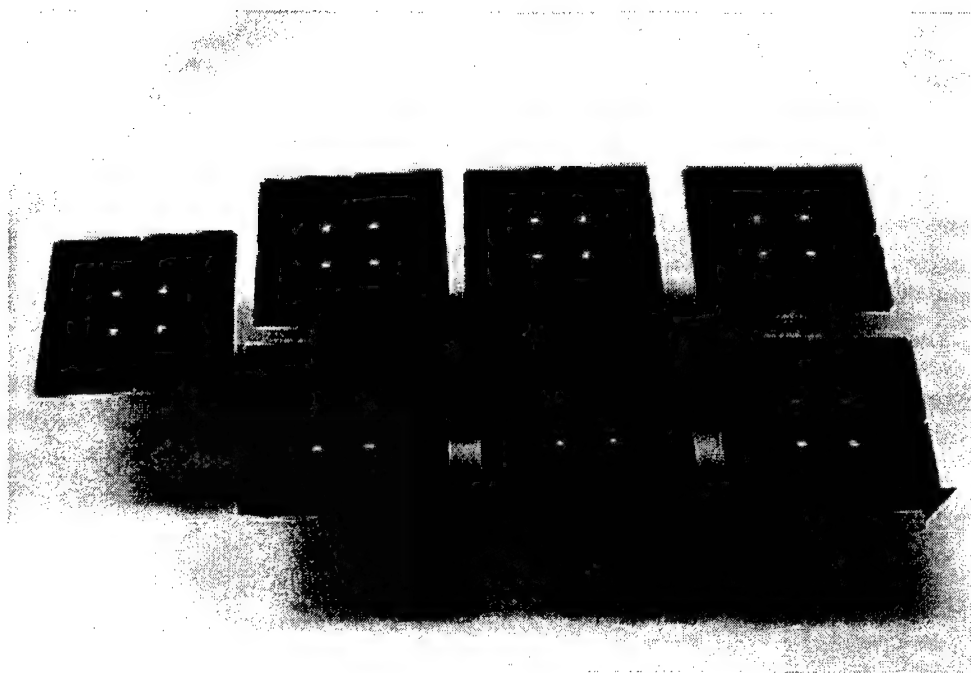
Figure 52 Photograph of fabricated 2x2 silicon modulator array chips after ICP etching and dicing.
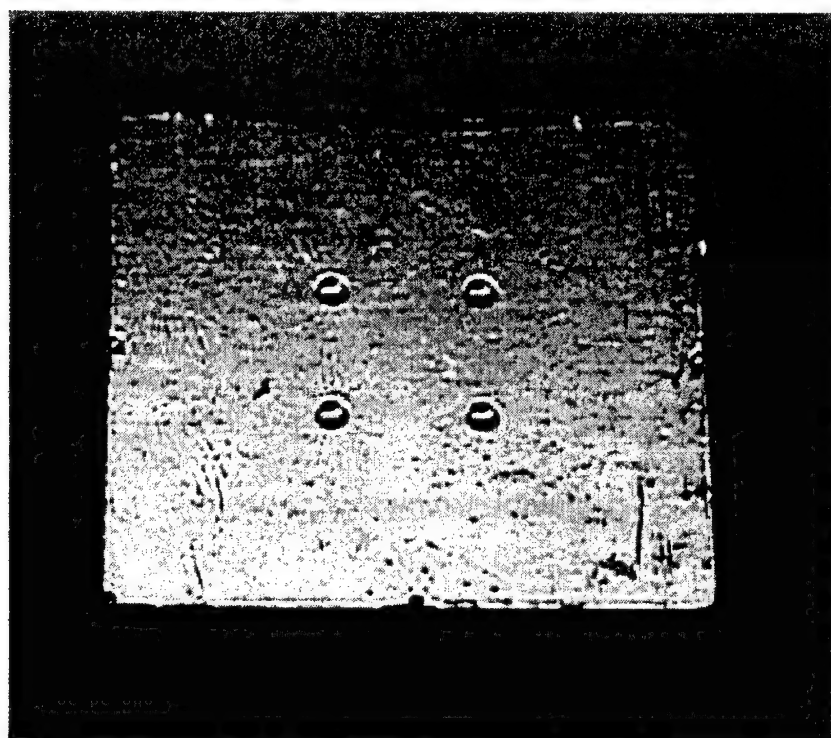
Figure 53. Photograph of 2x2 orifice laminated with Kapton and aluminum films.
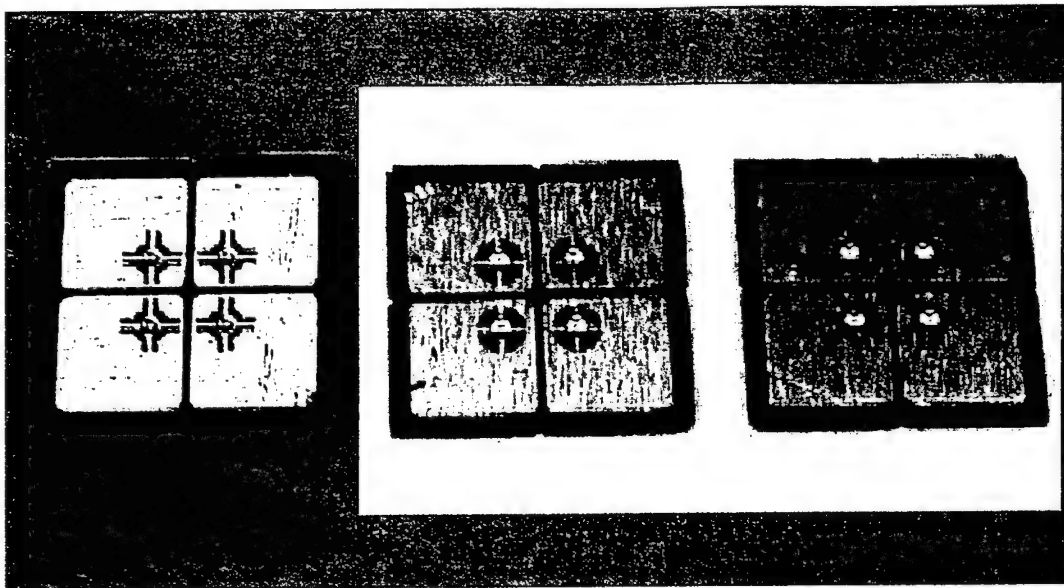
Figure 54. Photograph of released aluminum laminated microvalve modulator arrays showing several of the actuator designs being investigated.
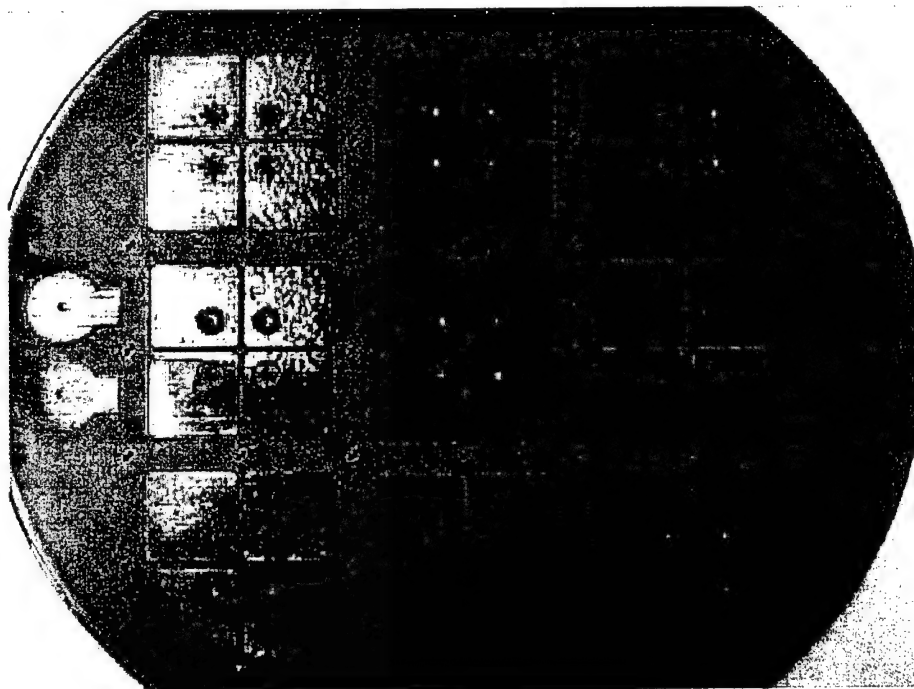
Figure 55. Photograph of released microvalve modulators fabricated using laminated copper films.

The membrane modulator fabrication procedure is based upon the process used to fabricate the microvalve modulators (Figure 56). These modulators are fabricated as two separate wafers, which are subsequently bonded together with epoxy. Separate fabrication permits spin coating of the membrane prior to the silicon etch or lamination of the polymer membrane after the silicon etch step. A tight seal between the two wafers is achieved by clamping the cavity and orifice chips together with magnets prior to application of epoxy. Figure 57 shows a photograph of a membrane modulator array fabricated using the method described in Figure 56.

Cavity Wafer   Orifice Wafer

Oxidized
Silicon
Wafer

Dielectric
Spin
Coat

Orifice
Photolithography

ICP
Deep
Silicon
Etch

Sputter
Deposition

Actuator
Photolithography

Epoxy Bonding
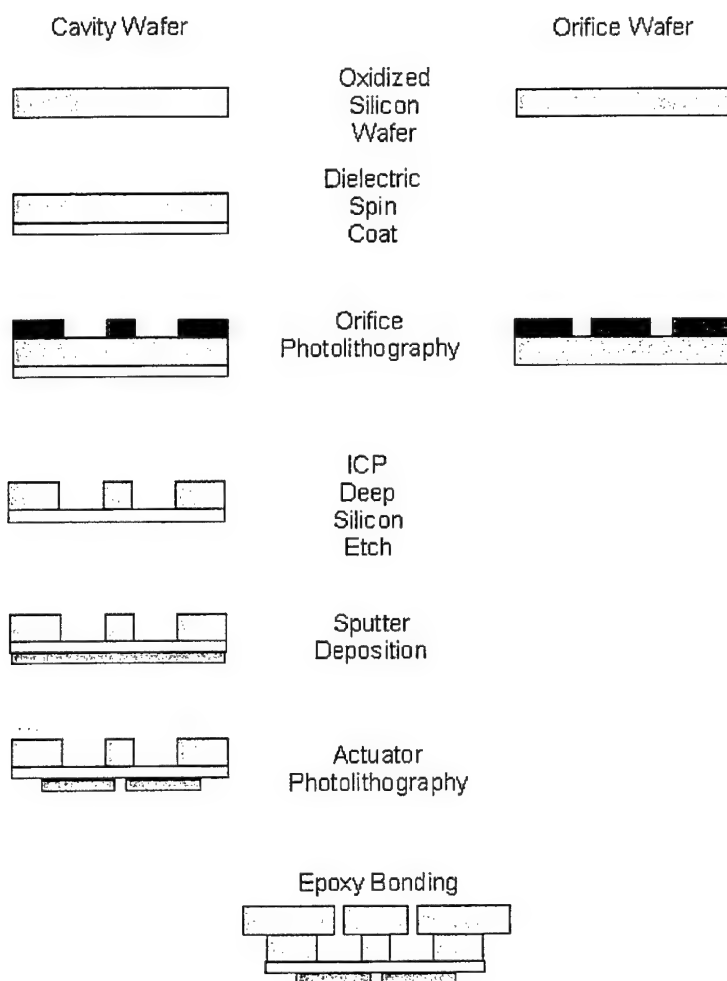
Figure 56. Fabrication sequence for membrane modulator arrays.

59
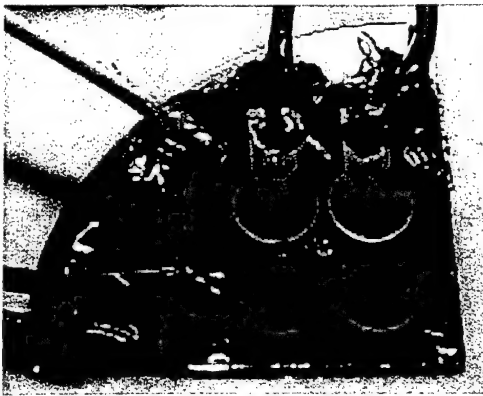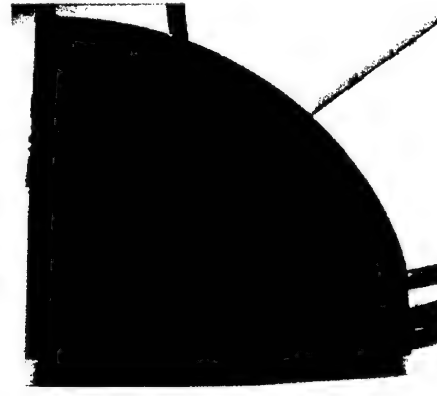
(a)   (b)

Figure 57. Photographs showing the back (a) and front (b) of a membrane modulator array fabricated using the method described in Figure 55.

It is important to note that in all three fabrication procedures, features on the front surface of a wafer must be aligned to features on the back of the same wafer and, in some cases, to features on a second wafer. This makes the use of alignment markers critical during photolithography and assembly steps.

Before the modulator array samples can be characterized, they must be packaged so that electrical contact can be made without compromising the airflow characteristics of the device. For the membrane type devices designed to generate the synthetic jet directly, a combination of epoxy and conductive epoxy are used to secure wires to the substrate and make electrical contact between the wires and the bonding pads, respectively (Figure 57).
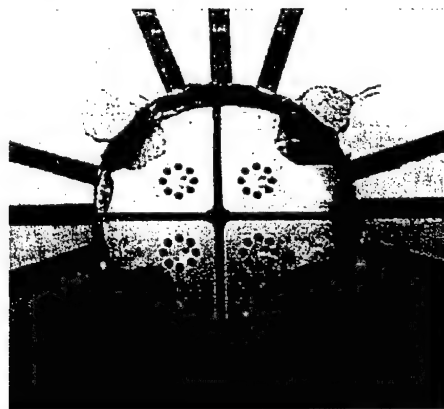
Figure 58. Photograph of a 2x2 aluminum-laminated microvalve modulator array mounted on a patterned copper-clad PC board for deflection and flow testing.

For the microvalve and membrane modulator samples, PC boards with patterned copper traces were prepared as sample mounting plates (Figure 58). The silicon samples are placed over a large hole drilled through the board and bonded with standard epoxy. Electrical connections are then made using conductive epoxy from the bond pads on the silicon sample to the patterned copper traces on the test board. Off-board connections can then be made merely be soldering

60

wires directly to the copper traces on the board. As shown in Figure 58, the board-mounted sample is ready for deflection testing.

For flow testing the sample mounting boards may be attached to the front of the piezoelectric driver mounting plate. (Figure 59). To ensure an airtight seal between the piezo mounting plate and the sample mounting plate, a rubber o-ring is used. Figure 60 shows a schematic of the piezoelectric membrane actuator used to generate the synthetic jets when testing the microvalve and membrane modulator samples. The driver can be bonded to the piezo mounting plate by a variety of adhesives.
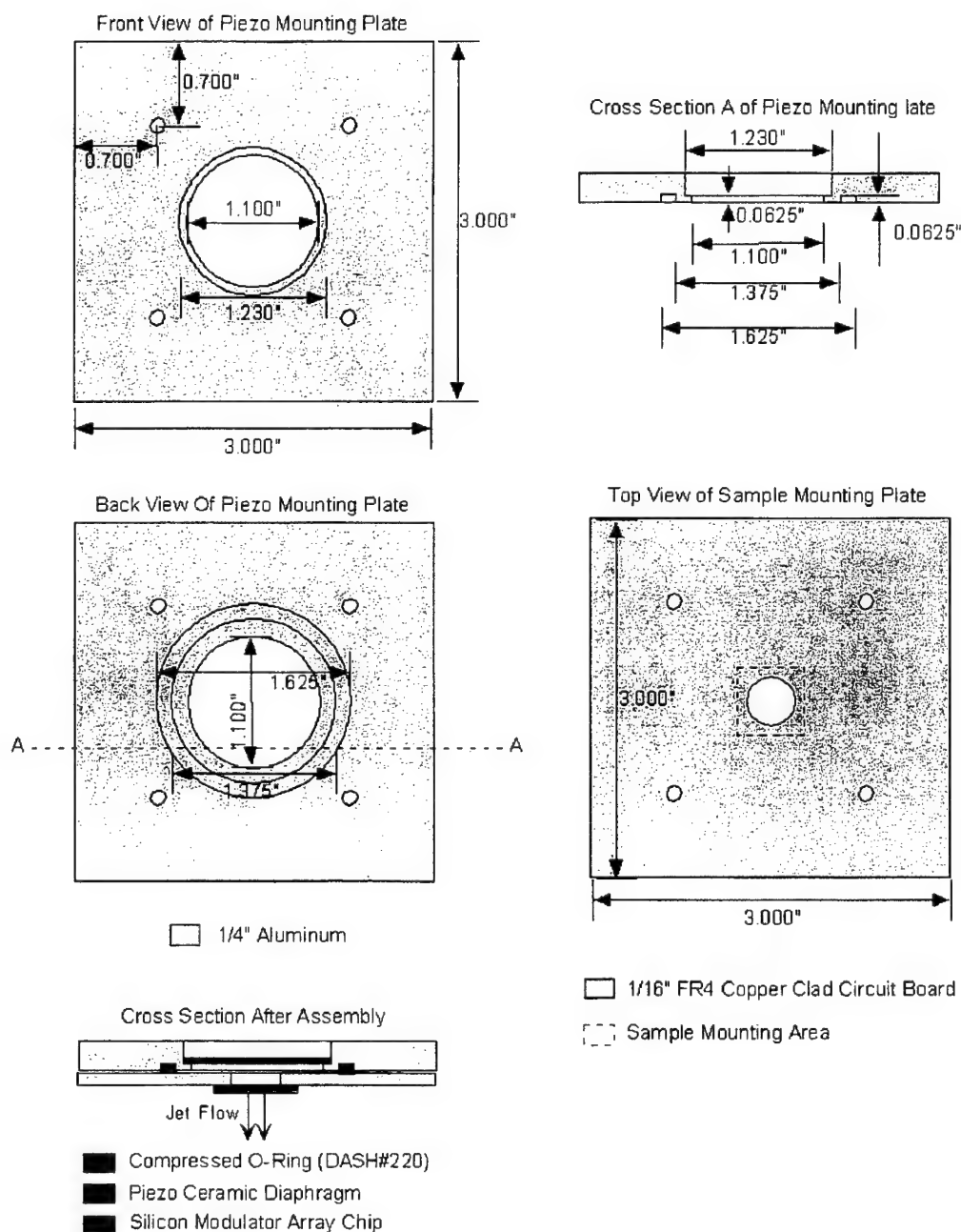
Figure 59. Schematic showing details of the piezo driver and sample mounting plates.

Piezo Ceramic Diaphragm
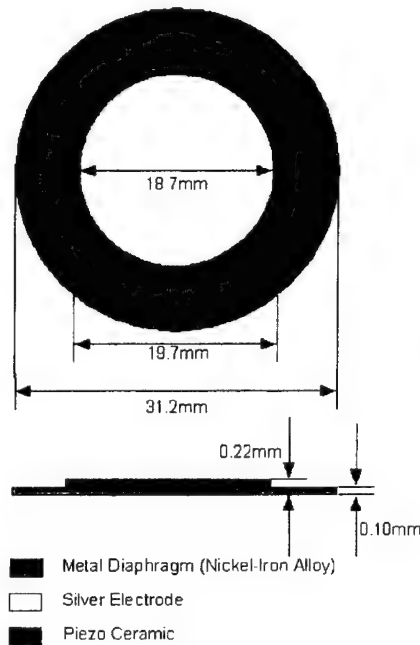
Murata 7NB-31R2-1 Specifications

Resonant Frequency = 1.3kHz
Resonant Impedance = 300 ohm
Capacitance (@120Hz) = 40nF

Operating Conditions During Testing

Drive Frequency = 1470 Hz
Drive Voltage = 40Vrms sine wave

18.7mm

19.7mm

31.2mm

0.22mm

0.10mm

■ Metal Diaphragm (Nickel-Iron Alloy)
☐ Silver Electrode
■ Piezo Ceramic

Figure 60. Schematic showing details of the piezoelectric driver element used in these experiments.

4.2.4 Characterization of Synthetic Jet Modulator Arrays

Prior to flow testing of the modulator arrays, deflection testing was performed to determine the minimum voltages required to close the microvalve actuators or to visibly deflect the polymer membranes of the membrane modulators. Mounted samples were photographed using a high-resolution video microscope as shown in Figure 61. By carefully adjusting the angle of the incident light α and the angle of the sample relative to the camera lens β, a high-resolution, high magnification image with minimal reflections could be obtained.

Video
Camera
and
Lens

Light
Source

β α

Sample
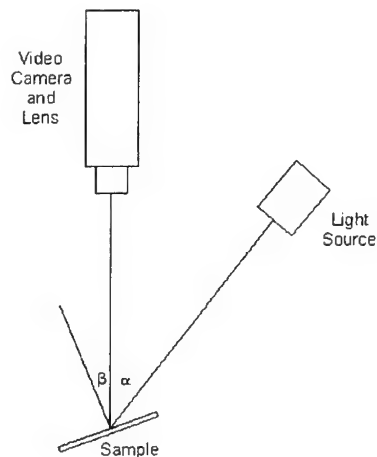
Figure 61 Deflection testing setup.

When tested without the synthetic jet actuator attached, microvalve modulator array elements have been shown to actuate using applied voltages as low as 100 volts. The lowest actuation voltages measured for the membrane modulators were significantly higher at 500 volts.

Once the minimum actuation voltage was determined, one or more flow visualization techniques were used to determine if the synthetic jet could be modulated using voltages at or above the minimum actuation voltage previously measured. The simplest visualization technique used is known as smoke visualization. Since synthetic jets are composed entirely of entrained ambient air, a smoke source placed near the orifice of the jet will allow the jet to entrain and eject smoke making the synthetic jet flow visible (Figure 62). Once the airflow is visible, one may visibly determine if modulation has been achieved.

Two types of smoke were used in these experiments. A commercially available liquid commonly used in theatrical fog machines can be heated electrically until smoke is produced. Smoldering incense was also used to generate smoke for jet entrainment. Since the smoke from either of these heated sources will rise, the sample was suspended vertically above the smoke source so that a thin sheet of smoke would rise past the sample's orifices. In practice, both types of smoke were found to clog the synthetic jet orifices and modulators quickly. Wherever the fog machine smoke touched the sample, it left an oily residue, which proved to be difficult to remove without destroying the sample. This residue cut the testing lifetime to a mere 5-10 minutes in some cases. The smoke particles from the incense also clogged the microjets, though at a slower rate. Another side effect of smoke visualization observed in earlier experiments was that the updraft caused by the rising smoke deflected the synthetic jets upwards so that they were no longer normal to the surface of the silicon chip. As such smoke visualization was found to be an inadequate method for testing the synthetic jet modulator arrays.
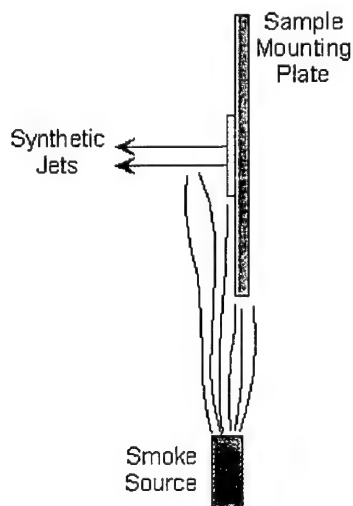
Figure 62. Smoke visualization of synthetic jet actuators.

A Schlieren optical system was also used to quickly determine if the modulator arrays were modulating the synthetic jets. As shown in Figure 63, a Schlieren optical system can be used to visualize small index of refraction changes occurring in the test area. The light passing through

the material with the different index of refraction refracts down a slightly different path where it is blocked by a knife edge producing a shadow in the image seen by the video camera.
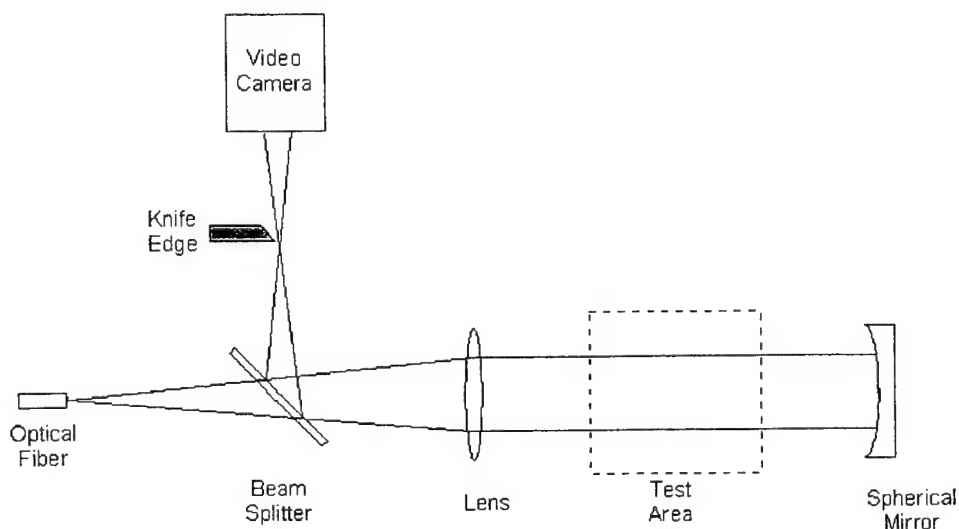
Figure 63. Schlieren optical system diagram.

To use this non-destructive means of flow visualization, we had to introduce an index of refraction change in the synthetic jet. One way to do this is to heat the air of the jet being tested. Previous experiments had shown, however, that heating of the jets would not only introduce thermal drafts that could obscure the synthetic jets, but the heat could also interfere with the operation of the microvalves.

Another way to make the synthetic jet visible is to allow it to entrain a gas with an index of refraction different than that of air. Helium entrainment produces an image with reasonable contrast, but we determined experimentally that the breakdown voltage of the electrostatic actuator was significantly lower in a helium rich atmosphere than in the normal ambient air environment used for measuring the deflection voltage. So, many microvalves, which would actuate in a normal air environment, would experience catastrophic failure during the Schlieren visualization experiment. In an attempt to solve this problem, carbon dioxide gas was also used. Since the breakdown voltage of a carbon dioxide-rich atmosphere is higher than that of normal air, modulators which deflect in normal air without breakdown will also deflect in the carbon dioxide-rich atmosphere without breakdown. The index of refraction change, however, is so small that the contrast in the images between the ambient air and the synthesized jet was too small most times to determine if the modulator arrays were operational. We also observed that the entrainment of the visualization gases could distort the synthetic jet as it emerged from the sample making the jet non-perpendicular to the surface of the silicon chip.

An additional difficulty in applying the Schlieren visualization technique is that the image contrast of the synthetic jets is reduced by the small size of the jets we were investigating. When imaging a larger jet, say a centimeter scale or larger jet, the overall distance that the light must travel within the material of different refractive index is physically longer than the path traversed through the sub-millimeter scale synthetic jet. The longer path generates more beam displacement at the knife edge and, hence, more contrast in the image. Another disadvantage of

using this technique to visualize the operation of the modulator arrays is that the only information this technique can provide is quick visual confirmation of modulator operation. No velocity information or any other data is gathered by this technique.

Other non-destructive methods have also been used to test the modulator arrays with various degrees of success. Pitot tube velocity measurements have been made of the microjet devices. For these measurements, a small diameter tube is connected to a baritron by thin tubing (Figure 64). The tube is positioned in front of the jet orifice such that the jet blows into the tube. For jets with relatively high velocities, the measurements of streamwise velocity are accurate provided that the pitot tube itself is far enough from the orifice that the size of the tube is not of the same order of magnitude as the size of the jet being measured. For low velocity jets, the accuracy of the measurement is limited by the sensitivity of the baritron and by the conductance of the tubing.
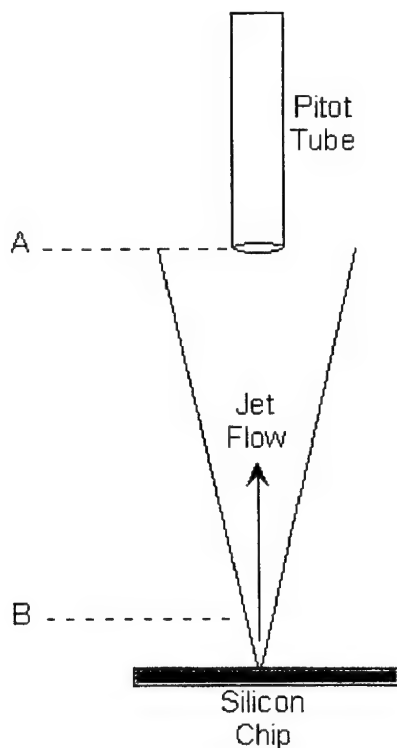
Figure 64. Pitot tube velocity measurement (A) good pitot placement and (B) pitot too close for accurate measurement.

A hot-wire anemometer has also been used for non-destructive testing of the synthetic jet modulators. In these experiments, the sample is mounted to a fixed stage and an x-wire probe is attached to an x-y-z positioning stage. Under computer control, the probe may be scanned across the sample to record 2-axis velocity data. The main disadvantages experienced using this technique were related to calibration and probe size. As built, our test setup was geared to testing larger, higher velocity jets, and the smaller velocities of the microvalve modulator jets were at or below the measurable range of the anemometer. As in the case of the pitot tube, the

probe size was also on the order of the size of the jet being tested making the accuracy of the measurements questionable, especially near the sample surface where the highest velocities were found. Finally, the x-wire probe was an impractical choice for our final jet impingement experiments (described later in this section) since the probe would block placement of the impingement plate.

The best technique we found for gauging the performance of the micromachined synthetic jet modulators is known as particle image velocimetry (PIV). To use this technique, a cross section of the flow field was illuminated by a thin sheet of laser light (Figure 65). A high speed, high resolution video camera was then used to photograph particles suspended in the flow field. Given the length scale of the flow and the sampling time, image processing software can determine the velocity vectors associated with various points in the image. As in the case of smoke visualization, the smoke particles used may clog the jets, but the PIV technique obtains a complete velocity map for the points illuminated by the laser sheet. Moreover, this technique allows velocity data to be recorded during the jet impingement experiment.

Top View of PIV Test Setup
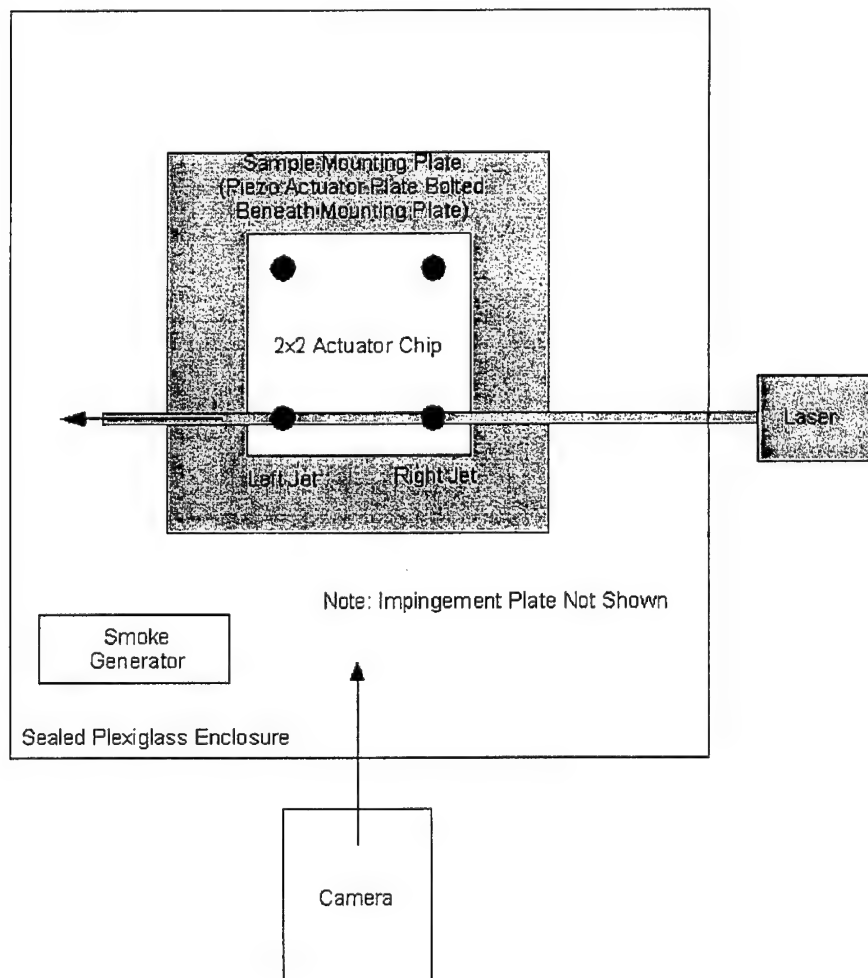
Figure 65. Particle Image Velocimetry (PIV) test setup.

Currently under investigation is a new imaging technique in which jet modulation is gauged by observing the cooling effect of the modulated synthetic jet upon a heated object. By examining infrared images of the cooled object, we hope to be able to demonstrate three-dimensional operation of the modulator array. As shown in Figure 66, the copper-clad Kapton substrate is heated by a thin-film Kapton heating element attached to the copper side of the substrate. The synthetic jet is positioned such that it will impinge upon the heating element. An infrared camera is used to view the temperature distribution of the substrate from the Kapton side. A major advantage of this test method is that it is non-destructive in nature, requiring no smoke or visualization gas entrainment that could interfere with the operation of the modulator array.

To calibrate the temperature measurement setup, an accurate emissivity value is needed for the copper-clad Kapton film. To determine the unknown emissivity, a material of known emissivity is used. A small piece of thin black tape with an emissivity of 0.95 was placed in the center of the heated substrate facing the infrared camera. With a constant power of 0.9W delivered to the heating element, the temperature of the black tape was allowed to stabilize, and the temperature of the tape was measured by the infrared camera using the known emissivity of 0.95 for the tape. The tape was then removed, and the temperature of the heated substrate was allowed to stabilize once again. The emissivity was then recalibrated to make the measured temperature of the substrate agree with the measured temperature of the black tape.

Infrared Testing Setup
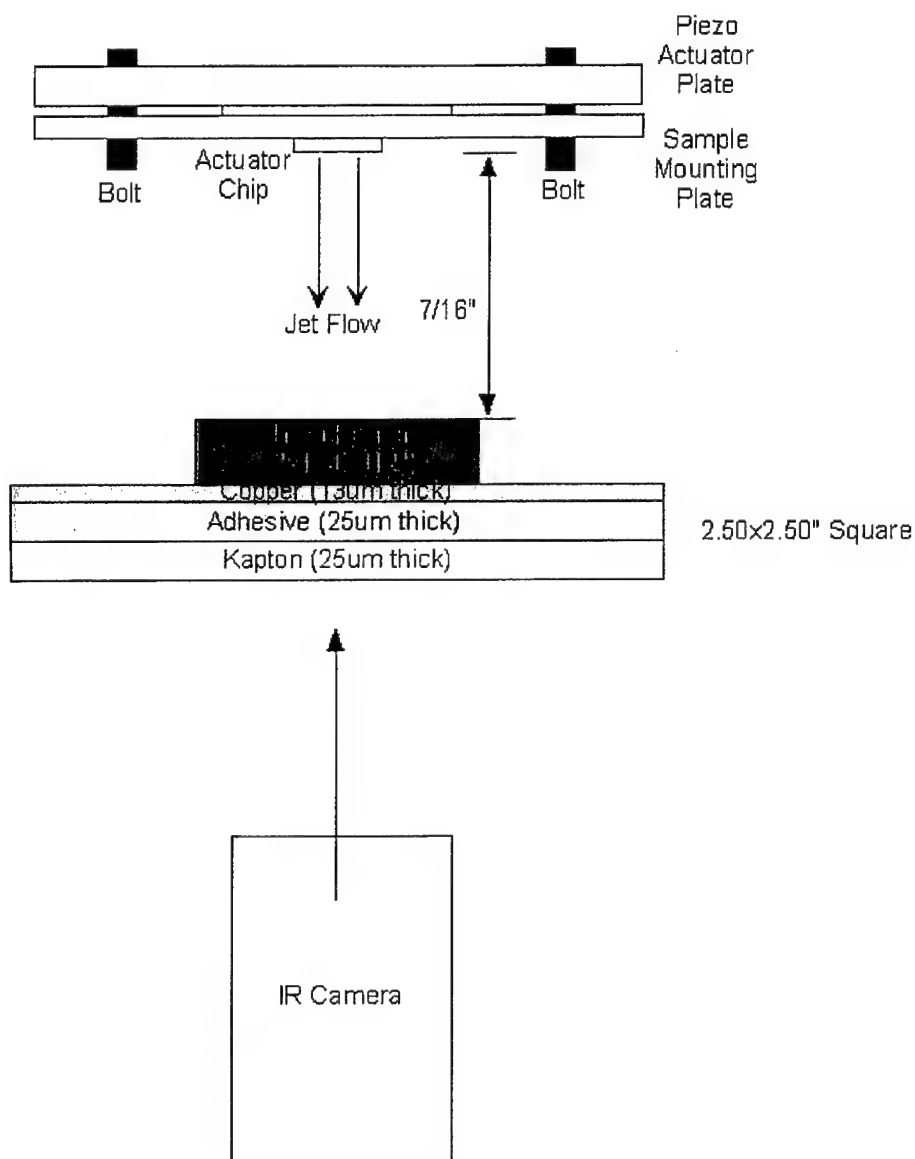
Figure 66. Schematic of infrared test setup used to evaluate the cooling effect of the modulated synthetic jet arrays on a heated surface.

4.2.5 Experimental Data

Given the volume of data collected, we first include a sample of the data collected during the characterization of a typical microvalve modulator array. The data presented is from a single microvalve modulator array (as pictured in the top left corner of (Figure 55) mounted for testing

as shown in Figure 59 with the piezoelectric driver element picture in Figure 60 used for synthetic jet generation. Initial deflection testing was performed using the video microscope setup pictured in Figure 61 with modulation voltages from 406V to 707V applied. Initial flow testing was performed using the pitot tube setup diagramed in Figure 64. Jet velocities from 7m/sec for all four jets operating to 9.7m/sec for a single jet operating were recorded using the pitot tube measurement apparatus with a 42Vrms, 1470Hz sine wave drive signal supplied to the piezoelectric driver. Subsequent testing was performed with a 40Vrms, 1470Hz sine wave to extend the lifetime of the piezoelectric driver. Temperature distributions of the synthetic jets impinging on a heated surface were measured using the infrared camera setup sketched in Figure 66, and corresponding velocity data for this experiment were collected using the PIV measurement setup pictured in Figure 65.

Actuator Layout Diagram

Orifice Layout Diagram

3.00mm

3.00mm

500um

Copper (13um thick)   Adhesive (25um thick)

Kapton (25um thick)   Silicon (300um thick)

Adhesive (12um thick)

Cross Section of Actuator Showing Layer Thicknesses
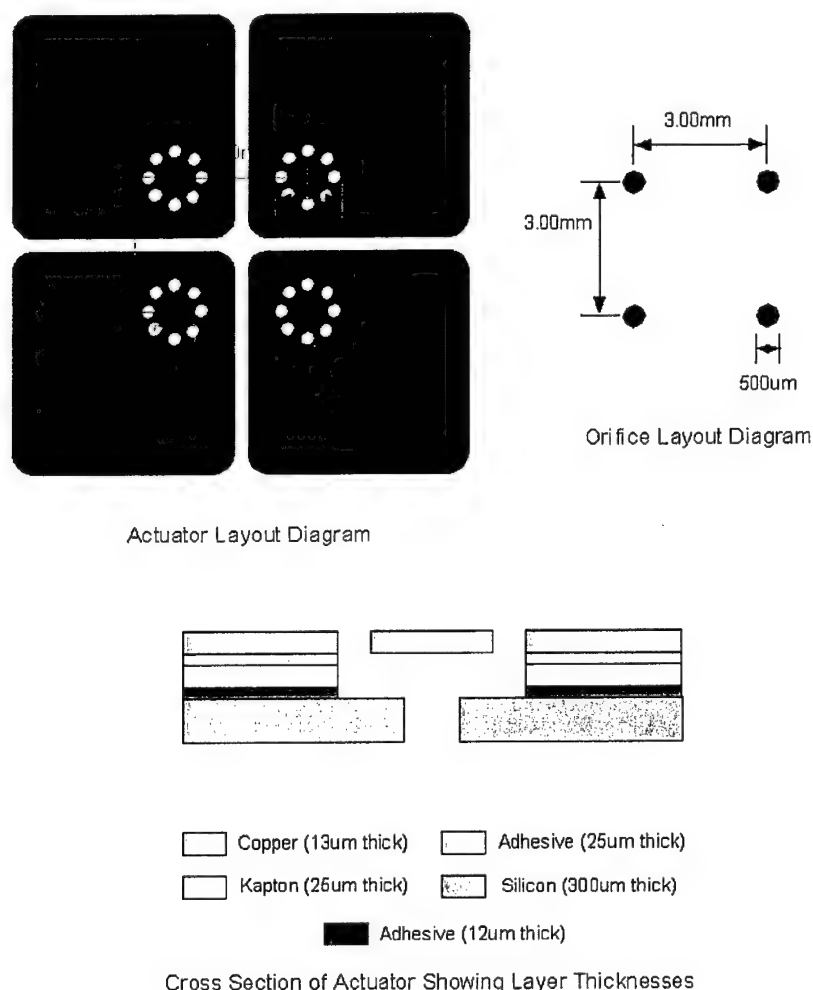
Figure 67. Schematic showing mask patterns and layer thickness of typical synthetic jet microvalve modulator array.

Figures 68, 69, 70 and 71 show vorticity plots for the two jets in the flow field illuminated by the PIV laser sheet (Figure 65). In these Figures, the synthetic jet modulator array flow is impinging upon the heated surface as pictured in Figure 66. Figures 72, 73, 74 and 75show PIV streamwise velocity (V) profiles for the Left Jet, Right Jet, Two Jets, and Four Jets cases, respectively.

Figures 76, 77, 78 and 79 are PIV velocity profiles showing the perpendicular velocity component U. Note that the sign of U changes depending upon the direction of entrainment. Figures 80, 81, 82 and 83 are PIV speed contours of the four cases examined, and Figures 84, 85, 86, 87 and 88 show the corresponding temperature distributions for no cooling, Left Jet, Right Jet, Both Jet, and Four Jets, respectively.
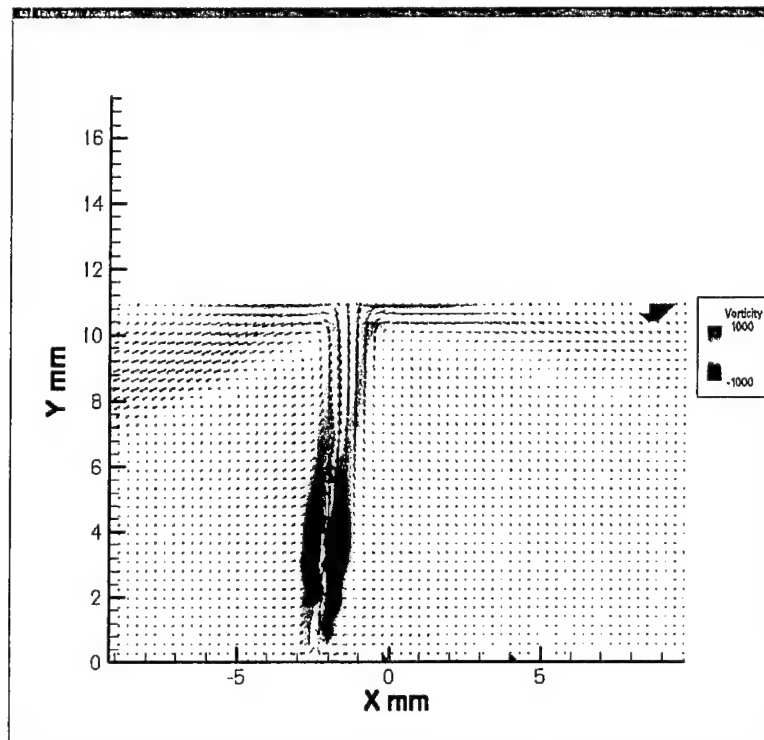
Figure 68. PIV vorticity plot for left synthetic jet (called "Left Jet") from microvalve modulator array.
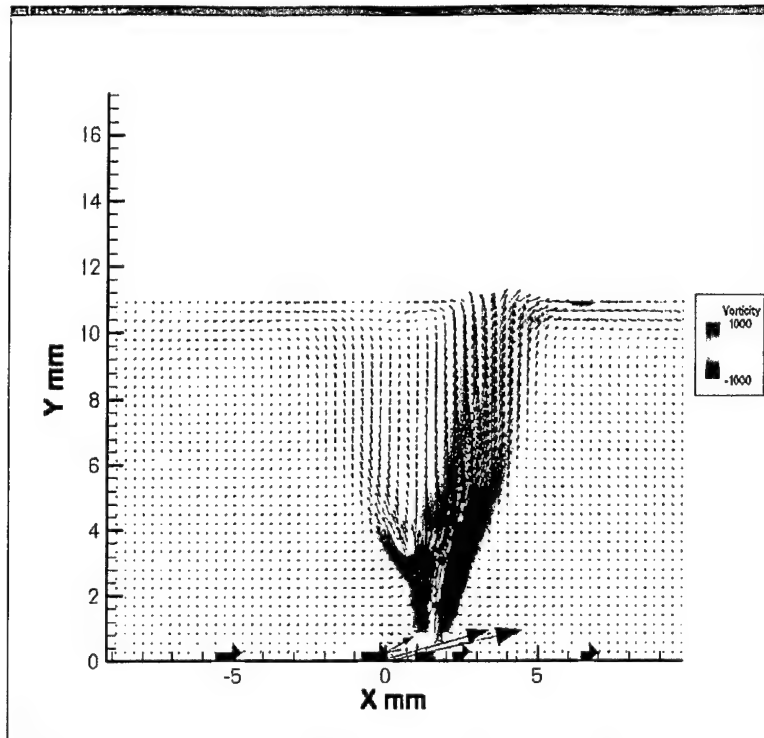
Figure 69. PIV vorticity plot for right synthetic jet (called "Right Jet") from microvalve modulator array.
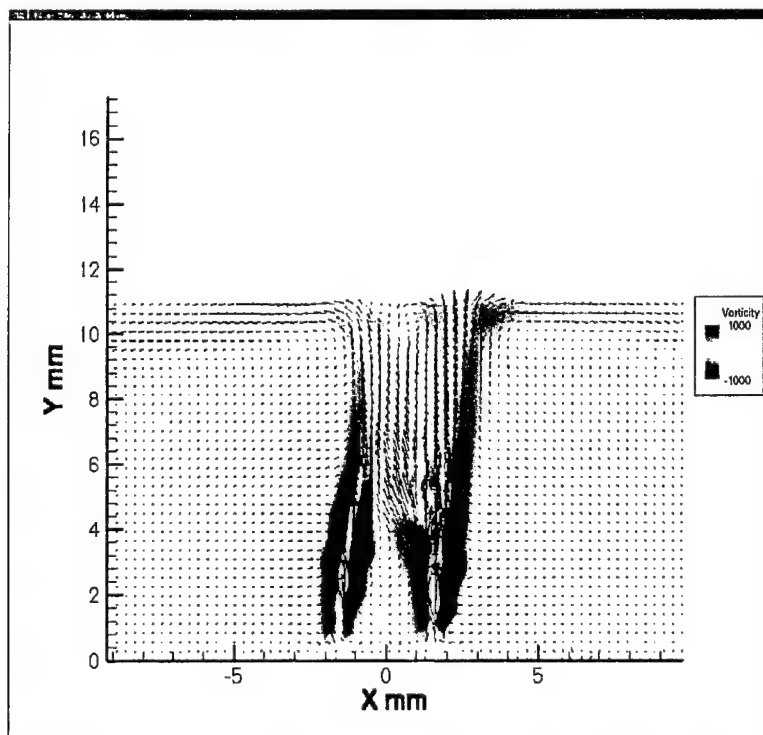
Figure 70. PIV vorticity plot for two synthetic jets (those two illuminated by the laser sheet known as "Both Jets") from microvalve modulator array.

71
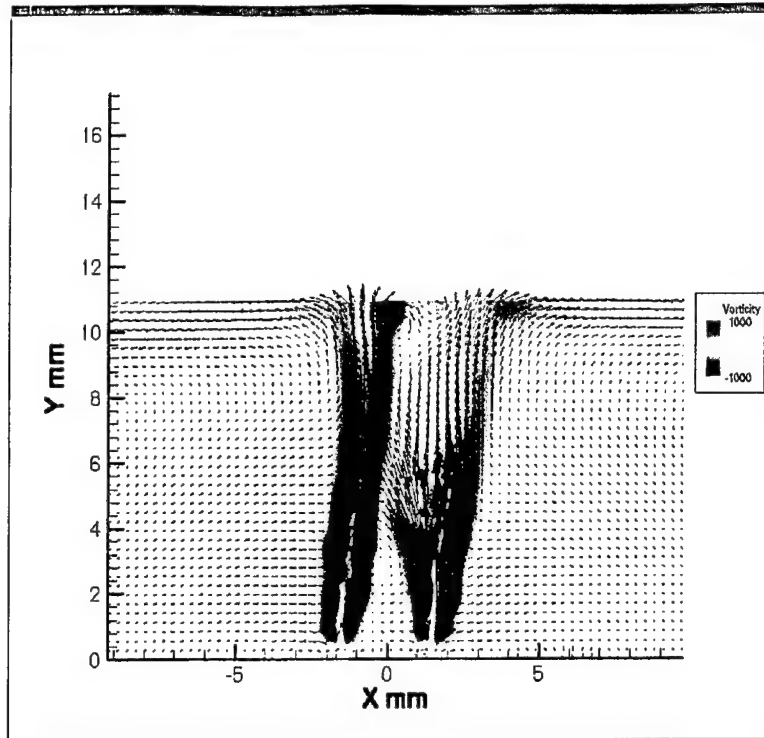
Figure 71. PIV vorticity plot for two synthetic jets from microvalve modulator array with all four of the microvalves open (called "Four Jets").
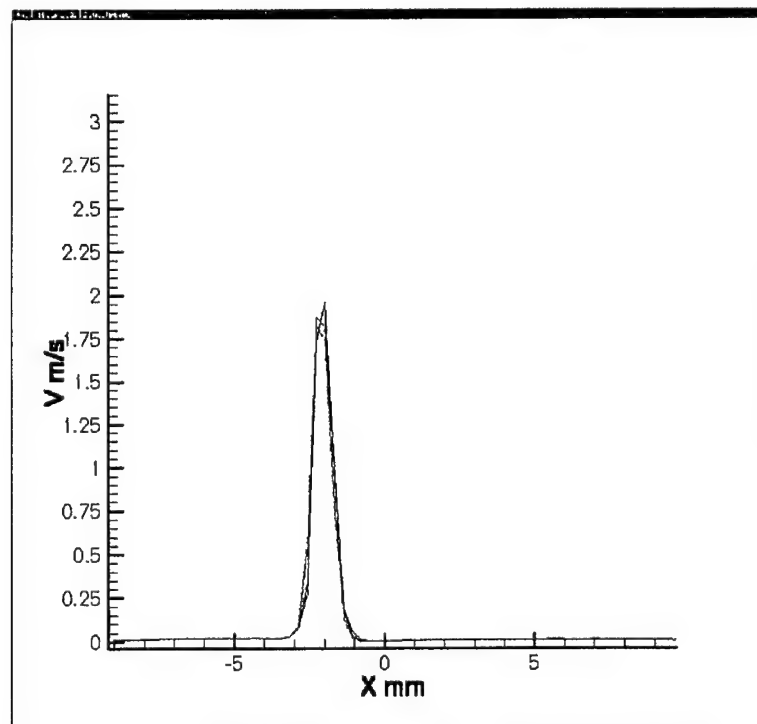
Figure 72. PIV streamwise velocity profileV for just the left synthetic jet from microvalve modulator array ("Left Jet").
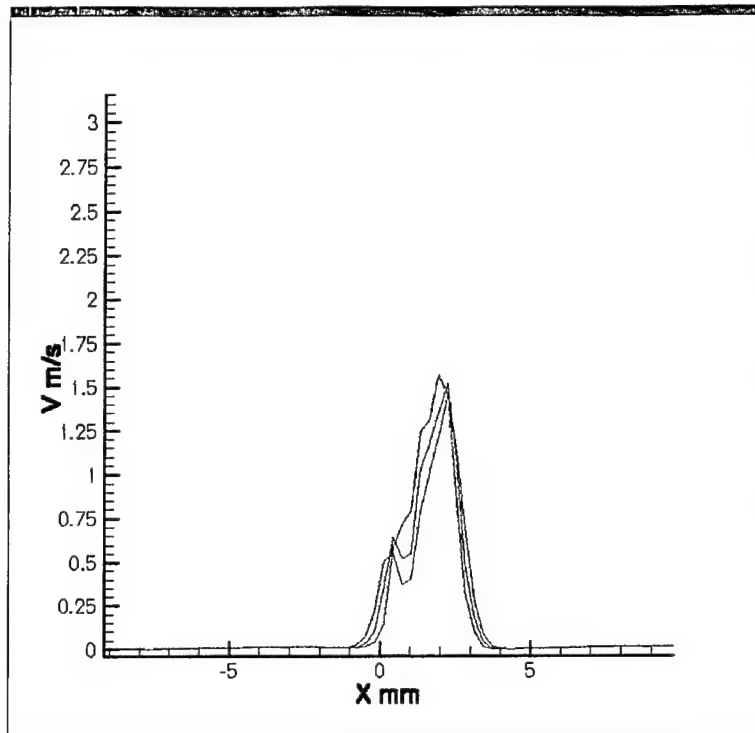
Figure 73. PIV streamwise velocity profile V for the right synthetic jet from microvalve modulator array ("Right Jet").
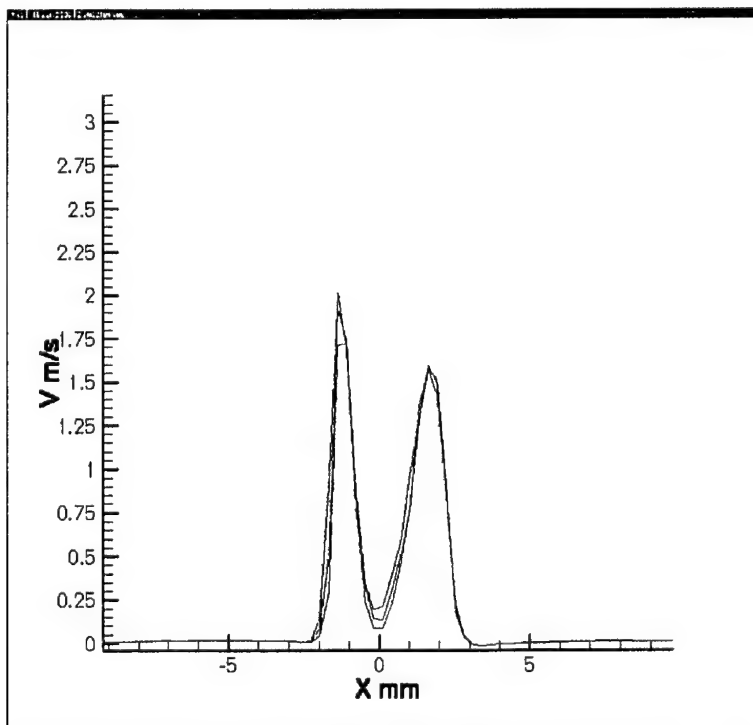
Figure 74. PIV streamwise velocity profile V for the two synthetic jets from microvalve modulator array illuminated by the laser sheet ("Both Jets").

73
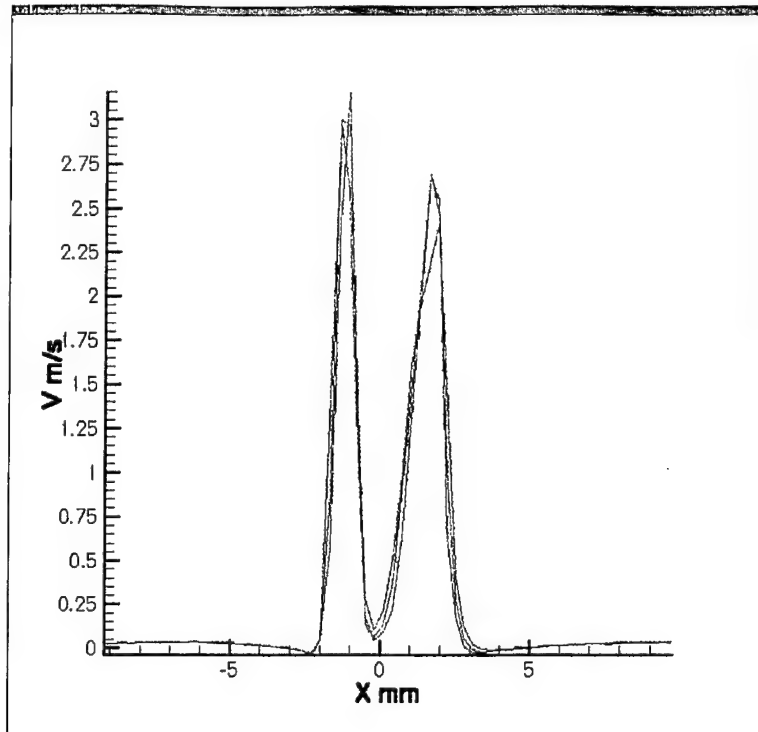
Figure 75. PIV streamwise velocity profile V for the two synthetic jets from microvalve modulator array when all four valves are open ("Four Jets").
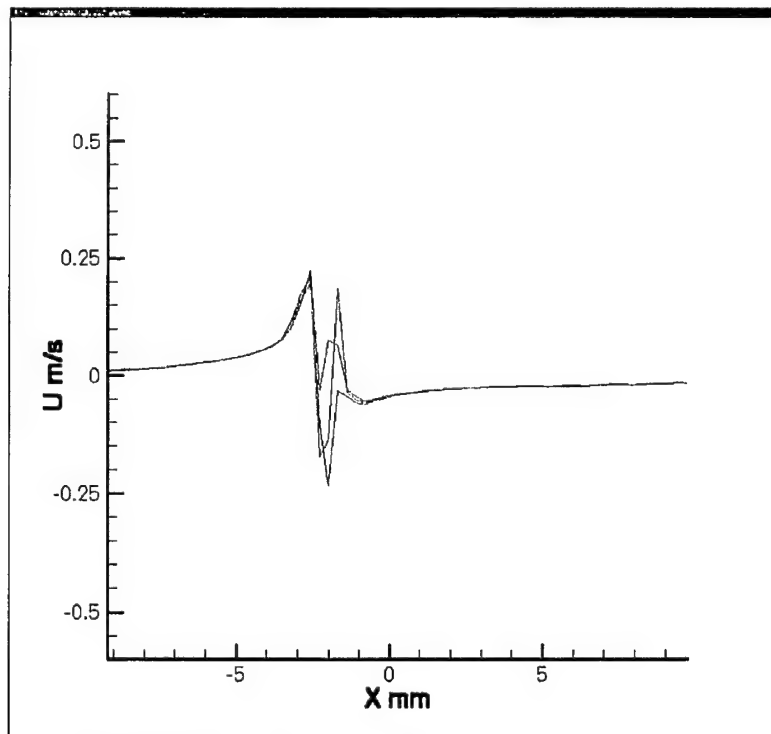
Figure 76. PIV perpendicular velocity profileV for just the left synthetic jet from microvalve modulator array ("Left Jet").

74
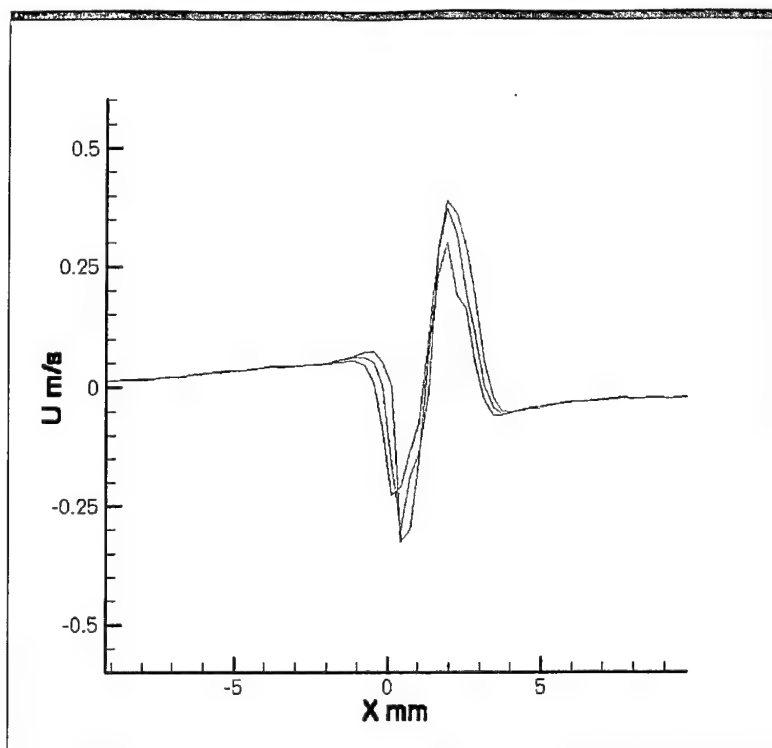
Figure 77. PIV perpendicular velocity profileV for just the right synthetic jet from microvalve modulator array ("Right Jet).
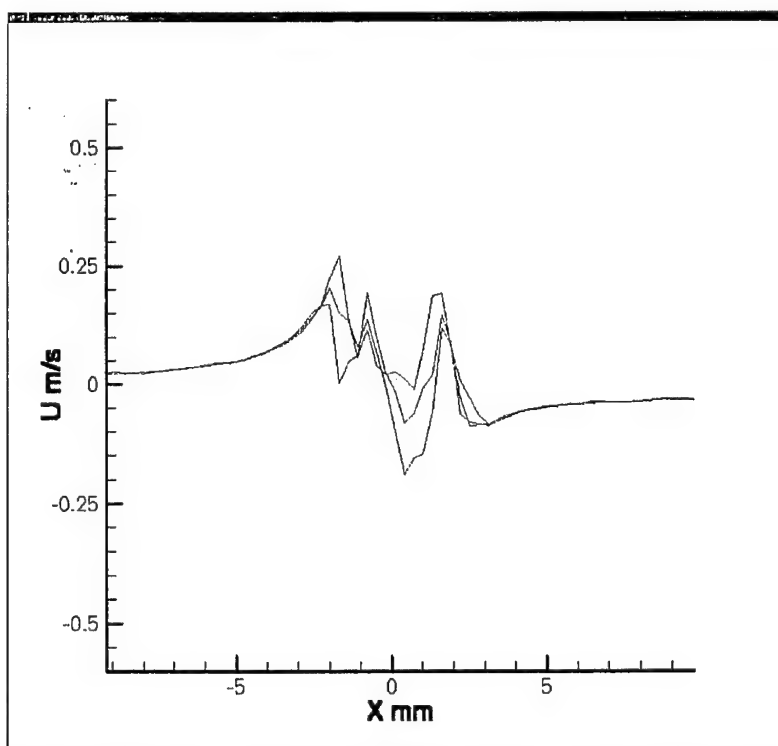
Figure 78. PIV perpendicular velocity profileV for both synthetic jets from microvalve modulator array ("Both Jets").
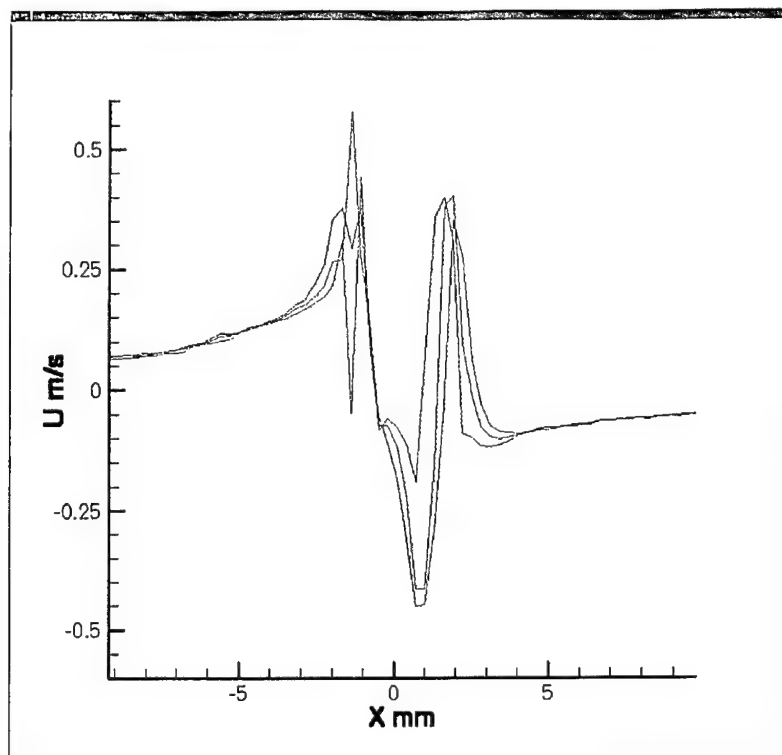
Figure 79. PIV perpendicular velocity profileV for both synthetic jets from microvalve modulator array illuminated by the laser sheet ("Four Jets").
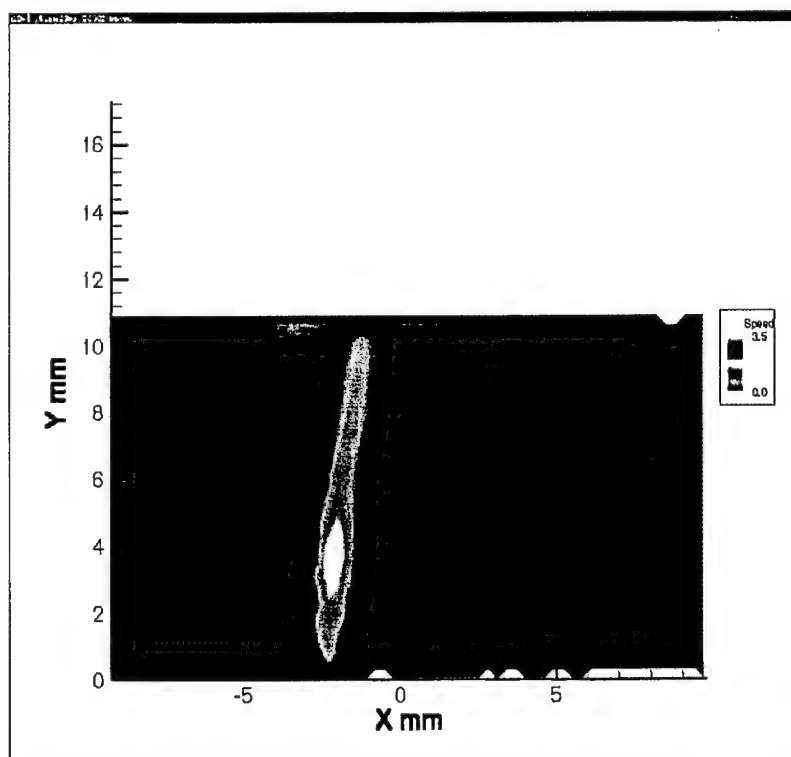
Figure 80. PIV speed contours for Left Jet case.
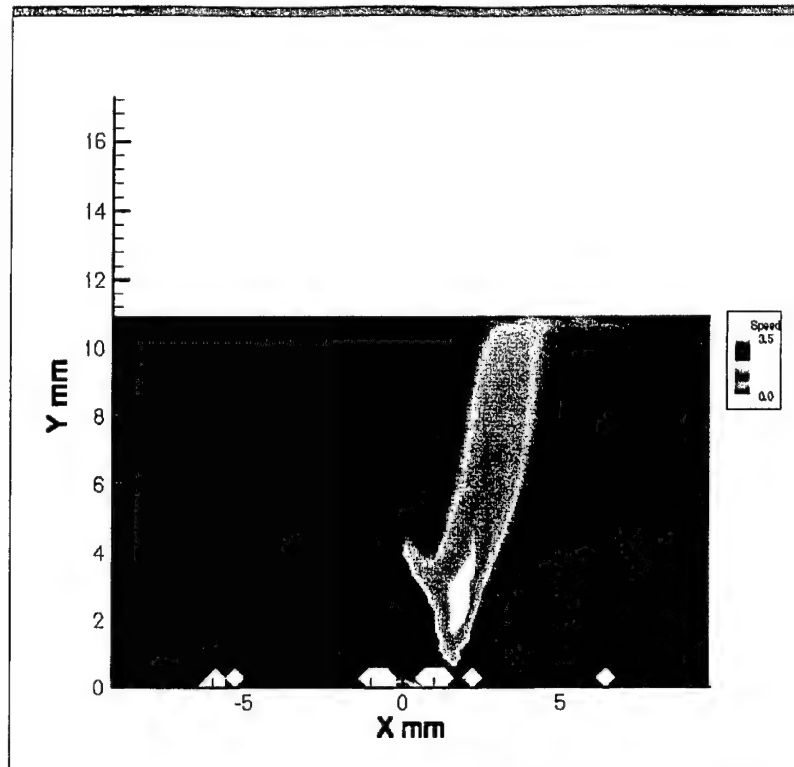
Figure 81. PIV speed contours for Right Jet case.
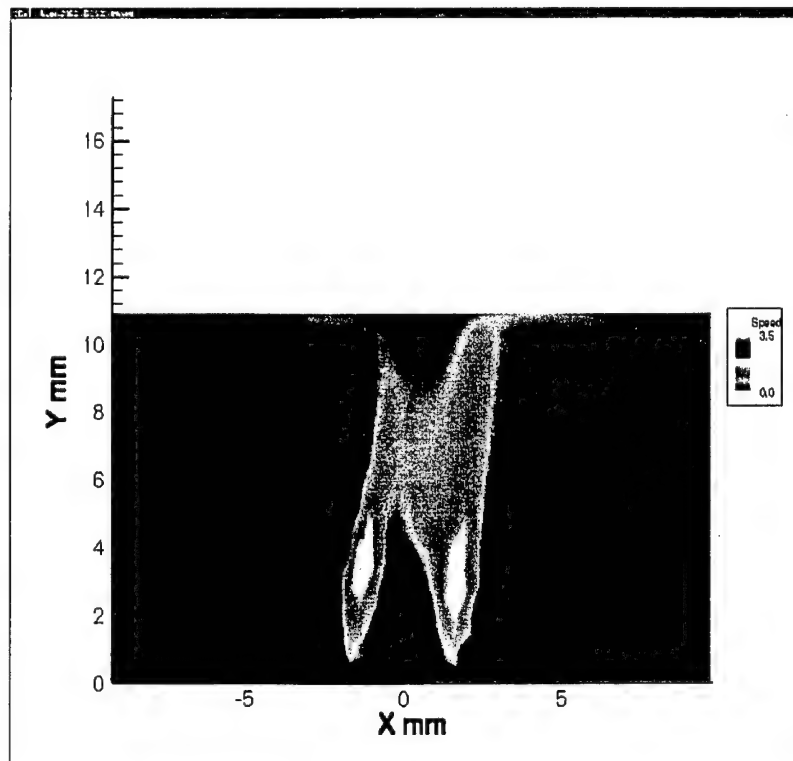
Figure 82. PIV speed contours for Both Jets case.
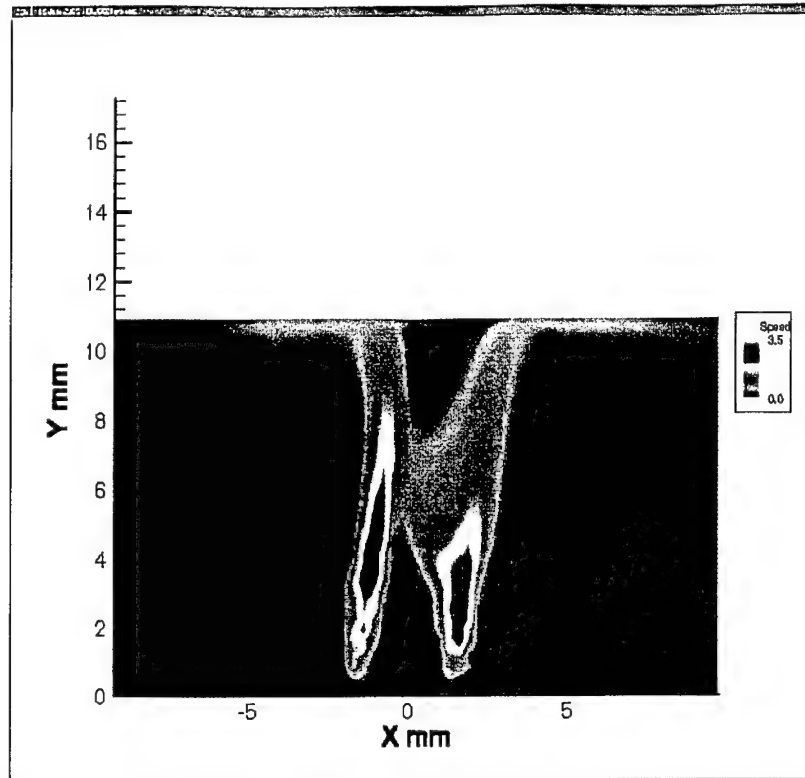
Figure 83. PIV speed contours for Four Jets case.
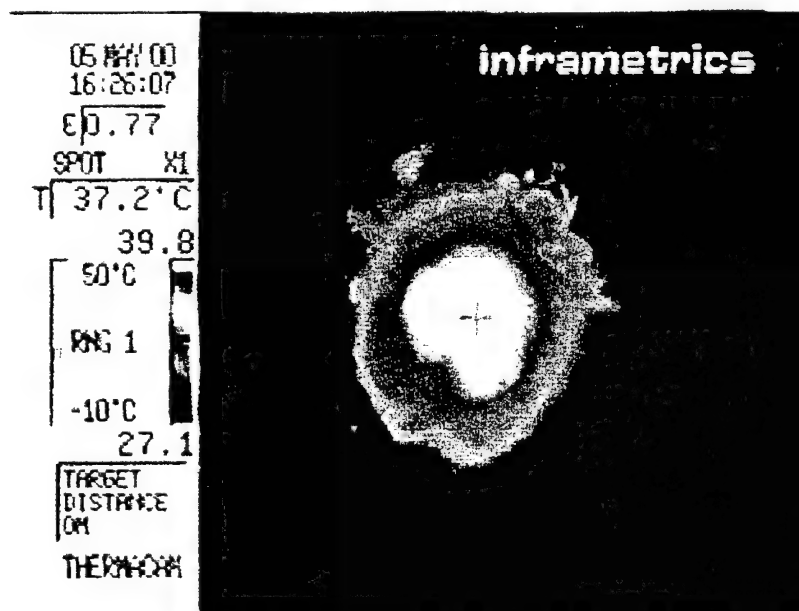
Figure 84. Inframetrics ThermaCAM image of temperature distribution of heated surface without jet cooling.

78
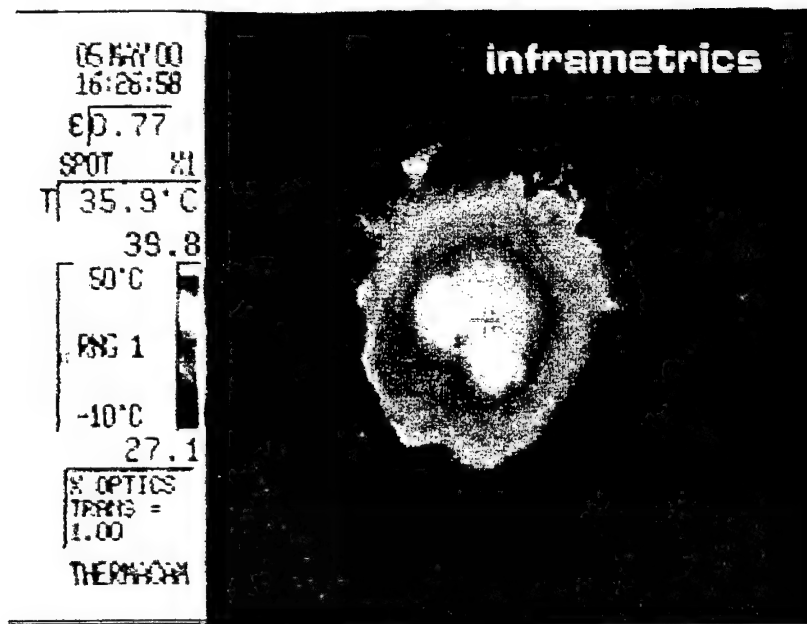
Figure 85. Inframetrics ThermaCAM image of temperature distribution of heated surface as cooled by the left jet only.
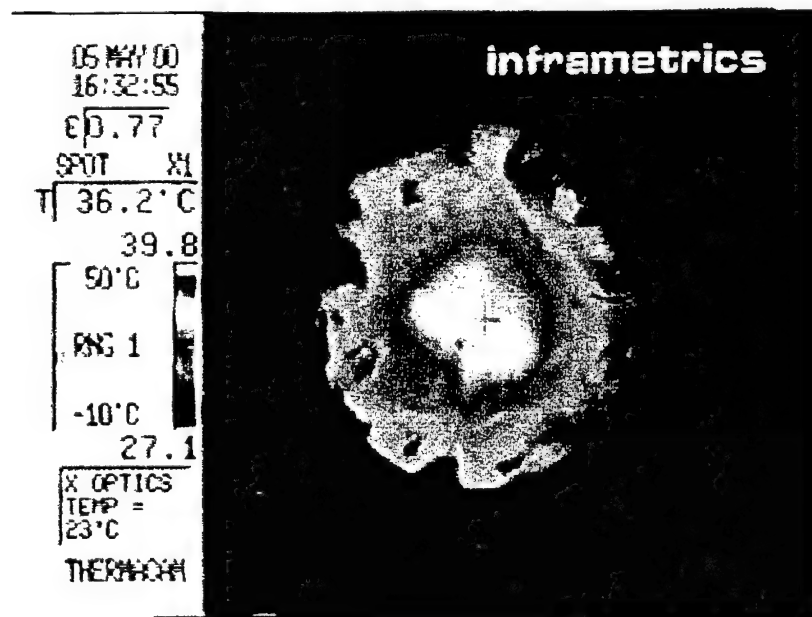
Figure 86. Inframetrics ThermaCAM image of temperature distribution of heated surface as cooled by the right jet only.
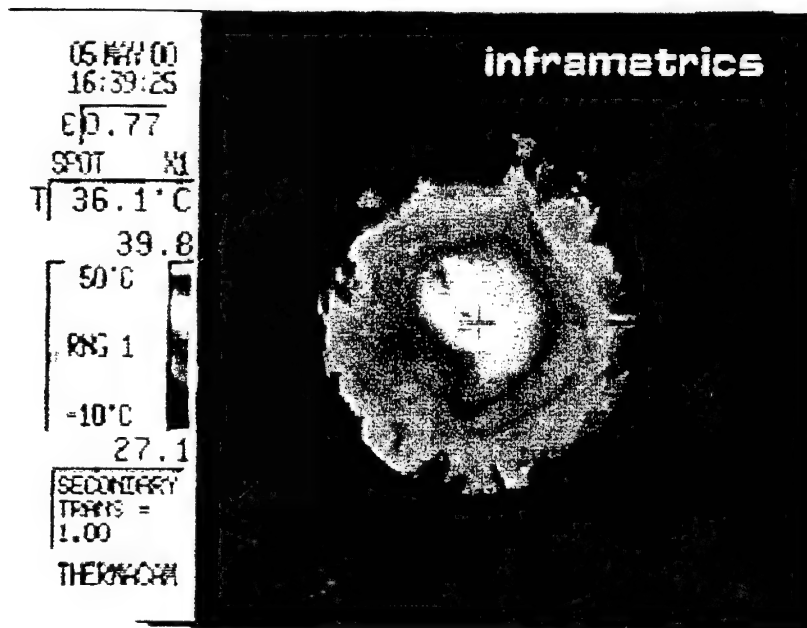
Figure 87. Inframetrics ThermaCAM image of temperature distribution of heated surface as cooled by both jets.
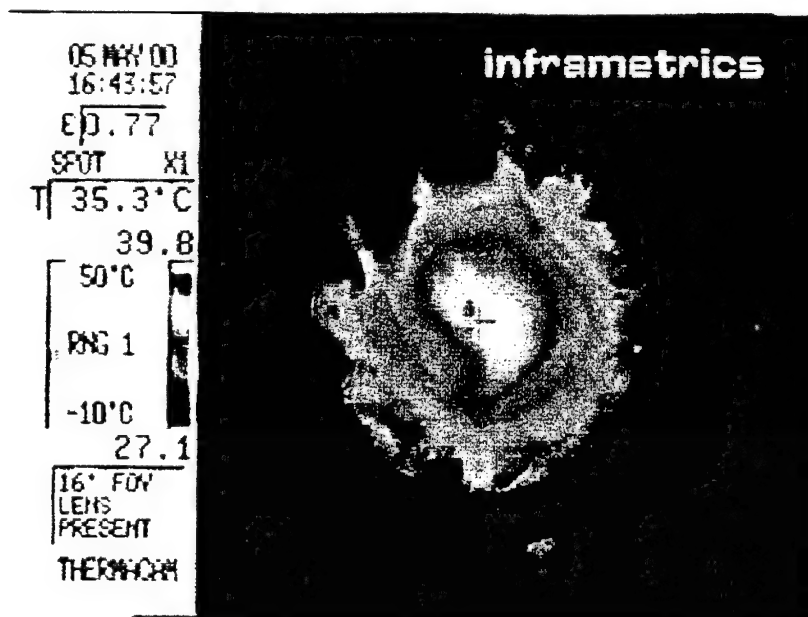
Figure 88. Inframetrics ThermaCAM image of temperature distribution of heated surface as cooled by all four jets.

We also include a sample of the data collected from experiments with the membrane modulator devices.

In this case the cavity side of the membrane modulator array tested is pictured in Figure 89a, and the orifice side of the modulator array is pictured in Figure 89b. Figure 89c shows the

80

undeflected membrane, and Figure 89d shows a membrane deflected by an 800V actuation signal. Figure 90 shows the results of the jet cooling experiment performed with this device. In this test a lower resolution infrared camera (Hughes Probeye) was used to visualize the heated surface. From Figure 90a to Figure 90b, one can see a decrease in the diameter of the hotspot as a result of the cooling action provided by the membrane modulator device. As typical for the membrane modulator devices, this sample later failed because the high actuation voltage required shorted out the actuators before PIV velocity data could be obtained.

(a)   (b)

(c)   (d)
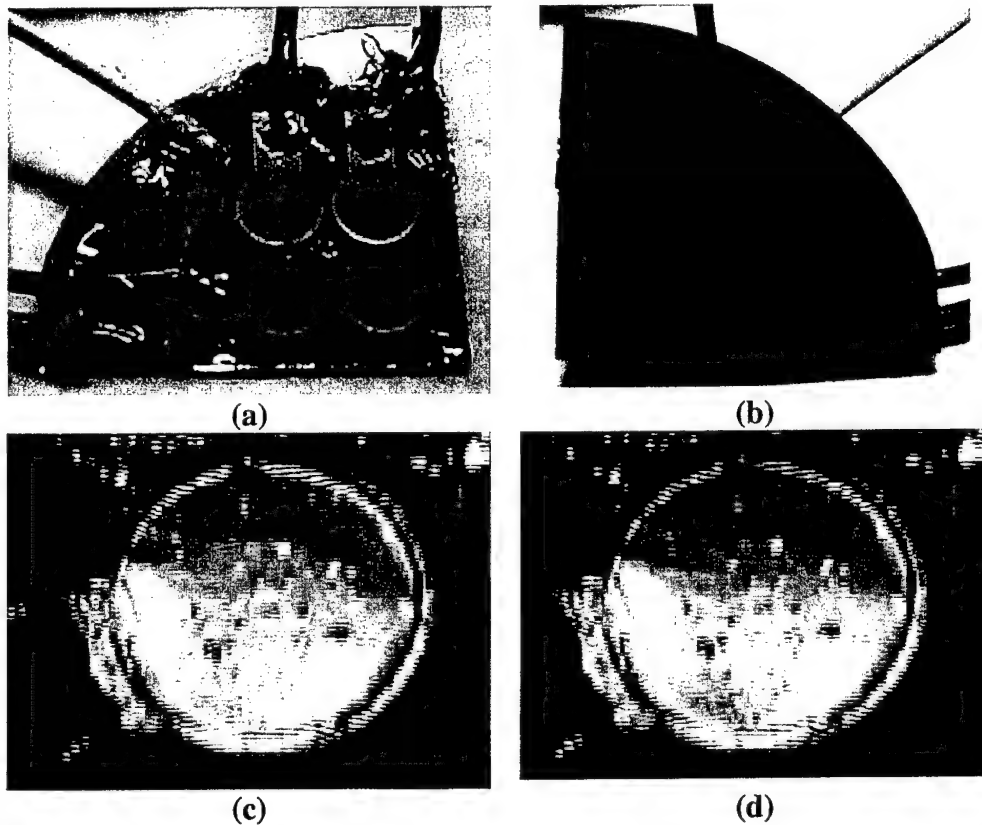
Figure 89. Photographs showing actuation of membrane modulator. Assembled sample Membrane side and (b) Orifice side.(c) Undeflected. (d) Deflected. Again note shadow and focal changes.
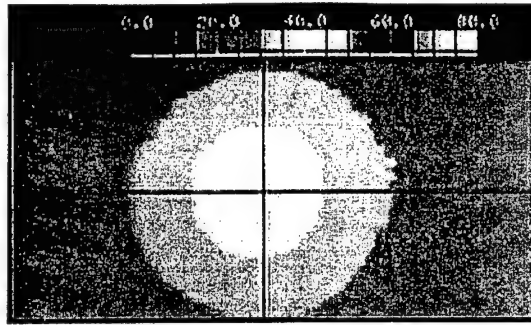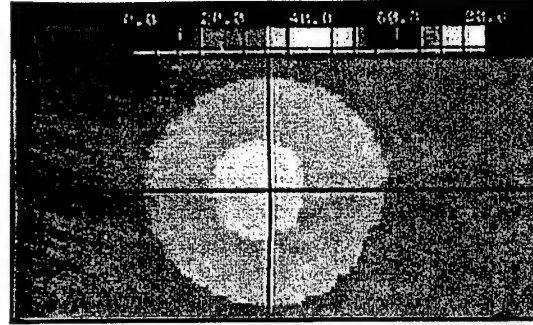
Figure 90. Infrared photographs showing the cooling of a heated surface with the synthetic jet produced by a membrane modulator device. (a) no synthetic jet. (b) synthetic jet activated. Note the decrease in diameter of the center hot spot upon activation of the synthetic jet.

4.2.6 High-Fidelity and Reduced Models

Synthetic jets are generated at the orifice of a partially open cavity with an oscillating membrane wall opposite to the orifice opening as shown schematically in Figure 91 [Smith and Glezer, 1998]. Microfabricated arrays of synthetic jets are being explored for applications in aerodynamic flow control, in cooling of electronics packages, and in mixing in microchemical reactors.
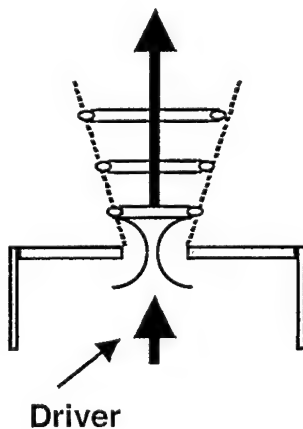
Figure 91. Schematic of synthetic jet.
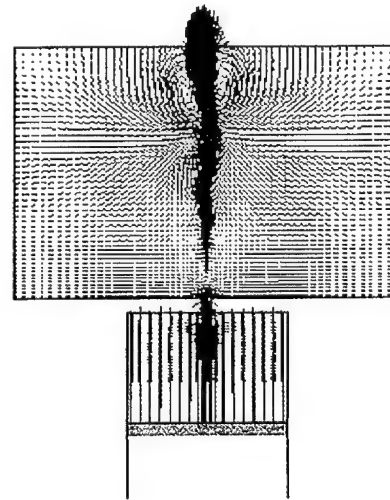
Figure 92. High-fidelity model of synthetic jet.

The unsteady flow dynamics inside the cavity of the synthetic jet is analyzed with CFD-ACE+. The code provides multi-disciplinary simulation capability by coupling: fluid flow, heat transfer, mixing and chemistry, stress/deformation, electrofluidics, electrostatics, electromagnetics, and other discipline field solvers specifically adapted for MEMS [Przekwas, 1999]. The fluid flow model solves the time dependent continuity equation, the pressure based Navier-Stokes equations and energy balance equation. In the present formulation they are written in a strong conservation integral form on time dependent arbitrary moving/deforming geometry and are equally applicable to incompressible and compressible flows. Numerical solution of this equation set

82

requires discretization of the computational domain into a large number of generalized control volumes. To allow full freedom in the control volume shapes, the governing equations are expressed in the integral flux form:

$$\frac{\partial}{\partial t}\int_v \rho dv + \oint_\sigma \rho\left(\overline{V} - \overline{V}_g\right)\cdot \overline{n} d\sigma = 0$$

$$\frac{\partial}{\partial t}\int_v \rho u_i dv + \oint_\sigma \rho\left(\overline{V} - \overline{V}_g\right)\cdot \overline{n} u_i d\sigma = -\oint_\sigma pn_i d\sigma + \oint_\sigma \tau_{ij} n_j d\sigma + \int_v f_i dv$$

$$\frac{\partial}{\partial t}\int_v \rho h_i dv + \oint_\sigma \rho\left(\overline{V} - \overline{V}_g\right)\cdot \overline{n} h_i d\sigma = \oint_\sigma q_j n_j d\sigma + \int_v \frac{\partial p}{\partial t} dv + \oint_\sigma \tau_{ij} u_j n_i d\sigma + \int_v f_i u_i dv$$

$$\tau_{ij} = \left(\mu + \mu_t\right)\left(\frac{\partial u_i}{\partial x_j} + \frac{\partial u_j}{\partial x_j}\right) - \frac{2}{3}\left(\mu + \mu_t\right)\left(\frac{\partial u_k}{\partial x_k}\right)\delta_{ij}$$

(4.10)

$$q_j = k\frac{\partial T}{\partial x_j}$$

where u_i is the ith Cartesian component of the velocity, V_g is the grid velocity due to grid motion, p is the static pressure, h_t is the total enthalpy, τ_{ij} is the stress tensor for both laminar and turbulent flows and f_i is the ith Cartesian component of body force. For turbulent flows, the Reynolds stress tensor is closed with a standard k-ε model. An implicit second order time-space control volume discretization method is used to solve the above equations on unstructured meshes.

The equations are solved using CFD-ACE+ software developed at CFDRC with specific application for MEMS. A unique feature of the flow solver is the application of generalized polyhedra control volumes for super resolution of jet cavities with a single control volume with large number of faces (cavity walls, membrane, orifice, …). A moving wall and deforming grid method is used to model the interior of the cavity and a free space environment is used to model the jet evolution (Figure 92). The oscillating membrane is periodically ingesting and expelling the air from the cavity. Several oscillation cycles are performed to obtain cycle independent results. The model is validated against the experimental data obtained GT for the jet actuated with 1 kHz oscillation frequency. Unsteady flow field have been experimentally measured using Particle Image Velocimetry (PIV) technique.

The height of the actuation cavity is 95 mm, cavity width is 19 mm and the orifice diameter is 6.35 mm. Transient computational simulations have been performed with membrane deformation dynamics represented as a moving wall with prescribed harmonic motion. As the membrane dynamics could not be measured in the experiments, a direct comparison between computational and experimental data was not possible. Instead, several computational runs were performed to match the maximum flow rate through the orifice with a membrane displacement as a parameter. A comparison between experimental and computational vortical flow structures at several time instances is presented in Figure 93. Time average velocity profiles at several axial locations, measured at GT and calculated with CFD-ACE are shown in Figure 94. Considering

83

the uncertainty of boundary conditions and assumed membrane dynamics, good agreement between predicted and experimental velocity profiles has been achieved (Figure 94).

PIV Measurements

3-D Simulations with CFD-ACE+
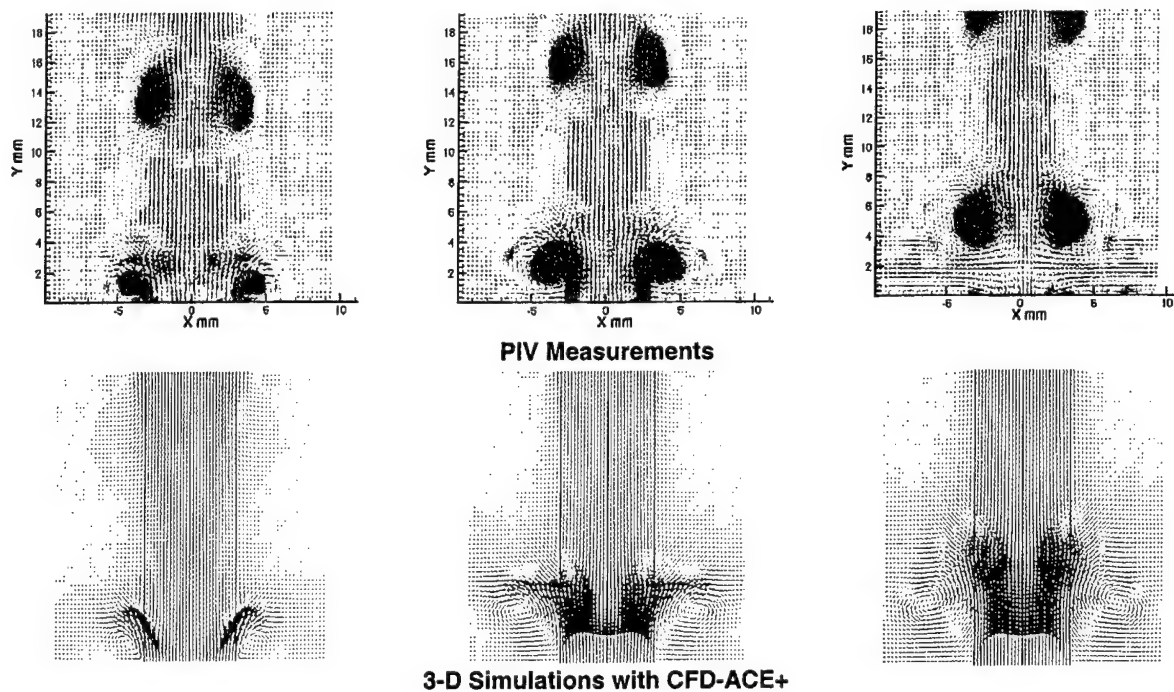
Figure 93. Synthetic jet simulation results compared to measurements.

z (mm) = ○ 0.35   ◇ 2.5   ▲ 5.0
          ▽ 7.5   ●12.5   ◆17.5
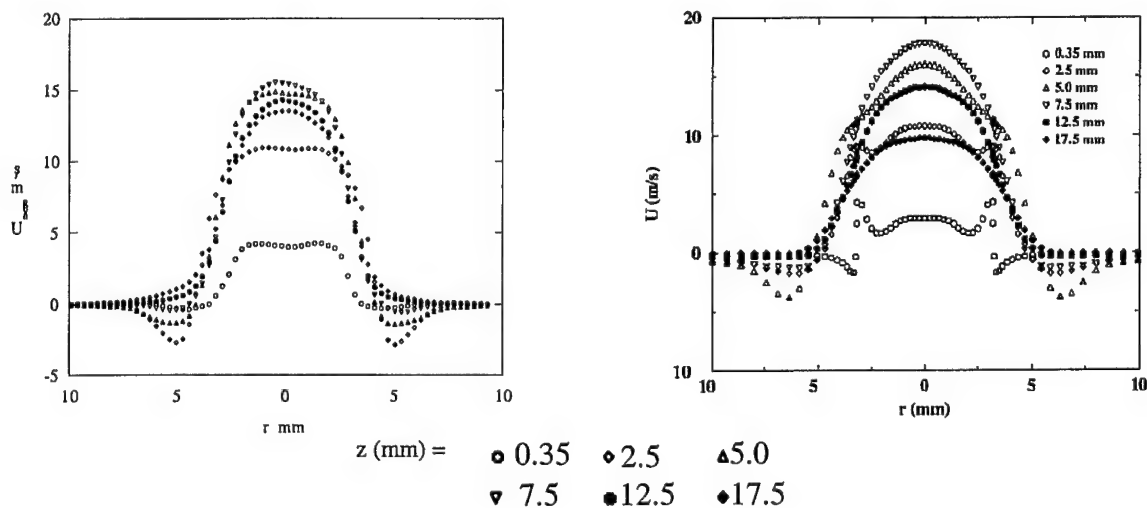
Figure 94. Mean velocity profiles at different height position over the synthetic jet orifice:
a) measured with PIV technique at Georgia Tech, b) obtained from CFD-ACE+ simulations at
CFDRC.

Reduced Models of Synthetic Jets

Computational modeling of large numbers of synthetic jet cavities with high fidelity 3-D models is not practical because of large computational cost. A "compact model" accounting for all essential physics expressed in terms of algebraic equations, or ordinary differential equations, is needed to model large arrays of jets. There are several approaches to formulate a compact model including analytical solutions, curve fits to experimental data, or equivalent electrical circuits. Equivalent circuit models of air dumping for inertial sensors have been recently demonstrated by the authors earlier.

Single-Cell Model of Synthetic Jet

In this project, we have developed a novel concept of mixed-dimensionality approach combined with the polyhedral grid capability to model a synthetic jet with a single control volume or a one-dimensional approximation. Both capabilities have been implemented in CFD-ACE+ tool. In the proposed approach, to represent the cavity, a single control volume (CV) fully conforming to the cavity geometry is used. This single polyhedral CV, however, has a large number of cell faces, some of them are fixed wall segments, the vibrating membrane, or the orifice opening. Full set of general conservation equations (mass, momentum, energy) is solved in a single cell in time-accurate manner. The cavity volume is linked through the orifice with the external flow field in a fully implicit manner resulting in a robust simulation algorithm. If a desired accuracy of the compact model is achieved, a large number of cavities can be modeled in a very cost effective manner.

Figure 95 shows the geometry of a reduced model of the synthetic jet, composed of three cylindrical domains, each of them modeled with a single discretization cell having 32 boundary faces.
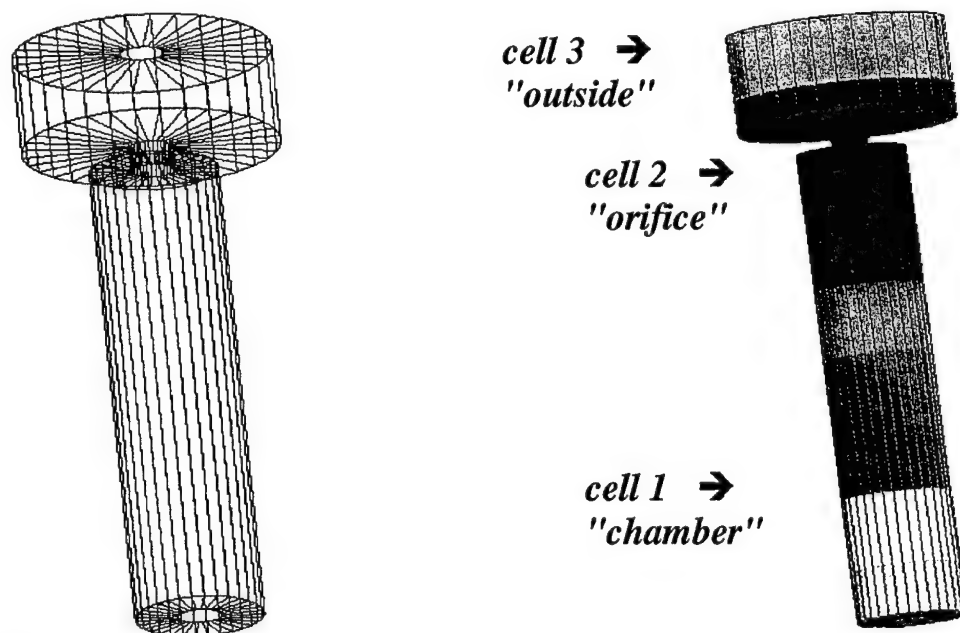
Figure 95. Single-cell model of synthetic jet (3 domains = 3 cells); (a) geometry; (b) velocity distribution, calculated using the 3-cell model of synthetic jet.

Discussion of Reduced Model Validity and Accuracy

Our initial studies of compact models of synthetic jets showed that for the present configuration a two-cell model (chamber and orifice) was needed for the cavity, and an additional domain for the external environment (surrounding air). Table 4.1 presents relative comparison of computational mesh requirements and CPU times for 3-D, 1D and one-cell models to simulate the single cycle of the oscillatory jet. CPU savings for a single cell are already apparent when compared with the 3-D (full cell) model. One of the model requirements is good accuracy for widest possible operating range (frequency, displacement, pressure level, geometry, etc.). Computational studies showed that for small frequencies (up to 200 Hz) incompressible and compressible flow models are very similar. For higher frequencies, large discrepancies in flow rate have been observed. Figure 96 presents both characteristics for up to 1 KHz. We recommend that a compressible version of the model should be used for entire range of frequencies.

Table 4.1. Computational mesh resolution and CPU Time for 3-D, 1D and one cell models of a synthetic jet.

Model Type	Number of Discretization Elements (axial x radial) in:				CPU Time (200 time steps)
	Chamber	Orifice	Outside	Total	
Full Cell	64 x 34	10 x 14	64 x 38	4748	41 min 44 sec
1D Cell	64 x 1	10 x 1	10 x 1	84	1 min 48 sec
One Cell	1 x 1	1 x 1	1 x 1	3	23 sec

At low frequencies, the pressure field inside the cavity is quite uniform. Above 300 Hz we found that acoustic (pressure wave) effects became important and a single cell cavity model would not capture the spatial variation of pressure along the axial direction within the cavity. For high frequency applications, we have proposed a one dimensional model with exactly the same equations as in the one-cell model but solved on axially arranged polyhedral elements.
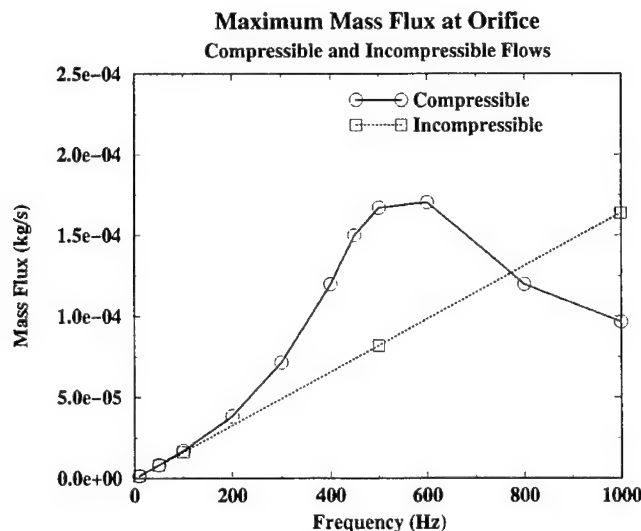
Figure 96. Results of 3-D high-fidelity computations of mass flow in synthetic jet orifice, using compressible and incompressible gas models.

Figure 97 presents the comparison of predicted mass flow rate through the orifice for 3-D, 1D and one-cell models for 100 Hz frequency. Good agreement between all three models has been observed.
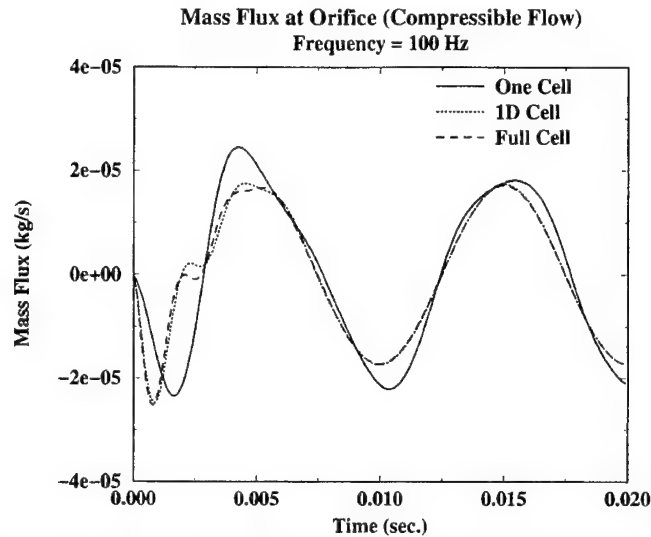
Figure 97. Mass flow calculated using various fidelity models for actuation frequency 100 Hz.

For high frequency (1 KHz) operation, as shown in Figure 98, a very large discrepancy exists between the one-cell model and 1D, 3-D models. At this frequency, pressure wave effects become dominant, and a 1D reduced model has to be used. Good accuracy agreement between 3-D and 1D models has been achieved without any "tuning" of the 1D model.
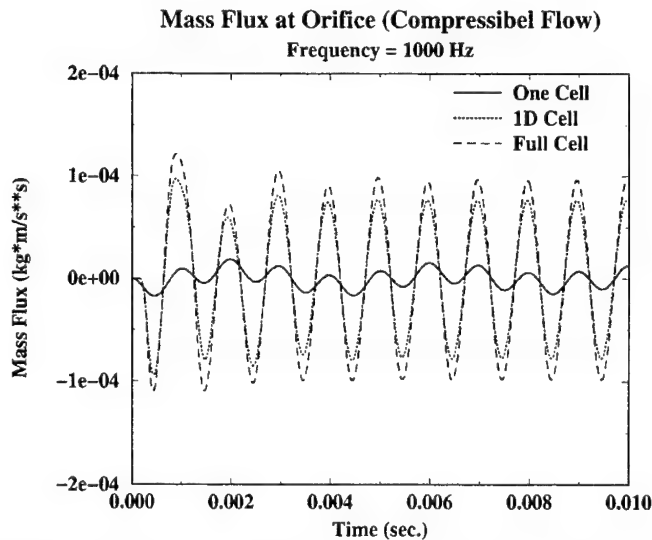
Figure 98. Mass flow calculated using various fidelity models for actuation frequency 1000 Hz.

Conclusions

We have developed a novel concept of compact models for synthetic jets. The model uses a polyhedral control volume capability of CFD-ACE+ software tool to model complex dynamic 3-D shapes with moving walls with multiple inlets/outlets with a single cell "super element". The model has been validated against 3-D high-fidelity simulation data obtained for a range of parameters such as geometry, actuation frequency, amplitude, operational pressure, etc.

It was found that the incompressible form of the model was valid for up to 200 Hz actuation. Large errors were observed at higher frequencies. Compressible formulation is more general and accurate for full range of frequencies. At high frequencies, where pressure wave effects become important within the cavity, one cell model has to be replaced by a one dimensional model. Substantial computational savings are achieved when compact models instead of high-fidelity models are used for synthetic jets. In the next section we will demonstrate the synthetic jet arrays simulations for two practical applications: aerodynamic control of airfoils and active spot cooling of electronic packages.

4.2.7 Evaluation of CFD-ACE+ Mixed-Dimensional Capabilities with Synthetic Jets

Microfabricated arrays of synthetic jets are being explored for applications in aerodynamic flow control, in cooling of electronic packages, and in mixing in microchemical reactors. Computational simulation of coupled unsteady fluid mechanics and electromechanical actuation of a single synthetic jet can be performed with available CFD tools. Modeling of flow physics of large arrays of synthetic jets is computationally very challenging. At CFDRC we have explored two complementary computational techniques: a three-dimensional high-fidelity model for detailed simulation of a single jet (validated with measurements results from GT), and a reduced "single-cell" model of a jet (described above) used to calibrate the compact model.

On the basis of the 3-D simulations, a reduced "single-cell" model of synthetic jet has been developed at CFDRC (see the previous section). The reduced model allows for simulation of large arrays of synthetic jets, for example, for active thermal control of microelectronic packages with a 2D array of synthetic jets. The single-cell models have been inserted into 3-D mesh in CFD-ACE, used for high-fidelity simulation of the entire array of synthetic jets, located above a high-power electronic module. An example of such a simulation is presented in Figure 99. The objective of this effort is to analyze active control of synthetic jets for spot cooling of electronic packages.

A similar technology utilizing Reduced Models of Synthetic Jets will be used within the other DARPA-funded *HERETIC* Program (Heat Removal by Thermo-Integrated Circuits), where CFDRC will support modeling and design of Arrays of Synthetic Microjets for active cooling of:
- VCSEL Arrays (Linear and 2D)   - *Georgia Tech + Honeywell*
- Microprocessor Chips   - *Georgia Tech + Intel.*
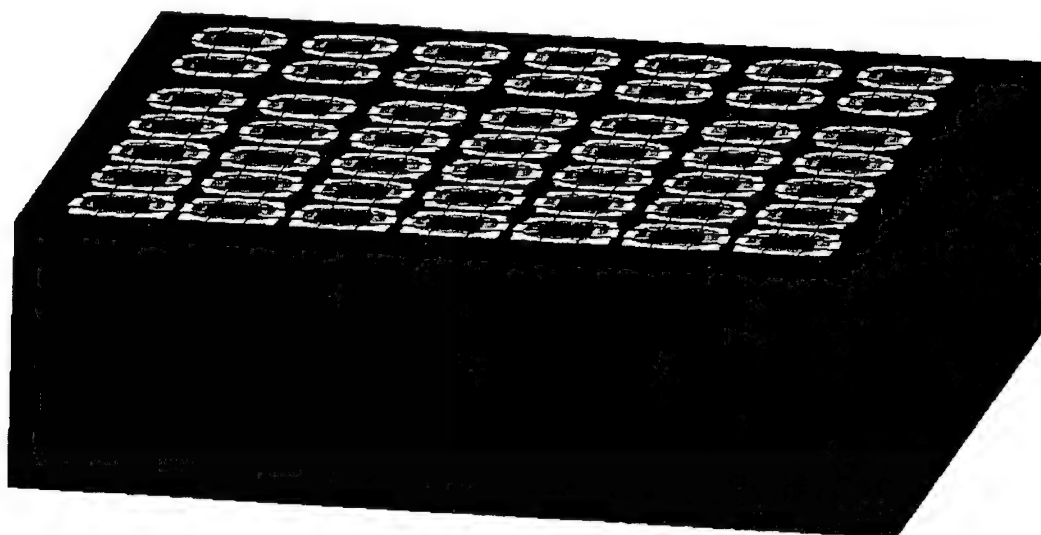
Figure 99. 3-D simulation of 7x7 array of synthetic jets, using reduced models: Pressure Distribution.

Reduced Models of Synthetic Jets for Aerospace Applications

Reduced single-cell model of synthetic jet has been used at CFDRC for simulation of arrays of these devices in the aircraft wing. They may be used for active control of wing aerodynamics and other possible applications, as illustrated in Figure 100. The reduced models have been inserted into 3-D high-resolution mesh in CFD-ACE, used for simulation of the unsteady aircraft wing aerodynamics. Figure 101 shows the CFD-ACE simulation results of airfoil aerodynamics control by an array of synthetic jets.

The reduced models can be also inserted into a full high-fidelity simulation of an airfoil, to analyze active flow control (Figure 101). A large array of synthetic jets is positioned on an airfoil and demonstrated on active aerodynamic control of lift, drag, stall, and other flow characteristics. This type of simulation enables "virtual flight control" which may be used in the process of design of Micro Air Vehicle (Figure 102).

3-D High-Fidelity Models
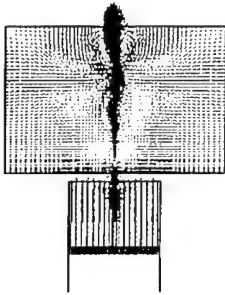
Compact/Reduced Models
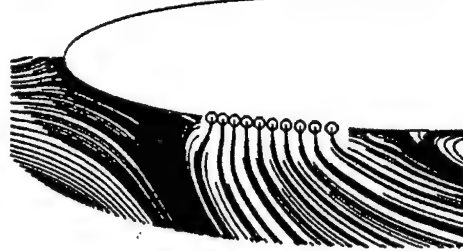
System-Level Simulation
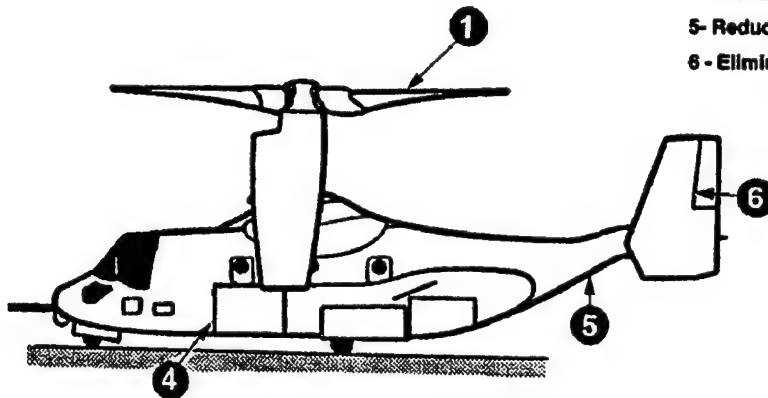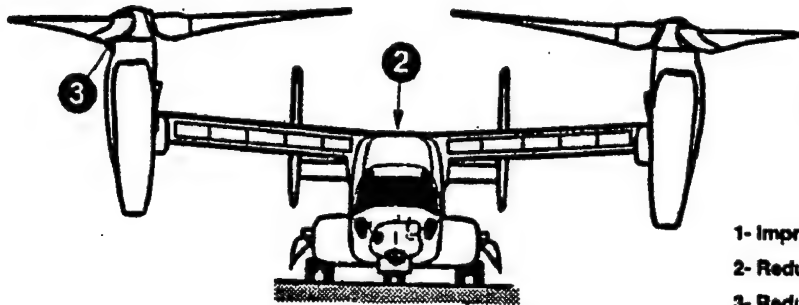
1- Improved blade aerodynamics (variable twist)

2- Reduce fountain flow in hover

3- Reduced vibration levels and BVI noise

4- Aerodynamic tailoring of blunt surfaces

5- Reduce fuselage upsweep drag

6 - Eliminate hinges on lifting surfaces

Figure 100. Modeling of synthetic jets in Aerospace Applications.
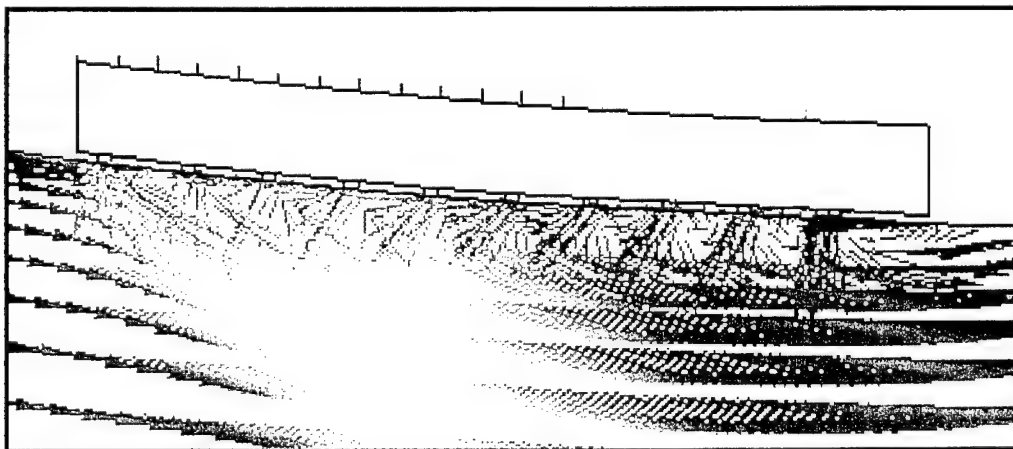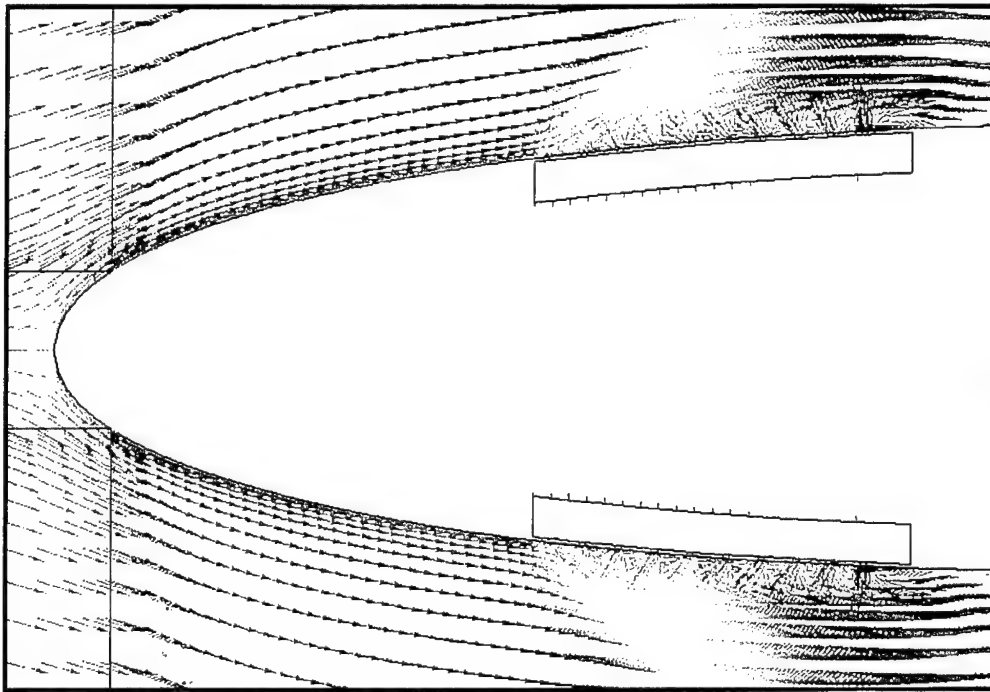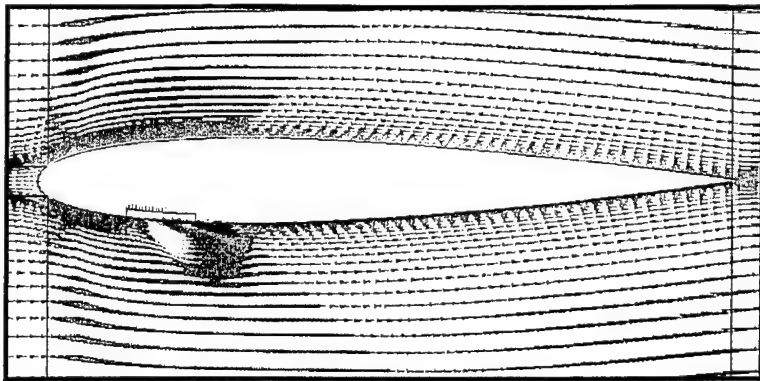
Figure 101. Results of CFD-ACE simulations at CFDRC, showing the use of reduced models of synthetic jets in high-fidelity 3-D simulations of airfoil: overall view, leading edge and jets, syn-jets array close-up.

91

Active jets on the bottom - Take-Off   Active jets on the top - Landing

1.1.2 Net Force   1.1.1 Net Force
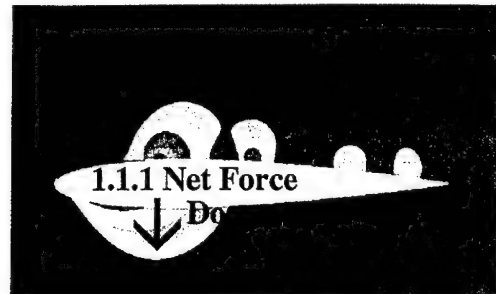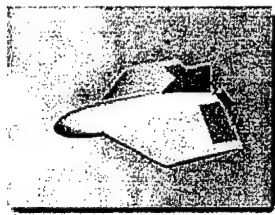
Figure 102. Micro Air Vehicle (MAV), and its virtual flight control, with 3-D CFD simulations and reduced models of synthetic jets.

The simulations as presented above demonstrate CFD-ACE+ Mixed-Dimensionality in the design with applications of microdevices. In those cases, reduced models (one-dimensional, or "single-cell" models) of microdevices were embedded in the high-fidelity simulations of larger systems.

4.2.8   Mixed-Dimensional and Mixed-Domain Modeling and Experimental Validation

Micromachined synthetic jets with integrated MEMS modulators have been fabricated and characterized. Several methods have been used to test the modulator arrays: visual deflection test, flow modulation test by smoke visualization, Schlieren visualization, pivot tube, x-wire anemometer, and particle image velocimetry (PIV). Most of these methods proved to be very destructive way of testing the devices because the types of smoke used led to rapid clogging of the jet orifices.

The GT team devised a way to nondestructively test the samples by viewing the cooling effect of our modulated synthetic jets upon a heated plate using an infrared camera. In these experiments, an electric heating element is placed on the copper side of a copper clad sheet of Kapton (Figure 103). The synthetic jets are directed at the heating element, and an infrared camera is used to view the temperature distribution of the heated surface cooled by the synthetic jets. The temperature distribution on the heated surface varies depending upon the number and strength of the jets impinging upon it.

Figure 104 shows sample IR camera results of the temperature distribution on the surface without cooling and cooled by various configurations of the synthetic jet actuators. The measured data are compared with numerical simulations at CFDRC, including use of reduced models in jet arrays.

Details of the development and measurements of synthetic jets at GT were described in Section 4.2.2.
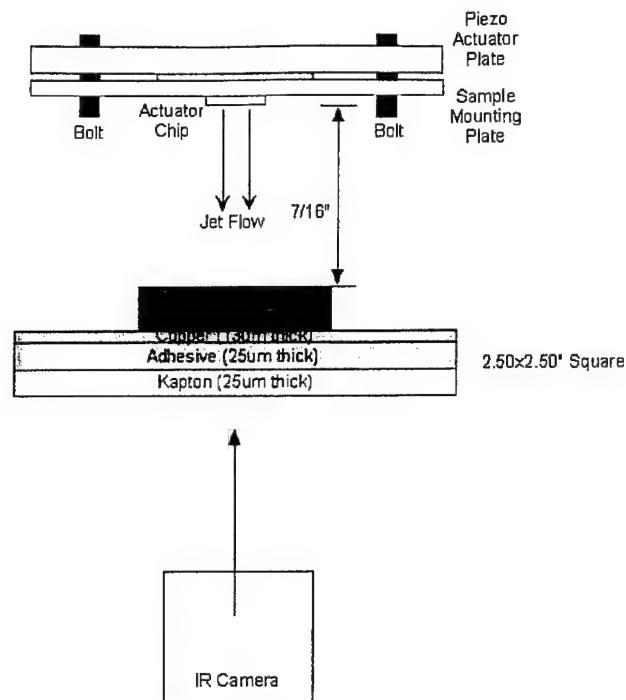
Figure103. Diagram of synthetic jet cooling experiment.

No Jets

Left Jet On

Both Jets On

Four Jets On
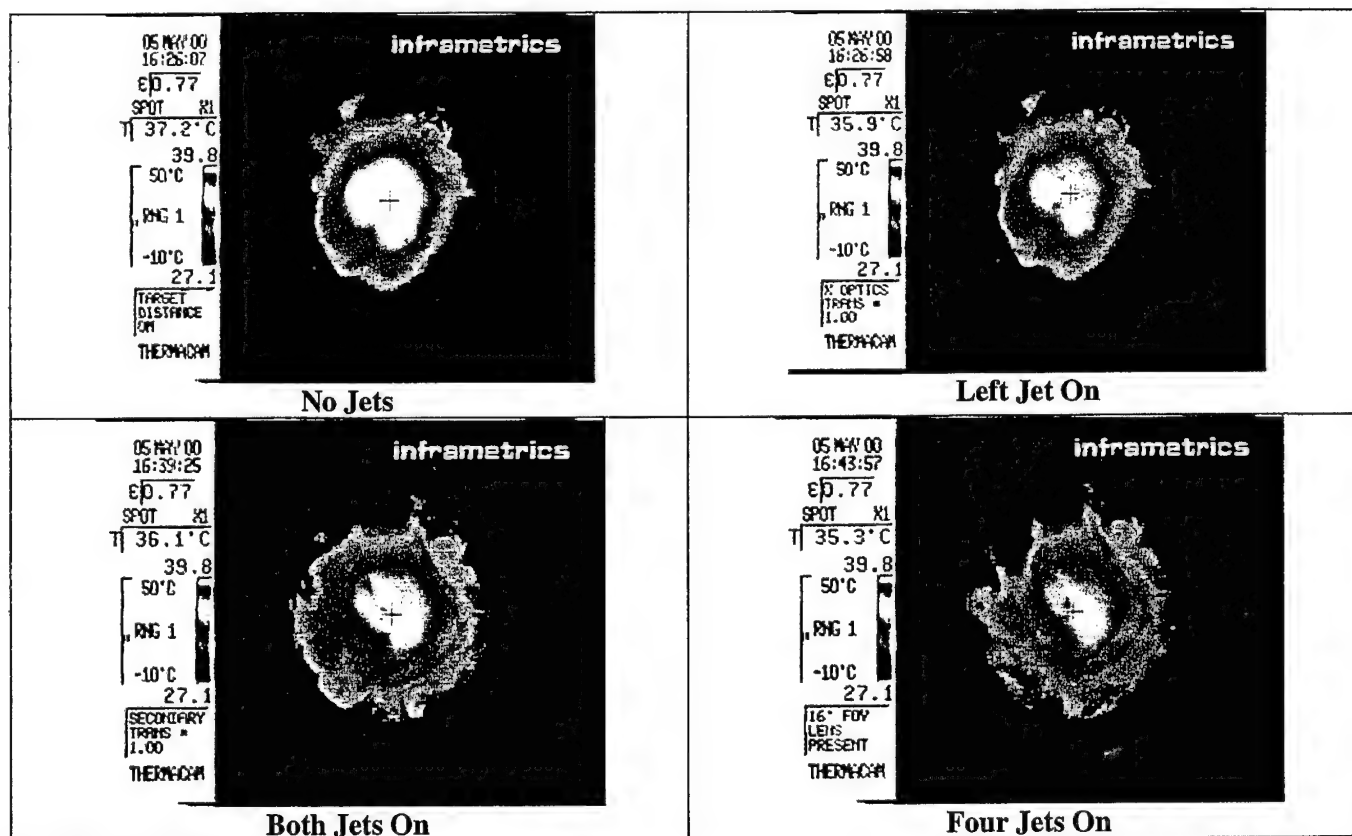
Figure 104. Sample IR camera results of the temperature distribution on the surface without cooling and cooled by various configurations of the synthetic jet actuators.

Mixed-Dimensional and Mixed-Domain Simulation of Temperature Control by Microjet Arrays

At CFDRC, a high-fidelity 3-D model has been built to run a set of simulations corresponding to the GT experiments, as described in the previous section. The CFD-Micromesh program was used to build a full 3-D model of the jet array and heated substrate (Figure 105).
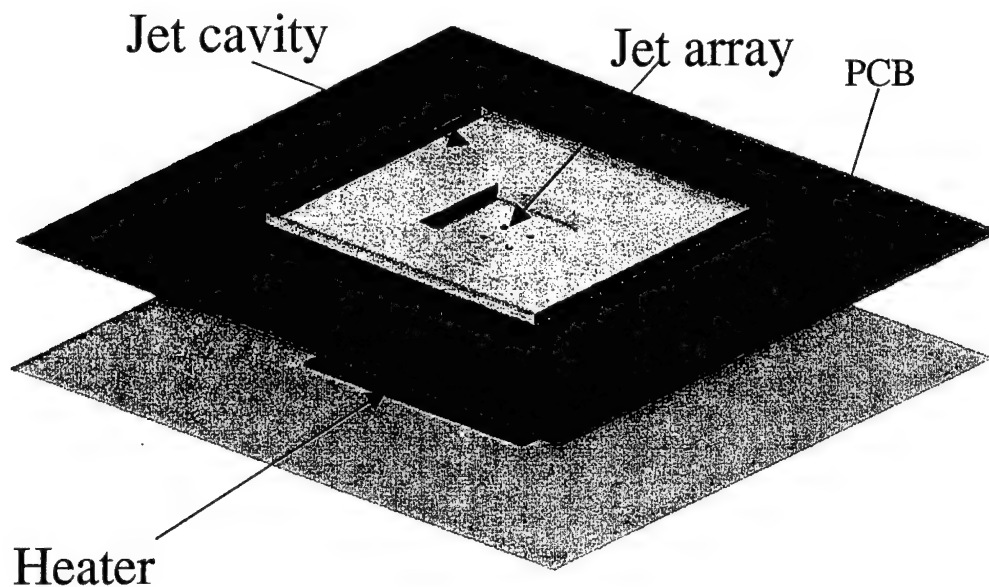
Figure 105. A high-fidelity 3-D model built with CFD-Micromesh, to run a set of simulations corresponding to the Georgia Tech experiments with microjet cooling.

The above model was used for a series of thermo-fluidic simulations, including the use of reduced models developed earlier in this project. The full model consisted also of an array of 2 x 2 synthetic jets, a cavity as a jets actuator, and a heater plate. For the synthetic jets, the single-cell reduced models were used, within the thermal enviroment represented by a full 3-D model.

A fully coupled mixed-dimensional and mixed-domain simulation of temperatutre control by microjet arrays was performed. As a result, we obtained the air flow pattern caused by the synthetic jets (reduced models) and temperature changes on the heater plate from the air-flow cooling – see Figure 106. The results were also compared with GT measurements for models validation and calibration.

94
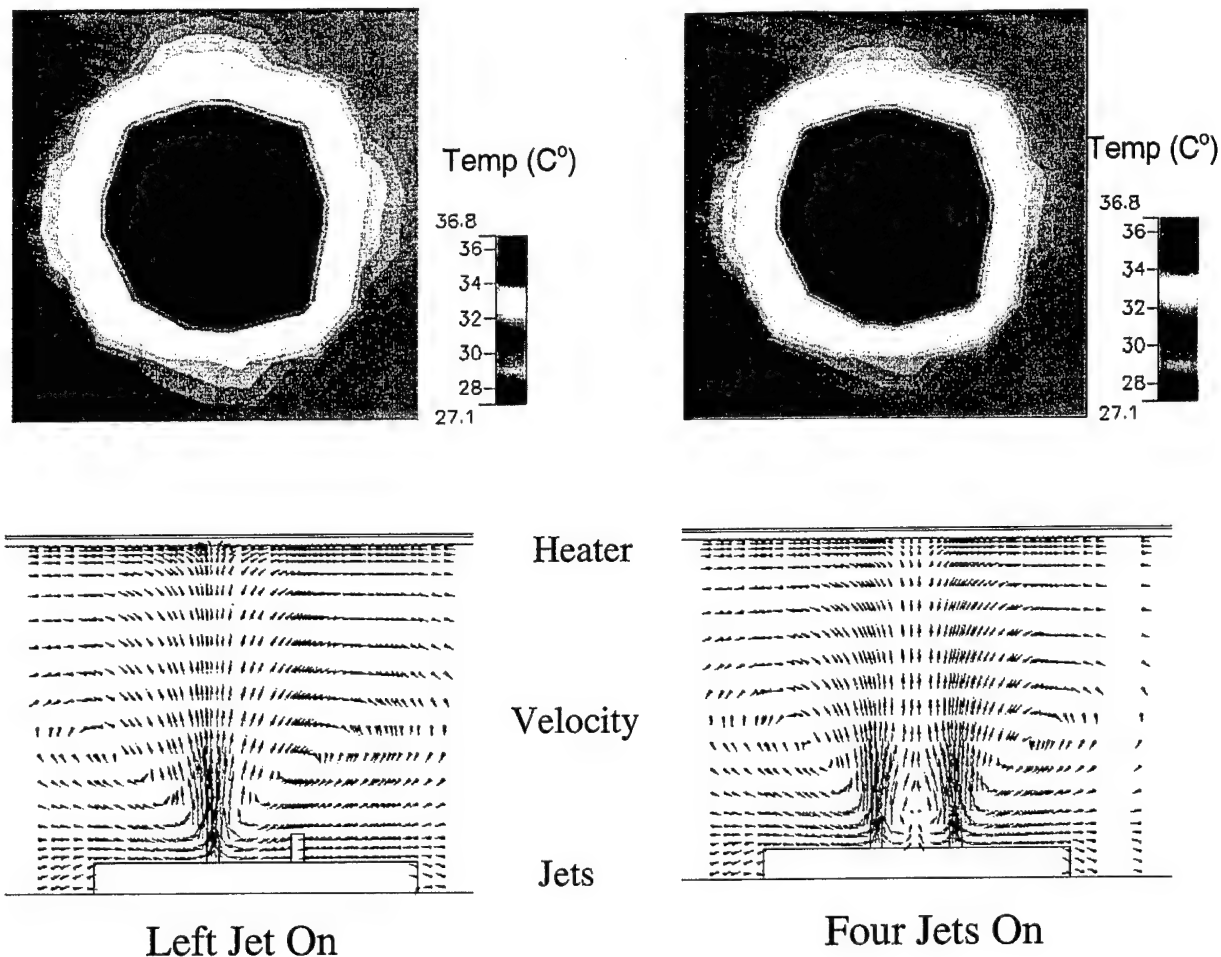
Figure 106. Coupled mixed-dimensional and mixed-domain simulation of temperature control by microjet arrays.

4.2.9 Synthetic Jet References

Amitay, M., Honohan, A., Trautman, M. and Glezer, A. "Modification of the Aerodynamic Characteristics of Bluff Bodies Using Fluidic Actuators," AIAA Paper 97-2004, 1997.

Campbell, S. J., Jr., Black, W. Z., Glezer, A., Hartley, J.G., Bhavnani, S. H., Kormann, G.B. and Nelson, D.J. "Thermal Management of a Laptop Computer with Synthetic Air Microjets,", *Sixth Intersociety Conference on Thermal and Thermomechanical Phenomena in Electronic Systems,* pp. 43-50, 1998.

Coe, D.J., Allen, M.G., Trautman, M.A. and Glezer, A. "Micromachined Jets for Manipulation of Macro Flows," *Technical Digest 1994 Solid-State Sensor and Actuator Workshop*, Hilton Head, SC, June 1994, pp. 243-247.

Coe, D.J., Allen, M.G., Trautman, M.A. and Glezer, A. "Addressable Micromachined Jet Arrays," *8ᵗʰ International Conference on Solid-State Sensors and Actuators and Eurosensors IX*, Stockholm, Sweden, 1995, pp. 329-332.

James, R.D., Jacobs, J.W. and Glezer, A. "A Round Turbulent Jet Produced by an Oscillating Diaphragm," *Physics of Fluids*, 8(9), pp. 2484-2495, September, 1996.

Lagorce, L., Kercher, D., English, J., Brand, O., Glezer, A. and Allen, M. "Batch Fabricated Microjet Coolers for Electronic Components," *Proc. of 1997 International Symposium on Microelectronics*, 1997, 494-499.

Minichiello, A. L., Hartley, J. G., Glezer, A. and Black, W.Z. "Thermal Management of Sealed Electronic Enclosures using Synthetic Jet Technology,", *INTERpack '97*, 2, pp. 1809-1812.

Smith, B.L. and Glezer, A. "The Formation and Evolution of Synthetic Jets,", *Physics of Fluids*, 10(9), pp. 2281-97, September, 1998.

Smith, B.L. and Glezer, A. "Vectoring and Small-Scale Motions Effected in Free Shear Flows Using Synthetic Jet Actuators,", AIAA Paper 97-0213, 1997.

Thompson, M. R., Denny, D. L., Black, W.Z., Hartley, J. G. and Glezer, A. "Cooling of Microelectronic Devices using Synthetic Jet Technology,", *Proc. of the 11ᵗʰ European Microelectronics Conference*, 1997, pp. 362-366.

5 MODEL REDUCTION PROCEDURES

5.1 Extraction of Lumped Capacitances from 3-D Electrostatic Simulations

One of the examples of coupled problems is the comb-drive resonator, used in MEMS accelerometers, gyroscopes, and electronic filters. In such a device, electrostatic actuation is coupled with structural/dynamics problems, and the air damping is very important too, which is a fluidic-type problem.

As one of the steps towards automatic generation of compact models of comb drives, procedures have been developed for automatic generation of compact model (extraction of lumped capacitances) for electrostatic behavior of a comb-drive resonator, using results of high-fidelity 3-D electrostatic simulations with FastBEM from CFDRC. The procedure is similar to the one described by the team of Analogy Inc. and Robert Bosch GmbH in [Teegarden 1998].
The procedure is illustrated below.

♦ **Micro-electro-mechanical structure design imported from CAD/EDA**

⇩
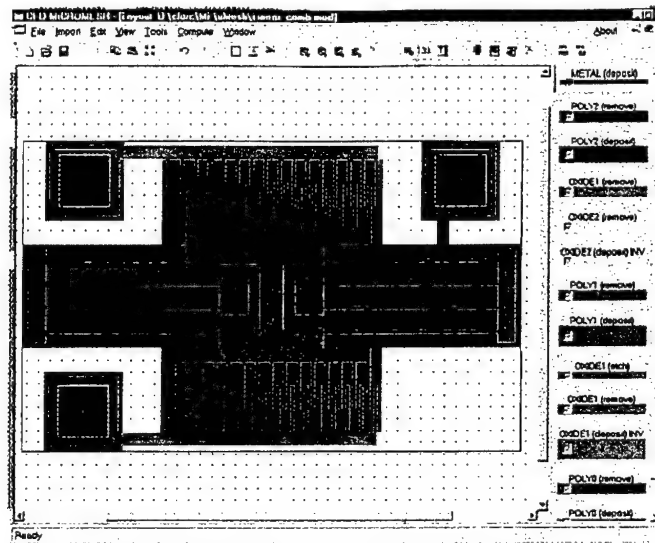
♦ **3-D model of the structure**

⇩
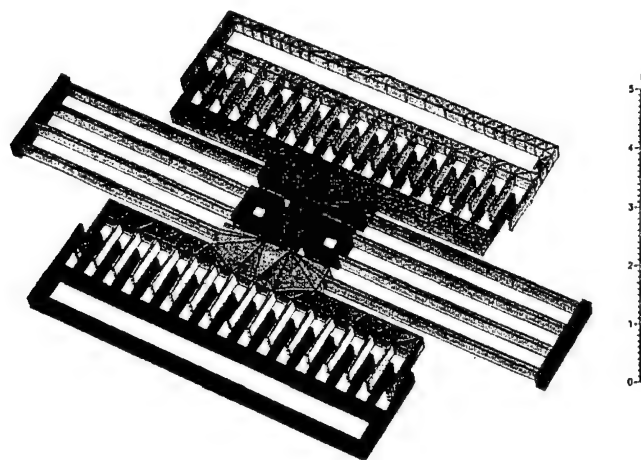
♦ **Results of repeated calculations with FastBEM**

⇩

♦ **Extracted capacitance vs. displacement**

Rotor-Ground Capacitance

⇩
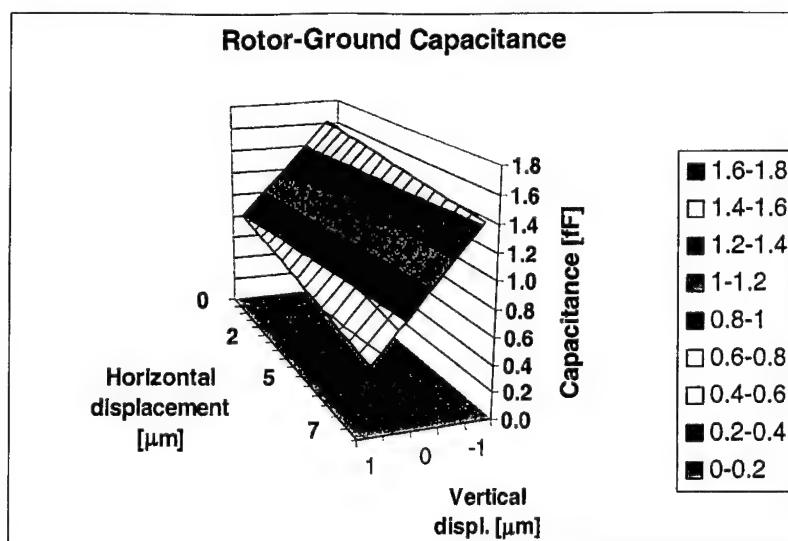
- ◆ **Fitted capacitance functions (Legendre polynomials)**
  C = f(x,z)

⇩

- ◆ **Electrostatic force calculation**

Repeat the same process for other capacitances:

Rotor-Stator Capacitance

Stator-Ground Capacitance
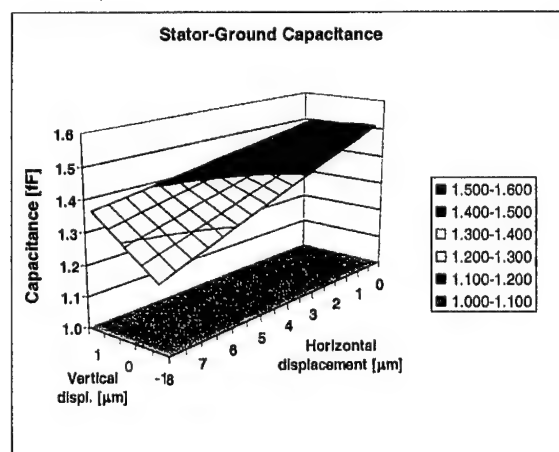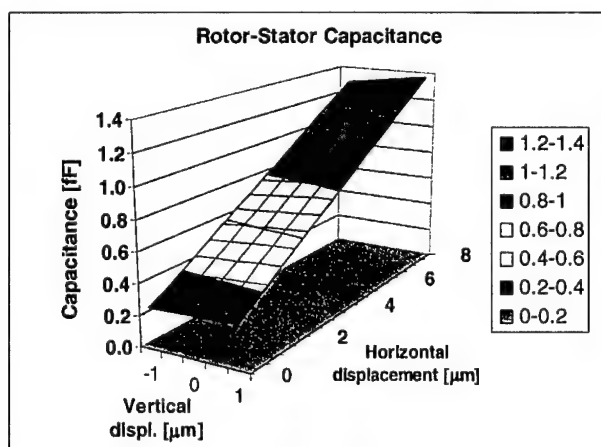
The fitted capacitance functions may be used directly in a system-level simulator, like Saber, where they can be coded into templates of the devices, using the MAST language.

5.2   Generation of Equivalent Circuit Models for Microfluidics

There has been a growing interest in last years in the development of fluidic microsystems containing microfluidic elements, like channels, valves, pumps, etc. Simulation and design of microfluidic systems requires various level models: high-fidelity (usually three-dimensional, or 3-D) models [Yang 1998], for design and optimization of particular elements and devices (e.g. their geometrical structure), as well as system-level models allowing for VLSI-scale simulation of such systems. For the latter purpose, reduced or compact models are necessary to make such system simulations computationally feasible [Voigt 1998], [Bourouina 1996].

In this project, we developed a design methodology and practical approach for generation of compact models of microfluidic elements. In this procedure we use high-fidelity 3-D simulations of the microfluidic devices to extract their characteristics for compact models, and subsequently, to validate the compact model behavior in various regimes of operation. The compact models are generated automatically in the formats that can be directly used in SPICE or SABER.

SPICE and SABER Models of Tesla Valve

To show an example for a nonlinear fluidic device, the generation of compact model for "Tesla valve" is described in detail in this section. Tesla valve is one of the no-moving-parts (NMP) valves used in micropumps in MEMS. Its principle of operation is based on the rectification of the fluid [Forster 1995]. For the same pressure drop, the flow in the forward direction through the valve is greater than the flow in the reverse direction (Figure 107). Hence, this device may be considered as "fluidic diode".
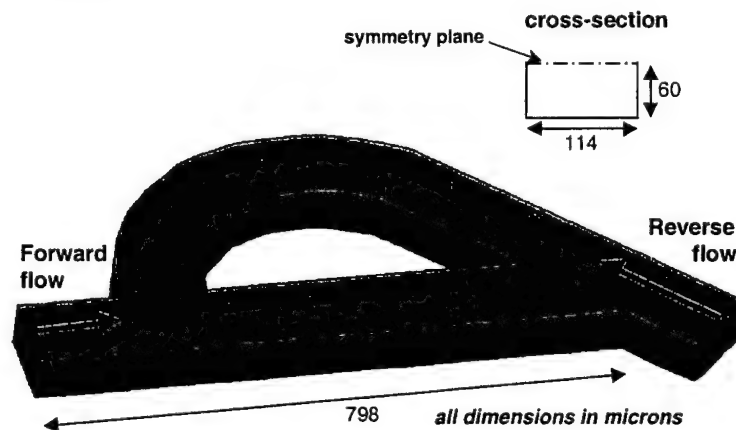
Figure 107. Geometry and dimensions of the analyzed Tesla valve.

In order to generate an equivalent circuit model (SPICE or SABER format) of our example microfluidic device - Tesla valve - we need to:

1. Build a 3-D model and computational mesh of the Tesla valve.

2. Perform a full 3-D simulation of fluid flow in the device, both steady and transient.

3. Perform a set of parametric runs to extract lumped parameters of the Flow-Pressure characteristics, in order to extract parameters for a compact model (equivalent RL circuit).

99

4. Write the compact model in the format compatible with SPICE or SABER.

Performing the steps 1 to 3 involves using CFDRC's new software CFD-Micromesh for automatic building of 3-D solid model and computational mesh (Section 3.1), and parametric computations of characteristics with CFD-ACE+ which is also a new feature added in this project (Section 2.2). An example unstructured mesh from CFD-Micromesh and sample results are shown in Figure 108.

(a)

(b)

(c)
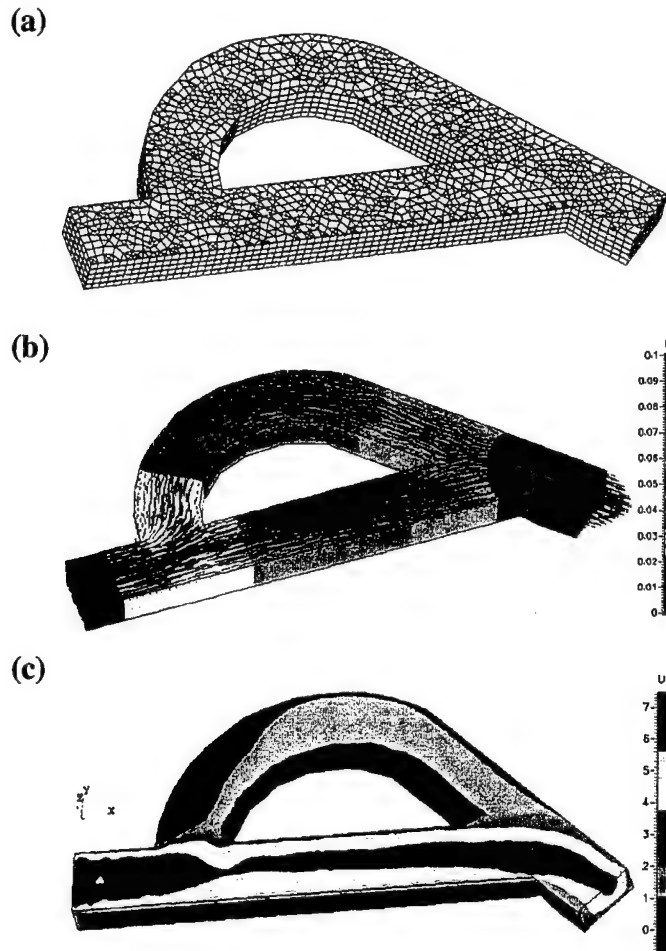
Figure 108. High-fidelity simulations: a) 3-D unstructured mesh, b) flow velocity (arrows) and pressure (colors) inside the device for forward flow, c) U-velocity component (along the X axis).

As a result of those parametric runs of 3-D simulations in CFD-ACE+, we obtain the static characteristics of flow versus pressure drop, as shown in the Figure 109 and Figure 110 below. Open circles represent data obtained from 3-D simulations, dark dots are the values measured experimentally at the University of Washington (Prof. Fred Forster), and the continuous line is an analytical fit (obtained in Excel). The entire static characteristic of the flow in both directions is presented in Figure 111.
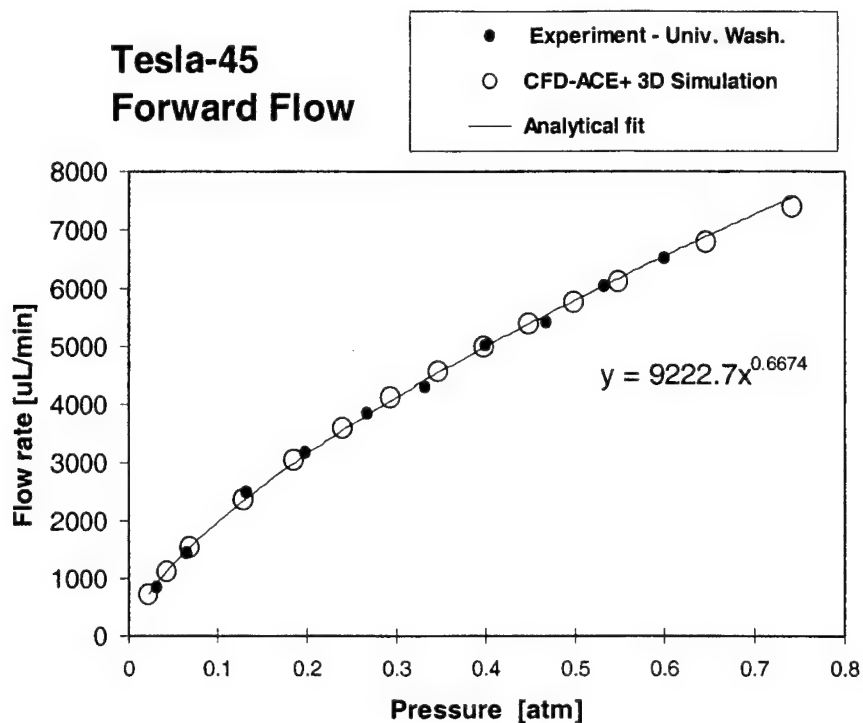
Figure 109. Forward flow static characteristic of the analyzed Tesla valve.
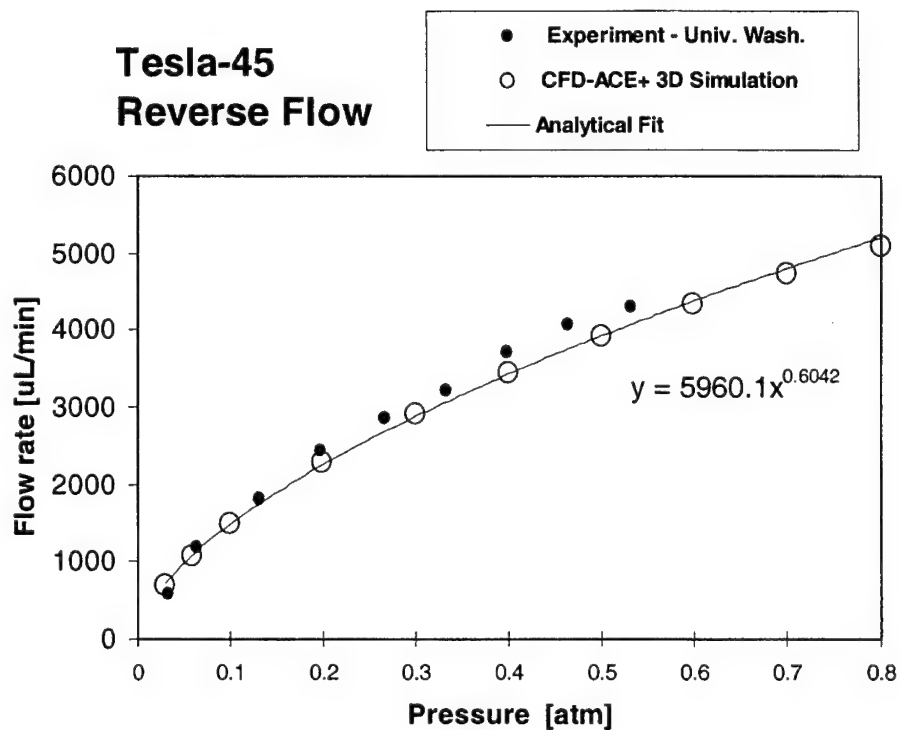
Figure 110. Reverse flow static characteristic of the analyzed Tesla valve.

101
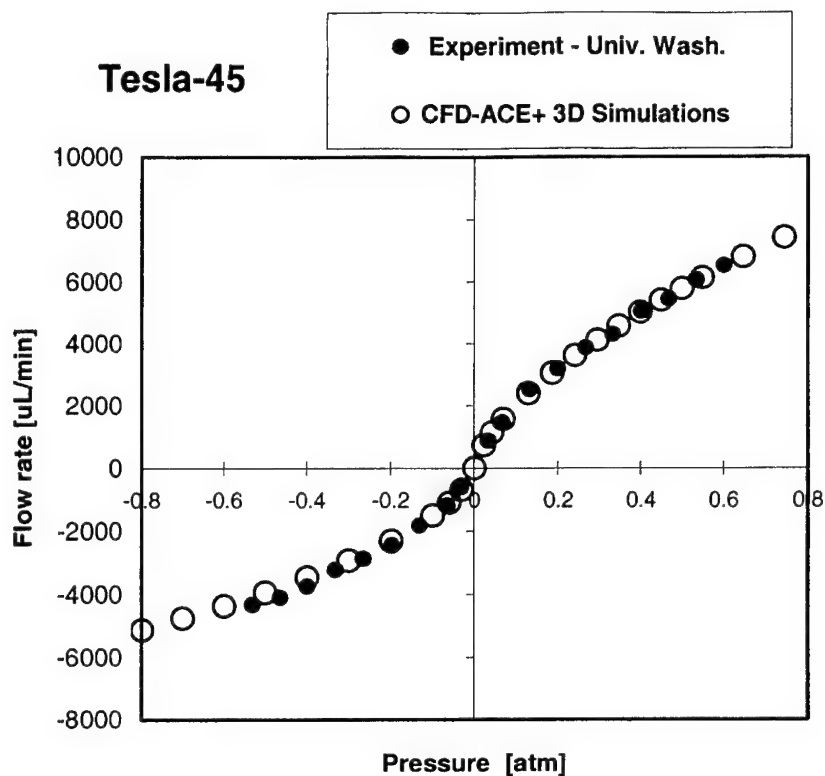
Figure 111. Static characteristic of the Tesla valve for both flow directions.

The new CFD-ACE+ version, expanded within this project, can generate output of the parametric runs in the form of a text table, as in the example below:

```
* * * * * * * * * * * * * * * * * * * * * * * * * * * * * * * * * * * * * * * * * * * * * * * * * * * * * * * * * * *
        Example of output file:   Tesla_CHANNEL_OUTLET.dat
* * * * * * * * * * * * * * * * * * * * * * * * * * * * * * * * * * * * * * * * * * * * * * * * * * * * * * * * * * *
Mass Flow
P_mean
  Case   1 :   Iter. #    100    1.556542E+03   6.869466E+03
  Case   2 :   Iter. #    100    2.385028E+03   1.288921E+04
  Case   3 :   Iter. #    100    3.044021E+03   1.857335E+04
  Case   4 :   Iter. #    100    3.610177E+03   2.405173E+04
  Case   5 :   Iter. #    100    4.114709E+03   2.938847E+04
  Case   6 :   Iter. #    100    4.574686E+03   3.461645E+04
* * * * * * * * * * * * * * * * * * * * * * * * * * * * * * * * * * * * * * * * * * * * * * * * * * * * * * * * * * *
```

These text tables can be easily copied and pasted into any convenient post-processing software. In our case, we used Microsoft Excel to draw the curves and fit the analytical curves (continuous lines and the equations in Figure 109 and Figure 110. The analytical equations are needed for a SPICE model.

SPICE model
The equivalent circuit model of the Tesla valve, to be used in any version of the popular SPICE simulator, can be represented in the form of a series connection of nonlinear resistance (R) element and linear inductance (L) element, as illustrated in Figure 112.

102
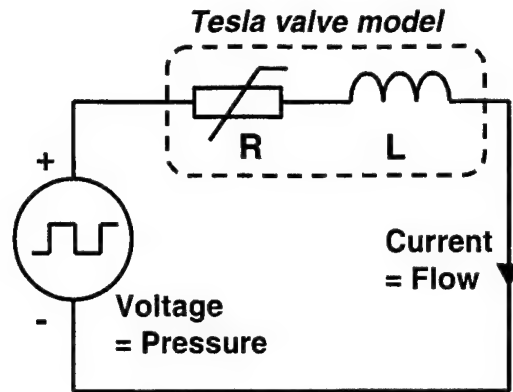
Figure 112. Equivalent RL circuit model of Tesla valve.

Most SPICE versions do not accept an arbitrary nonlinear R element, so it should be replaced by a voltage-controlled current source (VCCS), using the analytical relations derived in Figure 109 and Figure 110.

To obtain the L value from the high-fidelity simulations of any microfluidic device, we can use the relation of dynamic behavior of fluid pressure vs. flow rate and its electrical equivalent, voltage and current in an inductance:

$$P = L\frac{dQ}{dt} \quad \Leftrightarrow \quad V = L\frac{dI}{dt}$$

(5.1)

The L value can be easily found from the results of two first steps of transient simulation, as illustrated in the figure below:
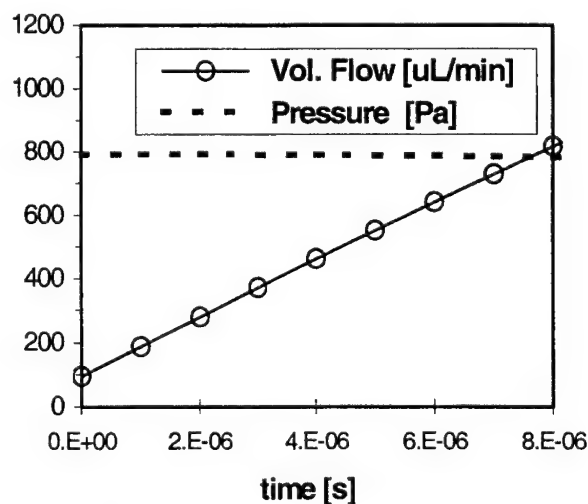
Figure 113. Transient response of fluid flow to step pressure change, used for extraction of L value in the equivalent circuit model.

The final form of the SPICE model is presented in the listing below. The nonlinear resistance (coming from the fitted equations in Figure 109 and Figure 110) is represented by voltage-controlled current source, G1, and the linear inductance (derived from the results in Figure 113) is represented by L1.

```
*****************************************************************
* Equivalent-circuit RL model of fluid flow in Tesla-45 valve

* inductance - fluid inertia
L1   1   2   1.413e-10

* VCCS - nonlinear resistance
G1   2   0   Value = {0.5*(SGN(V(2,0))+1)*9222.7*PWR(V(2,0),0.6674) +
+                     0.5*(SGN(V(2,0))-1)*5960.1*PWR(V(2,0),0.6042)}

V_dc   1   0   DC   0V

*** STATIC CHARACTERISTIC

.DC   V_dc   -0.8   0.8 0.02

.PRINT DC V(1) I(G1)
.probe
.END
*****************************************************************
```

A static characteristic of the Tesla valve, obtained using PSpice with the input deck as above, is presented in Figure 114 below. It represents very well the measured and 3-D-simulated characteristics shown earlier in Figure 111.
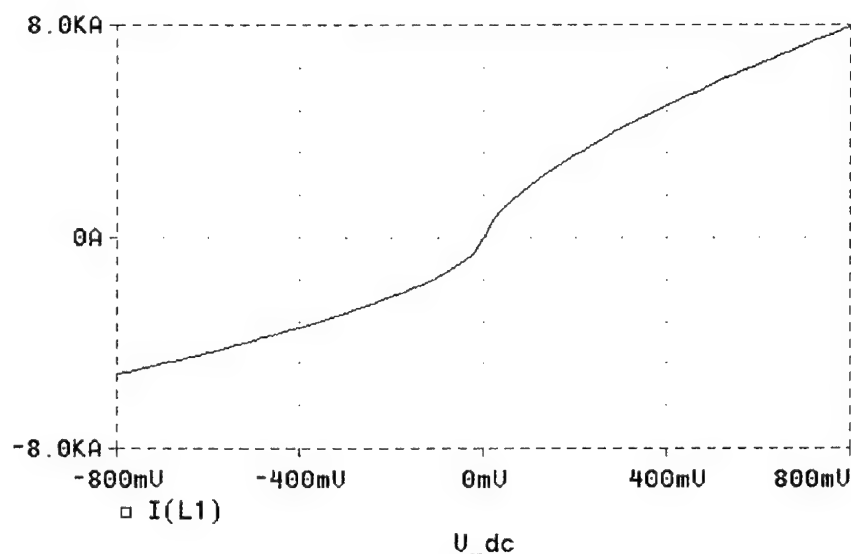
Figure 114. Static characteristic of Tesla valve, calculated with SPICE.

In order to verify dynamic behavior of the compact model in SPICE, a transient response of the Tesla valve flow for an oscillatory pressure change at the inlet has been calculated both by the 3-

D simulation using CFD-ACE+, and using the equivalent R-L model in SPICE. Example results obtained with full 3-D Navier-Stokes solution and equivalent-circuit RL model (solved by PSpice), for periodic pressure oscillations of frequency 3085 Hz (fluidic resonance of Tesla valve [Forster 1995]) and amplitude 0.5 atm, are presented in Figure 115.

3-D CFD Simulation Results   **Equivalent RL Circuit (SPICE)**
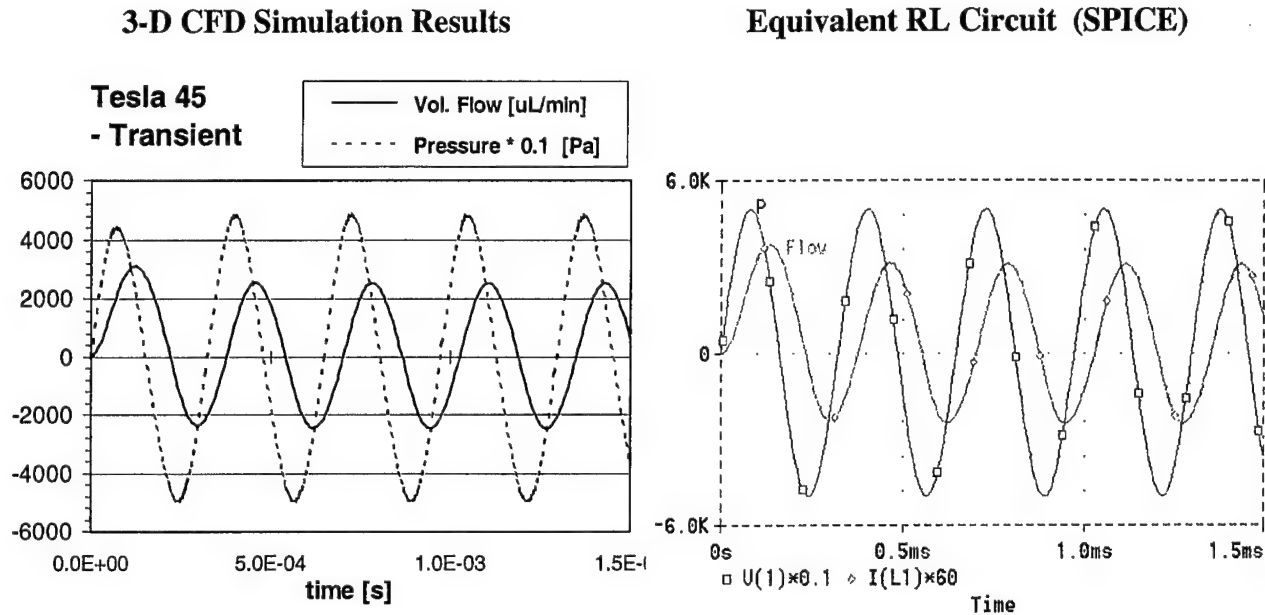
Figure 115. Transient response of the Tesla valve flow for an oscillatory pressure change at the inlet, calculated by the 3-D simulation with CFD-ACE+, and using the equivalent R-L model in SPICE.

SABER model
A behavioral model of the nonlinear fluid flow in Tesla valve has been also implemented for the Saber simulator with models written in MAST, an analog hardware description language of Saber. The Saber-MAST version of the compact flow model uses directly fluidic quantities: pressure drop as input (across variable) and fluid flow as output (through variable).

A compact model of the Tesla valve for Saber simulator can be generated even more directly than for SPICE. In Saber, a predefined template for fluidic "Piecewise-Linear Device" ("q_p_pwl" template) can be used for the non-linear viscous friction model (R). The tabularized pressure-flow results from CFD-ACE+ can be copied directly to the "q_p_pwl" template. A test Saber circuit with such a model of Tesla valve, and also a hydraulic pressure source available in Saber, is shown in Figure 116. The listing of the template is shown under the figure. The table of pressure-flow data in the template is generated directly in that format by CFD-ACE+ program, as a result of 3-D simulations.
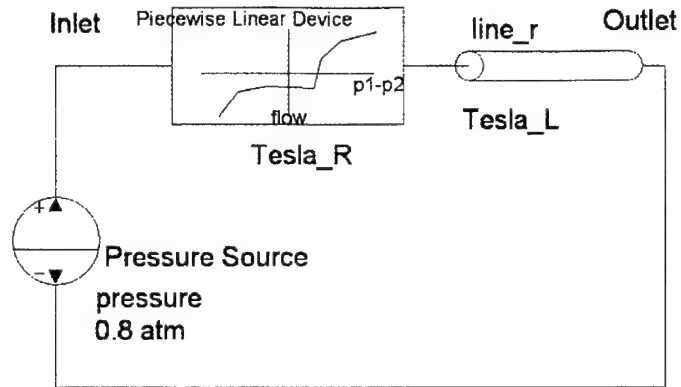
Figure 116. Test circuit in Saber, including PWL Tesla valve model and hydraulic pressure source for testing.

```
######################################################################
#  Saber netlist for design Tesla_static                             #
#  Created by the Saber Integration Toolkit   4.3-2.9 of Analogy, Inc. #
######################################################################

q_p_pwl.Tesla_45  p1:Inlet  p2:Outlet = data=[
(-8.00E-01, -5.12E+03),
(-7.00E-01, -4.75E+03),
(-6.00E-01, -4.35E+03),
(-5.00E-01, -3.92E+03),
(-4.00E-01, -3.45E+03),
(-3.00E-01, -2.92E+03),
(-2.00E-01, -2.29E+03),
(-9.97E-02, -1.50E+03),
(-5.98E-02, -1.09E+03),
(-2.99E-02, -6.96E+02),
(0, 0),
(2.26E-02, 7.17E+02),
(4.30E-02, 1.13E+03),
(6.87E-02, 1.56E+03),
(1.29E-01, 2.39E+03),
(1.86E-01, 3.04E+03),
(2.41E-01, 3.61E+03),
(2.94E-01, 4.11E+03),
(3.46E-01, 4.57E+03),
(3.98E-01, 5.00E+03),
(4.48E-01, 5.40E+03),
(4.98E-01, 5.77E+03),
(5.48E-01, 6.13E+03),
(6.46E-01, 6.80E+03),
(7.43E-01, 7.41E+03)]

pressure.P_Drop  p1:Inlet  p2:Outlet = dc=0.0

######################################################################
```

To include the transient effects in the model of a microchannel, that is inertial effects (inductance), and capacitance due to the fluid compressibility, we can use the "line_r" template

available in Saber. The line_r template models a rigid tube used for the transmission of hydraulic fluid.

The hydraulic inductance is modeled using the following equation [MAST, 1999]:

$$\Delta P = (rho \cdot len/area) \cdot dQ/dt$$

and the hydraulic capacitance is modeled using the equation:

$$Q = -(area \cdot len/bulk) \cdot dP/dt$$

where P is the pressure, Q is flow, *rho* is mass density of the fluid, *len* is the channel length, *area* is the cross-section area of the channel, and *bulk* is the fluid bulk modulus value. Figure 116 shows the full Saber model of the Tesla valve, including the viscous resistance part (Tesla_R) and inductance (Tesla_L). The capacitance due to the fluid compressibility can be neglected in most cases of microfluidic devices.

A static characteristic of the Tesla valve, obtained with Saber, using the template as above, is presented in Figure 117. It represents very well the measured and 3-D-simulated characteristics shown earlier.
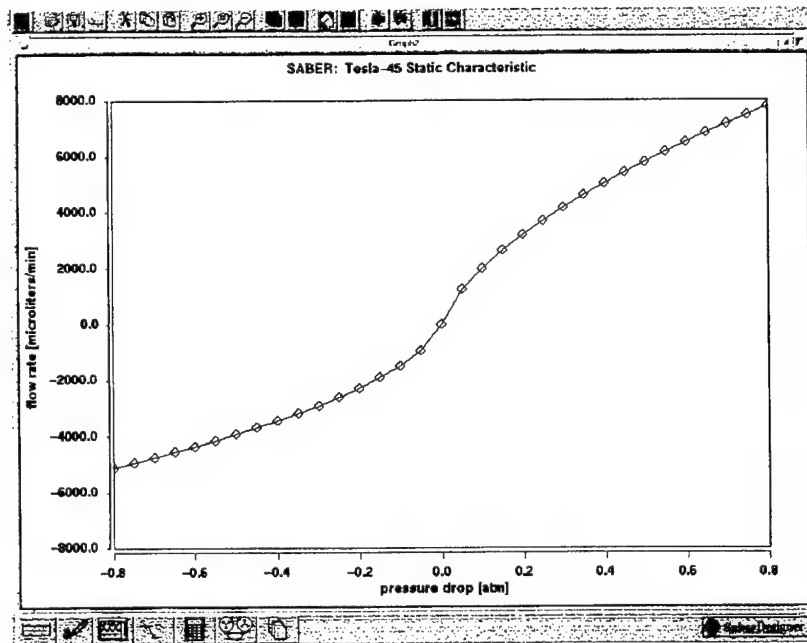
Figure 117. Static characteristic of Tesla valve, obtained in SABER.

The compact model of an arbitrary microfluidic channel presented here, in the form of nonlinear RL circuit, is very useful to a wide community of SPICE users who are very often also designers of microfluidic MEMS and microsystems in the domain of bio-medical and chemical engineering, integrated very often with control and drive electronics. On the other hand, the behavioral model implemented in SABER offers more direct simulation of fluidic phenomena, readily available to designers in hydraulic units, without additional translation to electrical equivalents.

107

The use of high-fidelity 3-D numerical simulations, together with the procedures described above, gives a possibility to obtain very useful compact/behavioral models of nonlinear microchannel behavior in fluidic microsystems, for wide range of driving conditions.

Circuit Modeling of Tesla-Micropump

In order to verify to performance of the above derived equivalent circuit models of Tesla valve, we used these models in a simulation of a bigger fluidic system, containing 8 Tesla valves and a pumping membrane. A 3-D model of the Tesla-Micropump with eight valves and a snapshot of flow results from transient 3-D CFD simulation is shown in Figure 118 below. The flow results show a time instant when the pumping membrane is moving up, pulling the fluid in. It can be clearly seen how the left branch of 4 valves is "forward biased" and the right branch is "reverse biased".
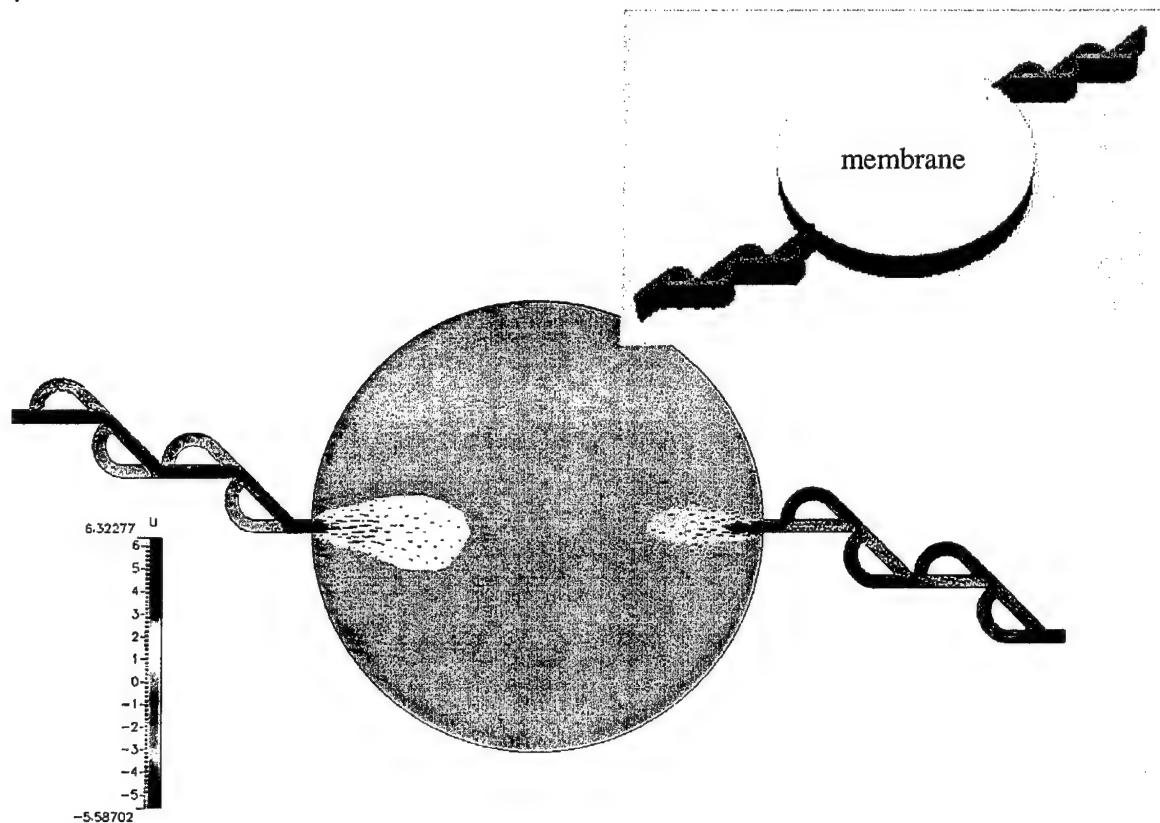
Figure 118. A 3-D model of the Tesla-Micropump with eight valves and flow results from transient 3-D CFD simulation.

Using the equivalent circuit model of a single Tesla valve, derived in the previous section, we have built a circuit model of the entire pump shown in the figure above. First, one branch of the four valves was modeled by means of the four elementary circuits connected in series, and the pressure changes forced by the moving membrane were represented by a pressure (voltage) source – see Figure 119 below.

108
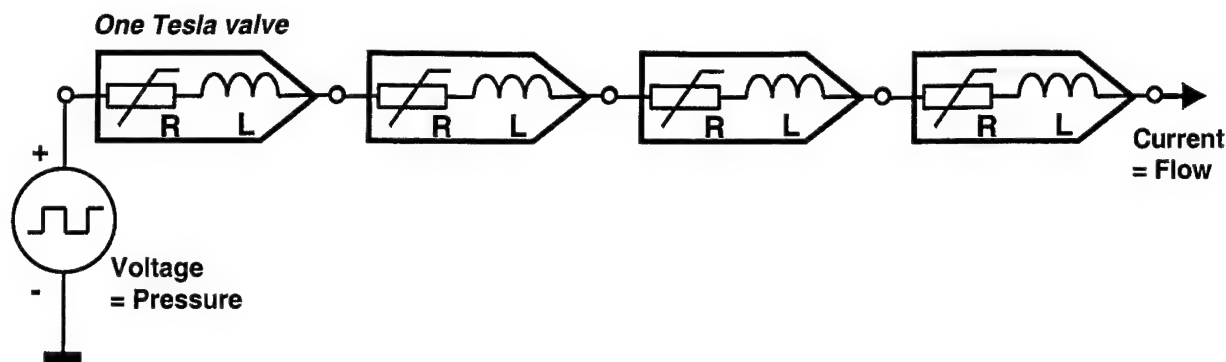
Figure 119. Equivalent circuit model of one micropump branch with four Tesla valves.

The above model was written as an input deck in SPICE format, shown in the listing below. The single valve model is coded as a subcircuit (SUBCKT) called *Tesla* with two terminals *IN* and *OUT*, and then it is used many times in the SPICE model of the entire pump.

```
--------------------------------------------------------------------
SPICE
* RL model of fluid flow (uL/s) in 4 Tesla valves in series

.SUBCKT Tesla IN OUT
* inductance - fluid inertia
L1   IN   N1   5.087e-2

* VCCS - nonlinear resistance (calculated from uL/s)
G1   N1   OUT   Value = {0.5*(SGN(V(N1,OUT))+1)*0.0707*PWR(V(N1,OUT),0.6674) +
+                   0.5*(SGN(V(N1,OUT))-1)*0.0946*PWR(V(N1,OUT),0.6042)}
.ENDS

X1   1   2   Tesla
X2   2   3   Tesla
X3   3   4   Tesla
X4   4   0   Tesla
V_dc   1   0   DC   0V

*** STATIC CHARACTERISTIC
.DC   V_dc   -8e4   8e4   2e3

.END
--------------------------------------------------------------------
```

Comparison of transient flow results obtained both from high-fidelity 3-D CFD simulations and with the equivalent circuit model of the full pump (Figure 120) are shown in Figure 121.
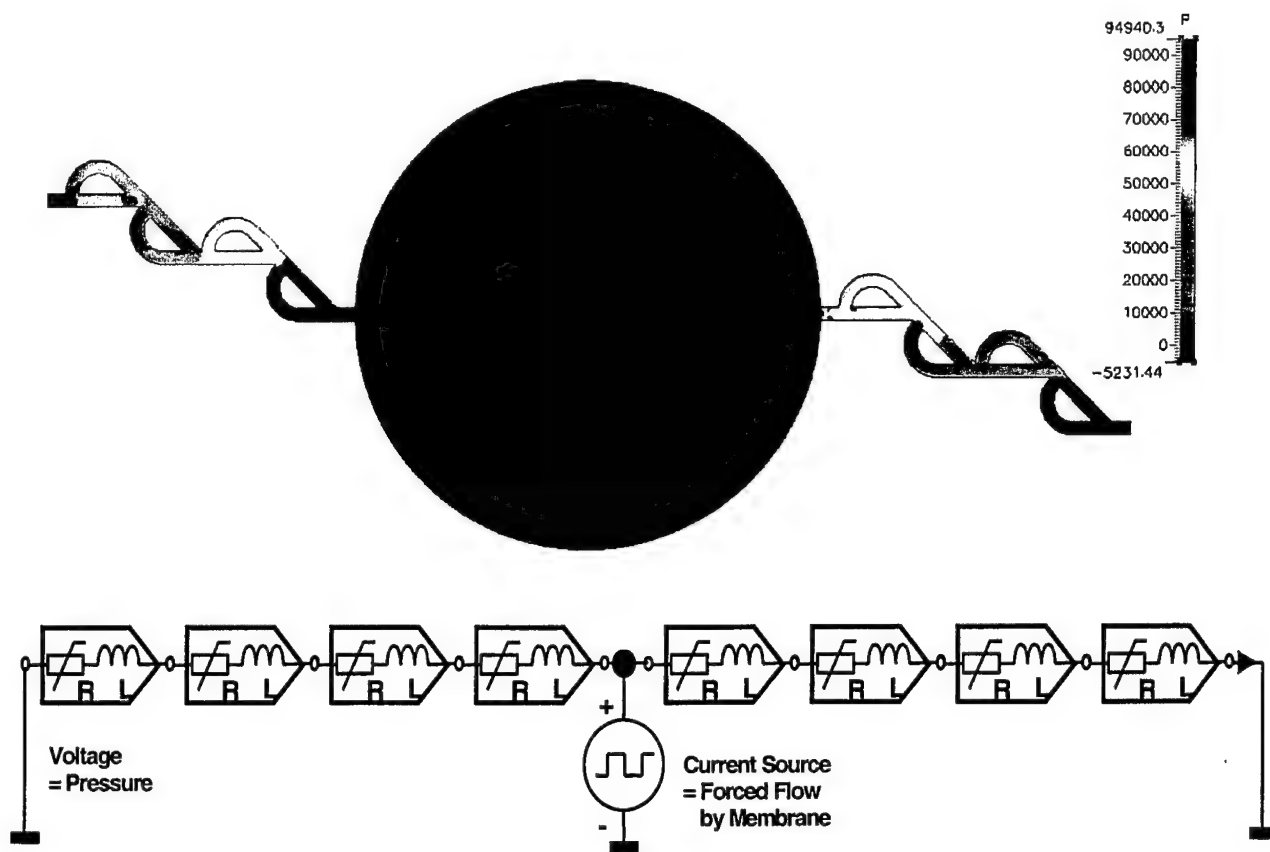
Figure 120. The high-fidelity CFD results (pressure distribution) in the micropump with eight Tesla valves and its full equivalent circuit model.

Results of 3-D CFD-ACE+ Simulations:

Pump: 4 + 4 Tesla valves
- Membrane: sin 100 Hz

Legend:
- —— INLET Flow [nL/s]
- - - - INLET P_mean [Pa]
- —— Membrane Move
- —— OUTLET Flow [nL/s]
- × OUTLET P_mean [Pa]
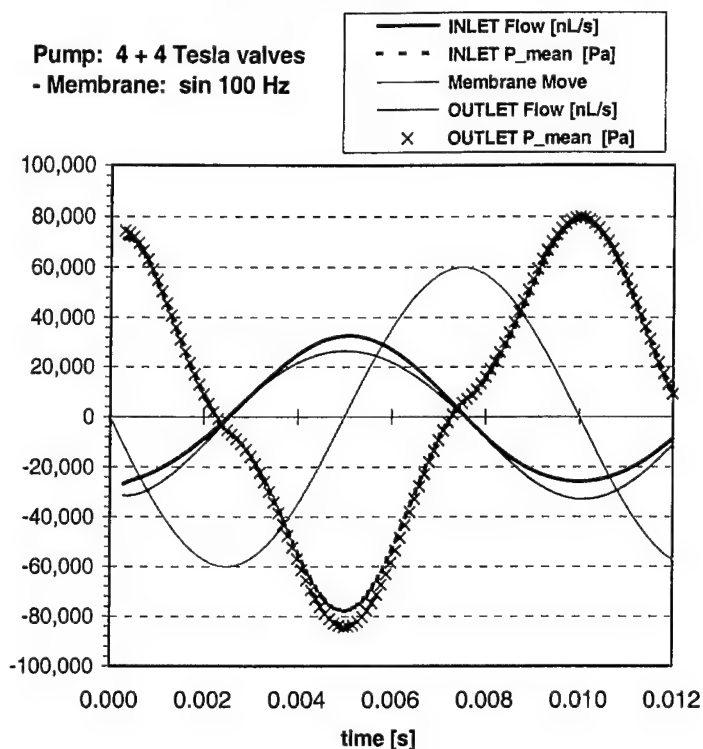
Equivalent Circuit (SPICE) Results:

1 □ I(X1.G1) ◦ -I(X8.G1) 2 - U(M1) • U1(I_sin)
Time
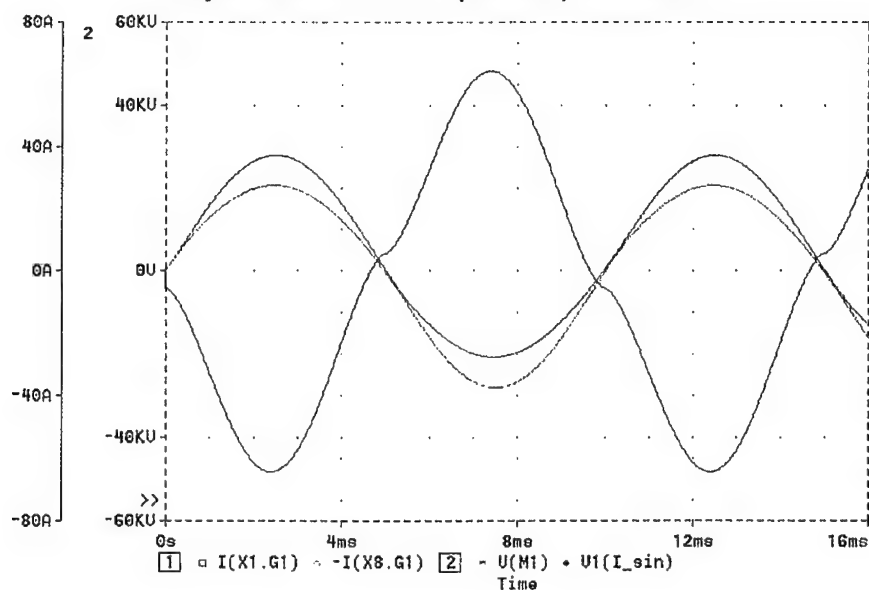
Figure 121. Transient flow results of Tesla micropump obtained from high-fidelity 3-D CFD simulations and with the equivalent circuit model solved by SPICE.

111

The validation results presented above show the compact model of an arbitrary microfluidic channel developed in this project and presented here can be very useful to a wide community of designers of fluidic microsystems who are very often also SPICE users.

5.3   Matrix Reduction Procedures for Electro-Mechanical Microdevices

5.3.1   UF Model Reduction Techniques

Within this project, the subcontractors at **University of Florida (UF)** worked on reduced order models for electro-mechanical devices, built on the basis of Finite Element Method (FEM) models. The UF team implemented the model-reduction code using both the Lanczos algorithm (see Lanczos [1950], Gallivan & Grimme [1996] and Bahram Nour-Omid [1991]) and Wilson-Yuan-Dickens (WYD) algorithm (see Wilson, Yuan & Dickens [1982]) in the CFD-ACEUN code of CFDRC. The codes were tested using a 3-D MEMS beam microstructure from MIT. We also studied Lanczos and WYD methods for higher efficiency and accuracy.

The comparison of the corresponding first several modes (up to seventh mode) from the full-order FEM model and reduced-order model created by the **Lanczos algorithm** was very successful. Also the step responses of the displacement at the central node from the full-order model and the reduced-order model (dofs = 9) agree very well. The transient analysis with the reduced-order model takes much less CPU time (0.033 sec.) than that with the full-order model (21.0 sec), which is more than **six hundred times faster**.

Similarly for the **Wilson-Yuan-Dickens (WYD) algorithm**, the comparison of the corresponding modes from the full-order model and reduced-order model showed that the first several modes (until fourth) found out by the WYD reduction method agree well with the full order modes. Tests with serpentine flexure MEMS structure showed that transient analysis with reduced model can be up to **10,000 times faster** than the full 3-D FEM computation. All the details and results are presented below.

The work at University of Florida was concentrated on developing reduced-order models for MEMS systems. In this project, we have implemented our model-reduction code using both the Lanczos algorithm (see Lanczos [1950], Gallivan & Grimme [1996] and BahramNour-Omid [1991]) and Wilson-Yuan-Dickens (WYD) algorithm (see Wilson, Yuan& Dickens [1982]) in the CFD-ACEUN code of CFDRC, and tested the codes using the 3-D MEMS beam microstructure examples in our previous reports. We also studied Lanczos and WYD methods for higher efficiency and accuracy. In Section 5.3.1.1, we give a brief description of our work in this project . In Section 5.3.1.2, we describe the validation of the implementation of our codes in CFD-ACEUN. In Section 5.3.2, we present the detailed implementation of our model reduction codes. In Section 5.3.3, we explain our research on Lanczos and WYD algorithms for higher effciency.

5.3.1.1 Research Summary

*   Validation of the implemented model reduction codes by testing MEMS models.
*   Implementation of the model reduction codes into CFD-ACEUN.

- Development of the corresponding model reduction codes.
- Investigation on model reduction methods (Lanczos and WYD) for MEMS FEM models.

5.3.1.2   The Validation of the Implementation

The validation of the implementation of Lanczos algorithm

In this subsection, we validate our implementation of Lanczos algorithm in CFD-ACEUN code by testing a new MEMS beam microstructure.

Because the separated mass matrix sky_ m of the model is still not available in the current CFD-ACEUN code, we have to read in the model information from input data files directly, which includes the stiffness matrix sky _k, the mass matrix sky _, and the pointer vector ma of the original model. In the model reduction code, the reduced-order model will be calculated from the full-order model and ready for the transient analysis in CFD-ACEUN code. In the updated CFD-ACEUN code with separated mass matrix sky_m, we will pass the three one-dimensional arrays sky_k, sky_m, and ma into our model reduction routines as arguments.

Here we will use a new 3-D MEMS beam microstructure (Figure 122) to validate the implementation of our model reduction code (Lanczos algorithm) in the CFD-ACEUN code. We use the geometric properties and the material properties in Hung & Senturia [1999]. The geometric properties are as follows:

$$l_a = 200\mu m, \quad l_b = 50\mu m$$
$$h = 2.2\mu m, \quad w = 40.0\mu m$$

The material properties are as follows:

$$E = 149 GPa, \quad \rho = 2330 Kg/m^3$$

The transverse step loading, at central point, along the axis ξ^3 is

$$F = 1000 nN, \quad for\ t \geq 0.$$

We use twenty-eight 3-D beam elements and the total active degrees of freedom (dofs) is 126. We have the reduced-order model with the number of retained degrees of freedom nine. The starting vector of computing the reduced-order model is the random vector. The comparison of computed eigenvalues obtained with different models (full-order and reduced-order model) is shown in Table 5.1. We found that in this case the first seven eigenvalues of reduced-order model (dofs = 9)are obtained accurately. The Table 5.2 shows the comparison of CPU time to generate different reduced-order models. Speed up factors are calculated with respect to the reduced-order model (dofs = 36). We found that the time taken on generating the reduced-order model is nearly proportional to the size of the reduced-order model.

113

The Table 5.2 shows the comparison of CPU time to generate different reduced-order models. Speed up factors are calculated with respect to the reduced-order model (dofs = 36). We found that the time taken on generating the reduced-order model is nearly proportional to the size of the reduced-order model.
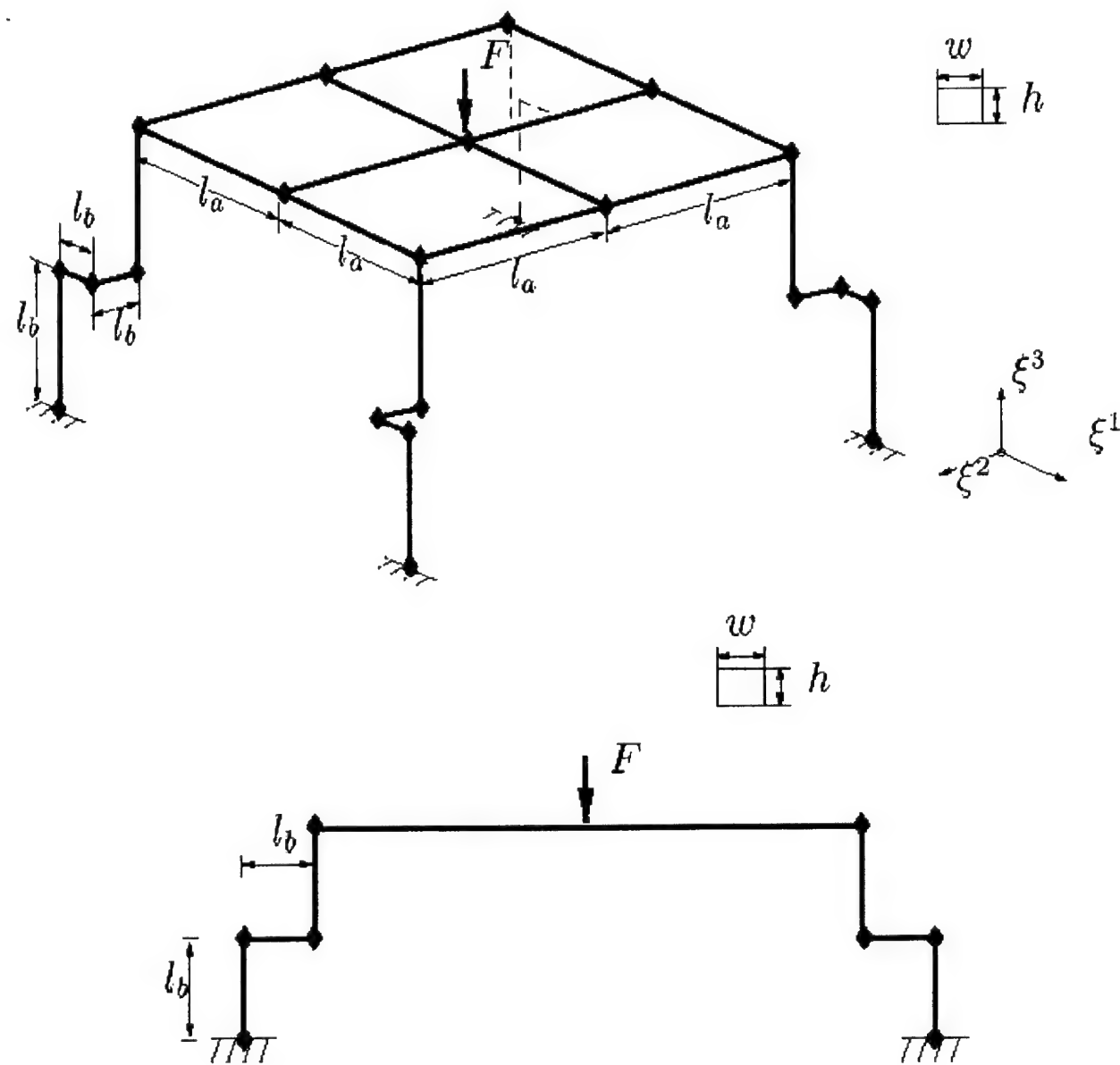
Figure 122. Finite-element model of 3-D MEMS beam microstructure.

Table 5.1 Step Response of the 3-D elastic beam microstructure. Comparison of eigenvalues from full-order model to reduced-order model.

Mode	Full-order ($dofs$ = 126)	Reduced-order ($dofs$ = p)	relative error
1	1.7804×10^{11}	1.7804×10^{11}	0
2	3.5952×10^{11}	3.5952×10^{11}	0
3	5.8118×10^{11}	5.8118×10^{11}	0
4	1.3904×10^{12}	1.3905×10^{12}	0.007%
5	1.4515×10^{12}	1.4518×10^{12}	0.02%
6	2.5810×10^{12}	2.5892×10^{12}	0.32%
7	3.2409×10^{12}	3.2591×10^{12}	0.56%
8	4.7345×10^{12}	8.1639×10^{12}	42%
9	7.9633×10^{12}	1.7243×10^{12}	53.8%

Table 5.2 Step response of the 3-D elastic beam microstructure. Comparison of CPU time for generating the reduced-order model with different size.

Reduced-order (dofs)	run time (msec)	speed up factor
9	25	3.64
18	46	1.98
36	91	1

The comparison of the corresponding modes from the full-order model and reduced-order model are shown in Figure 123 to Figure 132. We found that the first several modes (until seventh) are found out by the Lanczos reduction method successfully, which verified the calculation of eigenvalues in Table 5.1.

The comparison of the step response of displacement at the central node along the axis ξ^3 from the full-order model and the reduced-order model (dofs = 9) is shown in Figure 133. The Figure 134 is the frequency components of the time-domain response by Fast Fourier Transform (FFT), which shows the comparison of the corresponding frequency response from the full-order model and from the reduced-order model (dofs = 9). The corresponding velocity comparisons are given in Figure 135 and Figure 136. The results from the full-order model and the reduced-order model (dofs = 9) agree very well. On the other hand, the transient analysis with the reduced-order model takes much less CPU time (0.033 sec.) than that with the full-order model (21.0 sec), which is more than **six hundred times faster**.

From the above numerical results, we show that our implementation of the Lanczos algorithm in the CFD-ACEUN code was successful. We also establish the efficiency of the reduced-order model by Lanczos algorithm.
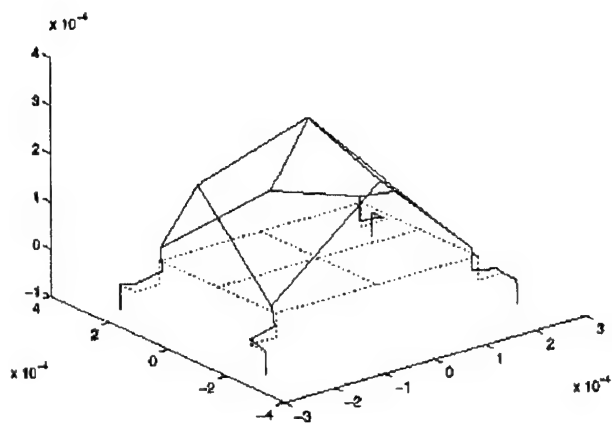
Figure 123. 1st mode in full-order model.
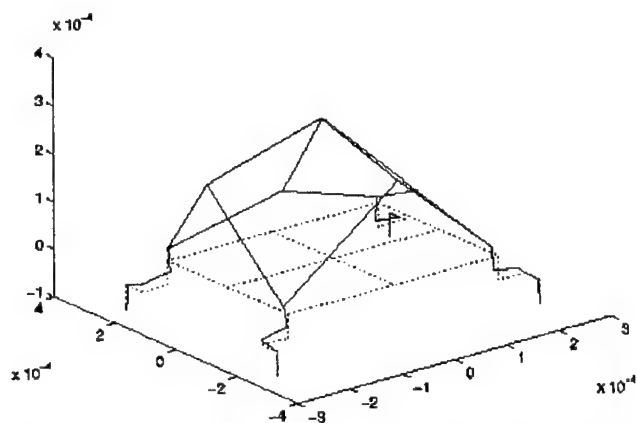
Figure 124. 1st mode in reduced-order model (dofs =9).
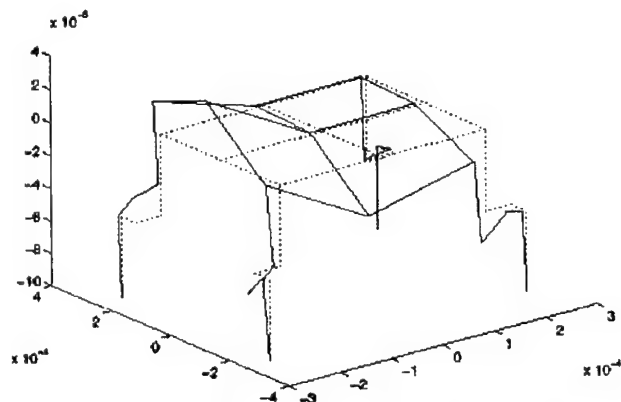
Figure 125. 2nd mode in full-order model.
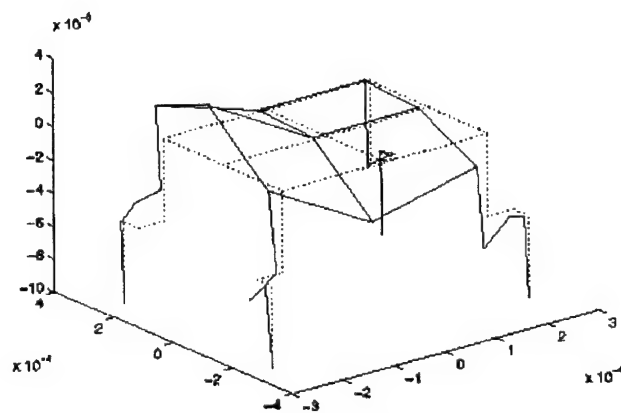
Figure 126. 2nd mode in reduced-order model (dofs =9).
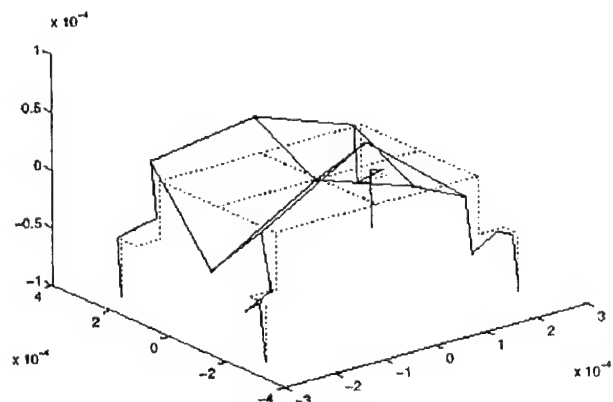
Figure 127. 3rd mode in full-order model.
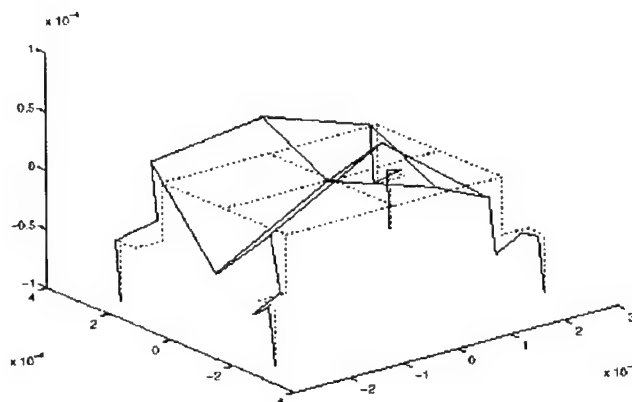
Figure 128. 3rd mode in reduced-order model (dofs =9).

116
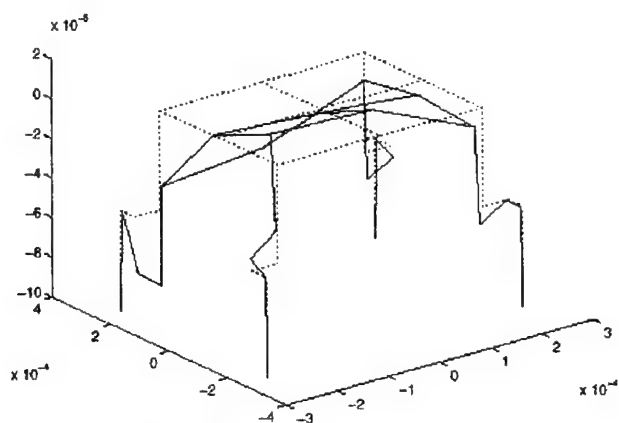
Figure 129. 4ᵗʰ mode in full-order model.
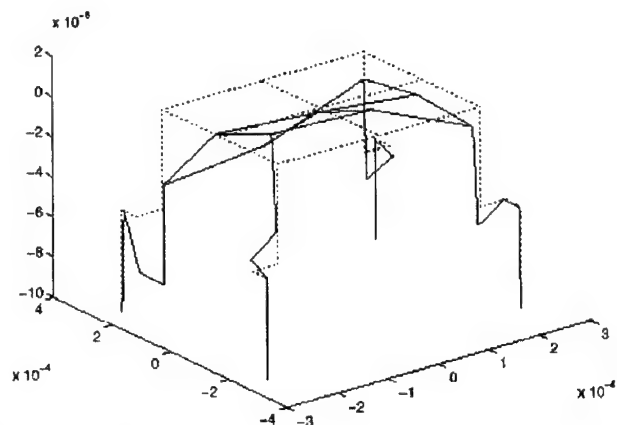
Figure 130. 4ᵗʰ mode in reduced-order model (dofs =9).
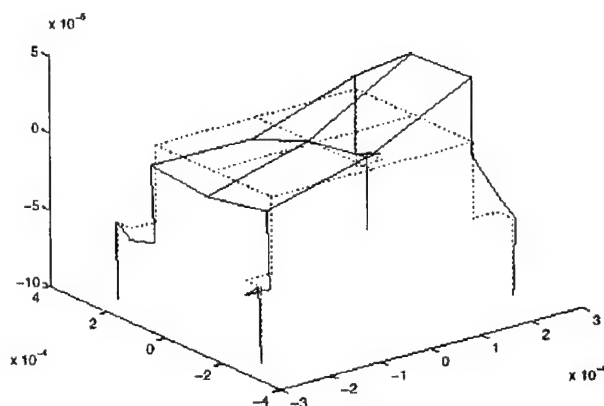
Figure 131. 5ᵗʰ mode in full-order model.
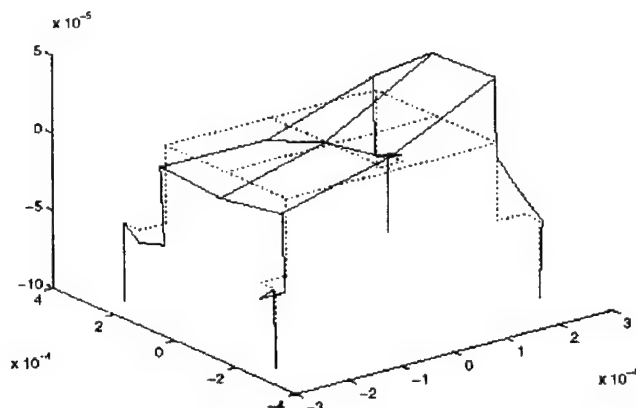
Figure 132. 5ᵗʰ mode in reduced-order model (dofs =9).

The Validation of the implementation of WYD algorithm

In this subsection, we will validate our implementation of WYD algorithm in CFD-ACEUN code by testing the MEMS beam microstructure (Figure 122) described in the previous subsection.

We use twenty-eight 3-D beam elements and the total active degrees of freedom (dofs) is 126. We have the reduced-order model with the number of retained degrees of freedom nine. The starting vector of computing the reduced-order model is the static solution.

The comparison of computed eigenvalues obtained with different models (full-order and reduced-order model) is shown in Table 5.3. We found that in this case for the simple constant concentrated force WYD method does not skip any of the first fourth modes. The mode participation factor shows that the first several modes are all important. No mode is orthogonal to the applied force as in our previous crab-leg model (see Fedder [1994]). We have the same above observation as in both WYD algorithm and Lanczos algorithm with static solution as starting vector, however, it seems WYD algorithm may pick up only one mode among some modes with

117

close eigenvalues. The comparison of the corresponding modes from the full-order model and reduced-order model shows that the first several modes (until fourth) found out by the WYD reduction method agree well with the full order modes, which verified the calculation of eigenvalues in Table 5.3. The comparison of the step response of displacement at the central node along the axis $\xi 3$ from the full-order model and the reduced-order model (dofs = 9) is shown in Figure 137. The Figure 138 is the frequency components of the time-domain response by Fast Fourier Transform (FFT), which shows the comparison of the corresponding frequency response from the full-order model and from the reduced-order model (dofs = 9). The results from the full-order model and the reduced-order model (dofs = 9) match very well. On the other hand, the transient analysis with the reduced-order model takes much less CPU time (0.033 sec.) than that with the full-order model (23.0 sec), which is more than six hundred times faster.
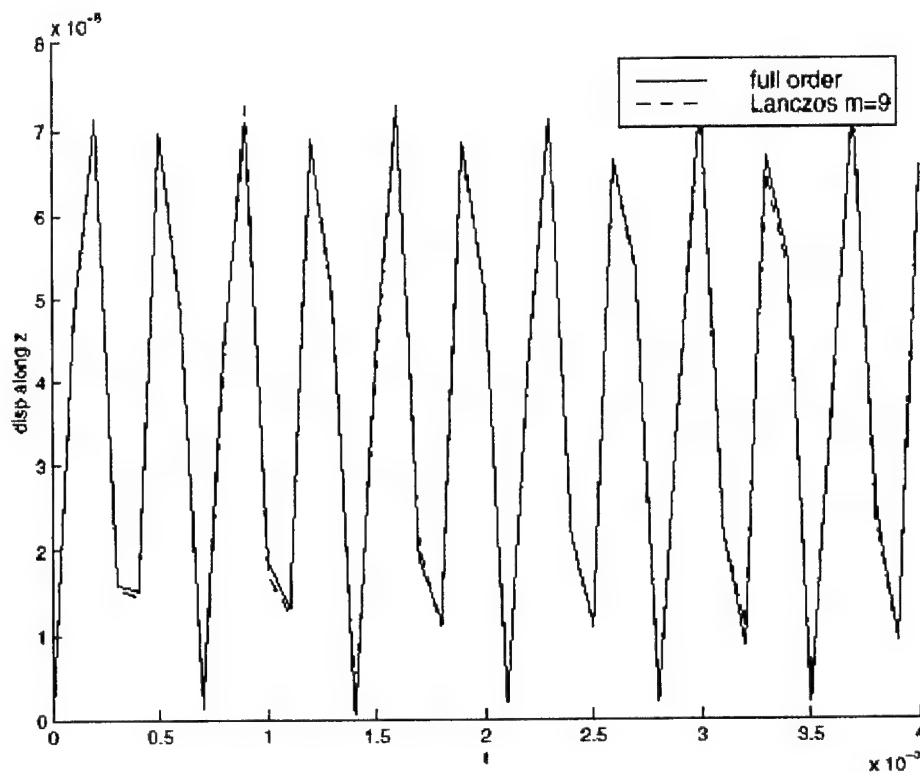
Figure 133. Step responses of displacement at central point from full-order model and reduced-order model (dofs = 9).

From the above numerical results, we show that our implementation of the WYD algorithm in the CFD-ACEUN code was successful. We also established the efficiency of the reduced-order model by WYD algorithm

5.3.2 Implementation of Model Reduction Algorithms in CFD-ACEUN

Implementation of the Lanczos model reduction code.

Next, we will describe the implementation of our model reduction code into CFD-ACEUN. We modified the make file of CFD-ACEUN to accommodate the routines related to our model

118

reduction code which includes the LANZ package, and the interface between LANZ and CFD-ACEUN.In the CFD-ACEUN, the routine fldprs_fem.f will reads in the finite element model from the preprocessor, and then the routine startfem.f set up the element properties for solving the problem. Then the element consistency is checked in routine check_elements:f. After that, the routine solved.f will assemble the element stiffness matrix and element mass matrix and apply the corresponding boundary conditions, and form the global matrix and residual force. The skyline solver will be used to solve the linear algebra system. Finally, the routine cfdview_output:f will create unstructured CFD-VIEW files for postprocessors. We will add the model reduction code in the routine solved.f.

To call the model reduction code, we are adding the subprogram model_reduction inside the routine solved.f. In the subprogram model_reduction, the routine lanz_io and the routine lanz_param will prepare the necessary data of the original model for LANZ. The routine lanz_driver will then call LANZ package for calculating reduced model. All the above three routines will be put in one module file, lanz_mod:f, which plays the role of the interface between LANZ and ACEUN. Another module lanz_variable_mod:f will declare all variables used in the reduced model code, which may be combined with the ACEUN variable declaration module file later on.
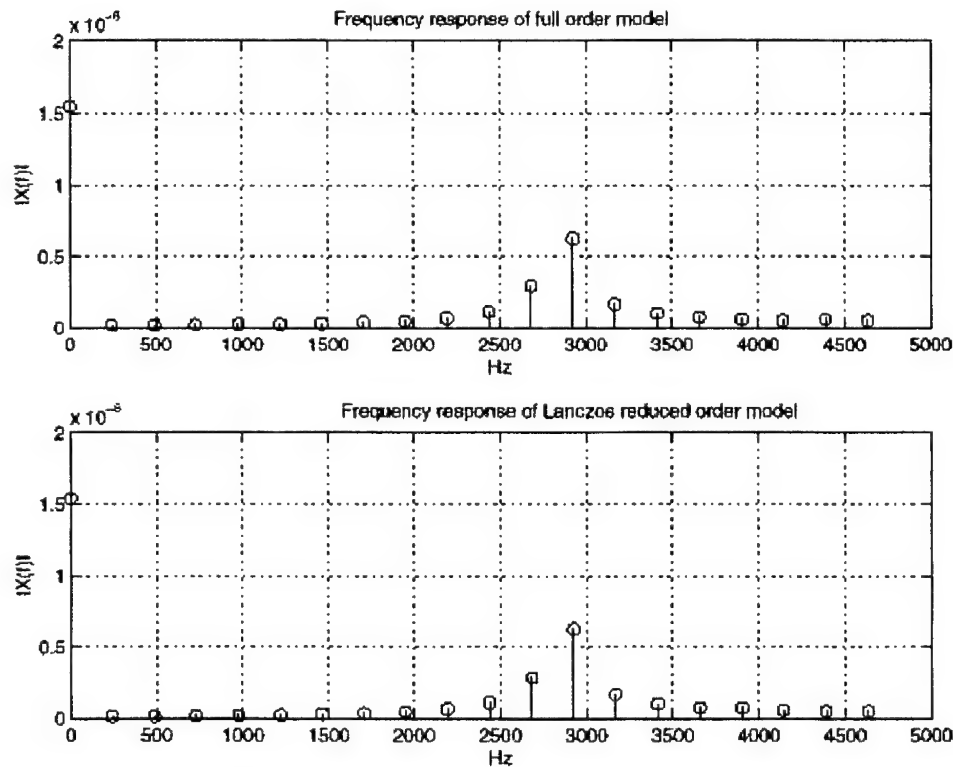
Figure 134. Frequency responses at central point from full-order model and reduced-order model (dofs = 9).

In the LANZ software package, the routine lanz.file3.f is the main subroutine for the Lanczos algorithm, which was coded by Fortran77. The routine lanz.file4.c is a C routine, which allocates and deallocates memory inside LANZ package. We have modified the LANZ in order to use

Fortran90 function ALLOCATE to allocate the arrays used in LANZ. Moreover, we have coded the routine lanz.file5.f inside the LANZ package, to obtain the reduced model, including the reduced matrices, reduced force vector, and the reduced initial conditions.

In our reduced model code, the stiffness matrix sky_k and the mass matrix sky_m, and the pointer vector ma, are read in from ACEUN. The matrices sky_k and sky_m are stored as one-dimensional arrays in ACEUN, and the vector ma points to the location of the main diagonal terms in the skyline storage. Until now the separated mass matrix sky_m , however, is not available in ACEUN. We appreciate the sky_m can be given in the updated CFD-ACEUN soon. For the convenience of testing our code, we also wish the beam element will be added in the element library of CFD-ACEUN.Once the stiffness matrix sky_k, mass matrix sky_m, the pointer vector ma, and the initial condition of the original model are delivered from ACEUN, the model reduction part in ACEUN will calculate the Lanczos vectors and the reduced model, including a symmetric tridiagonal matrix with the required reduced size and the corresponding reduced initial condition, then the dynamic response of the reduced model can be computed.
With the response of the reduced model and the calculated Lanczos vectors, the dynamic response of the original model will then be recovered. We will report the testing of the implementation of the reduced model code (Lanczos) in ACEUN.
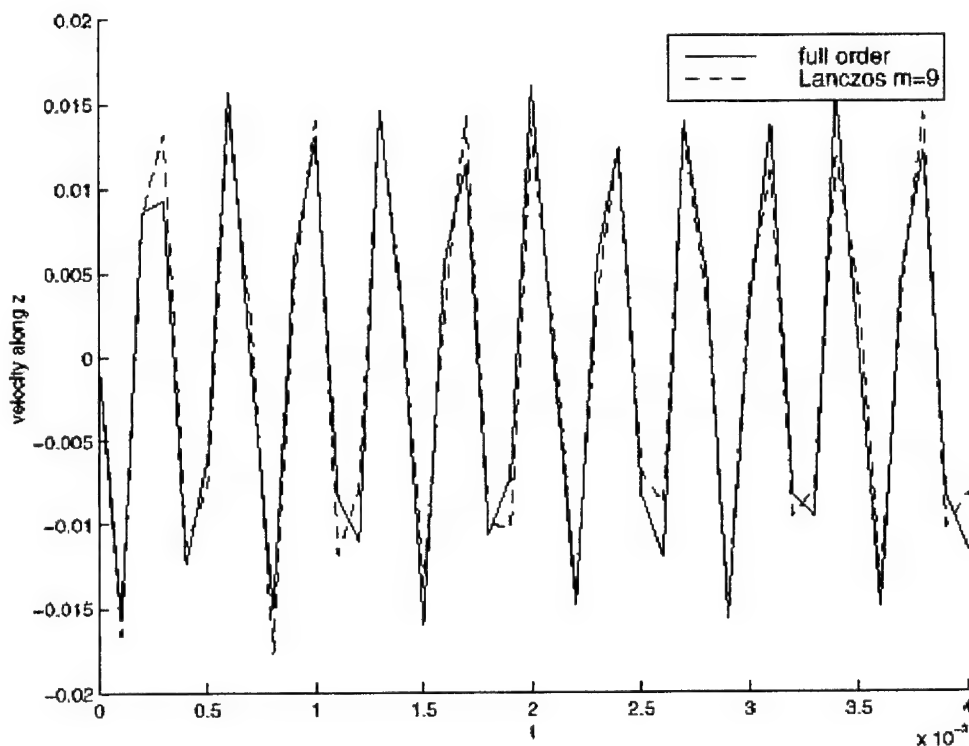
Figure 135. Step responses of velocity at central point from full-order model and reduced-order model (dofs = 9).

120

Implementation of the WYD model reduction code.

Here, we will further explain each routine in our model reduction codes. Inside the CFD-ACEUN routine solved.f, we have coded a subroutine model_reduction for generating the reduced model (WYD), which calls subroutine WYD_driver. WYD_driver is put in the module _le WYD_mod:f. In addition to the Gram-Schmidt or-thogonalization process, Inside subroutine WYD_driver, we have implemented selective reorthogonalization to ensure the linear independence among the generated WYD Ritz vectors. All variables used in the model reduction code (WYD) are put in another module file, wyd_variable_mod.f. We are describing the arguments of the above subprograms and module files as follows:

WYD_driver(reduce_active_dof, ma; sky_k,
           sky_m, WYD_vector, sky_rhs, reduce_rhs,
           reduced_k, reduced_m, ini_disp,
           ini_vel, reduce_ini_disp, reduce_ini_vel)
     reduce_active_dof : input, total equation number of the reduced model,
     ma : input, vector of the stiffness matrix,
     sky_k : input, stiffness matrix of the original structure,
     sky_m : input, mass matrix of the original structure,
     WYD_vector : output, WYD vectors for recovering the response,
     sky_rhs : input, the right hand side of the original model,
     reduce_rhs : output, spatial external force of the reduced mode,l
     reduced_k : output, stiffness matrix of the reduced model,
     reduced_m : output, mass matrix of the reduced model,
     ini_disp : initial displacement vector of the original model,
     ini_vel : input, initial velocity vector of the original model,
     reduce_ini_disp : output, initial displacement vector of the reduced model,
     reduce_ini_vel : output, initial velocity vector of the reduced model.

matrix_multip_sky(sky_index, mass, x, v)
     sky_index : input, point of vector of the skyline matrix mass,
     mass : input, mass matrix to perform multiplication wrt Ritz vectors,
     x : input, Ritz vector,
     v : output, product of mass matrix and a Ritz vector.

matrix_multip(reduced_dof, x, a, result_a)
     reduced_dof : input, total equation number of reduced model,
     x : input, matrix to perform multiplication wrt Ritz vectors,
     a : input, Ritz vector,
     v : output, product of matrix and a Ritz vector

matrix_product(reduced_dof, sky_index, a, x, redu_a)
     reduced_dof : input, total equation number of reduced model
     sky_index : input, point vector of the skyline matrix mass
     x : input, matrix to perform multiplication wrt Ritz vectors,
     a : input, Ritz vector,

redu_a : output, product of a Ritz vector, matrix and Ritz vector,

m_normal(sky_index, mass, force, n_vector)
       sky_index : input, point vector of the skyline matrix mass,
       mass : input, mass matrix a Ritz vector will be normalized to,
       force : input, a Ritz vector will be normalized,
       n_vector : output, a normalized Ritz vector.
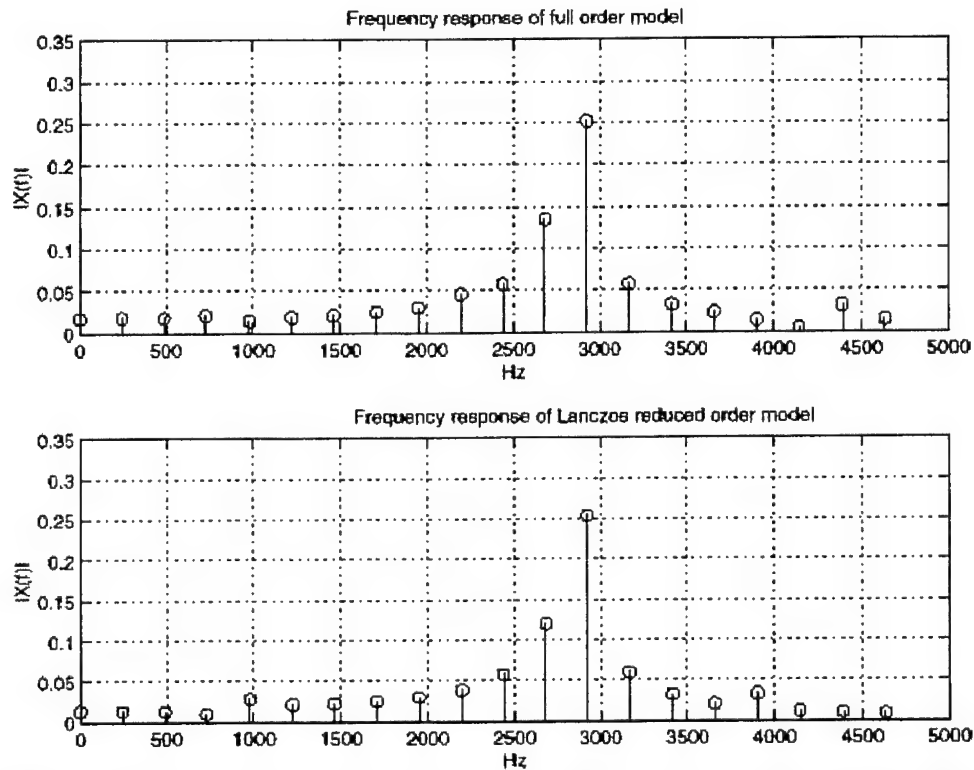
Figure 136. Frequency responses of velocity at central point from full-order model and reduced-order model (dofs = 9).
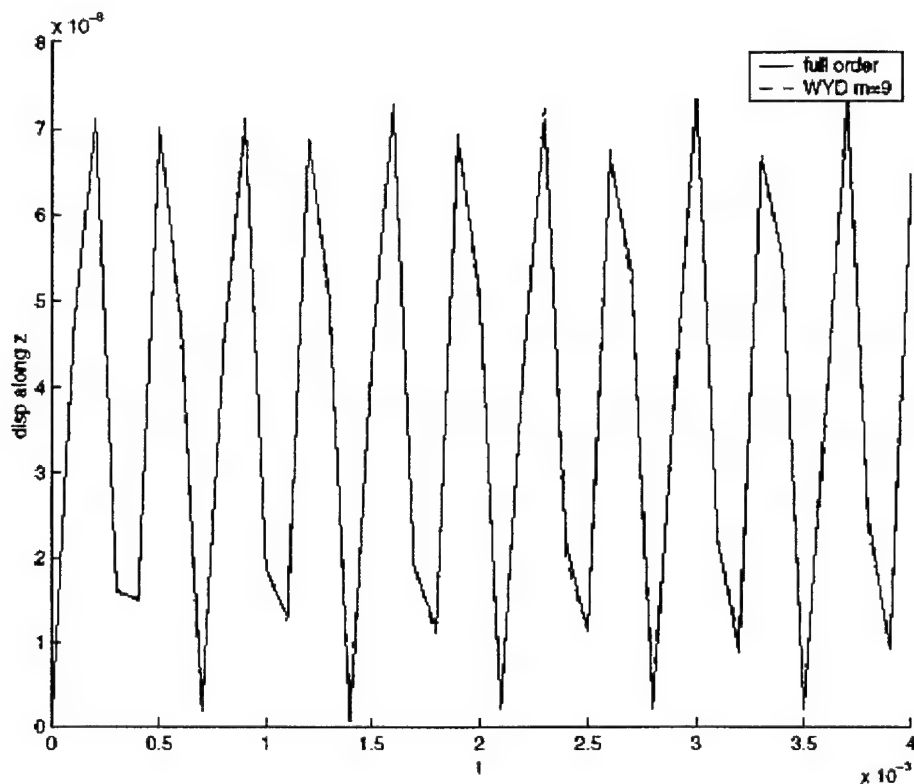
Figure 137. Step responses of displacement at central point from full-order model and reduced-order model (dofs = 9).

5.3.3 Research on the Model Reduction algorithms.

In this section, we present our study on the Lanczos Algorithm with static starting vector in Subsection 5.3.3.1. In Subsection 5.3.3.2, we describe our study on the Loss of orthogonality and reorthogonalization in WYD algorithm (see Leger [1986] and Paige [1972]). In Subsection 5.3.3.3, we test the Karhunen-Loeve decomposition model reduction method used by Hung & Senturia [1999]. Since a few full order model runs are needed to generate reduced-order model by Karhunen-Loeve decomposition, the overall computational cost is much higher than our WYD model reduction method with the same response accuracy. We also studied error estimation in the WYD algorithm based on the loading representation. The participation factors given in Table 5.3 clearly show which modes are important and which modes may be skipped by the WYD algorithm.
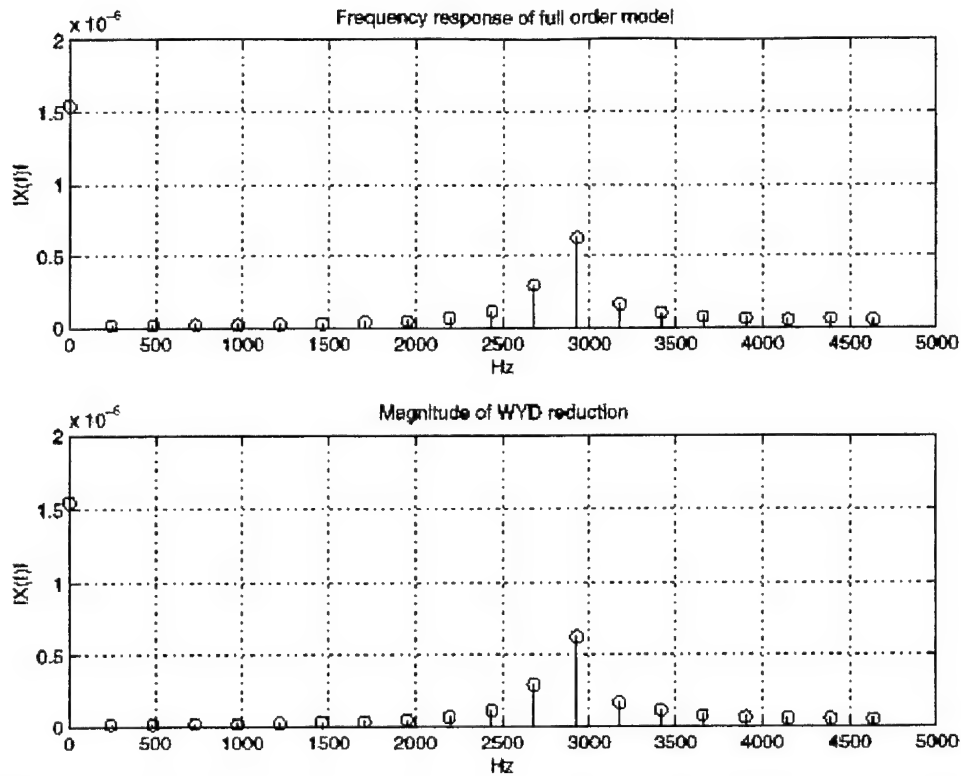
Figure 138. Frequency responses at central point form full-order model and reduced – order model (dofs = 9).

5.3.3.1 Lanczos Algorithm with Static Starting Vector

Unlike WYD method, the starting vector in the Lanczos method is usually chosen at random, ignoring the important information specific to the dynamic problem. The Lanczos method is expected to be more effective if the spatial distribution of the dynamic load is used to initiate the recurrence relationship in Lanczos vector generation process. The numerical results show the Lanczos method with static starting vector performs much better than random starting vector. We have coded it as one option when using Lanczos method in the model reduction code. Here we use the same example of the crab-leg flexure.

We still use 3-D Euler-Bernoulli beam elements to model the crab-leg exure. We use the same geometric properties and the material properties from Fedder [1994] as well. We use twenty 3-D beam elements and the total active degrees of freedom (dofs) is 78. We have two cases of reduced-order model, i.e., the number of retained degrees of freedom are nine and five. The comparison of computed eigenvalues obtained with different models (full-order and reduced-order model) is shown in Table 5.4.

If we use the random starting vector, we find that the first three of reduced-order model (dofs = 9) and two eigenvalues of reduced-order model (dofs = 5) are obtained accurately. Now we use the static solution as the starting vector, we find that the eigenmodes obtained are not necessarily the first modes in full model. For example, in the case of reduced-order model (dofs=5), the first eigenmode corresponds to the first eigenmode in the original model, the second eigenmode

124

corresponds to the sixth, the third eigenmode corresponds to the seventh eigenmode (see Table 5.4).

The comparison of the step response at the central node along the axis _from the full-order model and the reduced-order model (dofs = 9) is shown in Figure 133. Figure 134 is the frequency components of the time-domain response by Fast Fourier Transform (FFT), which shows the comparison of the corresponding frequency response from the full-order model and from the reduced-order model (dofs = 9).

From the above figures, we find that much better results are obtained with the static starting vector. It is observed when the size of the reduced-order model is 5, the responses in both time domain and frequency domain already agree very well, comparing to the full-order model. The Lanczos method with static solution as the starting vector is much better than with random starting vector. It is because the eigenmodes picked here in Lanczos method are the most important modes for dynamic response, not the first modes of the original model. Therefore, we strongly recommend to use Lanczos method with the static starting vector.

On the other hand, Lanczos method can achieve the same good results as WYD method, but with numerically a more efficient reduced model, i.e., a symmetric tridiagonal matrix T_r with the reduced size:

$$T_r \ddot{Y} + IY = f_r \qquad (5.2)$$

In WYD method, we obtained a full symmetric matrix Kr with the reduced size in the reduced model:

$$I\ddot{Y} + K_r Y = f_r \qquad (5.3)$$

where I is the identity matrix with reduced size. Obviously, Eq. (5.2) will be solved more quickly than Eq. (5.3).
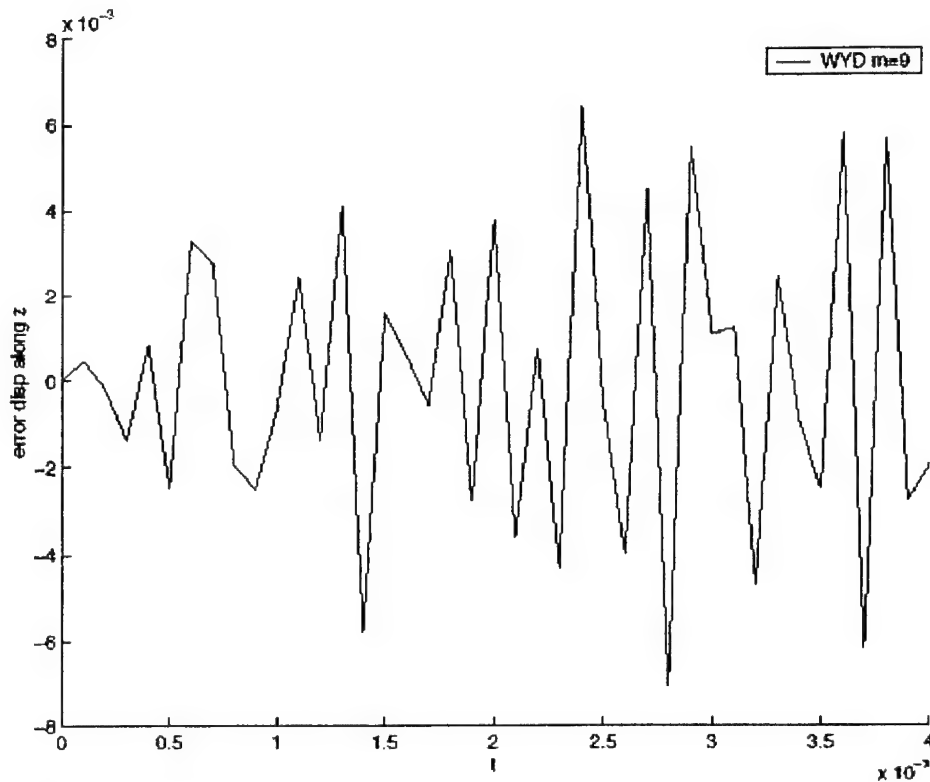
Figure 139. Relative step response error of displacement at central point bewteen full-order model and reduced-order model (dofs = 9).

5.3.3.2 Loss of Orthogonality and Reorthogonalization in WYD Algorithm

The selective reorthogonalization is used to maintain the necessary orthogonality among the trial vectors in WYD method. In this subsection, we will show that random starting vector is better than the static solution as starting vector in terms of orthogonality among the trial vectors. Loss of orthogonality happens until the spectral content of the starting vector is exhausted if we use random starting vector, and we can obtain a set of independent vectors which has the same number as the original order in the iterative process even without reorthogonalization. Instead of using random starting vector, if we use static solution as starting vector, the loss of orthogonality will happen when the number of generated WYD vectors is greater than half of the number of the original order without reorthogonalization. Even with reorthogonalization, the independency of generated WYD vectors is sensitive with respect to the reorthogonal tolerance.

We still use 3-D Euler-Bernoulli beam elements to model the crab-leg flexure. We use the same geometric properties and the material properties from Fedder[1994] as well. We use twenty 3-D beam elements and the total active degrees of freedom (dofs) is 78. If we use random starting vector the vector basis can be generated even without reorthogonalization until the spectral content of the starting vector is exhausted. The reduced number of dofs can keep going to the number of 72 without reorthogonalization. If we use static solution as starting vector, loss of orthogonality will happen when the number of generated WYD vectors is greater than 60 without reorthogonalization. After reorthogonalization, the number of independent WYD vectors can increase to 74.

126

Figure 140 shows the global orthogonality obtained for different starting vector without reorthogonalization from the original WYD algorithm in our code. It clearly shows that random starting vector will not loss orthogonality among trial vectors till the end of the generation process.

A random starting vector is usually chosen hoping that all required eigenvectors will be represented. Another observation is loss of orthogonality still may happen even after a few number of reorthogonalization iterations. That means we do not give a small enough tolerance as orthogonal criteria. This can be solved if we decrease the tolerance, from 1.0E-16 to 1.0E-20, for instance. However, it will cost more computational effort. Figure 141 shows the global orthogonality obtained for static solution as starting vector before and after reorthogonalization from the original WYD algorithm in our code. It shows that even after reorthogonalization it still may lose orthogonality among trial vectors in the end of generation process.

Our results show that random starting vector is good to generate almost the full set of WYD vector basis even without reorthogonalization. Therefore to study the sensitivity of the orthogonal degree among the generated WYD vectors with respect to the orthogonal tolerance, we use static solution as starting vector.

In Figure 142, we compared the relationship between number of iterations and the number of WYD vectors for different tolerance.

Our result shows that to generate a set of well independent WYD vectors, we need to be very careful in choosing the tolerance. If the tolerance is not small enough, the generated vectors will not be exactly independent (here not exactly independent means not independent enough to ensure the following WYD vectors being generated to be orthogonal with respect to vectors already been generated). Although it still can keep a satisfactory degree of orthogonality for generating a few number of WYD vectors, it will cost more computational effort if we want to generate more independent WYD vectors. The number of reorthogonal iterations will have a great increase in order to make the vector being generated orthogonal with respect to the previous generated vectors. On the other hand, if the tolerance is too small, it will obviously increase the number of reorthogonal iterations. For the crab-leg model Figure 142 shows that there is an optimal tolerance value TOL=1.0E-20 because of its less overall computational effort (less number of reorthogonal iterations). In our WYD model reduction code, we leave this as an option for users.
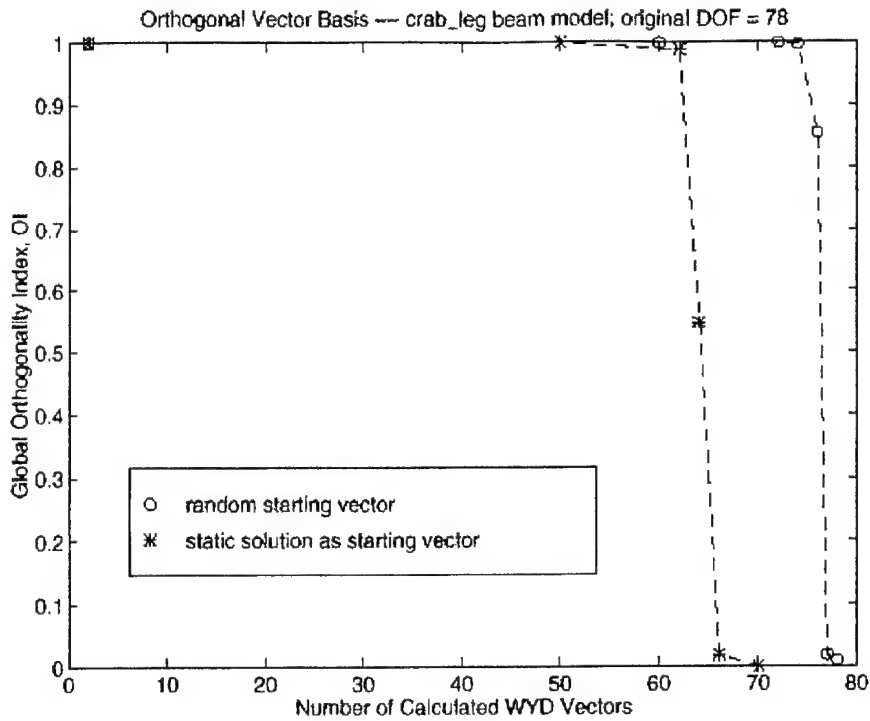
Figure 140. The global orthogonality level maintained by the original WYD algorithm for different starting vectors.
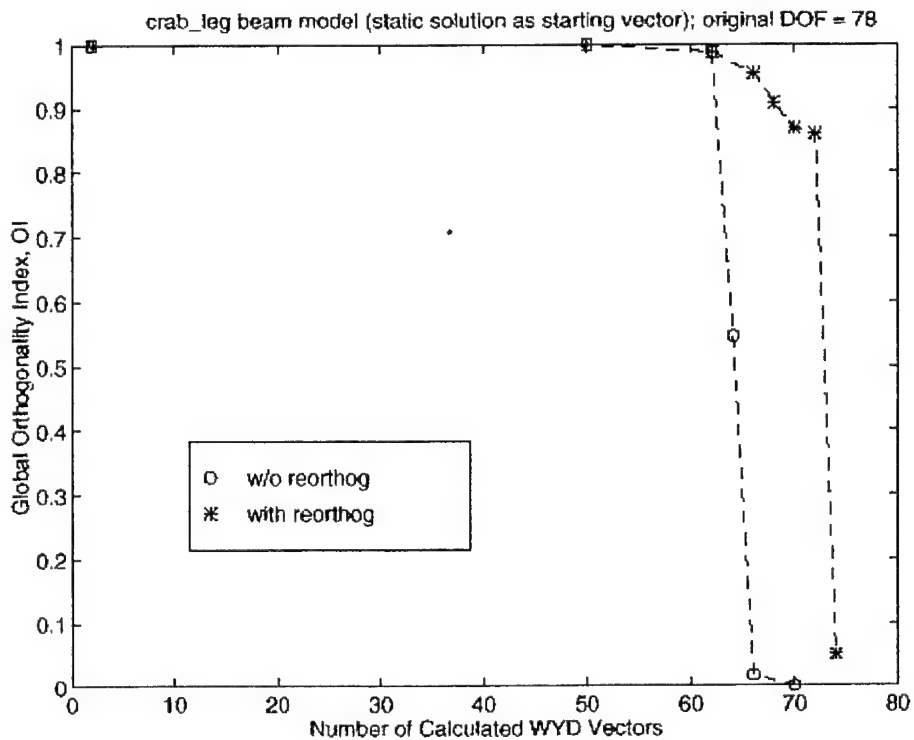
Figure 141. The global orthogonality level maintained by the original WYD algorithm for static solution as starting vector.
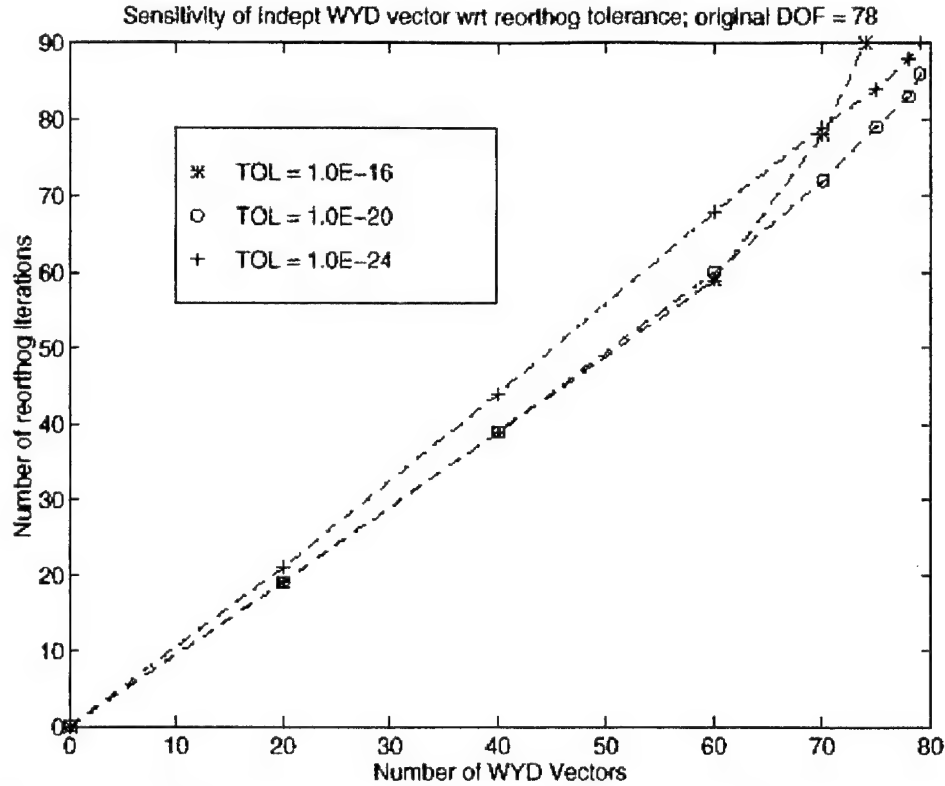
Figure 142. Sensitivity of independent WYD vector with respect to reorthogonal tolerance.

Table 5.3. Step response of the 3-D elastic beam microstructure. Comparison of eigenvalues from full-order model to reduced-order model.

mode	full-order (dofs = 126)	WYD (dofs = 9)	participation factor
1	1.7804×10^{11}	1.7804×10^{11}	8.0253×10^{-2}
2	3.5952×10^{11}	3.5952×10^{11}	1.2343×10^{-3}
3	5.8118×10^{11}	5.8118×10^{11}	1.2691×10^{-3}
4	1.3904×10^{12}	1.3985×10^{12}	3.3280×10^{-3}
5	1.4515×10^{12}	2.5351×10^{12}	3.6649×10^{-2}
6	2.5810×10^{12}	2.9967×10^{12}	4.5030×10^{-2}
7	3.2409×10^{12}	3.6242×10^{12}	3.0055×10^{-2}
8	4.7345×10^{12}	1.1441×10^{12}	6.7828×10^{-2}
9	7.9633×10^{12}	5.1978×10^{12}	4.4975×10^{-2}

mode	full-order (dofs = 126)	WYD (dofs = 16)	participation factor
1	1.7804×10^{11}	1.7804×10^{11}	8.0253×10^{-2}
2	3.5952×10^{11}	3.5952×10^{11}	1.2343×10^{-3}
3	5.8118×10^{11}	5.8118×10^{11}	1.2691×10^{-3}
4	1.3904×10^{12}	1.3904×10^{12}	2.9693×10^{-3}
5	1.4515×10^{12}	1.4515×10^{12}	1.6031×10^{-3}
6	2.5810×10^{12}	2.5810×10^{12}	4.2774×10^{-2}

129

7	3.2409×10^{12}	3.2409×10^{12}	4.8759×10^{-2}
8	4.7345×10^{12}	4.7345×10^{12}	2.1281×10^{-3}
9	7.9633×10^{12}	7.9635×10^{12}	2.2695×10^{-2}
10	8.7063×10^{12}	8.7222×10^{12}	5.7315×10^{-3}
11	1.2039×10^{13}	1.2041×10^{13}	6.4250×10^{-2}
12	1.4504×10^{13}	1.5566×10^{13}	6.1548×10^{-3}
13	1.8232×10^{13}	2.6336×10^{13}	1.6704×10^{-2}
14	2.5171×10^{13}	3.8518×10^{13}	2.7047×10^{-2}
15	2.7105×10^{13}	1.2596×10^{13}	2.3274×10^{-2}
16	3.2016×10^{13}	6.3128×10^{13}	5.9028×10^{-2}

Table 5.4 Step response of the crab-leg flexure. Comparison of eigenvalues form full-order model to reduced-order model.

mode	full-order (dofs = 78)	WYD (dofs = 9)	reduced-order (dofs = 5)
1	1.3869×10^{9}	1.3869×10^{9}	1.3869×10^{9}
2	4.6851×109	4.6848×10^{9}	9.8316×10^{9}
3	5.3343×10^{9}	9.8316×10^{9}	1.7985×10^{10}
4	8.1038×10^{9}	1.7985×10^{10}	8.1502×10^{10}
5	9.1761×10^{9}	8.1501×10^{10}	7.5029×10^{10}
6	9.8316×10^{9}	3.3673×10^{11}	
7	1.7985×10^{10}	6.0128×10^{11}	
8	1.9378×10^{10}	1.0280×10^{12}	
9	2.4627×10^{10}	1.4154×10^{12}	

5.3.3.3 Comparison of WYD Algorithm and Kahrunen-Loeve Decomposition

Karhunen-Loeve (KL) decompositions were originally used to generate basis functions for turbulence problems in fluid mechanics, fluid structure interactions in aerodynamical systems, and in chemical engineering systems. KL procedure uses the so-called snapshot method, where the problem of obtaining eigenmodes of a large system reduces to solving eigenmodes of matrices of order of only 100. Second, the method always produces real, optimal modes regardless of the damping characteristics of the system under consideration. Third, the method is a direct response approach that does not require a dynamic model describing the system. In this section, we present some test results using the MEMS microstructure by KL decomposition. Our simulation procedure using MATLAB is as follows:

- Construct the state space form of the full-order dynamic model.
- Run a few time steps to sample the state variables at a series of different times.
- Do single value decomposition for the state matrix consists of selected state vectors.
- Pick up basis vectors as Ritz vectors to construct reduced order model.

The comparison of the relative response error of displacement and velocity at the central node along the axis ξ_3 from the WYD algorithm and the Karhunen-Loeve decomposition is shown in Figure 139 - Figure 144. Table 5.5 shows the comparison of computime for generating the reduced order model using WYD algorithm and Karhunen-Loeve decomposition. It was clearly

shown that with the same order of response accuracy, Karhunen-Loeve decomposition has a much higher computational cost than WYD algorithm.

Table 5.5. Step response of the 3-D elastic beam microstructure. Comparion of CPU time for generating the reduced-order model with different algorithms.

Reduced-order (dofs)	Run time of WYD (sec)	Run time of KL (sec)
9	0.12	22.6
18	0.30	23.1
36	0.77	22.8
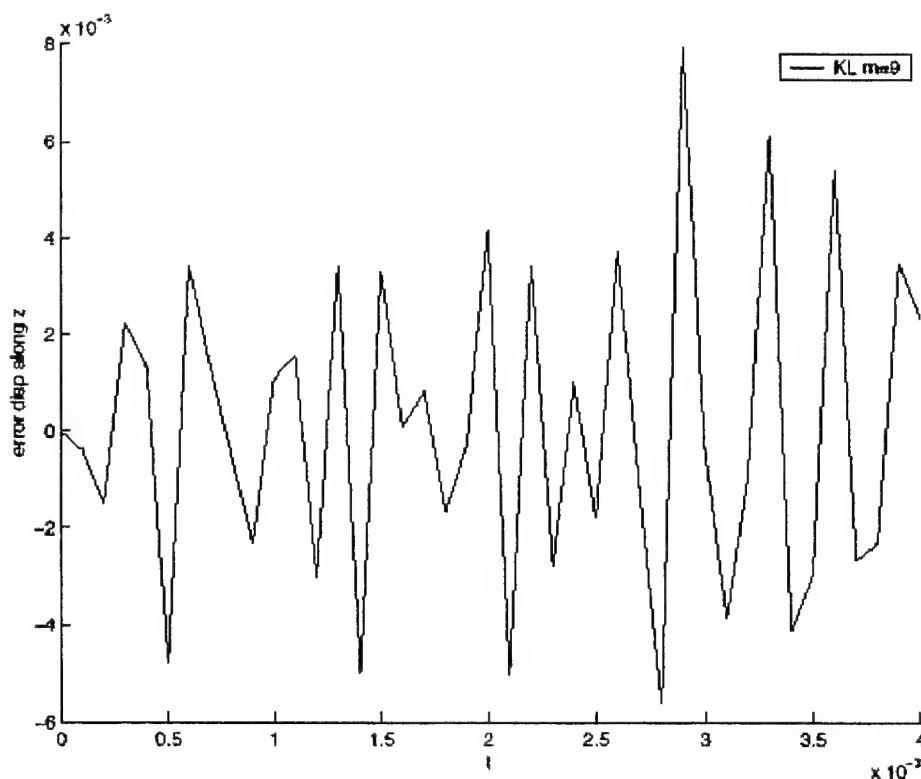
Figure 143. Relative step response of error of displacement at central point between full-order model and reduced-order model (dofs = 9).
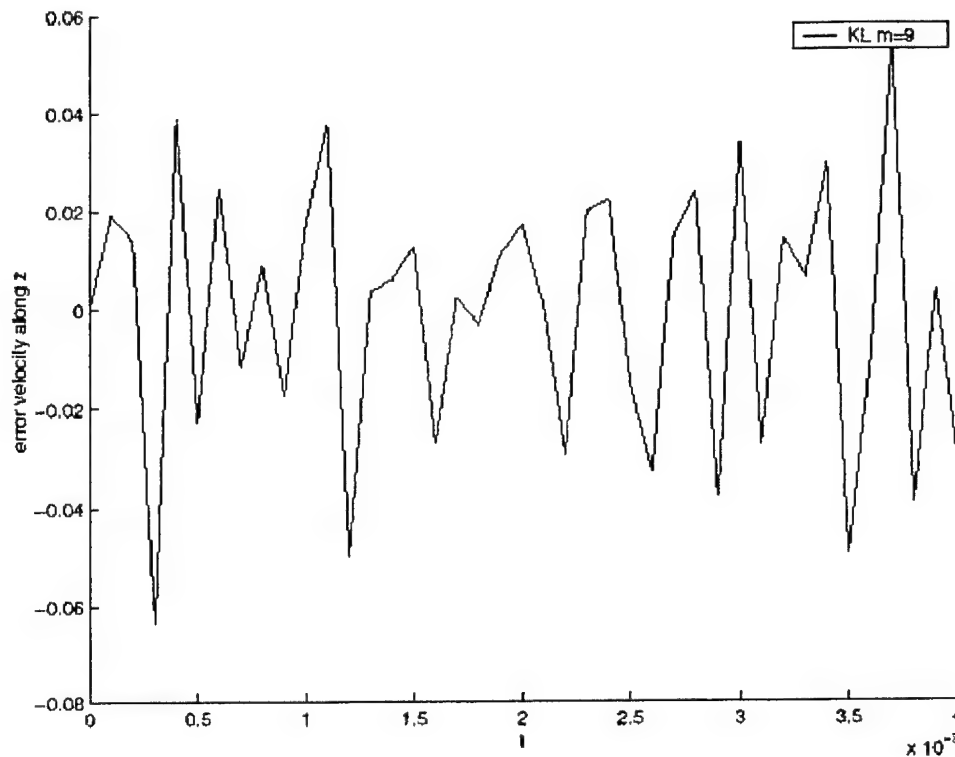
Figure 144. Relative step response error of velocity at central point between full-order model and reduced-order model (dofs = 9).

5.4 Implementation of MIT Model Reduction Procedure

In the frame of this project, we have also implemented at CFDRC the procedures of FEM model reduction based on **Arnoldi method** for electro-mechanical microdevices, developed at **Prof. Jacob White's group at MIT** within the Composite CAD Program. The codes have been implemented and installed at CFDRC and coupled with CFD-ACE+ code by Deepak Ramaswamy, PhD student from MIT, during his summer internship at CFDRC in Huntsville in August-September 2000. The new Arnoldi-based model reduction procedures were demonstrated and tested in coupling with CFD-ACE+ code.

The Model Reduction (MR) Procedure steps are:

1. Build a full 3-D FEM model of the electro-mechanical structure.

2. Perform one steady-state coupled-domain simulation (structures + electrostatics) with the full FEM model, for the applied bias Vo, using CFD-ACE+ and Femstress.

3. The MR procedure extracts M and a (partly implicitly) linearized K matrices from the full FEM solution, at the applied bias Vo. K and M are not required explicitly, only their product with arbitrary vectors.

132

4. The MR procedure uses Arnoldi Method to reduce K and M to smaller matrices K' and M'. If n is the order of the reduced model, i.e. K' is (n x n) and M' is (n x n), the reduced ODE system matches exactly n moments of the full problem.

5. Use Matlab, or similar matrix solver, to solve the reduced system to obtain quickly a frequency characteristic or time-domain (transient) response.

This process has to be repeated for any new bias point (voltage Vo).

INPUT for the MR Procedure (to be provided by user):
- name(s) of the surface(s) in the FEM model where the voltage is applied;
- node number of which position/displacement is of interest as a result;
- defined direction (x, y, z) of the node displacement of interest;
- order of the reduced matrices.

OUTPUT from the MR Procedure:
- the reduced matrices in the input format (.in file) ready for Matlab solution;
- sample Matlab scripts (.m files) to obtain frequency characteristic or transient response.

The above procedure was demonstrated and tested on the example of a MEMS beam actuated electrostatically (Figure 145). A full FEM model was build using CFD-Micromesh software from a layout. CFD-ACE+ (Femstress) was used as a coupled electrostatic-stress solver for the full FEM model.
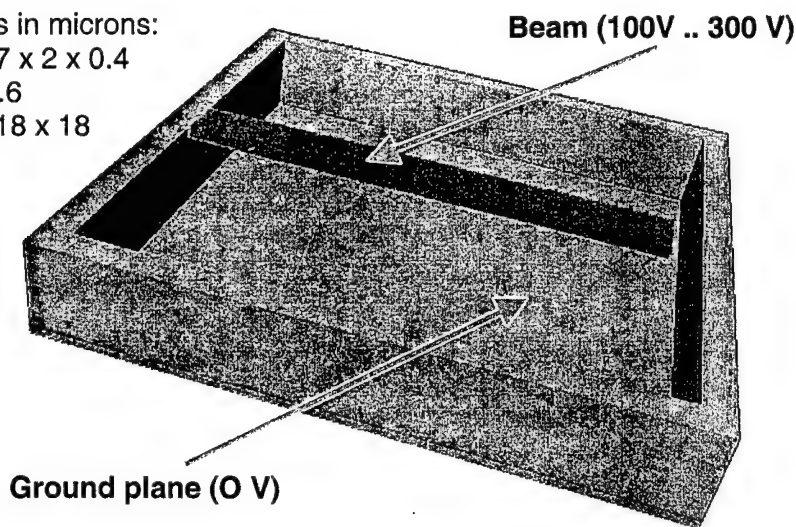
Figure 145. A coupled electromechanical system used as an example for the model reduction demonstration with the Arnoldi method.

Reduced Model vs. Full Model:
- full FEM model order: 954 DOFs
- reduced model order: 10 DOFs
- CPU time **acceleration** for transient simulations: **1 million times faster per time step!**

Figure 146 shows frequency-domain characteristics of the electrostatically actuated beam, calculated with different methods: full FEM non-linear transient simulation (stars in the plot), linearized modal analysis in CFD-ACE+ (full line), and the Arnoldi reduced model (circles).
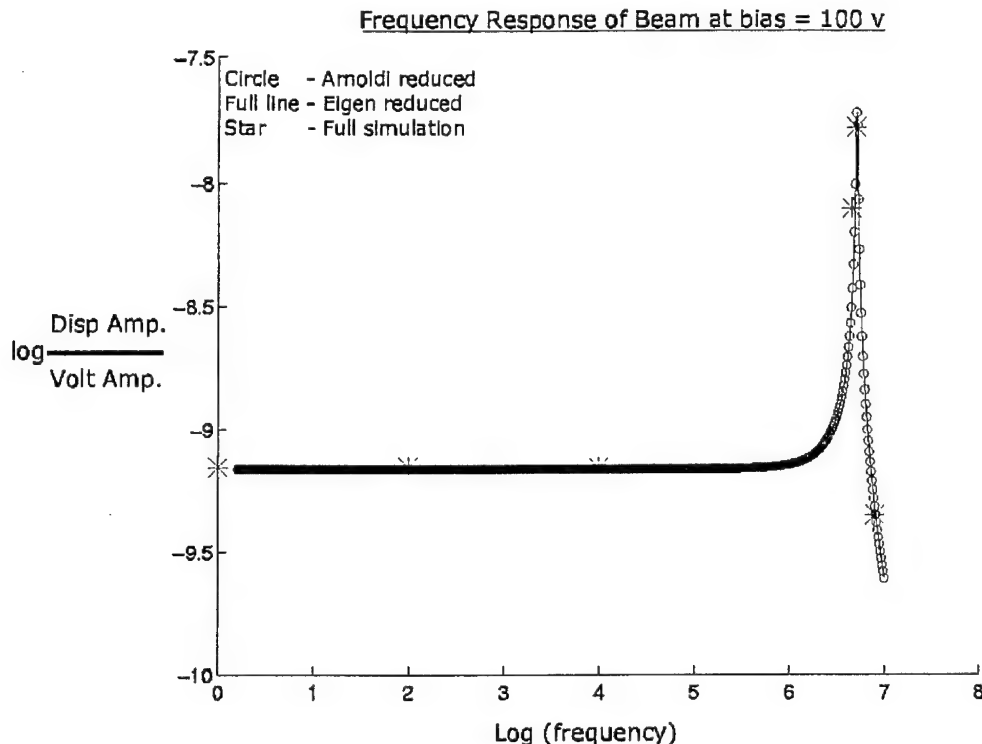
Figure 146. Frequency response of the MEMS beam calculated with different methods.

As it can be seen in this figure, all the characteristics match very well. On the other hand, the use of the reduced model in a transient simulation of the MEMS device (for example, with Matlab) may decrease the computation time by a factor of 1 million per one time step! This is very promising for system-level simulations of large MEMS circuits.

6   CONCLUSIONS AND RECOMMENDATIONS

6.1   Conclusions from the Project

This report has presented the current status and results of the DARPA BAA 97-17 project aimed at developing, demonstration, and validation of new concepts of reduced/compact models of electro-mechanical, fluidic, and thermal phenomena in MEMS, as well as at development of new Software System (in CFD-ACE+) for Automated Generation of Reduced or Compact Models of Microdevices from High Fidelity 3-D Simulations. All of the objectives of the project were met successfully. Many new reduced model concept have been developed and validated, both

134

through comparison with high-fidelity simulations and experimentally. New model generation procedures have been proposed, implemented, and tested. New reduced models have been demonstrated in output formats compatible with system-level simulators like SPICE or Saber/MAST. The air damping compact models resulting from this project have been included into NODAS library from CMU for the MEMS system-level design.

Several new interfaces and import/export procedures for CAD/EDA standards have been added to CFD-ACE+ software package, to enable easy and automatic building of 3-D models from EDA layouts and process data. The CFD-ACE+ solver itself has been extended and improved for reliable high-fidelity simulations of coupled physical phenomena specific for microdevices. New algorithms and tools have been implemented in CFD-ACE+ to enable the use of reduced or mixed dimensionality in 1D, 2D, or 3-D simulations of MEMS devices and systems.

The major achievements of the program have already been outlined before, and are presented below in brief:

New Reduced/Compact Models of Microdevices

- New nonlinear compact models of squeeze film damping in MEMS, validated with CFD-ACE+ 3-D simulations, and implemented in SPICE and SABER formats, and implemented in NODAS MEMS-CAD system at CMU.
- The new compact squeeze film model was successfully compared with experimental data from a CMOS-MEMS bandpass filter. The NODAS simulation results with the new damping model are in excellent agreement with the measurements.
- New compact model of lateral (shear) damping in MEMS, validated with CFD-ACE+.
- Developed mixed-dimensional and reduced fluidic models of microchannels, microvalves, micropumps, droplet generators, synthetic jets, and piezoelectric micropump.
- Novel concept of compact models for synthetic jets, using a polyhedral control volume capability of CFD-ACE+. The model was validated against 3-D high-fidelity simulation data obtained for a range of parameters.
- New equivalent-circuit models, in SPICE and SABER formats, for arbitrary-shaped fluidic microchannels, and procedures of their generation.
- New Matrix Reduction Techniques for structure dynamics: Lanczos method and WYD Ritz algorithm, developed at UF. Tests showed up to 10,000x acceleration in comparison to full 3-D FEM computation time.

Interfaces And Import/Export Procedures for CAD/EDA Standards, To Enable Easy And Automatic Building of 3-D Models from EDA Layouts And Process Data

- Enhancement of CFDRC software to process CAD data for MEMS design. We are now able to read input files in the formats: **DXF**, IGES, PATRAN, CIF, GDSII, and several others.
- Two new data formats, **CIF** and **GDSII**, have been implemented in CFD-GEOM, enabling input and conversion from external files coming from EDA tools.
- Implementation of **VRML** (Virtual Reality Modeling Language) into the computational environment of CFDRC.

- A new software, **CFD-Micromesh**, for automatic 3-D solid model generation and meshing from MEMS layouts imported directly from CAD/EDA systems. The CIF and GDSII layout files are imported easily into CFD-Micromesh, allowing coupling the software with several commercial IC design tools. The new tool is very fast and equipped with user-friendly graphical user interface. By clicking only a single button in CFD-Micromesh, a three-dimensional solid model is generated fully automatically from layout. Building the 3-D model as well as automatic generation of a full 3-D unstructured computational mesh, again only by clicking a single button in CFD-Micromesh, is performed typically within several minutes on a current PC workstation. The automatically generated three-dimensional device model, with the unstructured 3-D computational mesh in DTF format, is imported directly into CFDRC's simulator CFD-ACE+.
- Developed interfaces between CFDRC software and **Cadence** design tools.
- A new data format (called GBV – Geometry, Boundary and Volume conditions) for interchange of simulation data between Cadence Design Framework II schematic view and CFDRC ACE+ simulator has been developed at CMU.

New Features in CFD-ACE+ for High-Fidelity Simulations Specific for MEMS

- Second order boundary conditions for wall treatment.
- Second order time treatment, through modified Crank-Nicolson scheme.
- Automatic grid remeshing for arbitrary moving boundaries/bodies in 6 degrees of freedom (DOFs). A trans-finite interpolation (TFI) technique with mesh smoothing was developed and implemented, which allows for effective simulation of dynamic 3-D motion of mirrors, membranes, gyroscopes, and other MEMS structures.
- New capability in CFD-ACE+ for extraction lumped parameters (normal/tangential force, torque, total pressure and/or flow) for compact model generation.
- "Property Manager" - new interactive framework software for MEMS material property database.

Procedures And User-Friendly Interfaces For Extraction Of Compact-Model Parameters and Characteristics From High-Fidelity Simulations

- Capability to perform parametric runs in CFD-ACE+ through graphical user interface, for mechanical, electrostatic, and fluidic simulations, both steady-state and transient.
- A dedicated computer program Squeeze, written in portable C++ language, for automatic generation of input list in SABER or SPICE format, describing equivalent-circuit model of squeeze-film damping between moving plates.
- Procedures for automatic generation of compact model (extraction of lumped capacitances) of a comb-drive resonator, using results of high-fidelity 3-D electrostatic simulations with FastBEM from CFDRC.
- Procedures for automatic generation of equivalent-circuit models of microfluidic devices from parametric runs of CFD-ACE+; examples of SPICE and SABER compact models of Tesla valve.
- Procedures of FEM model reduction based on Arnoldi method for electro-mechanical microdevices, developed at Prof. Jacob White's group at MIT, have been implemented and installed at CFDRC and demonstrated and tested in coupling with CFD-ACE+ code.

Libraries Of Reduced Models for MEMS CAD System-Level Tools

- The new compact models of squeeze film damping have been incorporated into the NODAS MEMS-CAD system library from CMU.
- The new compact models of lateral shear damping have also been inserted into the NODAS MEMS-CAD system library.
- The frequency dependent transfer function of lateral damping has been implemented in Verilog-A as a Laplace transform and used in NODAS.

Validation/Demonstration of the New CFD-ACE+ Features and the New Reduced Models

- At Georgia Tech (GT):
  - Fabricated micromachined synthetic jets with integrated MEMS modulators.
  - Several methods have been used to test the synthetic jets and modulator arrays: visual deflection test, flow modulation test, Schlieren visualization, pitot tube, x-wire anemometer, and particle image velocimetry (PIV).
  - Characteristics of performance of arrays of synthetic jets in local active control of microsystem temperature were measured with infra-red (IR) camera.

- The PIV flow data from GT were compared successfully with 2D and 3-D numerical simulations from CFD-ACE+.

- The temperature-system data measured at GT with IR camera were compared successfully with numerical simulations at CFDRC, including the use of reduced models in jet arrays.

- At University of Florida (UF):
  - Validation of the implementation of Lanczos algorithm through comparison with a MEMS structure from MIT.

- At Carnegie Mellon University (CMU):
  - Experimentally verified the squeeze film model using a three resonator CMOS micromachined mechanical filter to show that the improved squeeze film model reduced error in quality factor (Q) computation from 20% to 2%.
  - Experimentally verified the lateral damping model using folded flexure MUMPS resonators. Inclusion of finite size effects reduced errors from 20% to 8%.

- At CFDRC, both the high-fidelity 3-D CFD simulations of Tesla valve and its compact models in SPICE and Saber were successfully compared with characteristics measured at University of Washington.

The mixed-dimensionality, multi-energy domain capability in CFD-ACE+ is the first ever computational software applicable to both micro-scale, system-scale, and mixed micro/system-scale simulations. The macro-scale (package, board) allows the user to verify the performance of the microdevice (sensor, transducer, actuator, power device, optoelectronic array) in an external system or environment.

6.2   Commercial Effects of the Project

6.2.1   "Success Stories"

- CFDRC has been awarded a new SBIR contract in 2000, for *U.S. Air Force (AFRL/VSSE)*, to develop new "High Speed Inertial MEMS Sensors with Field Emitter Array Readout" for application in novel gyroscopes for satellite and vehicle positioning, etc.

- CFDRC's High-Fidelity and Compact Models of Ink-Jets used by *Kodak*.

- Reduced Models of Synthetic Jets used for Virtual Flight Control Simulation.

- Air-Damping Compact Models under development for *Lucent Technologies*, for analysis and design of MEMS-based micromirrors for fast optical switching.

- Reduced Models of Synthetic Jets will be used within the DARPA HERETIC Program (Heat Removal by Thermo-Integrated Circuits), where CFDRC will support modeling and design of Arrays of Synthetic Microjets for active cooling of:
  - VCSEL Arrays (Linear and 2D)   *Georgia Tech + Honeywell*
  - Microprocessor Chips   -   *Georgia Tech + Intel.*

- Air-Damping Compact Models used by *Delphi Automotive Systems*.

The last point is presented below in more detail.

Air-Damping Compact Models used by *Delphi Automotive Systems*

Compact models of air damping for MEMS devices, developed by CFDRC under DARPA funding within the Composite CAD Program, appeared very helpful in the analysis process of accelerometers for air-bag deployment systems, being developed by Delphi Automotive Systems. The squeeze-film compact models allow to model the system using Saber simulator.

- A compact model of squeeze-film damping effects acting on accelerometer moving plate was developed in Saber (MAST) format, using three-dimensional CFD-ACE+ simulations in frequency domain for parameter extraction.
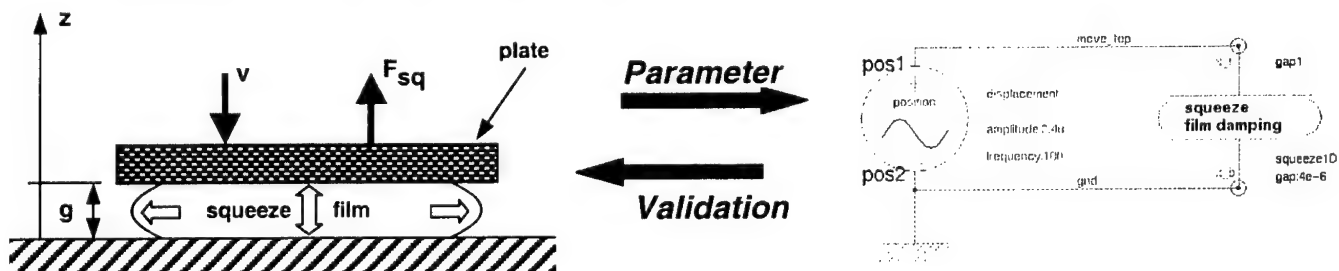
- For the model validation, a wider range of operating conditions (for instance, larger amplitudes, etc.) has been applied, and the results obtained in Saber using the compact model were compared to results of three-dimensional simulations of CFD-ACE+.

3-D Simulation - CFD-ACE+   System-level simulation - SABER

Squeeze Force (bottom)

Legend:
- Squeeze Force
- Displacement
- Velocity (arb. units)
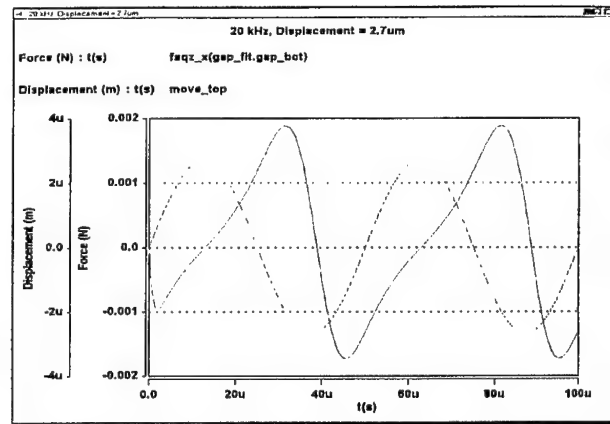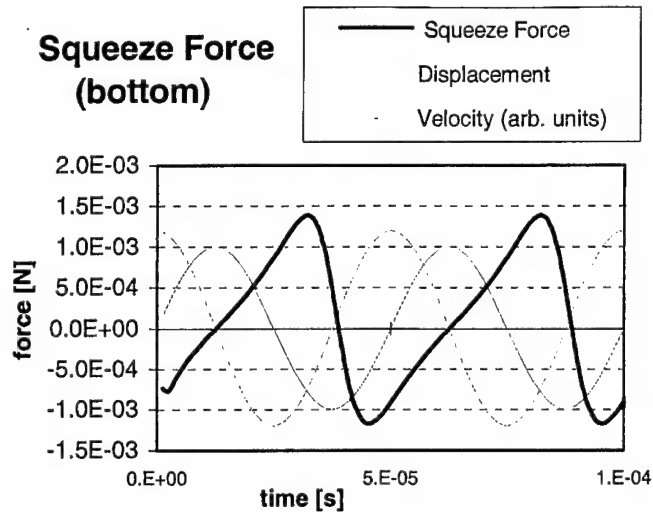
- The reduced model of squeeze-film damping appeared to be very helpful, both for Delphi and CFDRC, in understanding some physical phenomena involved, and in the analysis of the accelerometer structure behavior.

Success of CFDRC in Air Damping Modeling and Analysis in MEMS

As a result of CFDRC activities in this project, and resulting publications and presentations, CFDRC was approached by numerous commercial and academic institutions, both from USA and international, which expressed an interest in methods and tools for modeling the air damping phenomena in MEMS. It appears that thanks to this program **CFDRC has become the definite world leader in capabilities of viscous damping modeling in MEMS**, both in terms of high-fidelity flow modeling as well as in the generation and validation of reduced/compact models.

Institutions, which approached CFDRC with interest in Air Damping modeling and analysis in MEMS, including Compact Models, are as follows:

	Name	Institution
U.S.		
1.	Arjun Selvakumar	Input/Output, Inc., USA
2.	Bill Grande	Kodak Research Labs, Rochester, NY, USA
3.	Brady Davies	Kistler Instrument Corporation, USA
4.	Calvin Adkins	Harris Corporation, Melbourne, FL, USA
5.	Clarence Chui	Iridigm Display, San Francisco, CA, USA
6.	Dan Koch	Motorola, Semiconductor Products Sector, USA
7.	David Rich	Delphi Automotive Systems, Sensor Design, Kokomo, IN, USA
8.	Dick Nelson	MCC, Austin, TX, USA
9.	Edward Chan	Bell Labs, Lucent Technologies, NJ, USA
10.	Edward S. Kolesar	Texas Christian University, Dept of Eng., Fort Worth, TX, USA

11.	Heinz Busta	Sarnoff Corp., Princeton, NJ, USA
12.	Jason Tauscher	Silicon Designs, Inc., USA
13.	Joe Seeger	UC Berkeley, EECS Department, CA, USA
14.	Kamil Ekinci	Condensed Matter Physics, CalTech, Pasadena, CA, USA
15.	Kophu Chiang	Tellium, Inc., Oceanport, NJ, USA
16.	Richard Johansen	Rensselaer Polytechnic Institute, Troy, NY, USA
17.	Robert Conant	UC Berkeley, CA, USA
18.	Robert S. Okojie	Ford Microelectronics, Colorado Springs, CO, USA
19.	Sitaraman V. Iyer	ECE Dept, Carnegie Mellon University, Pittsburgh, PA, USA

International

20.	Cho NamKyu	Korea Electronics Technology Institute, Korea
21.	Eskild R. Westby	SensoNorasa, Norway
22.	George Raicevich	National Acoustic Laboratories, Chatswood, NSW, Australia
23.	Karsten Funk	Robert Bosch GmbH, Germany
24.	Kazuyuki Minami	Dept of Mechatronics and Precision Eng., Tohoku Univ., Sendai, Japan
25.	Matthias Maute	Sensortechnologiezentrum, Robert Bosch GmbH, Reutlingen, Germany
26.	Patrick Aldebert	SUPELEC, Service des Mesures, Gif/Yvette, France
27.	Peter Frere	LucasVarity Automotive Tech. Centre (part of TRW Automotive), UK
28.	Rose Zhang	Photonics Mat. & Proc., National Optics Institute, Que, Canada
29.	Roumiana Paneva	X-FAB GmbH, Erfurt, Germany
30.	Roy Knechtel	X-FAB GmbH, Erfurt, Germany
31.	Sangwoo Lee	Seoul National University, EE Dept, Korea
32.	Shawn Taylor	Virtual Science Limited, West Sussex, UK
33.	Tiansheng Zhou	Alberta Microelectronic Corporation, Edmonton, Alberta, Canada
34.	Youngho Kim	Hanyang University, Seoul, Korea

CFD-Micromesh: Fast 3-D Model Builder from Layouts

The new CFD-Micromesh software, developed during this project, for automatic 3-D solid model generation and meshing from electronic and MEMS layouts, has a **very big and promising commercial potential**. The popular layout description formats, CIF and GDSII, are imported easily into CFD-Micromesh, allowing coupling the software with several commercial EDA design tools. The model building in CFD-Micromesh is very fast and controlled by a user-friendly graphical user interface (GUI). The automatically generated three-dimensional device models, using the unstructured 3-D computational mesh in DTF format, can be imported directly into CFDRC's simulator CFD-ACE+ for multi-physics simulations.

CFD-Micromesh was recently extended with a capability to read a fabrication process (layer structures) description in a standard format called **SIPPs** (Standard Interconnect Performance Parameters). The format is being developed by several big semiconductor companies, like Si2, AMD, Motorola, IBM, Cadence, Avanti, Mentor Graphics, and others, with participation of

CFDRC (more info: http://www.si2.org/sipps/). SIPPs layer data are typically imported in connection with a layout in GDSII format, which makes together a complete 3-D description of a design. This capability makes CFD-Micromesh a very attractive modeling tool also for VLSI electronics industry, in particular for analysis of interconnects and PCBs. CFDRC has already started an aggressive entering into this market, and we are planning to expand it in near future.

As a part of the marketing campaign, a **free evaluation version of CFD-Micromesh** is offered for download (for a limited time) from the web site http://www.cfdrc.com/~micromesh.

This version of CFD-Micromesh imports CIF and GDSII layouts, reads the SIPPs process description format, and includes direct interface to Virtuoso$^{(TM)}$ layout editor from Cadence. The evaluation version builds automatically 3-D solid models from layout and process data, and allows the user to view them interactively.

Finally, CFDRC has negotiated an agreement with **Cadence Design Systems**, Inc. to develop interfaces and integration of CFDRC's MEMS simulation software with Cadence CAD tools. CFD-Micromesh will be a part of Cadence CAD Environment, used as a "3-D Project Viewer" from Virtuoso layout editor from Cadence (see Figure 5).

6.2.2 Technology Transfer

Technology Transfer to Industry

Additionally to the industrial contacts and projects mentioned in the previous section, as a result of this project CFDRC provided software, training, and support oriented for MEMS design to the following companies:
- **Aclara**
- **Procter and Gamble**
- **Kodak**
- **Lucent Technologies**
- **Hewlett-Packard**

Technology Transfer to Academia

The academic parties of this project have used CFD-ACE+ software as a design, research, and educational tool. CFDRC has provided software, training, and support in exchange for constructive feedback, technology qualification, and recommendations. The following academic institutions have been involved in those of activities within this project:
- **Carnegie Mellon University**
- **University of Florida**
- **Stanford University**
- **Cornell University**
- **Georgia Tech**
- **University of California Los Angeles (UCLA)**
- **University of California Berkeley**
- **Drexel University**

- **University of California, Irvine**
- **NC State University**
- **Pennsyl. State University**
- **MIT**
- **University of South AL**
- **University of Central FL**
- **University of Sydney**
- **University of Washington**
- **University of Neuchatel**
- **University of Minnesota**

Talks / Presentations (not listed in the published References)

The progress of the project was presented at each DARPA Composite CAD PI Meeting, between October 1997 and August 2000. In addition, the following presentations related to this project took place:

- During the *MSM'98 Conference* (April 6-8, 1998, Santa Clara, CA), three presentations were made:
  - A.J. Przekwas and A. Krishnan, "ACE+MEMS: An Integrated Multi-Disciplinary CAD System for Micro-Electro-Mechanical Systems (MEMS)"
  - H.Q. Yang and A.J. Przekwas, "Computational Modeling of Microfluidic Devices with Free Surface Liquid Handling"
  - M.M. Athavale, H.Y. Li, A.J. Przekwas, B. Piekarski, R. Zebo, and S. Tenney, "Modeling 3-D Fluid Flow for a MEMS Laminar Proportional Amplifier" (in collaboration with Army Research Laboratory, Adelphi, MD)

- At the *American Institute of Chemical Engineering (AIChE) Conference on Microreactors* in New Orleans, Louisiana, March 8-12, 1998, a CFDRC paper entitled, "Integrated Computational Tools for Interdisciplinary Design of Microreactors", by M.G. Giridharan, A. Krishnan, S. Krishnamoorthy, and A.J. Przekwas, was presented.

- Dr. A.J. Przekwas was invited to the European Workshop on MEMS Modeling (organized by Prof. J. Korvink of the Univ. of Freiburg, Germany, in fall 1998) to present ACE+MEMS R&D projects and software.

- Presentation "Generation of Reduced Models for MEMS" (by Andrzej Przekwas, CFDRC) at the *Workshop on Interdisciplinary Design and Simulation Tools for Microsystems*, in Munich, Germany, June, 1998.

- Presentation "Reduced Model Generation for Microfluidic Systems" (by Andreas Klein and Andrzej Przekwas, CFDRC) at the *2nd Workshop on Interdisciplinary Design and Simulation Tools for Micro- and Biomedical Fluidic Applications* in Berlin, Germany, June 17, 1999.

- "Multi-Physics Simulation Tools For Design And Optimization Of CBW Sensors", presented by Andrzej J. Przekwas and Vinod B. Makhijani, at DARPA SIMBAD Meeting, April 10, 2000, Washington DC

6.3   Recommendations and Plans for Further Research

During the course of this project several new capabilities have been implemented in CFD-ACE+ facilitating automated creation of 3-D models and automated generation of compact models for MEMS devices for system level simulations. In the last phase of the project, focused on demonstrations and practical applications, we received a substantial feedback and assessment of the ACE+ code in the area of multiphysics modeling, model setup, interfaces with EDA tools, compact model generation, and engineering data extraction. ACE+ proved robust in generation of reduced models for linear problems e.g. electrostatics, deformation, and unique for nonlinear air dumping. Several customers requested macromodel extraction capability for coupled domain physics e.g. electrostatics and deformation, thermal and mechanical disciplines. We have developed, demonstrated, and delivered this capability in the last year. Despite several efforts of our team and others (MIT, CMU, …) no robust general method could be established for nonlinear or strongly coupled problems e.g. fluidics, mixing, chemistry.

For nonlinear problems we recommend, and help, our customers to use simplified mathematical formulation of general conservation equations with semi-empirical parameters derived from 3-D simulations e.g. synthetic jet models, orifices, valves, …We have also developed a new modeling concept "Filament Model" to facilitate high (system) level modeling in ACE+. This technique is being further developed in the parallel DARPA project on "VLSI CAD for Microfluidics". CFDRC is fully committed to further development of system–level simulations and model extraction for microsystems. The demand for this capability will be steady growing as the basic MEMS and microfluidic devices are better established. We will further evolve, improve, and commercialize the model extraction and system-level modeling with existing resources from CFDRC, government, and industry.

Based on the experience gained in this project we have identified several areas for further research, model development, and CFD-ACE+ software improvement. They can be grouped in following categories:

A.   Interfaces with EDA Tools

In the present project, we have developed new tool, CFD-Micromesh, to interface microelectronic and mechanical CAD domains. The code is rapidly gaining acceptance and interest from broad range of applications. It is one of the biggest achievements of this project. It has however several limitations for applications in microfluidic MEMS and for BioMEMS. The most urgent CFD-ACE+ needs for system-level design are:
- semiautomatic block structured grid generation,
- mixed structured-unstructured grids,
- adaptive octree grids,
- two-way link with CFD-GEOM,
- parametric modeling in Micromesh,
- Python scripting model setup using Micromesh functions,
- automated construction of filaments in Micromesh,
- tighter link with process fabrication and layout tools,
- boolean operations on masks for multilayer microstructures.

B. Automation and Parameterization of Model Setup

At present, CFD-ACE+ is suitable for single runs of a specific design or pre-arranged multi-runs for single variation in e.g. boundary conditions. There is a strong need for parametric modeling, scripting, optimization, and inverse problem solutions. A first step has been recently made at CFDRC by developing a Python scripting capability for CFD-GEOM. We hope to expand this capability to all other modules of ACE+, like GUI, DTF, VIEW, and Micromesh. Advanced academic and industrial users should be able to link the functions and modules in ACE+ modeling dataflow. Coupling of ACE+ with an optimization module would answer requests from several customers who have requested device optimization capability.

C. Mixed-Dimensionality Modeling for Micro-Bio-Fluidics

In several circumstances, it will be very difficult to develop compact or circuit models for key devices, like bioreactor, biodetector, etc. We would like to develop a mixed-level and mixed-dimensionality modeling capability. We have demonstrated it on the coupling of ACE+ with SABER. There is a big academic and commercial interest to develop direct interface between ACE+ and SPICE. We also plan to expand the Filament modeling concept for mixed-dimensionality modeling. Further improvements in model setup, meshing, and data post-processing are needed.

D. Extension of Compact Model Generation for New Microdevices

New DARPA programs have been initiated in BioChips, Power MEMS, and other new areas are anticipated, e.g. MOEMS, RF-MEMS, Bio-Photonics, bio-medical, etc. Existing compact model extraction capabilities in ACE+ have been shown for mechanical, thermal, and some fluidic devices. There is a strong demand (from other DARPA project teams in particular) for compact models for other disciplines such as electrokinetics, electrochemistry, biochemistry, photonic devices, optoelectronic devices, VLSI interconnects, fluidic cooling circuits, etc.

E. Expansion of Model Libraries

Most of the high-fidelity models constructed in this project are nonparametric models saved as DTF files. There is an absolute demand for parametric models. We have started to develop Python scripts for MEMS. There is a great potential, but a lot remains to be done to implement Python in all other tools.

We would like to offer Python scripts over the Internet, and allow other users (e.g. students) to upload their models and share them. We will also explore the idea of e-business with others. Closer collaboration with the *MEMS Exchange*, which has already started, would be beneficial.

F. Strong Interface between ACE+ and System Level CAD (SPICE)

Most of the system-level simulations in the Composite CAD Program were tested and demonstrated with the Saber software from Analogy. The Analogy company has been recently acquired by Avant!, and the future of Saber and its market position is not sure. On the other

hand, behavioral models implemented in Saber had advantage over the SPICE models in that they offered more direct representation and simulation of non-electrical phenomena (fluidic, mechanical, thermal, etc), readily available to designers in hydraulic or mechanical displacement/force units, without additional translation to electrical equivalents. The MAST language in Saber has also offered a very flexible way of adding to simulations custom-designed models generated by users. This is why CFDRC has developed new software tools in CORBA to enable direct coupling between Saber and ACE+ simulations.

Nevertheless, SPICE remains the most popular circuit simulator in the world, and it is available in several free versions for many users. During this project, we have demonstrated generation of a compact model of an arbitrary microfluidic channel, in the form of nonlinear equivalent circuit. It is very attractive and useful to a wide community of SPICE users who are very often also designers of microfluidic MEMS and microsystems in the domain of bio-medical and chemical engineering, integrated very often with control and drive electronics. Because of that, and also due to not sure future of Saber, CFDRC will pursue the idea of integrating ACE+ with SPICE circuit modeling capabilities. In this endeavor we plan to collaborate with the group of Michael Shur at RPI (developers of AIM-SPICE), and the UC Berkeley CAD Group – original creators of SPICE and CIDER, as well as UC Berkeley BSAC (Kris Pister) Group which developed SUGAR, a system-level simulation program for MEMS devices.

G.   Software Verification on Design of Practical Microsystems

CFDRC is involved in MEMS related projects with several academic, commercial, and government partners. A lot of effort is provided to support our partners. We need to improve and adapt CFD-ACE+ environment to allow more flexible access to the modules of the code and to the dataflow.

More partnership projects with US industry are needed, and planned, to adapt the code for practical design environments. Much effort is needed to simplify and automate the design process for non-experts. Several of our key customers indicated that there is no available graduates with multiphysics expertise needed to operate the high-fidelity software such as CFD-ACE+. This indicates that even larger effort is required from CFDRC to make our multiphysics software more accessible for new users and to allow them a faster learning curve.

7   REFERENCES

7.1   Published Papers Resulting from This Project

Furmanczyk, M., Tan, Z.Q., Turowski, M. and Przekwas, A., "CFD-Micromesh: An Automatic 3-D Model and Mesh Builder for Microsystem Simulations", *Int. Conf. MIXDES 2000*, Gdynia, Poland ,15-17 June 2000.

Jing, Q., Luo, H., Mukherjee, T. Carley, L.R. and Fedder,G.K. "CMOS Micromechanical Bandpass Filter Design Using a Hierarchical MEMS Circuit Library", *IEEE Int. Conf. MEMS 2000*, Miyazaki, Japan, 23-27 January, 2000.

Mukherjee, T., "CAD for Integrated MEMS Design," *Proc. Design, Test Integration, and Packaging of MEMS/ MOEMS (DTIP 2000)*, Paris, France, 9-11 May, 2000, pp. 3-14.

Mukherjee, .T., Fedder, G.K. and White, J., "Emerging Simulation Approaches for Micromachined Devices," submitted for publication in *IEEE Trans. on CAD*, June 2000.

Przekwas, A., Chen Z. and Turowski, M. "High Fidelity and Compact Models of Synthetic Jets and Their Application in Aerodynamics and Microelectronics", *International Mechanical Engineering Congress and Exposition - Microfluidics Symposium,* Nashville, Tennessee, USA, 14-19 Nov. 1999.

Przekwas A., Turowski, M. and Chen Z.J., "High-Fidelity and Reduced Models of Synthetic Microjets", *Int. Conf. MSM 2000*, San Diego, California, 27-29 March, 2000.

Smith, B. L., Trautman, M. A., and Glezer, A., "Controlled Interactions of Adjacent Synthetic Jets," AIAA Paper 99-0669, *37th AIAA Aerospace Sciences Meeting*, Reno, NV, January, 1999.

Tan, Z.Q, Furmanczyk, M., Turowski, M. and Przekwas, A. "CFD-Micromesh: A Fast Geometrical Modeling and Mesh Generation Tool for 3-D Microsystem Simulations", *Int. Conf. MSM 2000*, San Diego, California, 27-29 March, 2000.

Turowski, M., Chen, Z.J. and Przekwas, A., "Automated Generation of Compact Models for Fluidic Microsystems", accepted for *CAD, Design and Test Conference*, Paris, France, 9-11 May, 2000.

Turowski, M., Chen, Z., and Przekwas, A. "Compact Models Of Microchannels For Fluidic Microsystems", *Int. Conf. MIXDES 2000*, Gdynia, Poland, 15-17 June 2000.

Turowski, M., Chen, Z. and Przekwas, A.: "High-Fidelity and Behavioral Simulation of Air Damping in MEMS" *Second International Conference on Modeling and Simulation of Microsystems, Semiconductors, Sensors and Actuators - MSM'99*, San Juan, Puerto Rico, U.S.A., 19-21 April, 1999, pp.241-244.

Turowski, M., Chen, Z. and Przekwas, A.: "Squeeze Film Behavior in MEMS for Large Amplitude Motion - 3-D Simulations and Nonlinear Circuit/Behavioral Models", *IEEE/VIUF International Workshop on Behavioral Modeling and Simulation (BMAS'98)*, Orlando, Florida, USA, 27-28 Oct., 1998.

Turowski, M., Przekwas, A., Vemuri, S. and Fedder, G.: "Physical And Behavioral Simulations Of Squeeze Film Damping in MEMS", *6th Int. Conf. "Mixed Design of Integrated Circuits and Systems" - MIXDES'99*, Kraków, Poland, 17-19 June 1999, pp.279-284.

Vemuri, S., "Behavioral Modeling of Viscous Damping in MEMS," *Master's Thesis, Carnegie Mellon University*, August 2000.

Vemuri, S., Fedder, G.K. and Mukherjee, T. "Low-order squeeze film model for simulation of MEMS devices", *Int. Conf. MSM 2000*, San Diego, California, 27-29 March, 2000.

Vu-Quoc, L., Deng, H., Tan, X.G., "Geometrically-exact sandwich shells: The dynamic case", *Computer Methods in Applied Mechanics and Engineering*, to appear, 2000.

Yu, E., Przekwas, A., Turowski, M. and Furmanczyk, M: "Automatic Generation of Reduced Thermal Models of Electronic Packages and Evaluation of These Models in System Level

Design Applications", *ASME International Mechanical Engineering Congress and Expositions*, Anaheim, California, USA, 15-20 November, 1998.

7.2 **Other References**

Arklic E.B., Breuer K.S. and Schmidt M.A., "Gaseous flow in microchannels," *ASME FED* 197, 1994, pp. 57-66.

Bahram Nour-Omid, W.S. Dunbar, A. W., "Lanczos and Arnoldi Methods for the Solution of Convection-diffusion Equation," *Computer Methods in Applied Mechanics and Engineering* 88, pp. 75-95, 1991.

Blech J.J., "On Isothermal Squeeze Films," *J. Lubrication Tech.*,105, pp. 615-620, 1983.

Bourouina T., Grandchamp J.-P., "Modeling Micropumps with Electrical Equivalent Networks", *J. Micromech. Microeng.*," 6, pp. 398-404, 1996.

Burgdorfer A., "The Influence of the Molecular Mean Free Path on the Performance of Hydrodynamic Gas Lubricated Bearings," *Journal of Basic Engineering*, Trans. ASME, 81, pp. 94-99, Mar. 1959.

Burgeois C., Portret F., and Hoogerwerf A., "Analytical Modeling of Squeeze-Film Damping in Accelerometers," *Transducers '97*, Chicago, Illinios, USA, June 1997, pp. 1117-1120.

Cercignani C. and Pagani, C. D. "Variational Approach to Boundary-value Problems in Kinetic Theory," *The Physics of Fluids*, 9, pp. 1167-1173, June 1996.

CFD-ACE+ Theory Manual, version 6.0, CFD Research Corporation, Huntsville, Alabama, January 2000, (http://www.cfdrc.com).

Cho Y., Pisano A. P., and Howe R. T., "Viscous Damping Model for Laterally Oscillating Microstructures," *Journal of Microelectromechanical Systems*, 3, pp. 81-87, June 1994.

Darling R.B., Hivick C., and Xu J., "Compact Analytical Model for Squeeze Film Damping with Arbitrary Venting Conditions," *Transducers '97*, Chicago, Illinois, USA, June 1997, pp. 1113-1116.

Deshpande M., J. Gilbert, R.L. Bardell, F.R. Forster, "Design Analysis of No-moving-parts Valves for Micropumps", *ASME 1998, DSC*-66, pp. 153-158, *MEMS-1998.*

Fedder, G. K., "Simulation of Microelectromechanical Systems," *PhD thesis, University of California at Berkeley*, Berkeley, California, 1994.

Forster, F. Bardell R., Afromowitz M., Sharma N., "Design, Fabrication, and Testing of Fixed-Valve Micropumps", *Proc. ASME Fluids Engineering Division, IMECE-1995*, 234, pp. 39-44.

Gallivan, K. & Grimme, E. "A Rational Lanczos Algorithm for Model Reduction," *Numerical Algorithm* 12, pp. 33-63, 1996.

Hassan, A.A., "Numerical Simulations and Potential Applications of Zero-Mass Jets for Enhanced Rotorcraft Aerodynamic Performance," AIAA-98-0211, 1998.

Hung, E. S. & Senturia, S. D. [1999], Generating effcient dynamical models for micro-electromechanical systems from a few finite-element simulation runs, IEEE Journal of Microelectromechanical Systems 8(3), pp. 280-289.

Krall, L.D., et al., "Numerical Simulation of Synthetic Jet Actuators," AIAA-97-1824, 1997.

Lanczos, C., "An Iteration Method for the Solution of the Eigenvalue Problem of Linear Differential and Integral Operators," *J. Res. Nat. Bur. Standards* 45, pp. 255-282, 1950.

Lai Y.G. and Przekwas A., "A Finite-Volume Method for Fluid Flow Simulations with Moving Boundaries", *J. Comp. Fluid Dynamics*, 2, pp. 19-40, 1994.

Leger, P. [1986], The Use of Load Dependent Vectors for Dynamic and Earthquake Analyses, *PhD thesis*, University of California at Berkeley, Berkeley, California.

MAST Reference Manual, Release 5.0, Analogy Inc., Beaverton, OR, 1999.

Paige, C., "Computational Variants of the Lanczos Method for the Eigenproblem," *Numerical Algorithm* 8(7), pp. 373-381, 1972.

Pan F., Kubby J., Peeters E., Tan, A.T. and Mukherjee S., "Squeeze Film Damping Effect on the Dynamic Response of a MEMS Torsion Mirror," *MSM'98*, Santa Clara, CA, April 1998, pp. 474-479.

Przekwas, A.J., Athavale, M.M. and Yang, H.Q., "Computational Design of Membrane Pumps with Active/Passive Valves for Microfluidic MEMS," *Proc. 2nd Int. Conf. On Modeling and Simulation of Microsystems, MSM '99*, San Juan, Puerto Rico, 1999.

Rizzetta, D.P., Visbal, M.R. and Stanek, M.J., "Numerical Investigation of Synthetic Jet Flow Fields," AIAA-98-2910, 1998.

Rohsenow W. M., Choi, H. "Heat, Mass and Momentum Transfer", Prentice-Hall, Inc, 1961.

Shakhov E. M., "Rarefied Gas Shear Flow Between Two Movable segments of Parallel Plates," *Fluid Dynamics*, 30(3), pp. 462-466, 1995.

Smith, B.L. and Glezer, A., "Vectoring and Small-Scale Motions Effected in Free Shear Flows Using Synthetic Jets," *Phys. Fluids*, 10(9), pp. 2281, 1998.

Stout P., Yang H.Q., Dionne P., Leonard A., Tan Z., Przekwas A., Krishnan A., "CFD-ACE+MEMS : A CAD System for Simulation and Modeling of MEMS", *Int. Symp. on Design, Test, and Microfabrication of MEMS/MOEMS*, Paris, France 1999, *SPIE* 3680, pp. 328-339.

Teegarden D., Lorenz G., and Neul, R. "How to Model and Simulate Microgyroscope Systems," *IEEE Spectrum*, July 1998, pp.66-75.

Vandemeer J.E., "Nodal Design of Actuators and Sensors (NODAS)," *M.S. Thesis, Carnegie Mellon University*, May 1998(a).

Vandemeer J.E., Kranz M.S., and Fedder, G. "Hierarchical Representation and Simulation of Micromachine Inertial Sensors," *MSM'98*, Santa Clara, April 1998(b), pp.540-545.

Veijola T., "Compact Damping Models for Lateral Structures Including Gas Rarefaction Effects", *MSM 2000*, San Diego, CA, March 2000.

Veijola T., "Accelerometer Level 3 and 4 Models in APLAC," *Tech. Rep. CT-36*, Helsinki University of Technology, Circuit Theory Laboratory, Helsinki, Finland, April 1998(a).

Veijola T., H. Kuisma, and J. Lahdenpera, "Dynamic Modeling and Simulation of Microelectromechanical Devices with a Circuit Simulation Program," *MSM'98*, Santa Clara, California, USA, April 1998(b), pp.245-250.

Veijola T., Kuisma H. and Lahdenpera J., "Equivalent Circuit Model of the Squeeze Gas Film in a Silicon Accelerometer," *Sensors and Actuators A,* 48, pp. 239-248, 1995.

Veijola T., Kuisma H., and Lahdenpera J., "The Influence of Gas-surface Interaction on Gas Film Damping in a Silicon Accelerometer," *Sensors and Actuators A*, 66, pp. 83-92, 1998(c).

Voigt P., G. Schrag, G. Wachutka, "Electrofluidic Full-system Modeling of a Flap Valve Micropump Based on Kirchhoffian Theory", *Sensors and Actuators A*, 66, pp. 9-14, 1998.

Wilson, E., Yuan, M. & Dickens, J. [1982], Dynamic Analysis by Direct Superposition of Ritz Vectors," *Earthquake Engineering and Structural Dynamics* 10(6), pp. 813-821.

Yang H. Q. and Przekwas A. J., "Computational Modeling of Microfluidic Devices with Free Surface Liquid Handling", *MSM'98*, Santa Clara, California, 1998, pp. 498-505.

Yang Y.-J. and Senturia S.D., "Numerical Simulation of Compressible Squeezed-Film Damping," *Solid-State Sensor and Actuator Workshop*, Hilton Head, South Carolina, 1996 pp. 76-79.

Yang Y.-J.,. Gretillat, M.-A and Senturia S.D., "Effect of Air Damping on Nonuniform Deformations of Microstructures," *Transducers '97*, Chicago, Illinois, USA, June 1997, pp. 1093-1096.

Zhang X. and Tang W. C., "Viscous Air Damping in Laterally Driven Microresonators," *Sensors and Materials*, 7(6), pp. 415-430, 1995.

Georgia Tech MEMS Materials

Material	Density (Bulk) g/cm^3	Density (Film) g/cm^3	Young's Modulus (Bulk) GPa	Young's Modulus (Film) GPa	Poisson's Ratio (Bulk)	Poisson's Ratio (Film)	Thermal Exp. Coeff. (Bulk) 1E-06/C	Thermal Exp Coe. (Film) 1E-06/C
Aluminum	2.70 [1]	N/A	70.0 [1]	47.24 - 74.14 [1]	0.346 [2]	N/A	23.2 - 33.8 [1]	23.0 [1]
Chromium	7.16 [2] - 7.19 [1]	N/A	277.0 [2]	140 [1] - 215 [1]	0.215 [2]	N/A	5.1 [2]	N/A
Copper	8.90 [3] - 8.96 [1]	N/A	110 [3] - 132 [2]	N/A	0.330 [3] - 0.360 [1]	N/A	16.12 [2] - 20.0 [1]	N/A
Diamond	3.515 [2]	N/A	1143 [1]	800 [1] - 1140 [1]	0.104 [2]	N/A	1.02 [2]	N/A
Gold	19.2 [1] - 19.3 [2]	N/A	77.2 [2]	80 [1]	0.425 [2]	N/A	14.1 [1] - 16.5 [1]	14.3 [1]
Nickel	8.91 [1]	N/A	210 [3] - 220 [2]	200 [1]	0.299 [2]	N/A	12.7 [1] - 17.2 [1]	N/A
Platinum	21.44 [1]	N/A	N/A	170 [1]	N/A	N/A	8.90 [1] - 10.2 [1]	N/A
Polyimide	N/A	N/A	N/A	7.5 [1] - 15.0 [1]	N/A	0.10 [1] - 0.45 [1]	N/A	6.0 [1] - 250.0 [1]
Polyimide - PI 2611D	N/A	N/A	N/A	8.3 [1]	N/A	N/A	N/A	3.0 [1]
Polysilicon	N/A	N/A	181 [1] - 203 [1]	N/A	N/A	N/A	N/A	N/A
PVDF	N/A	1.78 [1]	N/A	2.0 [1]	N/A	N/A	N/A	N/A
PVDF-TrFE	N/A	N/A	N/A	2.3 [1]	N/A	N/A	N/A	140 [1]
Silicon	2.30 [1] - 2.33 [1]	N/A	162 [2]	162 [1]	0.222 [2]	N/A	2.30 [1] - 4.30 [1]	2.6 [1]
Silicon Carbide	3.20 [1] - 3.22 [1]	N/A	N/A	100 [1] - 440.71 [1]	N/A	N/A	3.30 [1] - 5.94 [1]	N/A
Silicon Dioxide	2.19 [1] - 2.80 [3]	2.20 [1]	48 [3] - 83 [3]	N/A	0.14 [2] - 0.27 [3]	0.17 [1]	0.50 [2] - 0.55 [1]	0.40 [1]
Silicon Nitride Si3N4	3.10 [1]	3.10 [1]	385 [1]	130 [1] - 380 [1]	N/A	N/A	0.8 [1] - 3.66 [1]	N/A
Silver	10.50 [1]	N/A	19.2 [1] - 23.4 [1]	N/A	N/A	N/A	N/A	N/A
Stainless Steel	7.85 [3] - 7.90 [1]	N/A	190 [3] - 210 [3]	240 [1]	0.27 [3] - 0.30 [3]	0.3 [1]	17.0 [3] - 17.3 [1]	N/A
Titanium	4.50 [3] - 4.51 [1]	N/A	110.0 [3] - 115.0 [1]	102.6 [1] - 110.0 [1]	0.33 [3]	N/A	25.0 [3]	N/A
Tungsten	19.00 [3] - 19.30 [1]	N/A	340 [3] - 410 [1]	410 [1]	0.20 [3] - 0.280[2]	N/A	4.5 [3] - 4.8 [3]	N/A
Zinc Oxide	N/A	N/A	12.0 [1] - 20.0 [1]	14.0 [1] - 23.0 [1]	N/A	N/A	N/A	N/A

[1] MEMS Clearinghouse Materials Database (mems.isi.edu)

[2] "Materials Handbook for Hybrid Microelectronics", J.A. King, editor, Artech House, Inc., 1988.

[3] "Mechanics of Materials", J. Gere and S. Timoshenko, PWS-KENT Publishing Company, 1990.

150

CFD-Micromesh

## Fast Geometrical Modeling and Mesh Generation for Microsystems

Highlights

❖ **Fast, automatic generation of three-dimensional (3D) models:**
  - geometric modeling, and
  - mesh generation.

❖ **3D models built automatically <u>from layouts</u>:**
  - **CIF** and **GDSII** layout formats
  - any bitmap image (**GIF, JPEG, BMP**, etc).
  - designs from Electronic Design Automation (**EDA**) **Tools**, including direct interface from **Cadence's Virtuoso**™ layout editor

❖ **Accepts <u>fabrication process description</u>:**
  - user-defined layer properties (planar or conformal layers)
  - CFD-Micromesh **Technology Files**
  - **SIPPs** format (Standard Interconnect Performance Parameters, Si2)

❖ **Automatically generates 3D computational mesh for CFD-ACE+** multi-disciplinary physics solver. The user can define boundary condition types and define mesh resolution directly on layouts.

❖ Can generate meshes in solid regions, void spaces (fluid regions), or in both, in **time between 2 to 120 seconds**.

❖ **Very intuitive graphical user interface** (GUI) designed for microelectronics and microsystems engineers.
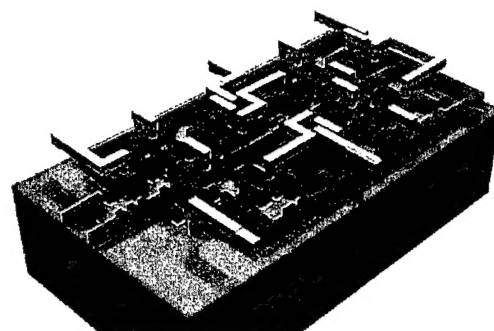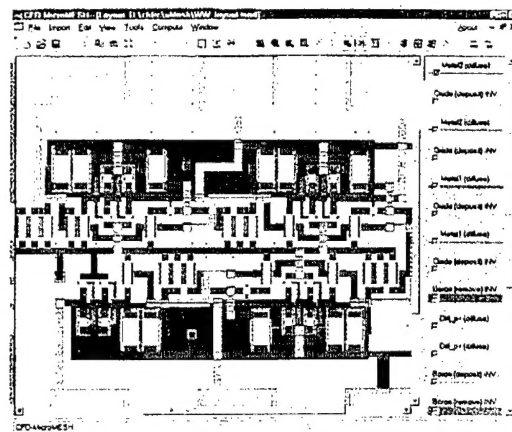
Layout (bitmap image, CIF, GDSII)

3D solid model

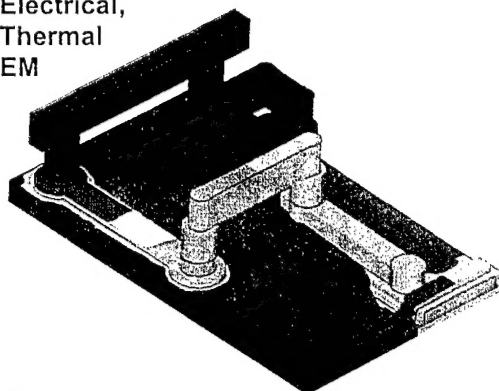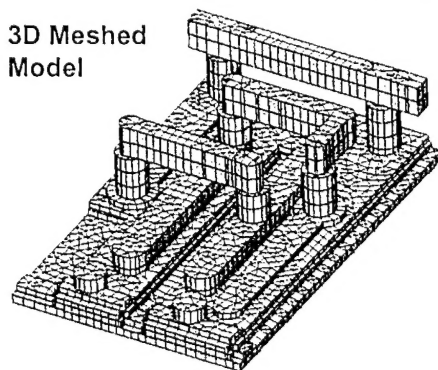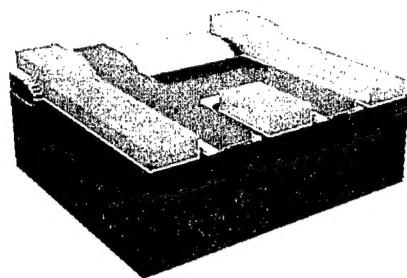Temperature and stress modeled in CFD-ACE+
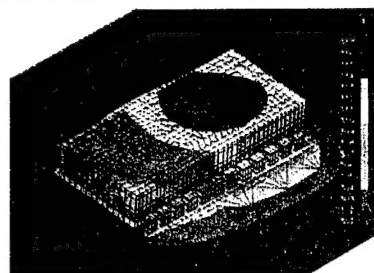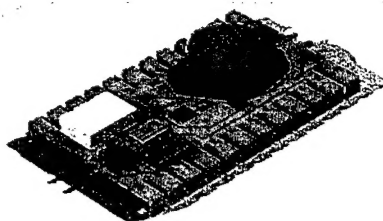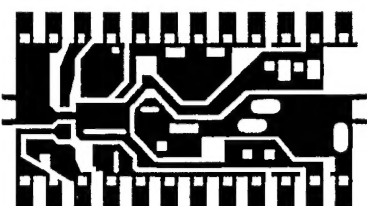
Semiconductor Devices, Process, and Packages

VLSI Interconnects

3D Meshed Model

3D Simulation:
- Electrical,
- Thermal
- EM

CFD Research Corporation
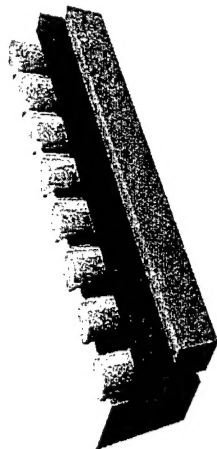
215 Wynn Drive , Huntsville, Alabama 35805, USA Tel. 256-726-4800, Fax: 256-726-4806, www.cfdrc.com
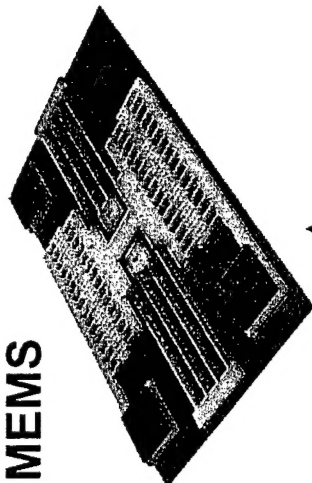
CFD-Micromesh - APPLICATION AREAS

CFD Research Corporation
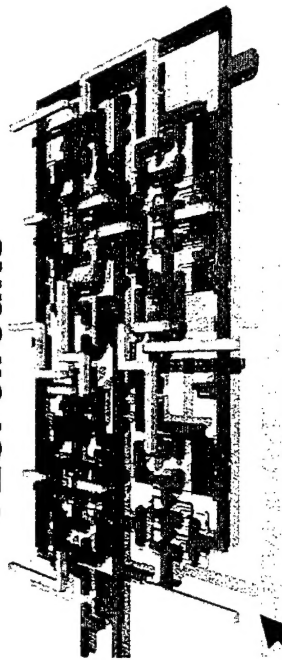
CFDRC

VLSI circuits

Interconnects

IC Devices

MEMS

OPTOELECTRONICS

3D DRC

Electronic Packages

μ Fluidics

CFD-MicroMESH - [Layout D:\cfdrc\uMesh\WW_layout]
File Import Edit View Tools Compute Window
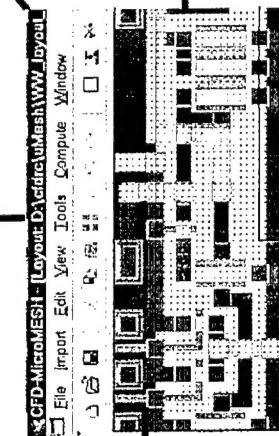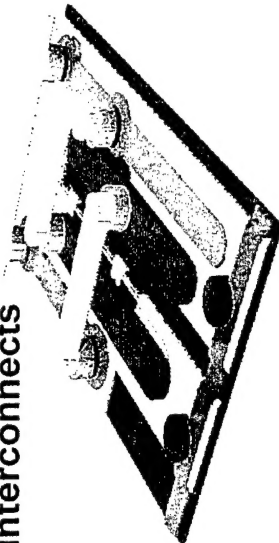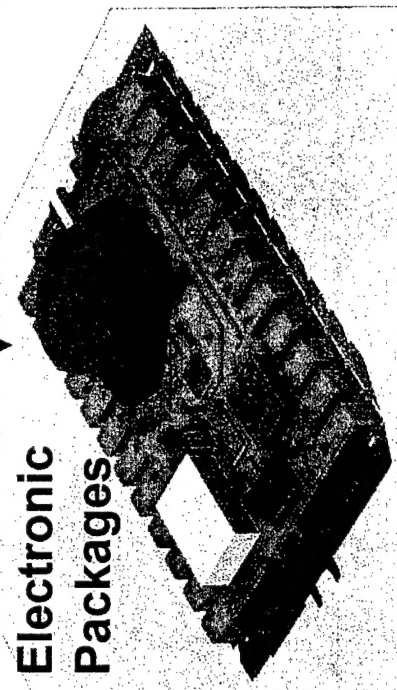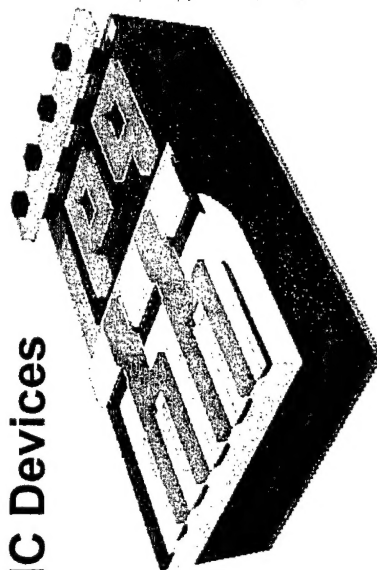
MISSION
OF
AFRL/INFORMATION DIRECTORATE (IF)

The advancement and application of Information Systems Science

and Technology to meet Air Force unique requirements for

Information Dominance and its transition to aerospace systems to

meet Air Force needs.